Optically Tunable Memristors Based On Organic-Inorganic Composite Materials

By

Ayoub H. Jaafar

BSc., MSc. (University of Technology)

A thesis submitted in partial fulfilment of the requirements for the degree of Doctor of Philosophy to the School of Mathematics and Physical Sciences

The University of Hull

November 2018

DECLARATION OF ORIGINALITY

I hereby declare that the results presented in the results chapters of this thesis are totally my own original work and has not been submitted in any form for another degree at any university. The literature and theoretical background from books and journals are fully cited in the text and a list of references is given at the end.

Abstract

Memristors or resistive memory devices (also called RRAMs) are one of the most promising emerging memory technologies for the next generation of memory devices with potential applications in computer memory, logic operations and neuromorphic computing. Memristor devices are unique because they have non-volatile memory operation in combination with fast nano-second switching, low power operation and high-density integration using nanoscale crossbar-array architectures. Fundamentally, memristors are two terminal devices; however, in certain applications, there are advantages in having an additional degree of freedom available to control their switching and electronic properties. This thesis work examines how this can be achieved using light.

Modulation of the electronic properties of memristors by optical means offers a new level of functional control, enabling the development of new types of optoelectronic devices and circuits, such as photonic integrated circuits with memory elements controllable by light. Memristors also have important applications in neuromorphic computing and in that context the dynamic and spatial patterning by light opens the route to new optically configurable and tunable synaptic circuits. In this thesis, two novel types of optically tunable switching memristors based on hybrid organic-inorganic composites are developed. The first type of device consists of vertically aligned zinc oxide nanorods (ZnO NRs) integrated with an optically active polymer, poly(disperse red 1 acrylate) (PDR1A), which expands and contracts upon irradiation by wavelength and polarization specific light. The second device type is instead based on gold nanoparticles (Au NPs) distributed in discrete conducting pathways throughout the same photoactive polymer. These break or re-connect upon exposure to light, and because there are only a few conducting pathways in a single device, much greater changes (3-4 orders of magnitude) occur in the electrical conductivity. Both device types exhibit optically dependent switching properties and have too the advantage of fabrication by very simple, low cost, solution-based methods.

The electronic properties of both optical RRAMs show bipolar switching behaviour with either sharp digital-like switching (Au NPs device) or a complex transition with space charge current limited like behaviour (ZnO NRs device). Both device types exhibit optical control of the devices' electronic properties and in particular, we demonstrate for the first time, latched optical SET and RESET switching processes.

Lastly, this thesis examines how optical memristors can be used to control learning in neuromorphic applications. We demonstrate optical control of short-term and long-term memory and tunable learning through spike timing dependent (synaptic) plasticity. We believe this has important applications in the dynamic patterning of memristor networks, whereby both spatial and temporal patterning *via* light allows the development of new optically reconfigurable neural networks, adaptive electronic circuits and hierarchical control of artificial intelligent systems.

Acknowledgement

I would like to use this opportunity to express my thanks to everyone who helped and supported me during my PhD research. First, I would like to express my gratitude to my supervisor, Dr Neil T. Kemp, for his advice, support, and encouragement during the last four years. His knowledge and experience have made my research period at the University of Hull successful and enjoyable. I was so lucky to have a great and friendly mentor. It is my pleasure to express my thanks to the Iraqi Ministry of Higher Education and Scientific Research, the University of Baghdad, and Iraqi Cultural Attachè in London for the scholarship and financial support of this research. I would also like to give a special gratitude to my family, relatives, and friends for all their love and support. I want to thank the University of Hull for facilitating the research environment during this research period. In addition, many thanks to my friends and colleagues at the University of Hull, specifically Rob Gray, Alex Gee, Huda Al Sulaimi, Charlotte Eling, and Abdullah Hamza for their help and support. I would also like to thank Dr Emanuele Verrelli and the technicians (Dave Stavenau, and Robert Farley) for their help. Finally, I would like to thank Ann Lowry and Garry Robinson for the help with the TEM and SEM imaging, respectively.

Table of Contents

List of Figures

LIST OF FIGURES

Abbreviations

μ	Electronic Drift Mobility
Ar^+	Argon Ion
Au NPs	Gold Nanoparticles
C-AFM	Conductive Atomic Force Microscopy
CFs	Conductive Filaments
CMOS	Complementary Metal Oxide Semiconductor
D	Thickness
DI	De-Ionized Water
DRAM	Dynamic Random Access Memory
E	Electric Field.
E_C	Energy of the Bottom of the Conduction Band
ECM	Electrochemical Metallization
EDX	Energy Dispersive X-ray Spectroscopy
E_F	Fermi Energy Level
E_t	Trap Energy
FRAM	Ferroelectric Random Access Memory
H	Planck’s Constant
HRS	High Resistance State
I	Current
ITO	Indium Tin Oxide
J	Current Density
k	Boltzmann’s Constant
LC	Liquid Crystal
LRS	Low Resistance State
LTM	Long-Term Memory
LTP	Long-Term Plasticity
M	Metal Atoms
m^*	Effective Electron Mass
MIM	Metal Insulator Metal
MRAM	Magnetic Random Access Memory
MTJ	Magnetic Tunnel Junction
M^{z+}	Positive Metal Cations

ABBREVIATIONS

N_C	Density of States
NNH	Nearest Neighbour Hopping
N_t	Concentration of Traps
NVRRAM	Non-Volatile Resistive Random Access Memory
O_i^{2-}	Oxygen Anions
O_o	Oxygen Atoms
ϕ_B	Tunnelling Barrier Height
PCRAM	Phase Change Random Access Memory
PDR1A	poly (disperse red 1 acrylate)
P_r	Remnant Polarisation
P_{sat}	Saturated Polarisation
Q	Electric Charge
$q\varnothing_T$	Trap Energy Level
RRAM	Resistive Random Access Memory
SCLC	Space Charge Limited Current
SEM	Scanning Electron Microscopy
SRAM	Static Random Access Memory
STDP	Spike-Time-Dependent-Plasticity
STM	Short-Term Memory
STP	Short-Term Plasticity
T	Absolute Temperature
T_c	Curie Temperature
TEM	Transmission Electron Microscopy
THF	Tetrahydrofuran
V	Voltage
V_o^{2+}	Oxygen Vacancies
VRH	Variable Range Hopping
ZnO NRs	Zinc Oxide Nanorods
ε_R	Relative Dielectric Permittivity
σ_0	Electrical Conductivity
Φ	Magnetic Flux

Chapter 1. Research Overview

In this chapter, an introduction to memristors is briefly presented. The research objectives are provided as well. At the end of this chapter, the thesis organization and a list of published work and conference presentations will be presented.

1.1 Introduction

The past decade has seen significant efforts to find new memory technologies or a “universal memory” type that combines the advantages of the three main and current memory technologies, SRAM, DRAM, and Flash memory. Each of these memory types have their own specific advantages and disadvantages. SRAMs, for instance, are considered to have high read and write speeds and low power consumption, however, have the disadvantages of volatile memory, low density, and large size with each memory cell requiring six transistors. Because of this, they are not desirable for applications that require very large amounts of memory. On the other hand, DRAM architectures are high density and take up little space (one transistor and one capacitor), making them widely used semiconductor memories in commercial applications. DRAMs, however, have a short data retention time, and high power consumption because the memory cell needs to be periodically refreshed to maintain the stored data.

In comparison, Flash memory provides non-volatile data storage memory, where the data is retained even after the power is removed. This makes the Flash memory a low power consumption technology. In addition, Flash memory offers a high-density information storage device. Although Flash memory has wide application as data storage in MP3 players, removable storage cards, and cell phones, they have slow write times, making them undesirable for applications where data needs to be re-written constantly like in the main memory of computers. Flash memory also leaks charge after several hundred thousands of cycles and because of the design needed to minimize this problem, the dimensions of the cell means they are unsuitable for nanoscale architectures [1]. Flash memory also requires its own high voltage driver [2].

Several competing technologies have emerged in the race to be the next generation of non-volatile memories. These include Magnetic Random Access Memory (MRAM), Ferroelectric Random Access Memory (FRAM), Phase Change Random Access Memory (PRAM or PCM), and Resistive Random Access Memory (RRAM). MRAM and FRAM technologies are based on the magnetic tunnel junctions and the two states of polarisation of ferroelectric materials, respectively. Both MRAM and FRAM have received great interest due to their non-volatility, high read and write speeds, good endurance and data retention, and low power consumption. However, both technologies suffer problems with scaling. PCM, on the other hand, which uses the structural phase change between an amorphous phase (RESET process) and a crystalline phase (SET process) to store information, has high scalability, low programming energy, excellent endurance and retention, [3] but has significant reliability issues.

Resistive random access memory (RRAM) or memristor is based upon the switching between two different resistance states, the high resistance state (HRS) and the low resistance state (LRS) [4]. RRAM has received considerable attention due to its low power consumption, high endurance and data retention, low cost, and fast switching characteristics. RRAM architectures have also other advantages like high-density and simple cell memory structure using a crossbar design and vertical and horizontal architectures.

In recent years, researchers investigating solid-state RRAM devices have made significant progress in understanding the physical switching mechanisms and improving their fabrication. However, hybrid memristor devices, which consist of organic and inorganic materials are much less investigated in the field. Hybrid devices offer desirable advantages, such as large area, use of lightweight, flexible and low-cost substrates, high repeatability and device performance, and simple and low-cost fabrication methods, such as spin coating techniques [5–7]. In particular, many solid-state devices require high vacuum and high temperature deposition methods which are slow and costly for large scale production [8–11].

Controlling memristors properties by light offers new types of optoelectronic devices for sensory and synapses applications [12]. Optical or electronic modulation switches the device between low and high conducting states whilst modulation by both facilitates fine-tuning of the resistive memory properties and switching characteristics of the device. Applications, where this device could be used, include integrated circuits with memory elements switchable by light, adaptive circuits and optically reconfigurable and tunable synaptic circuits for neuromorphic computing applications and brain-inspired artificial intelligent systems. Therefore, the need for further understanding of the physics of the resistive switching mechanism, behaviour, and applications of the hybrid optical and optoelectronic memristors has been the main motivation for the work of this thesis.

1.2 Research Objectives

The main objectives of the research presented in this thesis include:

1. To fabricate a novel optical organic-inorganic hybrid memristor device in which either the electronic properties of the device or the Set and Reset processes can be modulated by wavelength and polarisation specific light. To achieve this goal, two strategies have been adopted. Firstly, fabricating a hybrid memristor device based on vertically aligned ZnO nanorods embedded within an optically active poly (disperse red 1 acrylate) (PDR1A) polymer. Secondly, gold nanoparticles embedded within PDR1A at a specific volume fraction so as to maximize the effect of the optical switching. In both cases, the device consisted of a vertical-based structure.

2. To identify the relevant switching processes and electronic mechanisms involved and optimize where possible.

3. To investigate how the optical memristive devices can be used in synaptic and neuromorphic computing applications.

1.3 Thesis Organization

This thesis is organised into eight Chapters. Following **Chapter 1**, which presents an introduction, research objectives, thesis organization, and work published and conference presentations, the remainder of the thesis is arranged as follows:

Chapter 2 gives the definition of a memristor, historical background of memristor devices as well as hybrid and optical memristors. Also, emerging memory technologies are presented at the end of this chapter.

In **Chapter 3**, theoretical descriptions of Leon Chua's memristor and HP lab TiO_2 memristor will be given. The resistive switching mechanisms with the electrical conduction mechanisms, and neuromorphic theory will be discussed too.

In **Chapter 4**, the materials used, the experimentation designed to fabricate optical memristor devices and characterization equipment are described.

Chapter 5 introduces the results of ZnO NRs and PDR1A based hybrid optical memristor devices. This chapter also presents the resistive switching mechanism, and the application of devices in synaptic circuits and neuromorphic computing applications.

In **Chapter 6**, the results of resistive switching devices based on Au NPs embedded with a PDR1A polymer are presented. The responsible mechanism for conductivity change and resistive switching will be discussed. Moreover, application of these devices in the synaptic and neuromorphic computing systems will be examined as well.

Chapter 7 is concerned with the discussion of the obtained results of optical memristor devices based on ZnO NRs and Au NPs both embedded with a PDR1A polymer.

Finally, **Chapter 8** summarises the major conclusions of this research and evaluates the results critically in relation to their impact in the memristor field and their practical limitations. Possible suggestions for future research in the area will be included.

1.4 Work Published and Conference Presentations

Journal Publications

1. "*Reversible Optical Switching Memristors with Tunable STDP Synaptic Plasticity: A Route to Hierarchical Control in Artificial Intelligent Systems*", **Ayoub H. Jaafar**, R. J. Gray, E. Verrelli, M. O'Neill, S. M. Kelly, N. T. Kemp, *Nanoscale*, 2017, **9**, 17091-17098.

2. "*Method to Reduce the Formation of Crystallites in ZnO Nanorods Thin-Films Grown via Ultra-Fast Microwave Heating*", R. J. Gray, **Ayoub H. Jaafar,** E. Verrelli, N. T. Kemp, Thin Solid Films, doi.org/10.1016/j.tsf.2018.07.034.

3. "*Large Polarization-Specific Reversible Optical Switching in a Resistive Memory Devices: Light Tunable Learning in Artificial Synapses*", **Ayoub H. Jaafar,** M. O'Neill, S. M. Kelly, E. Verrelli, N. T. Kemp, (drafting).

4. "*Effect of Nanostructure Geometry on Resistive Switching behaviour in Hybrid Organic-Inorganic Based Non-Volatile Memory*", **Ayoub H. Jaafar,** N. T. Kemp, (drafting).

Conference Publications and Presentations

5. "*Chua Mem-Components for Adaptive RF Metamaterials*", J. Georgiou, K. M. Kossifos, M. A. Antoniades, **A.H. Jaafar**, N. T. Kemp, paper 2793, ISCAS 2018, IEEE International Symposium on Circuits and Systems, Florence, Italy, May 27-30.

6. "*An Optically-Programmable Absorbing Metasurface*", Kypros Kossifos, Marco Antoniades, Julius Georgiou, **Ayoub Jaafar**, Neil Kemp, paper 2679, ISCAS 2018, IEEE International Symposium on Circuits and Systems, Florence, Italy, May 27-30.

7. "*Hybrid Memristor Devices for Low Cost Non-Volatile Memory Storage*", **Ayoub H. Jaafar**, E. Verrelli, R. J. Gray, M. O'Neill, S. M. Kelly, N. T. Kemp, The 7th PhD Experience Conference, 19-20 April 2016, The University of Hull, (poster presentation).

8. "*Hybrid Memristor Devices*", **Ayoub H. Jaafar**, E. Verrelli, R. J. Gray, M. O'Neill, S. M. Kelly, N. T. Kemp, 2nd MemoCIS Training School on Memristor Theory, Models and Device Technology, 7-9 May 2016, Alghero, Italy – COST Action IC1401, (poster presentation).

9. "*An Optically Tuneable STDP Synaptic Plasticity Memristor*", **Ayoub H. Jaafar**, R. J. Gray, E. Verrelli, M. O'Neill, S. M. Kelly, N. T. Kemp, The

7th MemoCIS Workshop, 12-13 March 2018, Dubrovnik, Croatia – COST Action IC1401, (poster presentation).

10. "*Optical and Non-Volatile Switching in Memristor Devices Based On Hybrid Organic-Inorganic Materials*", **Ayoub H. Jaafar**, R. J. Gray, E. Verrelli, S. M. Kelly, N. T. Kemp, NanoBio Conference 2018, The 1st International Conference on Nanotechnologies and Bionanoscience, 24-28 September 2018, Heraklion, Crete, Greece, (oral presentation).

Chapter 2. Memristors, Hybrid and Optical Memristors

This chapter gives the definition and historical background of memristor devices. This is followed by a more specific background on the topic of hybrid devices based on hybrid and non-hybrid ZnO nanostructures and Au NPs embedded in either organic or polymeric materials. In addition, optical memristors will be briefly reviewed as well as an introduction given to the topic of emerging non-volatile memory technologies and resistive random access memory. The chapter finishes with a review of organic and hybrid organic-inorganic memory technologies.

2.1 Definition of Memristor

Alongside the existence of three circuit passive elements the resistor, capacitor, and inductor, Leon Chua in 1971 proposed a fourth circuit element called a memristor [13], which fills the missing link between magnetic flux (φ) and electric charge (q) on a current-voltage-flux-charge phase diagram. Fig. 2.1 demonstrates this relationship whereby a resistor, capacitor, and inductor form the following relationships between Voltage and Current ($dv = Rdi$), Voltage and Charge ($dq = Cdv$), and Flux and Current ($d\varphi = Ldi$), respectively. It was proposed that in addition to these relationships there should also be a link between magnetic flux (φ) and electric charge (q). The two-terminal device in which this relationship was envisaged to occur was called a memristor (short for memory – resistor) and can be described by ($d\varphi = Mdq$).

The memristor is different from a capacitor and inductor in the ability to retain the data even when the power is turned off. It also can remember all the inputs applied and retains the last resistance when the inputs applied are removed [14]. Memristors show two resistance states; the high resistance state (HRS) and the low resistance state (LRS) depending on the applied voltage, where the resistance increases when the voltage is applied in one direction and decreases when the voltage is applied in the opposite direction.

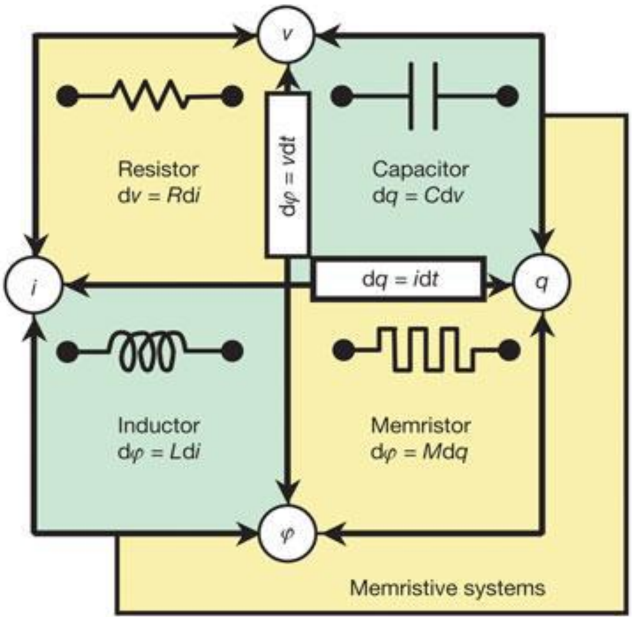

Figure 2.1: The four fundamental passive circuit elements: resistor, capacitor, inductor, and memristor taken from [15].

The defining feature or fingerprint of a memristor and memristive devices is the occurrence of a pinched hysteresis loop in the current-voltage plane. This occurs at the origin such that the current passing through the device is zero when the applied voltage is zero. The pinched hysteresis loop shape, however, changes with frequency of the input waveform. For instance, increasing the frequency of the input signals leads the pinched hysteresis loop to shrink and collapse to a straight line, and this is because high frequencies do not give the memristor the time required to switch from one resistance state to another [16]. The pinched hysteresis loop of a voltage-controlled memristor at different frequencies for the same amplitude of applied voltage is shown in Fig. 2.2.

Memristors exhibit a linear and nonlinear response to current or voltage. Linear behaviour means that the resistance of the memristor depends on the relatively small variation in current or voltage. On the other hand, nonlinear memristors rely on a threshold value of current or voltage in which the resistance can decrease or increase rapidly [17]. From a practical point of view, nonlinear memristor behaviour is more desirable than linear behaviour because the switching between two resistance states can be more than one order of magnitude, and that means a higher on/off ratio.

Memristors are unique in that they combine the non-volatility properties of Flash Memory with the high speed of Static Random Access Memory (SRAM) and the low cost of Dynamic Random Access Memory (DRAM). For this reason, some people call this a universal memory and a promising candidate for future-generation memory applications.

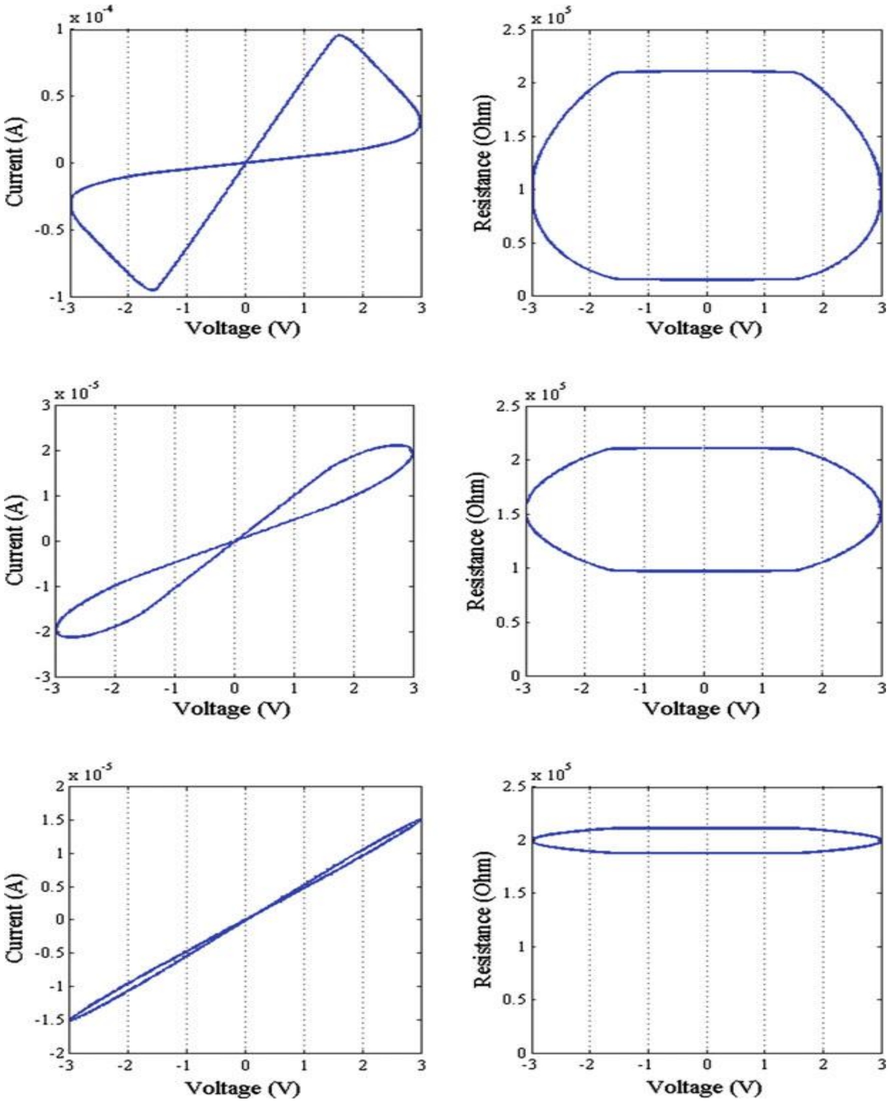

Figure 2.2: The pinched hysteresis loops for various frequencies for (I-V) curves, (left) and non-pinched (R-V) curves, (right) taken from [18].

Memristors are non-volatile, low power consumption, along with high speed, long data retention and endurance, potentially large on/off ratio, and high density. Some state-of-the-art values of these are fast switching (5 ns) [19], excellent endurance of about 10^{12} cycles, and long retention of more than 10^6 s [6].

Generally speaking, memristor devices can easily be fabricated and consist of a resistive switching layer sandwiched between two metal electrodes. The resistive switching layer can be polymers, e.g. poly(methyl methacrylate) (PMMA) and polystyrene [20], binary transition metal oxides, e.g. TiO_2 [21,22], NiO [23] and ZnO [24], perovskites, e.g. $SrZrO_3$ [25], and composites, e.g. ZnO nanorods embedded in PMMA [26]. Memristors also are an increasingly important area in high-density architectures integrated into crossbar arrays at the nanoscale compared to the Flash memory which suffers from a limitation in cell feature size and leakage challenges [27].

Memristors have the potential for a wide range of applications, such as non-volatile random access memory, integrated and synaptic circuits, neuromorphic computing, and nonlinear analogue circuits.

2.2 Historical Background

The theoretical description of memristor was first predicted in 1971 by Leon Chua when he announced that there should be a fourth passive circuit component [13]. The memristor combines the missing relationship between the electric charge and the magnetic flux and is most easily seen from symmetrical considerations of a current-voltage-phase-charge diagram, as shown in Fig. 2.1. As a component, the memristor is a two-terminal passive device that shows nonlinear characteristics that is different from the properties of resistors, capacitors, and inductors. In particular, the memristor was generalised further by Leon Chua and his student in 1976 [28] to memristive devices and systems and are now generally described as being any two-terminal devices that show a pinched hysteresis loop in the i-v plane, where the current will be zero if the voltage is zero.

It is worth mentioning that in the period between 1976 and 2008 there were many types of devices fabricated that exhibited behaviour similar to that of the memristor, but only the Hewlett-Packard (HP) laboratory team were successful in establishing the link between their work on resistive switching in TiO_2 devices and the theoretical description of a memristor proposed by Chua. Strukov et al. (2008) showed a hysteresis behaviour in nanoscale TiO_2 devices in which the resistive switching was based on solid-state electronic and dopant motion when different voltage polarity is applied [15]. In fact, these results were considered the basis for understanding the physics behind the resistive switching of already fabricated devices and motivated researchers for more investigation.

Since then, a considerable amount of literature has been published in the memristor field. Emerging memory technologies, such as MRAM [29], FRAM [30], PCM or (PRAM) [31], and RRAM [32] have received a significant interest and serious attempts in order to improve their performance over the past decade. Among them, RRAM is considered as a promising candidate because not only due to its simple device structure, consisting of a MIM design, but also other good characteristics such as high speed, long data retention time, low operation power, and high-density cells [33]. Because of these properties, extensive research has been focused on the study of resistive switching phenomenon and switching mechanisms for different materials based RRAM devices, including binary transition metal oxides [21,34,35], perovskites [36,37], polymers [20,38], carbon nanotubes and graphene [39], and hybrid organic-inorganic materials [40–45]. In this context, RRAM devices based on zinc oxide (ZnO) thin films and ZnO nanostructures and gold nanoparticles (Au NPs) embedded with polymer/organic layers will be briefly reviewed.

In general, the resistive switching effect has been reported in different structures of ZnO including thin films, nanorods, nanowires, and nanoparticles. Bipolar switching behaviour was demonstrated by Gul *et al*. [46] in a RRAM device consisting of ZnO film with a thickness of 300 nm deposited by a sputtering technique in between two aluminium electrodes. It was found that the device showed symmetric switching for both polarities of the applied voltage with an ON/OFF ratio of about 3 and no electroforming process was needed. Similarly, bipolar resistive switching was also reported in ZnO films with thicknesses of 50 nm [47] and 23 nm [48] with device structures of Cu/ZnO/Al-doped ZnO (AZO), and Au/Zn/stainless steel (SS), respectively. The effect of changing the thickness of ZnO films, dopants, and the combination of bottom and top electrodes on the switching behaviour were investigated by Qiu *et al*. [49]. It was observed that increasing the thickness of ZnO film from 0.4 μm to 1 μm increased the ON/OFF ratio but decreased the device stability. They also observed that the Al-doped ZnO films showed an ON/OFF ratio larger than using Mg and Mn dopants. In addition, devices that were fabricated by sandwiching the ZnO films between Cr and Al with device configurations of Cr/ZnO/Al and Al/ZnO/Al exhibited the largest ON/OFF ratio and stable resistive switching properties in comparison with other used combination of metal contacts, e.g. Ti/Au, Zn/Zn, Cr/Cr, Pt/Al, and Zn/Al.

Recently, ZnO nanorod and nanowire-based resistive switching memories have been investigated. Lai *et al*. [50] studied the effect of an argon plasma treatment on the active switching layer of ZnO nanowires (ZnO NWs) synthesised in between two metal contacts of titanium (Ti) on the device performance. It was noticed that the treatment process improved the reliability of the device for more than 100 cycles and enhanced the switching effect: the set and reset voltages spanning from 3 V to 22 V and –3 V to –31 V were reduced from 0.5 V to 8 V and from –1.5 V to –10 V, respectively. Improvement in resistive switching was also reported by Sun *et al*. [24], where the ON/OFF ratio of a RRAM device with a structure of Au/ZnO nanorods/ Al-doped ZnO (AZO) was improved from 10 to about 10^4 after annealing. The enhancement in the ON/OFF ratio was attributed to increasing the concentration of oxygen vacancies in the active switching layer by thermal annealing of the ZnO nanorods in a hydrogen atmosphere. Another attempt was made by Younis *et al*. [51] to improve the performance of a memristor device that was based also on vertically aligned ZnO nanorods sandwiched between fluorine-doped tin oxide (FTO) and gold as the bottom and top electrodes, respectively. This approach depends on forming a nanocomposite film by dispersing ceria (CeO_2) quantum dots (QDs) as charge trapping sites on the surface of ZnO nanorods using a drop casting method. It was found that this approach enhanced the device stability and uniformity as well as increased the ON/OFF ratio by more than two orders of magnitude.

Alternatively, ZnO nanoparticles (NPs) have been also proposed for fabricating memristive devices. Wang *et al*. [52] for example, fabricated a RRAM device consisting of a ZnO nanocrystal film with a thickness of 100 nm deposited by a spin coating solution process in between a transparent ITO bottom electrode and an aluminium (Al) top electrode. Wang and co-workers observed that the hysteresis loop was strongly dependent on the length of ligand on the ZnO nanocrystals. Increasing the ligand length from *n*-octylamine to *n*-octanoic acid decreases the hysteresis effect. The device showed resistive switching behaviour with an ON/OFF ratio of five orders of magnitude in the case of ZnO nanocrystals coated with short ligands (*n*-butylamine ligands), whereas small or no hysteresis was observed in devices based on long ligand-coated ZnO nanocrystals (*n*-octanoic acid ligands). Another example of ZnO NPs based switching memristors was reported by Qi *et al*. [53] using a self-assembled single crystalline ZnO nanoisland with a diameter of 30 nm and a height of 40 nm as an active switching material deposited on a silicon (Si) substrate. A conductive atomic force microscopy (C-AFM) tip was used for electrical measurements as a top contact. The devices showed bipolar switching behaviour with a large resistance contrast between the HRS and LRS in order of the 10^6. Qi and co-workers also reported in [54] that ZnO nanoisland based resistive switching devices exhibited not only bipolar switching but also multimode resistive switching which includes threshold-like behaviour and self-rectifying behaviour.

These three different resistive switching behaviours were obtained by changing the current compliance utilized during the electrical characterization. It was found that an increase of current compliance changed the switching effect from a threshold-like to a self-rectifying and then to a bipolar behaviour. The authors attributed the multimode switching behaviour to the movement of oxygen vacancies and formation and rupture of conductive filaments at the high applied electric field.

We move on now to the hybrid organic-inorganic materials that include ZnO nanorods and nanoparticles embedded in polymers. In recent years, hybrid systems have been considered as competitive technologies for resistive switching devices because they have the electronic properties of semiconductors as well as the advantages of organics like low fabrication cost, low temperature solution processing, and are easy to deposit on different substrates. As demonstrated by Tseng *et al*. [55], a bistable switching behaviour is observed in the hybrid system consisting of ZnO nanorods embedded in poly(methyl methacrylate) (PMMA). In separate work, Verrelli *et al*. [26] also observed the same behaviour using the same device structure and material, e.g. ITO/ZnO nanorods/PMMA/Al. In both cases, the pinched hysteresis loop occurred at the same applied voltage swept between -3 V and 3 V with almost the same ON/OFF ratios and SET and RESET voltages. This indicates that the operating voltage of these hybrid systems is about 3 V. In addition, Verrelli and co-workers found that adding the PMMA insulator layer plays a significant role in improving the switching effect and the stability of devices in comparison with a device fabricated with no insulator layer. The effect of adding an insulator layer for ZnO NRs based RRAM devices was also investigated by Valanarasu *et al*. [45]. In this investigation, PMMA layers with thicknesses of 40 nm and 70 nm were introduced between the ITO contact and ZnO NRs to give a device structure of ITO/PMMA/ZnO NRs/Al. It was observed that increasing the thickness of PMMA to $\leq$ 70 nm improved the ON/OFF ratio (more than three orders of magnitude) by increasing the resistance of the HRS due to an enhancement of charge trapping induced by the PMMA layer. Cheng *et al*. [56] stated a similar improvement in resistive switching memories based on CuSCN nanopyramids/ZnO nanorods p-n heterojunction with an interlayer of PMMA introduced between them. The authors found a considerable difference between devices with and without interlayer of PMMA. The device containing no PMMA interlayer did not show resistive switching, whereas the device with a PMMA interlayer showed a pinched hysteresis loop with relatively large ON/OFF ratio for negative applied voltages. This change in device behaviour was also explained by charge trapping within the PMMA interlayer, and resulted in a memory window (resistive switching bewteen two resistance states). Moreover, Anoop *et al*. [57] employed a multilayer stacking structure of vertically aligned ZnO NRs and graphene oxide (GO) as a hybrid material for resistive switching devices. It was noticed that all the devices, irrespective of the number of stacking layers, exhibited bipolar resistive switching behaviour. However, the stability and resistance contrast enhanced by increasing the number of GO/ZnO NRs stacking multilayers. The ON/OFF ratio for a device with three stacking layers was higher by three orders of magnitude than of a device fabricated with a single layer of ZnO NRs (no GO layer) between two electrodes.

ZnO NPs blended with organic layers have also emerged as the active switching material for two-terminal non-volatile RRAM device applications. As reported by Verbakel *et al*. [58], asymmetric bipolar switching is observed with a low ON/OFF ratio, i.e. less than one order of magnitude, in a ZnO NPs embedded in a polystyrene (PS) layer hybrid resistive switching devices. In separate work, Yun and co-worker [59] formed devices that showed write-once-read-many-times (WORM) operation also using ZnO NPs in a PS layer as a switching matrix with a ITO/ZnO NPs:PS/Al configuration. Compared with an ON/OFF ratio of only 1.4 for a device containing no ZnO NPs, a large resistance contrast of three orders of magnitude was observed in the hybrid ZnO NPs and PS devices. Instead of PS, the non-volatile WORM switching behaviour was demonstrated in [60,61] where the ZnO NPs were suspended in a PMMA layer and sandwiched between ITO and Al electrodes. The large memory effect in these regimes was attributed to the presence of ZnO NPs, which act as charge trapping sites within the insulating layers. Additionally, the authors reported that the devices' conductivity, ON/OFF ratio, and SET/RESET voltages are controllable by changing the loading content of ZnO NPs in the insulating matrix [61]. It has been established that introducing fullerene (C_{60}) (C_{60} is a class of *n*-type organic semiconductors that acts as an electron transoprt layer in the bistable organic devices) layers enhanced the hysteresis characteristics of RRAM devices. Two layers of C_{60} were used to sandwich the active switching material that consists of ZnO NPs embedded in a PMMA layer and a polyimide (PI) layer in ITO/C_{60}/ZnO NPs:PMMA/C_{60}/Al [62] and ITO/C_{60}/ZnO NPs:PI/C_{60}/Al [63] memristor devices. In both cases, the devices with and without the C_{60} layers showed a bipolar behaviour and a memory effect resulted from the charge trapping effect in the ZnO NPs. However, the ON/OFF ratio improved from 10^2 to 10^4 by sandwiching the active switching layers within C_{60} layers. The authors attributed the enhancement to the presence of C_{60} layers, which were used as injection and transfer layers for charges between the ITO and resistive switching matrix.

We turn now to Au NP-based RRAM devices. The first use of Au NPs was reported by Simmons and Verderber in 1967 [64] to describe resistive switching in thin insulating films in an Al/SiO/Au device structure. During the deposition of the top Au contact, some of the gold ions were introduced to the insulating SiO films. It was found that the gold ions can act as localised impurity sites within the band gap of SiO thin films. The electric charge carriers can be transported between neighbouring impurity sites through tunnelling as well as trapping effect induced by impurity sites within the insulating films.

Subsequent work in this area on memristor devices based on Au NPs embedded in insulators has highlighted two main architectures; a trilayer structure, and a monolayer structure. In the trilayer structure, the metal nanoparticle layer is deposited in between two organic/polymer layers, and all the three layers are sandwiched between two metal contacts, i.e. the top and bottom contacts. Jin *et al.* [65], for example, formed trilayer RRAM devices by depositing a Au NP layer using thermal evaporation technique. The Au NP layer was deposited on an insulator layer of polyimide (PI) and then covered by a layer of poly(3-

hexylthiophene) (P3HT) and [6, 6]-phenyl-C61-butyric acid methyl ester (PCBM) with Al top and bottom electrodes. It was seen that the devices exhibited a resistive switching behaviour with a sudden switch between the ON and OFF states. The resistive switching effect was explained by trapping of electrons within the Au NPs, which facilitate current transport between the (P3HT) (PCBM) layer and PI layer. The injected electrons from one Al electrode into (P3HT) (PCBM) layer are trapped by Au NPs. Once all the traps are filled, electrons can transport *via* a tunnelling mechanism through the thin insulator layer of PI (10 nm) into the other Al electrode.

On the other hand, the monolayer structure is a dominant design used for fabrication of RRAM devices due to it being a simple and easy synthesis process, which involves a single deposition of hybrid nanoparticles mixed with organic/polymer materials. Additionally, a trilayer structure requires high vacuum systems like thermal evaporation to deposit the middle layer of nanoparticles, which also need strict parameters to modify the morphology and discontinuous nanoparticle layer. Memristor devices formed using Au NPs in 8-hydroxyquinoline (8HQ) and polystyrene (PS) with a device configuration of Al/Au+8HQ+PS/Al, were developed by Ouyang *et al*. [8]. Switching between the high resistance state (HRS) and low resistance state (LRS) with a resistance contrast of more than 4 orders of magnitude with a nanosecond switching response was reported. In separate work, Ouyang *et al*. [66] fabricated organic bistable memory devices based on PS and 2-naphthalenethiol (2NT)-capped Au NPs with Al top and bottom electrodes. Asymmetric switching was obtained along the two polarity directions for the device after the transition with a sharp transition from OFF state to ON state for an applied voltage higher than 7 V. It was reported that the conductivity and threshold voltage are strongly dependent on the Au NPs loading and the thickness of switching layer, respectively. As suggested by the authors, the conduction mechanism in these devices is due to electric field-induced charge transfer between the Au NPs and 8HQ and 2NT, where the Au NPs act as electron acceptors and 8HQ and 2NT as donors.

This conduction mechanism was also demonstrated by Tseng *et al*. [10], but in this case, the charge transfer took place between the Au NPs and polyaniline nanofibers. The Au NPs and polyaniline nanofibers blended with poly(vinyl alcohol) were used as a switching layer sandwiched between two Al electrodes. It was observed that the device showed data retention for 14 hours as well as a resistance contrast of 3 orders of magnitude. Further, Tseng and co-workers used the conductive AFM tip as the top electrode with Al bottom electrode for a device containing Au NPs and polyaniline nanofibers but without poly(vinyl alcohol) to study the resistive switching effect in a nanoscale dimension device. They found that resistive switching occurs by sweeping the device from 0 to −5 V. RRAM devices based on Au NPs embedded in poly(4-n-hexyltriphenyl) amine (*x*HTPA) and poly (1,1′-biphenyl-4,4′-diyl-9H-fluoren-9-ylidene) (*x*BP9F) with device structures of ITO/*x*HTPA:Au NPs/Ca/Al and ITO/*x*BP9F:Au NPs/Al have been investigated by Bozano *et al*. [67]. In both systems, the electrical characteristics established the switching was due to the existence of Au NPs because no resistive switching was reported for devices without NPs. Also, the devices showed threshold voltage switching and a NDR behaviour where the current decreases by increasing the applied voltage. They established that the switching mechanism in their devices is similar to that reported by devices reported by Simmons and Verderber, which are dominated by tunnelling between the Au NPs. Simon *et al.* [68] studied the resistive switching effect in Au/MEH-PPV:Au NP/Au and Al/*x*HTPA:Au NP/Al devices where the Au NPs were embedded in poly(2-methoxy-5(2$'$-ethylhexyloxy)-p-phenylene vinylene) (MEH-PPV), and poly(4-n-hexylphenyldiphenylamine) (*x*HTPA), respectively. It was observed that the MEH-PPV:Au NPs based RRAM devices showed a higher ON/OFF ratio (4 orders of magnitude) than the *x*HTPA:Au NP based RRAM devices (1 order of magnitude). However, in both devices, a negative differential resistance (NDR) was observed in which the current decreased at higher applied voltage. The switching and NDR were attributed to the charge trapped on the Au NPs, and elimination of trapped charge by recombination or being swept away by the field at high bias, respectively.

Another non-volatile two-terminal RRAM device developed by Khurana *et al.* [69] included Au NPs embedded in a graphene oxide (GO) film (85 nm thick) between ITO and Al electrodes. The authors observed a significant improvement in the device switching characteristics by embedding the Au NPs in the GO film, from a poor ON/OFF ratio for a device with no Au NPs to 10^6 for a device with Au NPs. The devices exhibited a sharp set and reset processes with voltages less than ±1 V. These switching characteristics were attributed to charge trapping and de-trapping at Au NPs trap sites in the GO film. It was also found that no forming step was needed as the pristine devices showed a high conductivity due to the initial conducting channels formed by defects, i.e. oxygen vacancies, which were introduced during the device fabrication process.

Several conduction mechanisms have been proposed to explain the charge transfer and resistive switching behaviours in all the above-mentioned devices. These mechanisms include Schottky emission (SE), Ohmic conduction, Poole-Frenkel (PF) emission, Fowler-Nordeim tunnelling, thermionic emission, space charge limited current (SCLC), charge trapping and de-trapping, and electric-field-induced charge transfer [46,48,49,51,57,60,66,70–73].

However, so far very few attempts have been made to modify the electronic properties of resistive switching memories by optical means. In 2012, Ungureanu *et al.* [74] published a paper entitled˝a light-controlled resistive switching memory˵ which was the first effort to control the resistance state of resistive memories by optical means. In this study, both electrical and optical pluses were used to control the resistance state of a metal-insulator-semiconductor-based resistive switching memory with a $Si/SiO_2/Al_2O_3/Pd$ device configuration. The device showed a light-dependent resistive switching behaviour under illumination with UV-IR light with different optical powers used for programming the devices. The I-V curves of these devices exhibited a rectifying behaviour with a saturation current dependent upon the optical irradiation level at a positive applied voltage. It was also observed that the memory effect in these multilayer devices was controllable by the irradiation conditions and the light ring-exposed areas around the circular top contacts radii ranging from 53 µm to 1 cm, corresponding to ring areas. Ungureanu *et al*. interpreted these results as being due to photogenerated electrons from the Si/SiO_2 interface, which resulted in a trapping and de-trapping effect in the Al_2O_3 layer by changing the polarity of the applied voltage.

Subsequently, Park *et al*. [75] studied the effect of optical irradiation on the resistive switching characteristics of RRAM devices based on ZnO NRs with a FTO/ZnO NR/Au structure. It was noticed that the device showed a photoresponse with optical illumination, where the resistive switching and ON/OFF ratio were modifiable by controlling the intensity of the light in comparison with a device studied in dark conditions which showed relatively negligible resistive switching. As reported by the authors, the formation and rupture of conductive filaments formed by oxygen vacancies were strongly associated with optical illumination. Since electron-hole pairs are generated upon irradiation, desorption on the surface of ZnO NRs occurred when the holes combined with the charged oxygen ions which resulted in unpaired electrons in the ZnO NRs that can increase the photocurrent.

An optical readout resistive switching memristor (plasmonic memristor) has been demonstrated by Emboras *et al*. [76] using a-Si as a switching matrix and Ag and p-Si as the top and bottom electrodes, respectively. It was shown that the transmission of propagating light through the device was strongly dependent on the set and rest processes induced by electrical stimuli. As reported by the authors, the formation/annihilation of conductive silver filaments, (redox process), switched the device to the LRS/HRS, and that resulted in a low/high optical transmission of the propagating light. Similarly, Emboras *et al*. [77] in a separate work, reported plasmonic RRAM devices consisting of an SiO_2 film sandwiched between ITO and gold contacts. In the same vein, the optical transmission switched between low and high due to the resistive switching being induced by the formation and rupture of a nanoscale absorbing and scattering metallic filaments in the insulating SiO_2 film.

A study by Huebner *et al*. [78] demonstrated the capability of colloidal-based non-volatile resistive memristors to be electrically written/read and optically erased. It was shown that the device switched to the ON state when the applied bias exceeds a threshold voltage, but it did not switch back to the OFF state when the reverse voltage is applied with a magnitude either similar or larger than the set voltage. The reset process, however, occurred when the device was irradiated with UV light (360 nm) for an exposure time of two minutes. According to the authors, the optical erasing of the device is due to the redistribution of the local electric field, causing a distribution of alignment of the carbazole rings that act as percolation pathways for current transport within the active switching material.

Bogle and co-workers [79] investigated the effect of optical irradiation on the switching behaviour of $BiFeO_3$ (BFO)-based RRAM devices. It was observed that the set voltage shifted from 10 V to 2 V when the device was exposed to light with a wavelength of 590 nm for 10 ms. As the authors proposed, the results were ascribed to the drift of photogenerated charge carriers towards their respective metal contacts, resulting in the creation of conducting paths for current along grain boundaries of the $BiFeO_3$ film under an external applied potential. An electrically read and optically written/erased memory consisting of an 8 nm thick film of a liquid crystal azobenzene polymer (PA-AZO) as an active layer between a Au bottom contact and gallium-indium drop top contact has been reported by Mosciatti *et al*. [80]. Due to the photoisomerization effect between *trans* and *cis* isomers of the azobenzene containing polymer, the electrical characteristics were modulated by optical illumination using two wavelengths of 365 nm and 455 nm to switch the current to ON and OFF states, respectively. Although the electrical characteristics showed an optical response, no resistive switching has been demonstrated when the authors measured the current after each individual optical illumination. It is worth mentioning that azobenzene-containing polymers have been also reported in [81–83] as active switching matrices for RRAM devices. However, no optical stimuli have been used to investigate the switching phenomenon in these reports.

All the studies reviewed so far, however, do not show any resistive switching devices that can be SET and REST by purely optical means. In addition, all the previously mentioned studies related to the effect of optical irradiation on the resistive switching properties have been only carried out on organic or inorganic-based optical RRAM devices. No study has been made on the hybrid organic-inorganic systems which are the main focus of this thesis.

2.3 Emerging Memory Technologies

Recently, several non-volatile memory technologies have emerged as promising candidates for the universal memory. These technologies are Ferroelectric RAM (FRAM), Magnetoresistive RAM (MRAM), Phase-Change RAM (PCRAM), and Resistive RAM (RRAM). These technologies have received considerable interest due to their unique characteristics, such as high spatial density, non-volatility, high speed, low power consumption, long data retention and high endurance [84]. The following is a brief description of these emerging technologies.

2.3.1 Ferroelectric Random Access Memory (FRAM)

FRAM (also called FeRAM) is a kind of non-volatile random access memory based on capacitance. FRAM as an early emerging memory technology was first reported in 1987 using a ferroelectric thin film capacitor integrated with CMOS circuitry [85]. The structure of an FRAM device is similar to a DRAM and consists of a transistor and a capacitor. The main difference between FRAM and DRAM is that the ferroelectric material is deposited between two plates of an FRAM capacitor rather than the dielectric in a DRAM capacitor [86]. The basic structure diagram of FRAM is illustrated in Fig. 2.3.

The storage of data in an FRAM cell depends on the polarisation (an electric dipole moment per unit volume) phenomenon of the ferroelectric material. Ferroelectric materials show a spontaneous polarisation in the absence or presence of an external electric field.

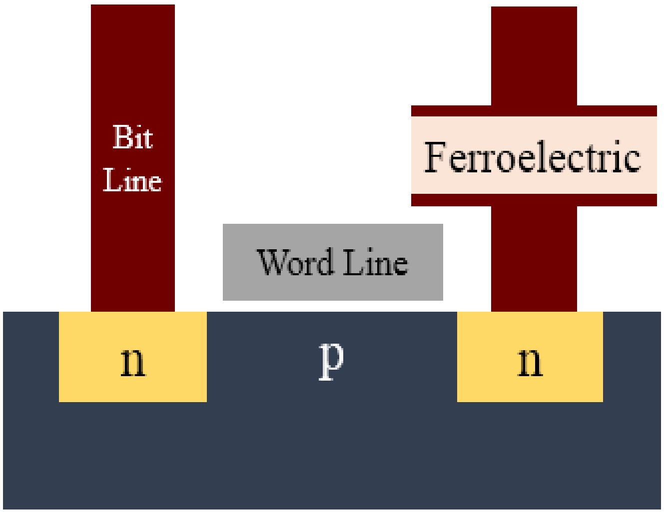

Figure 2.3: Basic architecture of a non-volatile FRAM cell.

The ferroelectric effect is widespread in perovskite structures, which are defined as ABO_3 crystals [87]. A schematic of the ABO_3 perovskite crystal structure is shown in Fig. 2.4. Depending on the inherent temperature (Curie temperature (T_C), defined as a temperature at which certain magnetic materials undergo a sharp change in their magnetic properties) of the ferroelectrics, the relative shifts up and down of B^{4+} in each cell causes a distortion of the perovskite lattice structure and as a result, a spontaneous polarisation appears. Similarly, the polarisation effect can also arise when an external electric field is applied [88].

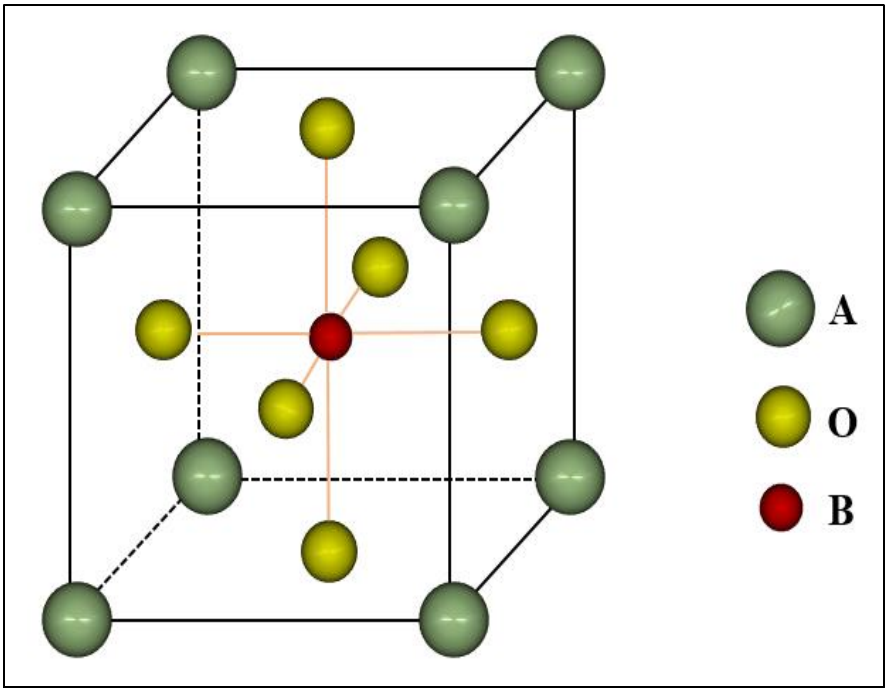

Figure 2.4: Schematic structure of ABO_3 perovskite crystal.

For FRAM applications, the switching between two reversible states of spontaneous polarisation can be used to read and store information. For example, applying an electric field between two capacitor plates polarises the ferroelectric material in a specific direction with respect to the electric field. The polarisation of the ferroelectric material shows a non-linear response to the electric field and, as a result, a hysteresis loop arises. Fig 2.5 shows a typical hysteresis loop of a polarisation response versus electric field. The material shows a saturated polarisation (P_{sat}) when all domains are oriented in the same direction, and at this point, the material maintains its polarisation state (defined as a memory state) if the applied electric field is turned off. This polarisation is named as a remnant polarisation (P_r) which gives FRAM the non-volatility characteristic [86]. The ferroelectric material, however, can be polarised in another direction when the same magnitude of the electric field is applied in the opposite direction [89]. These two polarisation states (±P_r) referred as “up” and “down” or as binary “1” and “0” for memory applications.

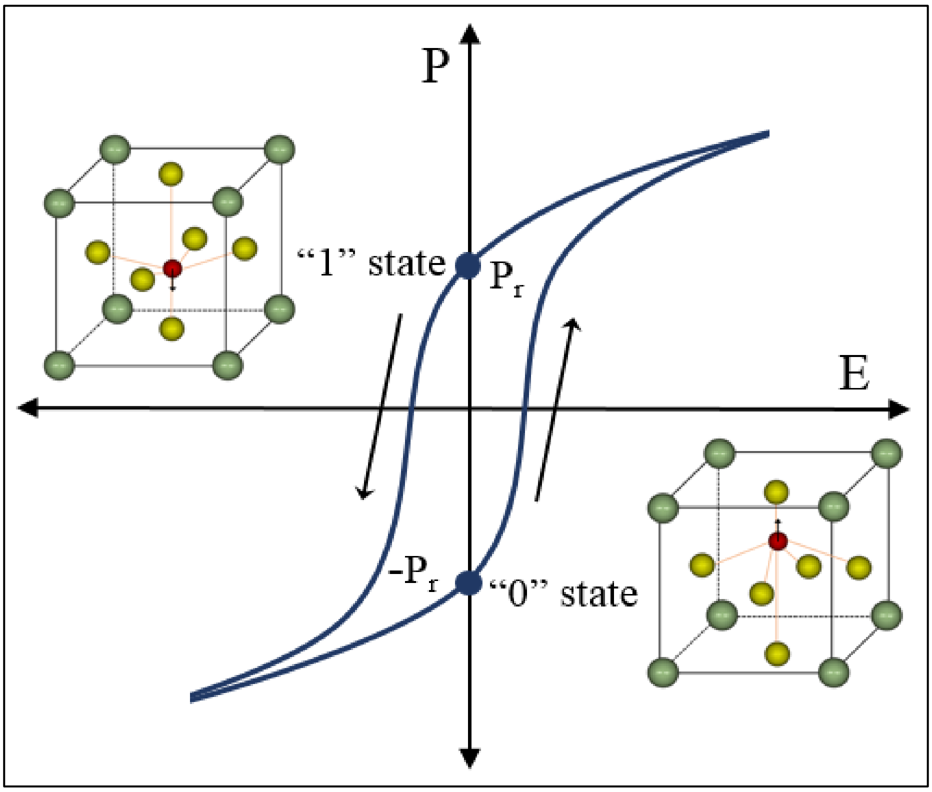

Figure 2.5: A typical polarisation versus electric field hysteresis loop. ±P_r are equally stable, and no applied electric field is needed to maintain the memory state. The inserts show the displacements of B^{4+} upward and downward depending on the polarity of the applied electric field.

Practically, ferroelectricity has been investigated in many thin film perovskite materials such as $SrBi_2Ta_2O_9$ (SBT) [90], $(Bi,La)_4$ Ti_3O_{12} (BLT) [91], and $Pb(Zr_{0.3}Ti_{0.7})O_3$ (PZT) [92], [93].

From an application point of view, FRAM as an emerging memory technology offers promising characteristics, but it also suffers from some limitations which prevent it being a universal memory. FRAM is a non-volatile owing to its ability to retain data even when the external applied source is removed, and there is no need to be periodically refreshed as in DRAM [94], [95]. It also has low power consumption (because it maintains their states without any external power supply), high endurance (10^{14} cycles), and high-speed operation in comparison with a DRAM [96]. FRAM can also be easily incorporated into large-scale integrated circuits [97]. Nevertheless, poor reliability and the difficulty of achieving high density are the main challenges of FRAM devices [97].

2.3.2 Magnetoresistive Random Access Memory (MRAM)

Magnetoresistive Random Access Memory (MRAM) is considered one of the competitive candidates that can be an alternative to current memory technologies, owing to its attractive properties such as high density, non-volatility, fast operation, cheap CMOS integration process and long data endurance [98]. MRAM utilises electronics and magnetics to read-out and store data, respectively.

MRAM is based on the magnetic tunnel junction (MTJ). A simple structure of an MRAM cell consists of two ferromagnetic storage layers separated by an insulator layer. One of these two ferromagnetic layers has a fixed magnetic field polarity (also called a reference layer); the other has a changeable polarity (a free layer) that depends on the external applied field [96]. A schematic MRAM cell is illustrated in Fig. 2.6. According to the magnetic tunnel effect, the resistance of the device can be switched between two states when a current passes through the device. For instance, the device shows low resistance (*ON* state) when the magnetic moments of both layers are parallel, while it shows low conductance (*OFF* state) when the magnetic moments of both layers are antiparallel [99].

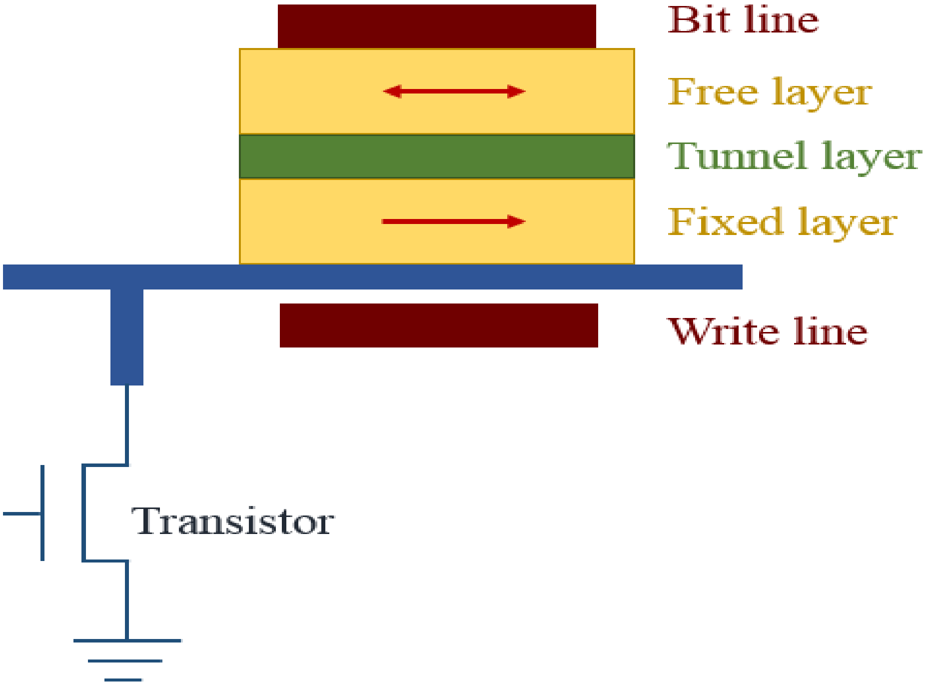

Figure 2.6: Schematic MRAM cell design with a transistor for reading.

The difference between two resistance states is described as a tunnel magnetoresistance (TMR) [100], also called a magnetoresistance ratio (MR), which can be given by

$$MR = \frac{\left(R_{AP} - R_p\right)}{R_p} \tag{2.1}$$

where R_{AP} and R_p represent the resistance for antiparallel magnetisation (*OFF* state) and parallel magnetisation (*ON* state), respectively.

Fig. 2.7 shows the magnetic tunnel junction and two resistance states as a result of parallel and antiparallel aligning of the magnetic moments of the two ferromagnetic layers. As shown in Fig. 2.7, the current can pass easily through the tunnel layer and switch the device to the *ON* state when the free and fixed layers are aligned in parallel. However, antiparallel aligning of the layers increases the impedance of the tunnel layer, which switches the device to the *OFF* state. This tunnelling effect can be attributed to the difference in the density of states at Fermi energy level on both sides of the tunnel layer [101]. When the magnetic moments of the layers are in the same direction, symmetric band structure of majority and minority takes place on both sides of the tunnel layer. As a result, the majority/majority and the minority/minority tunnelling across the tunnel layer occurs. In contrast, when the magnetic moments of the layers are aligned in different directions, asymmetric band structure arises on both sides of the tunnel layer, which causes a forced tunnelling into the minority/majority bands on both sides of the tunnel layer. The reduced number of states available for tunnelling between the ferromagnetic layers when the layers are antiparallel results in an increased tunnelling resistance [101,102].

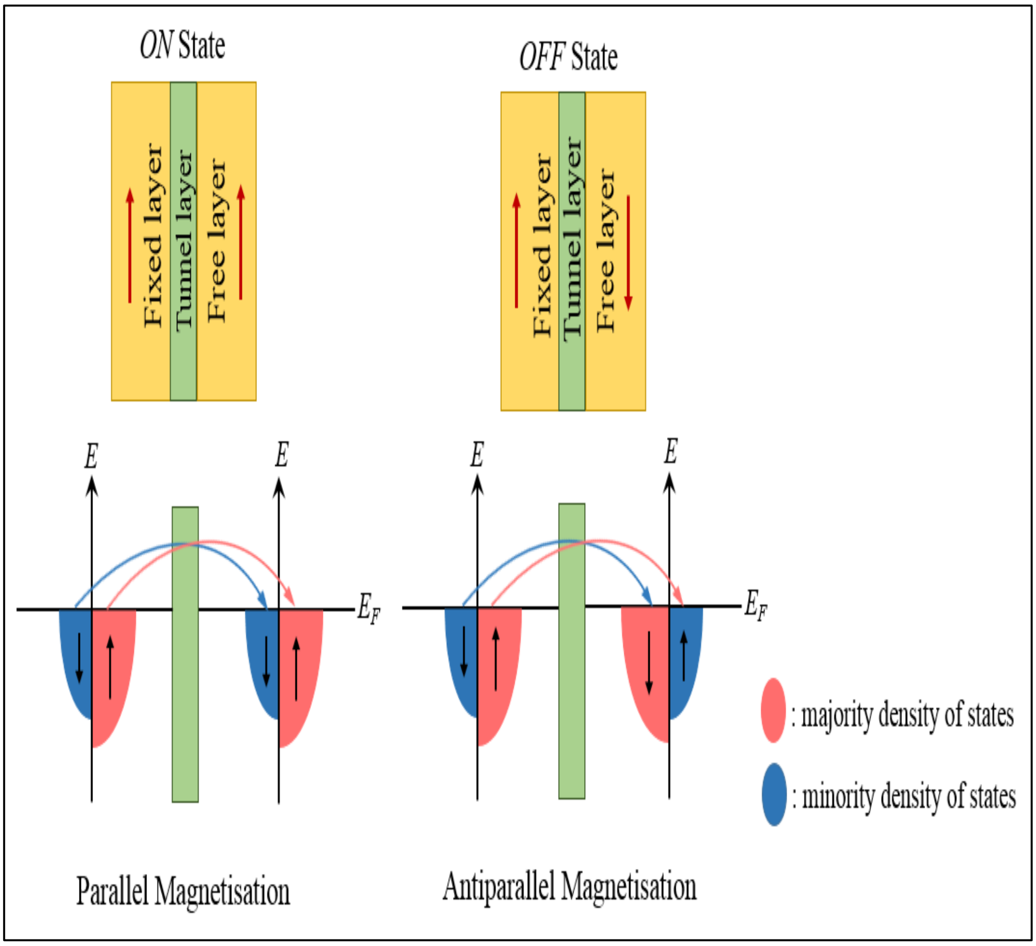

Figure 2.7: Schematic of the tunnel effect and density of states in an MRAM cell. The resistance in the ON and OFF states when the magnetisations in parallel and antiparallel directions, respectively.

MRAM offers desirable memory attributes, such as unlimited endurance, low power consumption, non-volatility and high-density data storage [103]. However, minimising the cell size can adversely affect MRAM device performance by the extension of the magnetic field into neighbouring cells during the write process. Further, the high cost of MRAM devices is another drawback in comparison with the current commercial technologies where their prices are higher than all the currently established memory technologies. For example, MRAMs cost about £2 to £3 ($3 to $5) per megabyte, and that makes them in excess of 1,000 and 10,000 times the prices of Flash memory and hard disk drives, respectively [96].

2.3.3 Phase Change Random Access Memory (PCRAM)

PCRAM has emerged as a powerful candidate technology for next non-volatile solid-state memory applications. The principle of operation that this technology is based on is the fast and reversible transition between two states of a material-the ordered (crystalline) state and disordered (amorphous) state [104]. This phenomenon has been known since 1968, when the reversible change between a crystalline phase and amorphous phase was observed in alloys of III, IV and VI group elements of the periodic table [105]. These alloys are called chalcogenide glasses. The most commonly used chalcogenide is $Ge_2Sb_2Te_5$, referred to as GST [106].

A simple PCRAM cell structure is illustrated in Fig. 2.8. Usually, the chalcogenide material of a fresh PCRAM device is in the crystalline (ordered) phase. In this case, the device is in the low resistance, SET state. Applying a large voltage pulse for a short time anneals the material in the programming region above its melting point, and then allows it to cool down quickly. This local atomic disruption changes the chalcogenide material to the amorphous (disordered) phase, which RESETs the device to the high resistance state. However, applying a low voltage pulse for a long time anneals the amorphous phase of the programming region above the crystallisation temperature but below the melting temperature and transforms the chalcogenide material into the crystalline phase. As a result, the PCRAM device switches to the low resistance state [107–109]. The transition between the two phases can be achieved quickly in less than 100 ns [110]. Reading stored data from a PCRAM cell is accomplished by measuring the resistance by applying a voltage pulse smaller than the SET and RESET pulses [111]. Schematic voltage pulses for the SET and RESET states are shown in Fig. 2.9. For data storage applications, the ordered and disordered phases represent the low electrical resistance (logic value 0) and high electrical resistance (logic value 1), respectively [31].

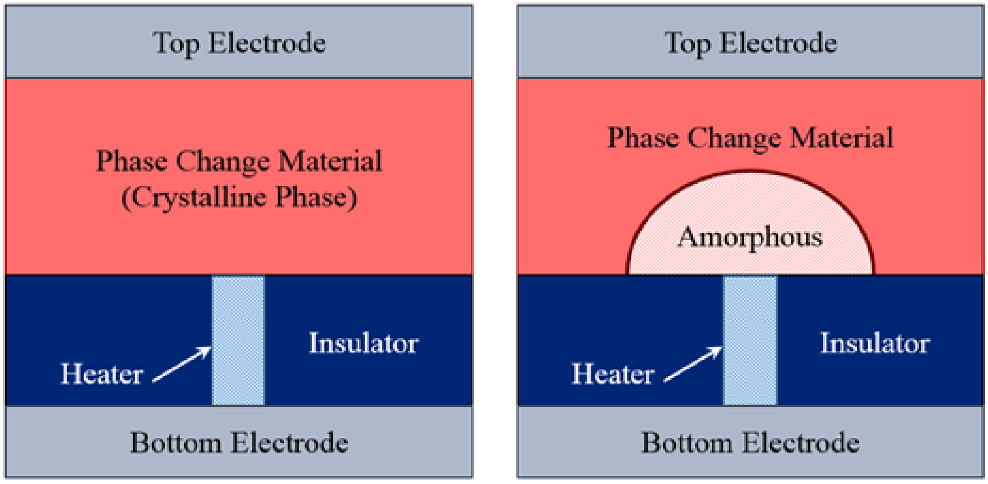

Figure 2.8: A basic diagram of the PCRAM cell in the crystalline and amorphous phases.

Besides the non-volatility property, PCRAM provides interesting properties which make it in competitive with current commercial technologies. For example, it has high endurance due to its ability to switch between the SET and RESET phases for many cycles [107]. It also offers long retention up to 10 years at high temperature (110℃) and fast read and write speeds [112]. The main challenge for PCRAM, however, is the large voltages needed for the RESET process, which makes PCRAM consume high power. Several cell designs have been proposed in order to overcome this issue, such as bridge cell, pillar cell and pore cell [104]. Pore cell design, for instance, provides a scalable size PCM cells which reduce the current consumption required for SET and RESET processes.

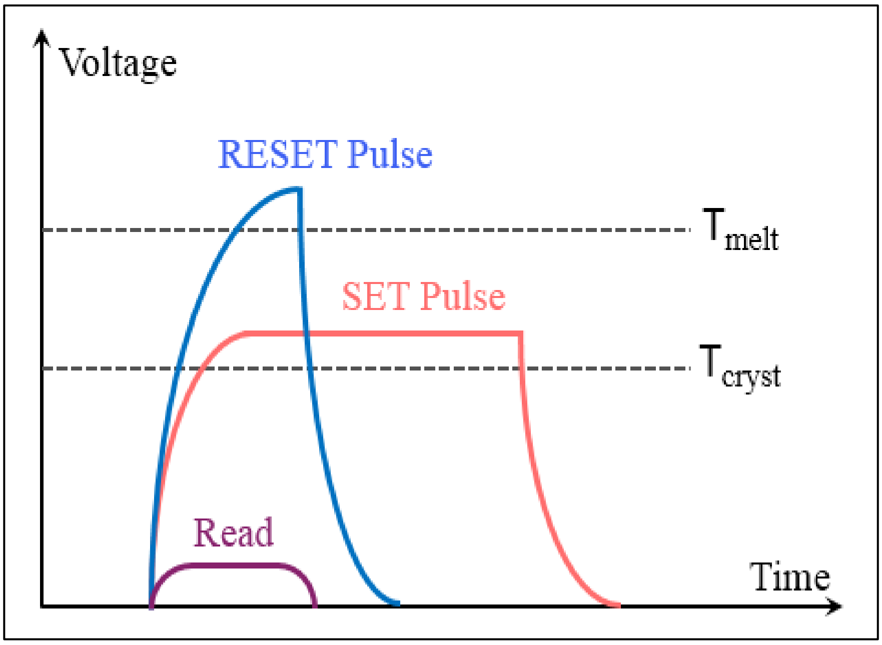

Figure 2.9: Programming of the PCRAM cell by changing the temperature when an external electrical pulses are applied.

2.3.4 Resistive Random Access Memory (RRAM)

Resistive random access memory is considered one of the most competitive technologies to be as a “universal memory,” due to its unique characteristics, such as low cost, low power consumption, high endurance, scalability, and high ON/OFF ratios. RRAM can be defined as a non-volatile two-terminal cell based on the resistive switching phenomenon in which its resistance can be switched between an HRS and an LRS.

RRAM offers a simple cell structure using a MIM architecture, which provides the advantage of high-density crossbar memory devices manufacturing. A schematic MIM structure of RRAM crossbar device is shown in Fig. 2.10. In the MIM structure, an insulator (resistive switching material) is sandwiched between two metal electrodes. The resistance of the RRAM can be switched from the HRS to the LRS and vice versa when an external voltage is applied. A RRAM cell maintains its resistance state for a long period of time when the power is switched off, making it a non-volatile memory. Regarding the polarity and amplitude of the applied voltage, RRAMs show bipolar and unipolar switching behaviours.

Interestingly, these types of devices can be easily fabricated using a range of materials as the active layer for the resistive switching. These materials can be binary metal oxides, such as TiO_2 [113], ZnO [49][34], HfO_2 [114], NiO [115], perovskite oxides, such as $SrTiO_3$ [36], $SrZrO_3$ [37], hybrid organic-inorganic materials, such as ZnO/PMMA [71][55], nanoparticles/polymers [116–118], and carbon nanotubes and graphene [39] amongst other materials. Several mechanisms have been proposed to explain the origin of the resistive switching in RRAM devices. These mechanisms will be presented in details in the next chapter. The comparison characteristics between the conventional memories and emerging memory technologies are summarised in Table 2.1.

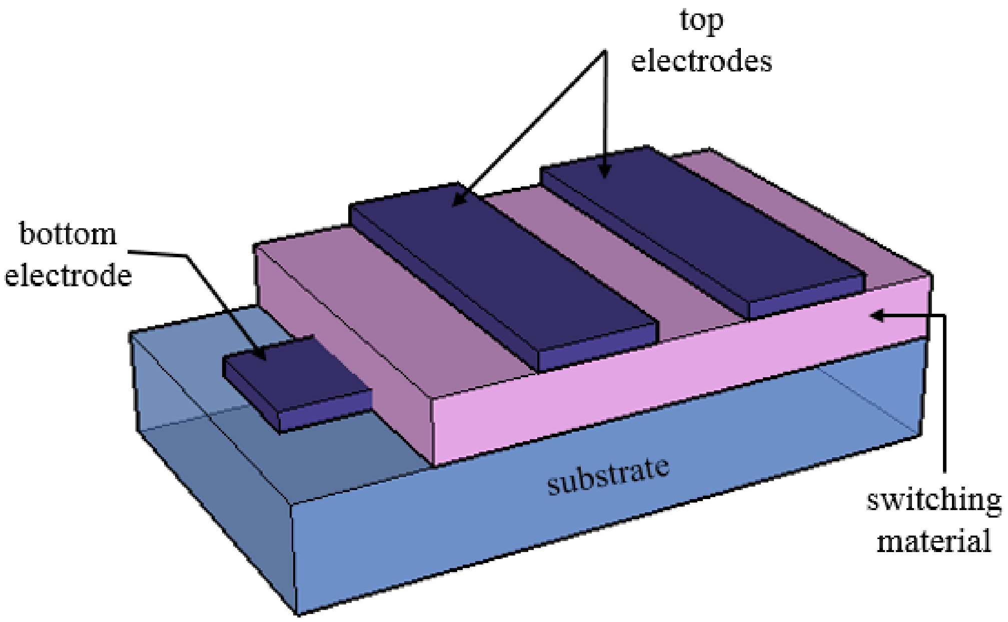

Figure 2.10: Schematic of a crossbar RRAM device structure.

Table 2.1: Characteristics of commercial memories in comparison with the emerging memory technologies, taken from [1].

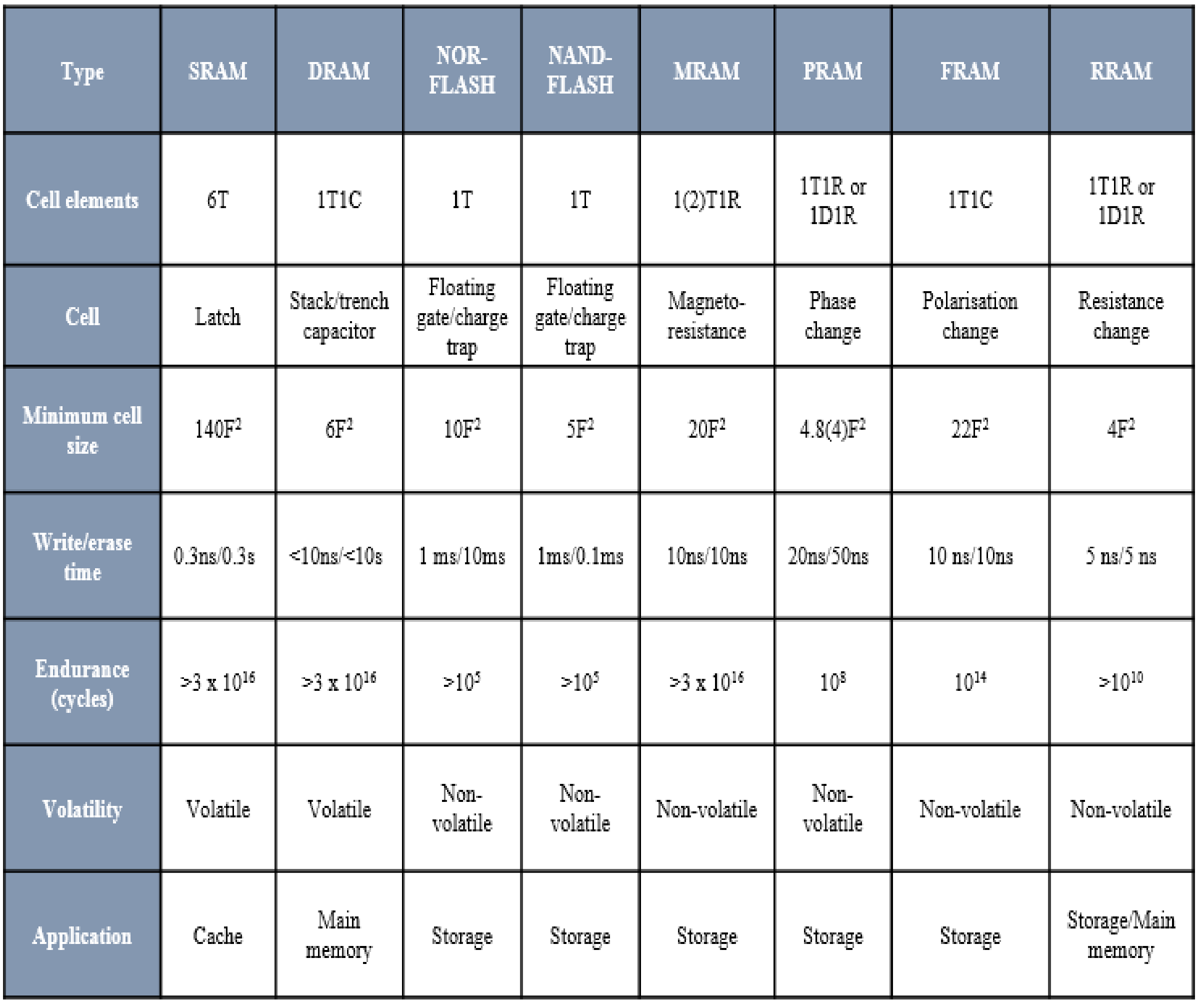

Type	SRAM	DRAM	NOR-FLASH	NAND-FLASH	MRAM	PRAM	FRAM	RRAM
Cell elements	6T	1T1C	1T	1T	1(2)T1R	1T1R or 1D1R	1T1C	1T1R or 1D1R
Cell	Latch	Stack/trench capacitor	Floating gate/charge trap	Floating gate/charge trap	Magneto-resistance	Phase change	Polarisation change	Resistance change
Minimum cell size	$140F^2$	$6F^2$	$10F^2$	$5F^2$	$20F^2$	$4.8(4)F^2$	$22F^2$	$4F^2$
Write/erase time	0.3ns/0.3s	<10ns/<10s	1 ms/10ms	1ms/0.1ms	10ns/10ns	20ns/50ns	10 ns/10ns	5 ns/5 ns
Endurance (cycles)	$>3 \times 10^{16}$	$>3 \times 10^{16}$	$>10^5$	$>10^5$	$>3 \times 10^{16}$	10^8	10^{14}	$>10^{10}$
Volatility	Volatile	Volatile	Non-volatile	Non-volatile	Non-volatile	Non-volatile	Non-volatile	Non-volatile
Application	Cache	Main memory	Storage	Storage	Storage	Storage	Storage	Storage/Main memory

2.4 Organic and Hybrid Memristors

In recent years, organic/polymeric materials have been of increasing interest in the electronic devices field. In particular, organic materials have attracted great attention as promising resistive switching materials for RRAM memory cells due to their properties, such as inexpensive matrix, easy fabrication based on solution processing using a simple spin-coating technique at room temperature, high density, flexibility, and large area and scalable fabrication [119]. RRAM/memristor devices based on organic materials exhibit bistable resistive switching with two distinctive resistance states that can be switched between the HRS and LRS when an external electric field is applied [120]. They also provide a non-volatile characteristic because the cell can retain its resistance state when the applied field is turned off.

Organic memories are two terminal elements that can be fabricated using either a polymer material or hybrid organic-inorganic composites as an active layer for the resistive switching. For the two terminal architectures, organic memory devices can be simply synthesised by sandwiching the matrix between the top and bottom electrodes. Experimentally, four architectures have been demonstrated. These designs are: firstly, a monolayer of organic medium sandwiched between two electrodes. Secondly, bilayer structures of two different organic materials. Thirdly, trilayer structures of organic/nano-traps layer/organic materials sandwiched between the top and bottom electrodes. The fourth sandwich structure of organic memories is based on a hybrid organic-inorganic composites between two electrodes[120]. Schematic structures of these organic memory types are shown in Fig. 2.11.

Several organic semiconductors and polymers have been demonstrated as an active switching layer in RRAM devices based organic materials, such as pentacene [9], 8-hydroquinoline aluminium (Alq3) [121], 2-amino-4,5- imidazoledicarbonitrile

(AIDCN) [122], polystyrene [38], poly(methyl methacrylate) (PMMA) [123], and poly(N-vinylcarbazole) (PVK) [124].

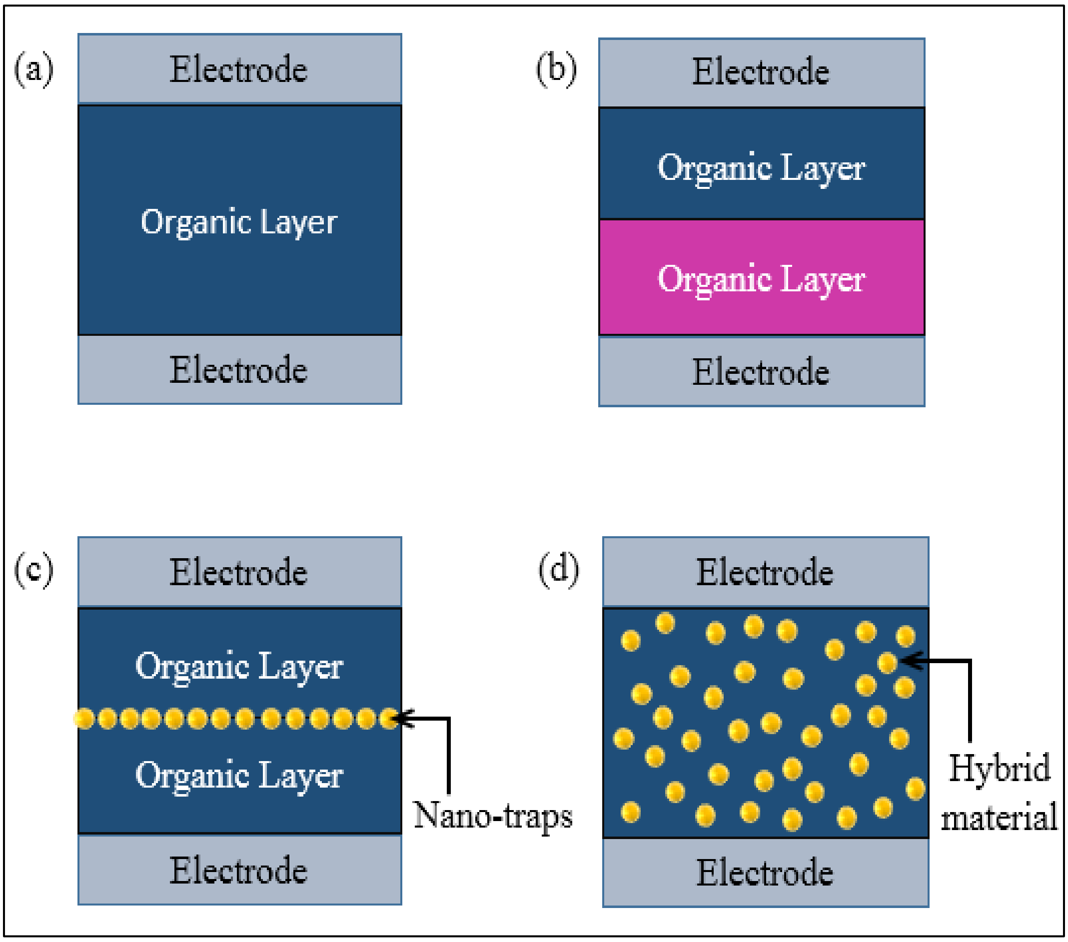

Figure 2.11: Schematic architectures of organic memristor cells. (a) A monolayer architecture containing only organic material, (b) a bilayer architecture including two organic materials, a tri-layer architecture containing two organic layers separated by nano-traps layer, and (d) a hybrid organic-inorganic monolayer architecture containing NPs suspended in an organic/polymer matrix.

For the hybrid devices, in particular, a wide range of organic and inorganic materials embedded in a host polymer matrix have been used. These include an organic acceptor and donor [125], nanowires and nanorods [26,44,55], nanofibers [70], graphene [41], carbon nanotubes [126], and nanoparticles [71,73,117,127,128]. Among them, nanoparticles are the most commonly used for fabricating hybrid devices by dispersing the nanoparticles in the host polymer medium. Although the mechanism responsible for the resistive switching in these devices is still unclear, several mechanisms for carrier transport and switching have been proposed, which include Schottky emission, Ohmic conduction, Space-Charge-Limited-Current (SCLC), thermionic emission, tunnelling current, hopping conduction, and ionic conduction. These mechanisms will be explained in the next chapter.

Chapter 3. Theoretical Background

This chapter illustrates the theoretical description of memristors. In the first part of this chapter, Leon Chua's memristor and a more general class called memristive systems are explained. Also, the theoretical description of HP Labs TiO_2 memristor is presented. The second part of this chapter is devoted to the resistive switching behaviours of memristors, conduction mechanisms, and neuromorphic theory.

3.1 Leon Chua's Memristor and Memristive Systems

In general, there are three basic two-terminal circuit elements, namely the resistor, R, the capacitor, C, and the inductor, L. Each of these three circuit elements can be defined by two pairs of fundamental variables; electric current (i), voltage (v), electric charge (q), and magnetic flux (φ), and the mathematical equations are:

$$dV = R \cdot di \quad \text{(resistance)}$$

$$dq = C \cdot dv \quad \text{(capacitance)}$$

$$d\varphi = L \cdot di \quad \text{(inductance)}$$

Leon Chua (1971), however, predicted a fourth circuit element that he called a memristor, which is defined by the missing relationship between the electric charge and magnetic flux [13]. The symbol and the q - φ curve of the memristor can be seen in Fig. 3.1. The electric charge and magnetic flux are time integrated functions of current and voltage, respectively, and are given by

$$q(t) = \int_{-\infty}^{t} i(\tau)d\tau \tag{3.1}$$

and

$$\varphi(t) = \int_{-\infty}^{t} v(\tau)d\tau \tag{3.2}$$

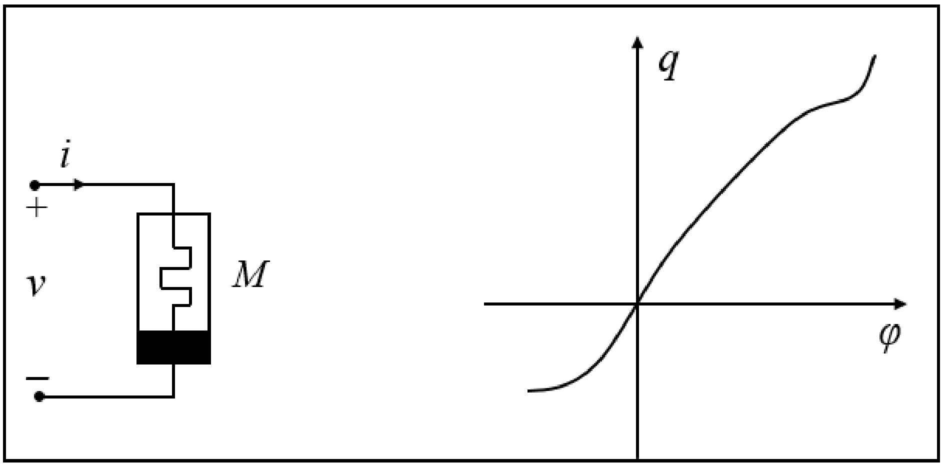

Figure 3.1: The symbol and q - φ curve of the memristor taken from [13].

Chua pointed out that a memristor can be described by a relation of the type $g(\varphi, q) = 0$. Depending on this relation, he also defined two types of memristors; charge-controlled memristors and flux-controlled memristors. A memristor can be charge-controlled or flux-controlled when the relation is expressed as a singlevalued function of the charge q or flux-linkage φ, respectively. The definition of the voltage of a charge-controlled memristor can be given by

$$v(t) = M(q(t))i(t) \tag{3.3}$$

where

$$M(q) \equiv \frac{d\varphi(q)}{dq} \tag{3.4}$$

Also, the current of a flux-controlled memristor can be given by the formula

$$i(t) = W(\varphi(t))v(t) \tag{3.5}$$

where

$$W(\varphi) \equiv \frac{dq(\varphi)}{d\varphi} \tag{3.6}$$

$M(q)$ is described as an incremental memristance that has the resistance unit (Ω), and $W(\varphi)$ as an incremental memductance that has the unit of conductance (S). Equation (3.4) shows the definition of the memristor as a functional relation between flux-linkage (φ) and charge (q).

In his seminal article, Chua demonstrates that the value of the incremental memristance or memductance at any time t_0 relies on the time integral of the memristor current or voltage respectively from $t = -\infty$ to $t = t_0$. The choice of the memristor name came from the behaviour of the device, which unlike an ordinary resistor at a given instant of time, t_0, its resistance or conductance is dependent “or remembers” the last current pass through it [13]. In addition, the memristor can behave like a linear time-varying resistor when the current $i(t)$ or the voltage $v(t)$ is fixed. Chua also points out that the memristor shows a straight line in its φ - q curve where $M(q) = R$, or $W(\varphi) = G$, and the memristor reduces to a linear time-invariant resistor. The instantaneous power dissipated by the charge-controlled memristor can be given by the formula

$$p(t) = v(t)i(t) = M(q(t))[i(t)]^2 \tag{3.7}$$

Similarly, the instantaneous power dissipated by the flux-controlled memristor is given by

$$p(t) = i(t)v(t) = W(\varphi(t))[v(t)]^2 \tag{3.8}$$

The following criteria are proved by Chua [13].

Theorem 1. Passivity Criterion

“A memristor described by a differentiable charge-controlled φ - q curve is passive if, and only if, its incremental memristance $M(q)$ is nonnegative; $M(q) \geq 0$”. As a memristor behaves like a linear resistor at any instant of time, this criterion can be viewed as analogous to the behaviour of an ordinary resistor, in that the resistance of an ordinary resistor cannot be negative, as a result of Ohm’s Law. This passivity criterion exhibits the type of a physical memristor to be achieved in future without internal power supply to operate.

Theorem 2. Closure Theorem

“A one-port containing only memristors is equivalent to a memristor”.

Theorem 3. Existence and Uniqueness Theorem

“Any network containing only memristors with positive incremental memristances has one, and only one, solution”.

Chua and Kang, however, generalised the theoretical description of the memristor into a broader class of dynamical systems that can include any two-terminal devices whose variable resistance relies on the internal state of the system. They named this class of systems memristive systems. These memristive systems show the same pinched hysteresis loop (Lissajous figure) in the *i*-*v* plane where the current must be zero whenever the voltage is zero [28]. The resistance of a memristor depends directly on the electric charge *q* or flux linkage *φ*. In contrast, in memristive systems, the resistance depends on the past history of current or voltage experienced by the device. Memristive systems can be defined by

$$\dot{x} = f(x,u,t) \tag{3.9}$$

$$y=g(x,u,t)u \tag{3.10}$$

where u and y denote the input and output of the system and *x* represents the state of the system.

An *n*th-order current-controlled memristive one-port is described by

$$\dot{x}=f(x,i,t) \tag{3.11}$$

$$V_M(t)=M(x,i,t)i(t) \tag{3.12}$$

where *n* donates the dimension of the state space of the dynamical system, V_M(t), and i(t) denote the voltage and current across the device, and *M* is the memristance.

Similarly, an *n*th-order voltage-controlled memristive one-port can be found by

$$\dot{x}=f(x,v,t) \tag{3.13}$$

$$i(t)=G(x,V_M,t)V_M(t) \tag{3.14}$$

where *G* is the memductance.

In the special case when the one-port is time-invariant, and *R* (resp. *G*) is not an explicit function of *i* (resp. *v*) we have

$$\dot{x} = f(x,i) \qquad (resp., \dot{x} = f(x,v)) \tag{3.15}$$

$$v = R(x)\,i \qquad (resp., i = G(x)v) \tag{3.16}$$

The memristor that was proposed by Chua was considered as a mathematical description, but the physical memristor device was first announced by Hewlett-Packard Labs researchers in 2008. A more detailed description of the HP memristor is given in the following section.

3.2 HP Labs TiO_2 Memristor

In 2008, the HP Lab research group declared that they had found the missing memristor, and published an article on their results in Nature [15]. The device structure consists of a thin TiO_2 film sandwiched between two platinum electrodes using crossbar architecture [129]. Fig. 3.2 shows a schematic of the HP memristor.

The TiO_2 thin film was designed to include two layers: a high concentration of oxygen vacancies layer, (TiO_{2-x}), and a low or zero concentration of oxygen vacancies layer, (pure TiO_2). Oxygen vacancies are considered as positively charged ions. In particular, the layer that has a high concentration of oxygen vacancies represents the low resistance state (R_{ON}), while the low concentration oxygen vacancies layer represents the high resistance state (R_{OFF}).

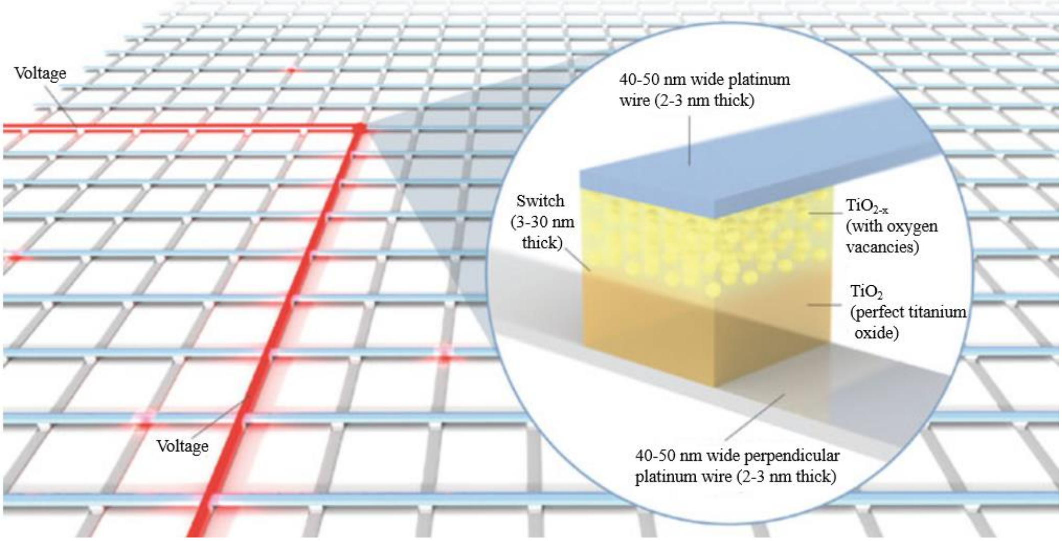

Figure 3.2: The crossbar structure of the HP memristor device taken from [129].

Resistive switching in this device is based on the drift of oxygen vacancies between two parts of the TiO_2 thin film when an external voltage is applied. When a positive voltage is applied, positively charged oxygen vacancies will migrate toward a negatively biased electrode and move the boundary between the two parts, as shown in Fig. 3.3.a. In this case, the TiO_{2-x} part expands, which leads to a decrease in the resistance of the whole device, and switches the device to the ON state. However, by applying a negative voltage, the oxygen vacancies will move in the opposite direction and push the boundary toward the negative electrode, see Fig. 3.3.b. In this case, the thickness of the pure TiO_2 layer (high resistance) will be increased. As a result, the whole resistance of the device will increase and change the device to the OFF state [129]. The device is considered as a non-volatile memory because the device can maintain its last resistance and keep the boundary between two parts of TiO_2 layers unchanged when the applied voltage is removed.

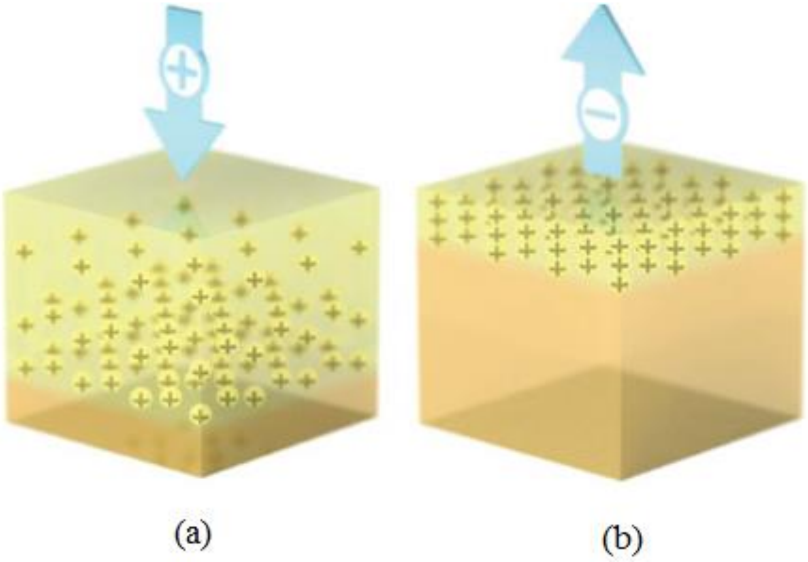

Figure 3.3: The effect of applied voltage on dopant drift taken from [129].

Regarding the previous resistive switching mechanism, a mathematical model of a two-terminal TiO_2 film memristor device has been introduced by the HP group. The equivalent model of the Pt/TiO_2/Pt structure device is illustrated in Fig. 3.4. This model is based on two regions of TiO_2; a doped region (rich in oxygen vacancies), and undoped region (deficient of oxygen vacancies). The doped region with width w has a low resistance (R_{ON}), and the undoped region has a high resistance (R_{OFF}). In this model, R_{ON} and R_{OFF} are linked in series. The entire resistance of the TiO_2 film is given by the sum of the R_{ON} and R_{OFF} over the full length of the device (D).

It is found that applying an external voltage across the TiO_2 memristor device causes the oxygen vacancies to drift and change the position of the boundary between the two regions, depending on the polarity of the applied voltage [15].

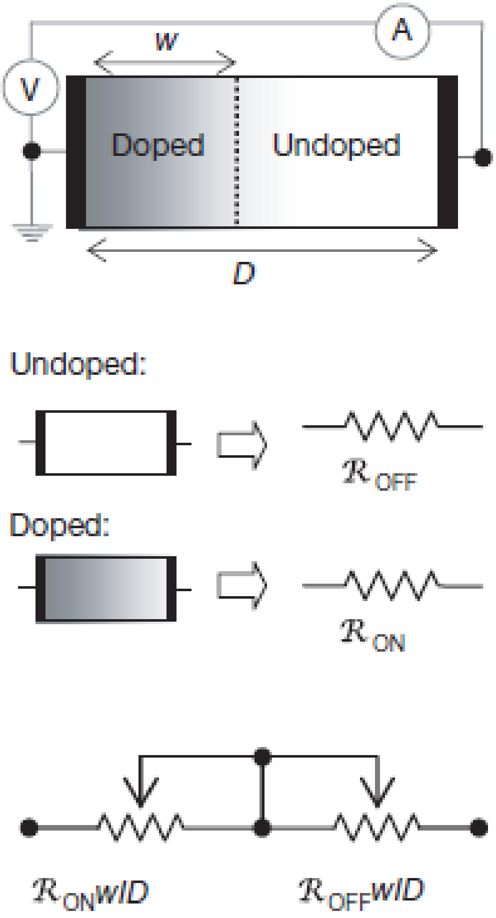

Figure 3.4: Coupled variable-resistor model of the HP memristor taken from [15].

The mathematical description of this model that shows how the memristance of the device can be influenced by dopant drift is given by the following relations:

$$v(t)=\left(R_{ON}\frac{w(t)}{D}+R_{OFF}\left(1-\frac{w(t)}{D}\right)\right) \tag{3.17}$$

$$\frac{dw(t)}{dt}=\mu_v\,\frac{R_{ON}}{D}i(t) \tag{3.18}$$

where μ_v is the average ion mobility.

If $R_{ON} \ll R_{OFF}$, the memristance is given by

$$M(q)=R_{OFF}\left(1-\frac{\mu_v R_{ON}}{D^2}q(t)\right) \tag{3.19}$$

The pinched hysteresis loop of the HP memristor is shown in Fig. 3.5. This figure shows that at high frequencies the pinched hysteresis loop shrinks to a straight line and the device behaves like a resistor. This is because the oxygen vacancies are unable to move and change the resistance of device from high to low and vice-versa when the polarity of applied voltage is changed too rapidly. An AFM image of the crossbar memristor array fabricated by the HP group is shown in Fig. 3.6.

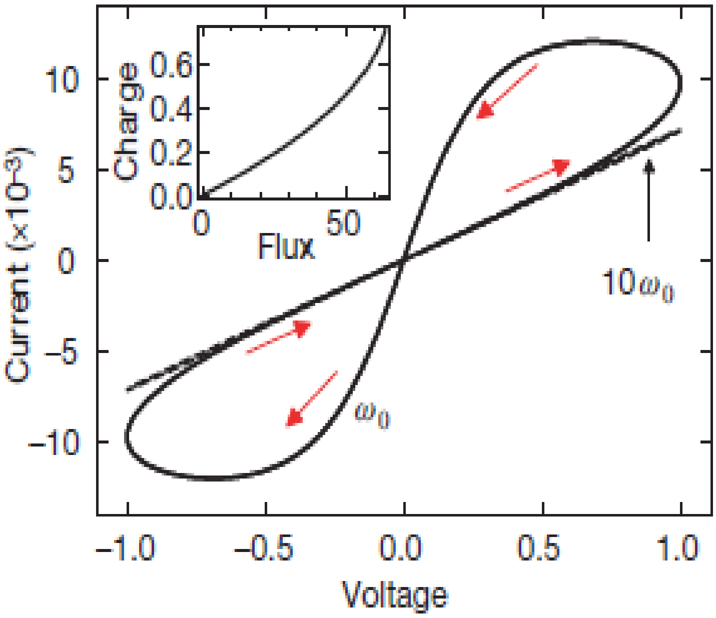

Figure 3.5: Pinched hysteresis loop of the HP memristor taken from [15].

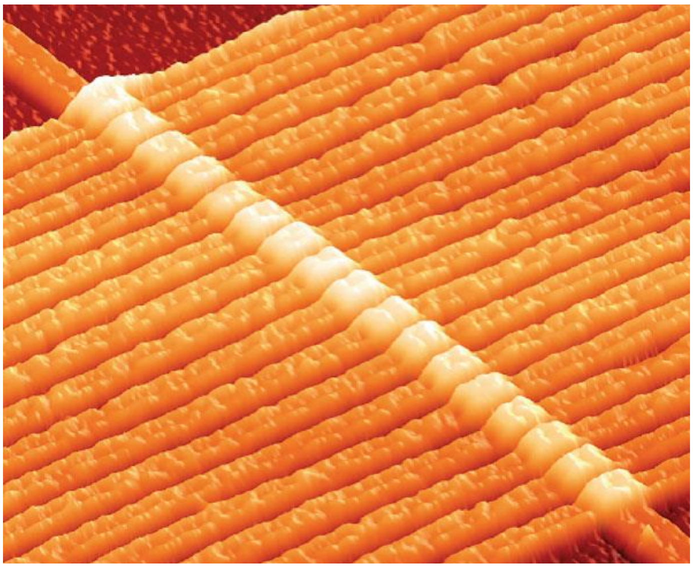

Figure 3.6: AFM image of a TiO2 crossbar memristor array taken from [129].

3.3 Resistive Switching

The term resistive switching is generally understood to mean the change of the memristor or RRAM resistance from HRS to LRS and vice-versa. The changing of the device resistance from HRS to LRS is named as a '*SET*' process or '*ON*' state. The switching from LRS to HRS is termed as a '*RESET*' process or '*OFF*' state. Unused devices (as prepared devices) frequently show low currents and/or no switching at low applied voltages. This is because the resistive switching material has no conductive paths of filaments. In this case, these devices need to be activated by applying a high voltage, higher than the set voltage. This is called the electroforming process [130]. Before applying high voltages, the device current must be limited in order to prevent breakdown of device. Practically, the electroforming process is not desirable because it makes the devices high power consumption.

Regarding the current-voltage curves, the phenomena of resistive switching in memristors or RRAM devices can be classified into two types: unipolar and bipolar [131] as shown in Fig. 3.7. In unipolar resistive switching, both the SET and RESET processes occur in the same voltage polarity, whether positive or negative, but at two different magnitudes of applied voltage. On the other hand, bipolar resistive behaviour depends not only on the magnitude but also on the polarity of the applied voltage. In this case, if the SET process occurs at a specific magnitude positive voltage, the same voltage (polarity and/or magnitude) will not switch the device to the RESET process [132].

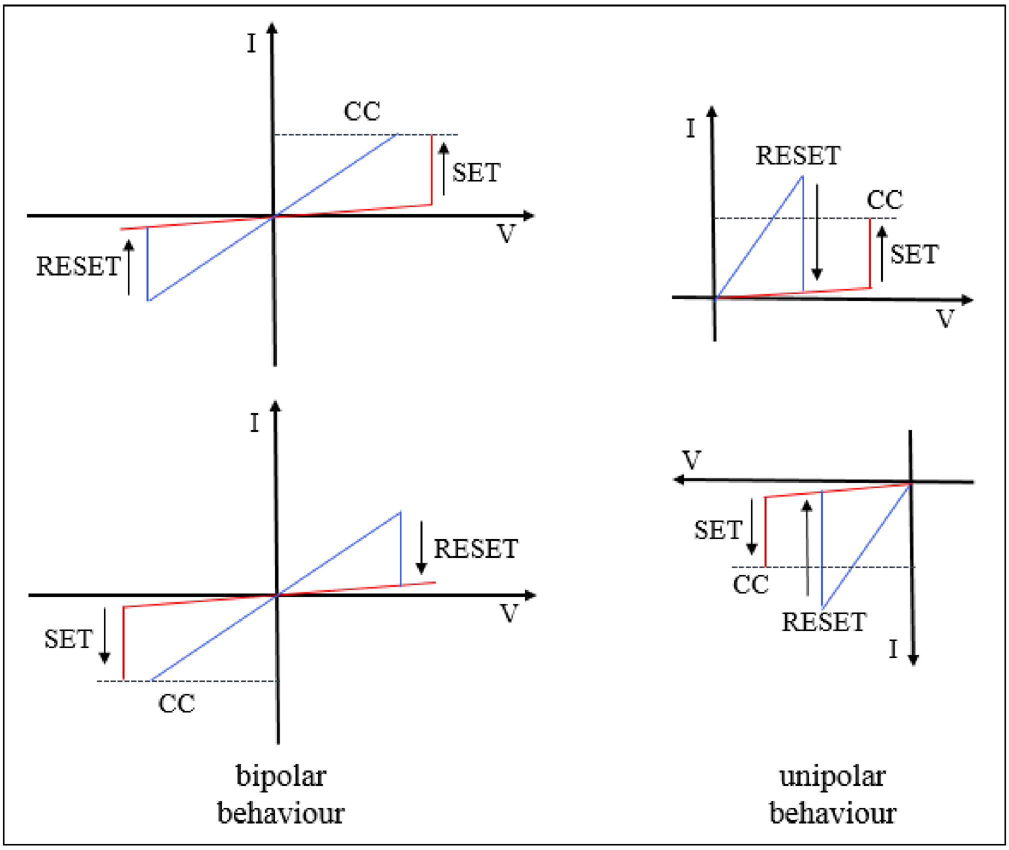

Figure 3.7: Bipolar and unipolar switching behaviours.

It seems that switching from one state to another can be changed either gradually or suddenly. For example, in our devices that consist of ZnO nanorods embedded in PDR1A, the device showed gradual switching between the SET and RESET states. In contrast, another type of our device that consisted of Au nanoparticles embedded in PDR1A exhibited a sudden switching between ON and OFF states.

Resistive switching has been found in a wide range of materials. Regarding the switching medium and architecture of the device, it is found that in some cases the same resistive switching medium can show both unipolar and bipolar behaviours.

For example, ZnO thin films exhibited unipolar [133] and bipolar [134] switching depending on the defects in the ZnO thin film and the oxide/electrode interfaces, respectively.

Basic RRAM devices have a Metal-Insulator-Metal (MIM) structure [130]. In this structure, the switching matrix is sandwiched between two metal electrodes. A schematic of the MIM architecture is shown in Fig. 3.8. The MIM structure is increasingly important in high-density memory cell structures, specifically in crossbar architectures [135]. It offers resistive switching memory based on two-terminal devices rather than three terminal devices as in DRAMs [136]. Using this advantage to fabricate a nano crossbar arrays of bottom electrodes and perpendicular top electrodes with a switching material between them integrated on top of a CMOS architectures. This approach provides a small size cell of 4F^2 for each crosspoint with a density of 1 Tb/cm^2.

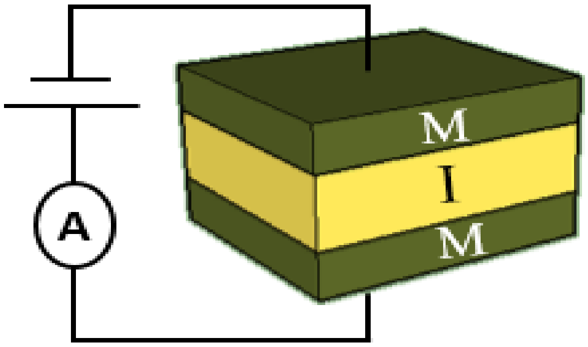

Figure 3.8: Schematic of the Metal-Insulator-Metal memory cell structure.

3.4 Electronic Transport Mechanisms

As mentioned previously, resistive switching has been seen in a wide range of materials, e.g. binary metal oxides, organics/polymers, perovskites, and hybrid organic-inorganic composites. The mechanism responsible for conduction and switching in some devices can be elucidated using various experimental techniques. For example, the formation and rupture of conductive filaments can sometimes be seen by SEM and TEM. However, the conduction mechanism in other devices is complicated in which two or more of the conduction mechanisms can be used to explain the change in the resistance states. As illustrated in Fig. 3.9, the conduction mechanisms can be classified into two types: electrode-limited conduction mechanisms that rely on the electrical properties of the interface between the electrode and the resistive switching layer, and bulk-limited conduction mechanisms that rely on the electrical properties of the switching material itself. Here, an overview of the carrier transport and conduction mechanisms are described in detail.

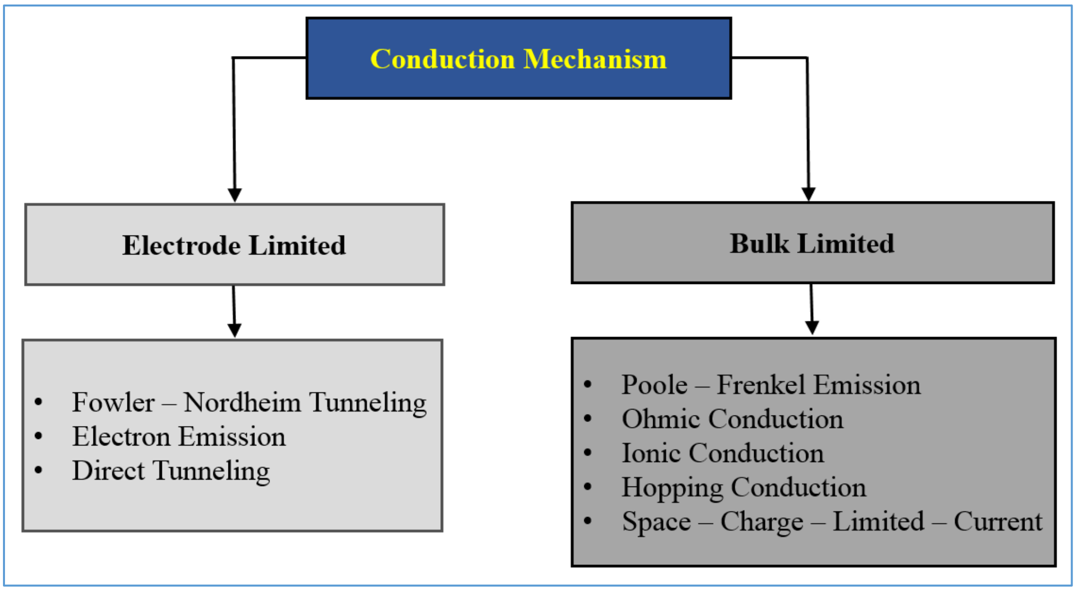

Figure 3.9: Types of conduction mechanisms in RRAM devices.

3.4.1 Electrode – Limited Conduction Mechanisms

3.4.1.1 Fowler – Nordheim (F-N) Tunnelling

Fowler-Nordheim tunnelling occurs at the metal/insulator interface in the presence of sufficient electric field for electron tunnelling. In this mechanism, the electrons in the metal can penetrate through the triangular shape potential barrier into the conduction band of the insulator or oxide [137]. A schematic of F-N tunnelling is shown in Fig. 3.10. The current density (J_{FN}) expression of F-N tunnelling is given by

$$J_{FN} = \frac{q^2 E^2}{8\pi h \phi_B} \exp\left(\frac{-8\pi\sqrt{2qm^*}}{3hE} \phi_B^{3/2} \right) \tag{3.20}$$

where ϕ_B is the barrier height at the metal-insulator interface, m^* is the electron effective mass in the insulator, h is Planck's constant, and q and E are the electronic charge and electric field respectively. As can be seen, there is no temperature dependence of the electron tunnelling process.

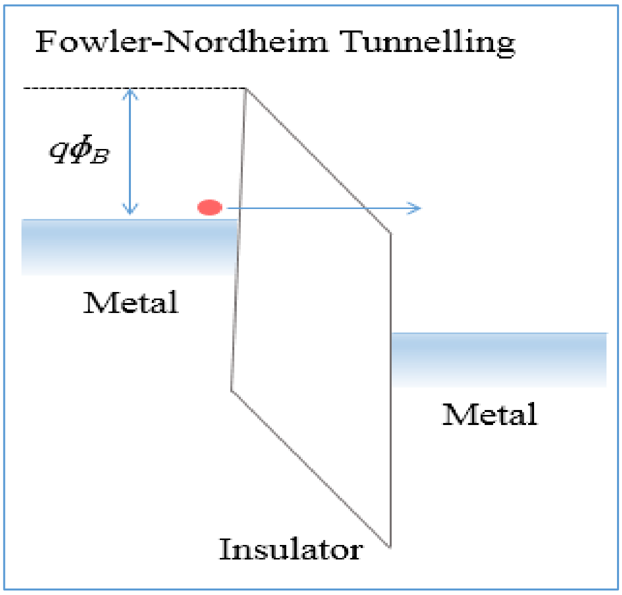

Figure 3.10: The Fowler-Nordheim tunnelling conduction mechanism in a metal-insulator-metal structure.

At high electric field, electrons existing in the metal that are injected through the triangular barrier will be trapped by defects and/or dopants, e.g. nanoparticles in the oxide or insulator. As a result, this can modify the electrostatic barrier property of the MIM structure and, hence, the resistance of the device will be changed [32]. This mechanism has been reported in an Al/Au-DT+8HQ+PS/Al device structure using gold nanoparticles and a polystyrene composite as an active layer [8].

3.4.1.2 Electron Emission

There are three mechanisms of electron emission that can take place at the metal/insulator interface in the MIM structure. These mechanisms are thermionic emission (Schottky emission), field emission, and thermionic-field emission. The schematic energy band diagrams of these emission processes are presented in Fig. 3.11.

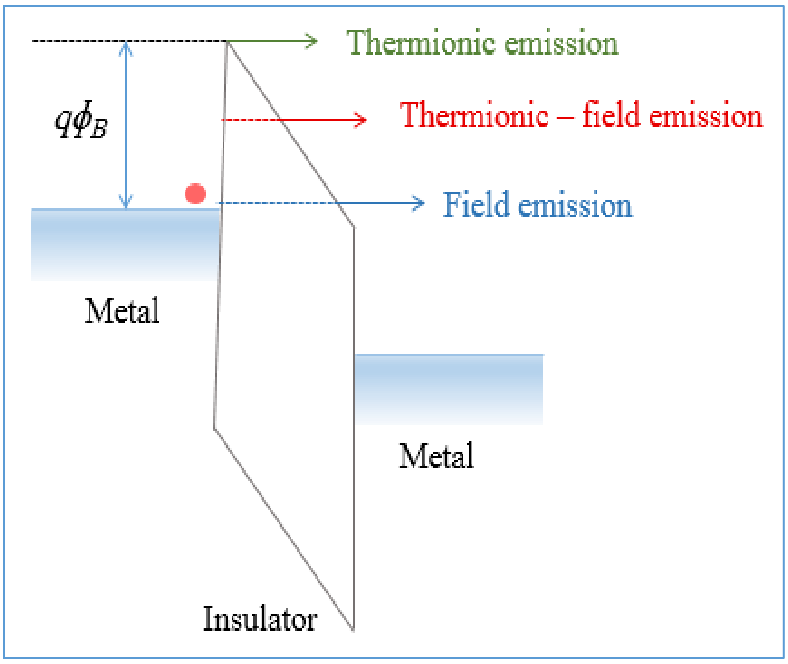

Figure 3.11: Schematic diagram of three emission processes at the metal/insulator interface in metal-insulator-metal structure.

The main parameters that determine which process can dominate are the temperature and the strength of the applied field. For example, when the applied field is low and the temperature is high enough, electrons are emitted over the barrier. This mechanism is called thermionic emission. In this mechanism, the variation of current mainly depends on the temperature. In contrast, in the case of the high electric field and low temperature, emission process is dominated by the electrons that have energies below the Fermi level. This mechanism is defined as field or cold emission [138]. Thermionic-field emission, however, represents the intermediate case between the thermionic emission and field emission where the temperature and electric field do not belong either to the thermionic field region or the field emission region [139]. It relies on the emission of carriers through the tunnelling barrier. Since the electrons have sufficient energy, conduction in the MIM takes place by the tunnelling of electrons between the Fermi level of the metal and the conduction band of the insulator. Equations 3.21, 3.22, and 3.23 show the mathematical expression of the current density due to thermionic emission, field emission, and thermionic-field emission, respectively [140]

$$J = \frac{4q\pi m\, k^2 T^2}{h^3} \exp\left[-\frac{\chi}{kT}\right] \exp\left[\frac{\beta_s}{(kT)}\sqrt{E}\right] \tag{3.21}$$

where

$$\beta_s = \sqrt{\frac{q^3}{4\pi\varepsilon\varepsilon_0}}$$

$$J = \frac{q^3 E^2 \sqrt{m}\left(kT\right)^{1/2}}{8\pi h\, \chi t^2(y)} \exp\left[-\frac{8\pi\sqrt{2m}\,\chi^{3/2}\theta(y)}{3hqE}\right] \tag{3.22}$$

$$J = \sqrt{\frac{2m\pi kT\varphi(z)}{h^2}}\, q^2 E \exp\left[-\frac{\chi}{kT} + \frac{(hqE)^2 \varphi(z)}{96m\pi^2 (kT)^3}\right] \tag{3.23}$$

where χ is the metal/insulator work function, ε the relative dielectric permittivity of the insulator, ε_0 is the permittivity of vacuum, m is the electron effective mass in the insulator, h is Planck’s constant, k is Boltzmann’s constant, T is the absolute temperature, $t(y)$ and $\theta(y)$ are functions of the field intensity, $\varphi(z)$ is the Murphy-Good function, and q and E are the electronic charge and electric field, respectively. As can be seen from the equation, thermionic-field emission relies on both temperature and applied field.

This conduction mechanism has been reported in some resistive switching devices. Shuxiang *et al.* demonstrated that the thermionic emission is the dominant conduction mechanism for the ITO/LAO/STO structure in the HRS by tunnelling the electrons through the Schottky barrier at the ITO/LAO interface [141]. Thermionic emission also reported by Wei *et al.* as a mechanism in the ON state of a Au/MoS_2/Au structure [142]. Further, Gul [46] investigated the resistive switching behaviour of ZnO thin films in an Al/ZnO/Al structure, suggesting that Schottky emission is the dominant conduction mechanism in the high applied electric field region. In a TiW/Cu_2O/Cu structure, Schottky emission was also suggested by Yan *et al*. [143] as the responsible mechanism for conduction in the HRS at the Cu_2O/Cu interface.

3.4.1.3 Direct Tunnelling

According to quantum mechanics, conduction in the MIM structure happens by direct tunnelling of an electron from one electrode to another through the insulator; even the electron energy is less than the barrier energy. Usually, this mechanism occurs in very thin insulators, and there is no requirement for high electric fields. In the case of thicker insulators and sufficiently high applied fields, Fowler-Nordheim tunnelling dominates [144]. Figure 3.12 shows a schematic energy band diagram of direct tunnelling.

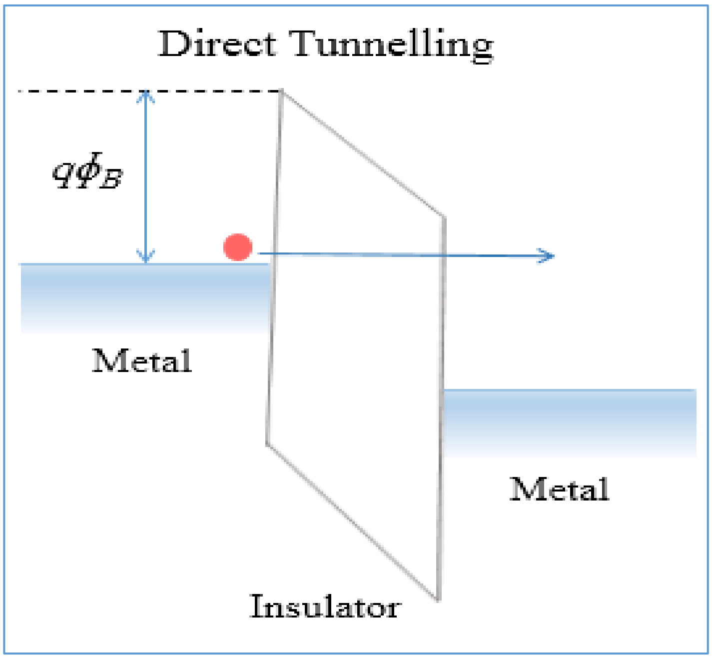

Figure 3.12: Schematic energy band diagram illustrating direct tunnelling in an MIM structure.

The current density relationship can be given by [139]

$$J = AC\left(V_G, V, t, \phi_B\right)\exp\left\{-B\cdot\left[1-\left(1-\frac{|V|}{\phi_B}\right)^{3/2}\right]\right\} \tag{3.24}$$

$$A = \frac{q^2}{8\pi h\varepsilon\phi_B},$$

$$B = \frac{8\pi\sqrt{2m^*}\left(\phi_B\right)^{3/2}}{3hq|E|}$$

where t is the thickness of the insulator, V is the voltage across the insulator, ε the relative dielectric permittivity, m^* is the effective electron mass in the insulator, h is Planck's constant, q is the electronic charge, $\emptyset_B$ is the tunnelling barrier height, E is the electric field.

3.4.2 Bulk – Limited Conduction Mechanisms

3.4.2.1 Poole – Frenkel Emission

Poole-Frenkel (P-F) emission depends on the thermally excited electrons that have sufficient energy to be emitted from traps into the conduction band of the insulator. The P-F emission schematic band energy diagram is depicted in Fig. 3.13. Since both mechanisms use thermally excited electrons, the P-F emission is sometimes named internal Schottky emission. However, the main difference between Schottky emission and P-F emission is that the electric field reduces the Schottky barrier height at the metal/insulator interface, whereas in P-F emission, the electric field reduces the Coulomb potential energy of electrons (lowering the depth of traps). This mechanism arises at high applied electric fields. When an electric field is applied across the MIM device, the electrons in the trapping sites can be thermally excited, and at the same time, the Coulomb potential energy of the electrons can be decreased. Consequently, the probability of electrons being emitted from the trap sites into the conduction band of the insulator increases, and that leads to conduction takes place [145].

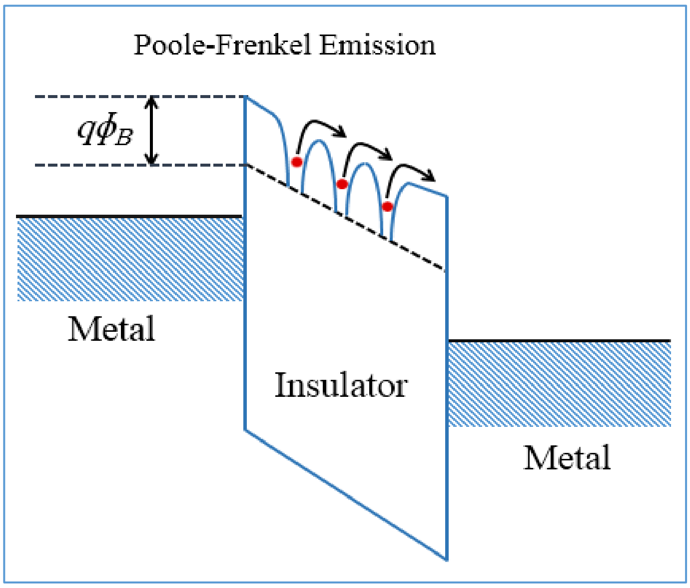

Figure 3.13: Schematic energy band diagram of P-F emission conduction mechanism.

The current density relationship due to P-F emission is

$$J = q\mu N_C\, E \exp\left[-\frac{q\left(\phi_T - \sqrt{qE/\pi\varepsilon_i\varepsilon_0}\right)}{k_B\, T}\right] \tag{3.25}$$

where q is the electronic charge, μ is the electronic drift mobility, N_C is the density of states in the insulator conduction band, E is the electric field across the insulator, $q\emptyset_T$ is the trap energy level, ε_i is the permittivity of the insulator, ε_0 is the permittivity of vacuum, and T is the absolute temperature.

Experimentally, P-F emission can be distinguished from the current-voltage curve if a plot of the logarithm of the current density against the square root of the applied potential is linear [146]. This conduction process has been commonly noticed in several unipolar and bipolar RRAM devices. By way of illustration, Nagashima *et al.* [147] investigated the resistive switching behaviour of SnO_2 thin films sandwiched between Pt bottom electrode and different top electrodes (Pt, Au and Ti). In the high electric field region of the HRS, the linear plot of ln J/E versus $(E)^{1/2}$ has good agreement with the P-F emission in which the hopping of electrons from the trap sites into the conduction band of the SnO_2 dominates. Similarly, the linear fitting ln (J/E) – $E^{1/2}$ curve of crossbar devices based on an Al/ZnO/Si structure fabricated by Chen *et al.*[148] shows that the current in the HRS is governed by P-F emission.

3.4.2.2 Ohmic Conduction

This mechanism happens through the movement of thermally stimulated mobile electrons into the conduction band. These electrons can be stimulated from dopants or from the valence band into the conduction band. Ohmic conduction dominates in the LRS at low applied voltages. This may be due to the large band gap of the insulator, which makes the number of thermally activated electrons very small [139]. The Ohmic conduction schematic diagram is shown in Fig. 3.14.

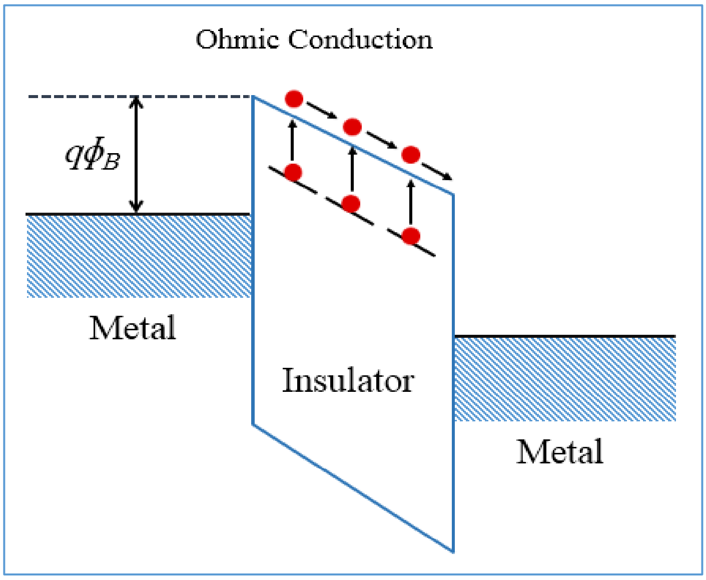

Figure 3.14: Ohmic conduction schematic diagram in MIM structure.

The current density relationship due to Ohmic conduction can be expressed as:

$$J = \sigma E = q\mu N_C E \exp\left[-\frac{(E_C - E_F)}{kT}\right] \tag{3.26}$$

where σ is electrical conductivity, *q* is the electronic charge, *μ* is the electronic drift mobility, N_C is the density of states of the conduction band, *E* is the electric field across the insulator, and T is the absolute temperature, k is Boltzmann's constant, and E_C and E_F are the conduction band and Fermi energy levels, respectively.

To identify this conduction mechanism, the relationship between the current density (J) and electric field (E) in the I-V characteristics of the RRAM devices should be linear. For example, Chiu *et al.* [149] reported that the I-V characteristic of the Pt/ZnO/Pt device is fitted very well the Ohmic conduction mechanism in the LRS. In another work, Chiu [150] also observed a similar conduction mechanism in boron-doped ZnO film-based RRAM devices, in which the linear relationship between J and E confirmed Ohmic conduction in the ON state. Ohmic conduction is further distinguished as the responsible conduction mechanism in Pt/$LaHoO_3$/Pt device as reported by Sharma *et al.* [151]. The linear fitting of J against E in ON state with a slope of ~1 clearly indicates the Ohmic conduction.

3.4.2.3 Ionic Conduction

Ionic conduction is based on the movement of positively and/or negatively charged ions from one place to another when an electric field is applied across the insulator. Ions in trap or defect lattice sites excited by an electric field can hop over a potential barrier from site to site [152]. Fig. 3.15 illustrates the ionic conduction process. This conduction mechanism takes place in cases when one site is occupied by an ion and the neighbouring site is empty. Also, in order for an ion to move from its site to the neighbour site, its energy should be sufficient to pass over an energy barrier.

The current density relation due to ionic conduction can be given by [139]:

$$J = J_0 \exp\left[-\left(\frac{q\phi_B}{kT} - \frac{Eqd}{2kT}\right)\right] \tag{3.27}$$

where J_0 is a proportionality constant, $q\emptyset_B$ is the potential barrier height E is the electric field across the insulator, q is the electronic charge, T is the absolute temperature, k is Boltzmann's constant, and d is the distance between the two adjacent sites.

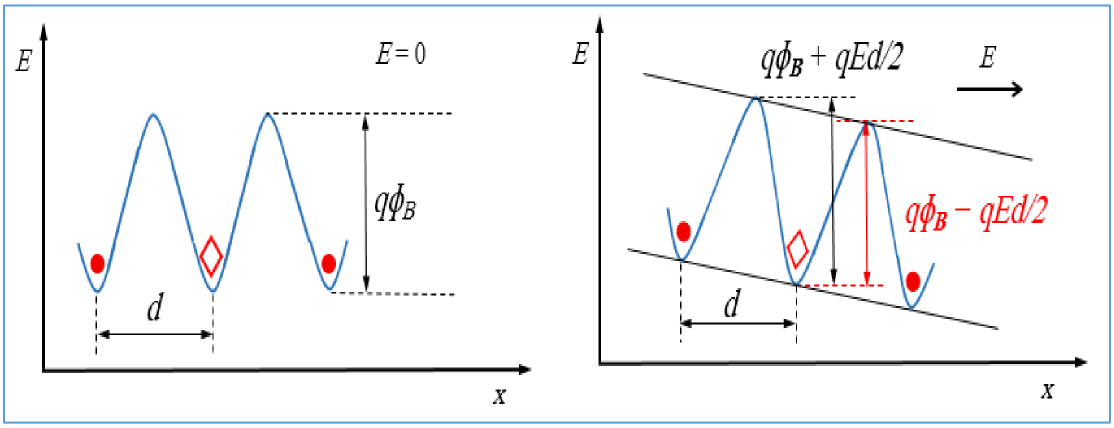

Figure 3.15: Schematic diagram of ionic conduction; (left) in the absence of electric field, and (right) in the presence of electric field.

This conduction mechanism has been reported in some RRAM devices such as those containing ZrO_2 nanoparticles [153] and HfO_2/TiO_{2-x} stack thin films [35] in the LRS.

3.4.2.4 Hopping Conduction

Hopping conduction is another bulk-limited conduction mechanism based on the existence of dopant/impurity trap sites and intrinsic thermal free carriers within the bulk of insulator or semiconductor materials. Carriers can hop in two ways; nearest neighbour hopping (NNH), and variable range hopping (VRH). In the case of nearest neighbour hopping, charge carrier transport occurs *via* a tunnelling effect in which the trapped carriers can hop from their sites into the nearest neighbour sites when the carriers receive sufficient thermal energy. Variable range hopping, however, occurs through the hopping of trapped carriers from their sites into other sites which are far away but with low trap energies [137]. These two hopping conduction mechanisms in MIM structures are shown in Fig. 3.16.

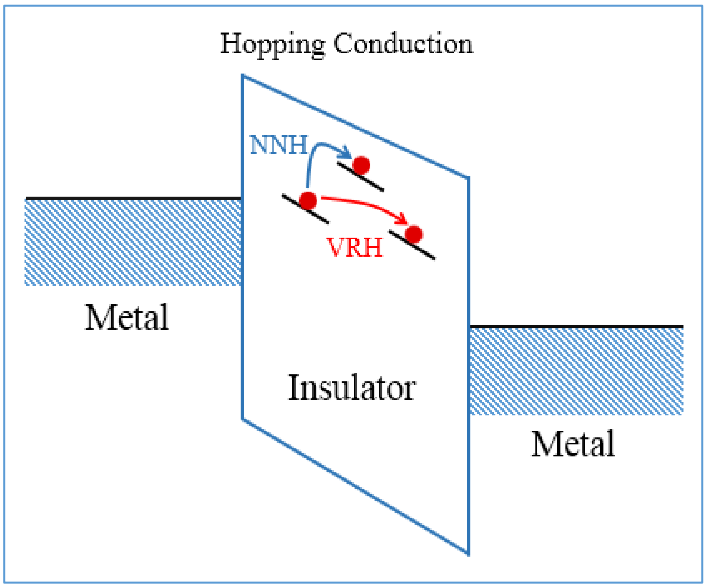

Figure 3.16: Schematic representation of nearest neighbour hopping (NNH) and variable range hopping (VRH) in an MIM structure.

The hopping current density relationships of NNH and VRH are given by equations 3.28 and 3.29, respectively.

$$J_{NNH} = \sigma_0 \exp\left(\frac{-T_0}{T}\right) . E \qquad (3.28)$$

$$J_{VRH} = \sigma_0 \exp\left(\frac{-T_0}{T}\right)^{1/4} . E \qquad (3.29)$$

where σ_0 is the electrical conductivity at a temperature of T_0, and E is the applied electric field across the insulator.

Hopping conduction is a commonly reported mechanism in RRAM devices. Hopping conduction dominates in the HRS, and exhibits different temperature dependencies. For NNH, $\ln(\sigma) \alpha T^{-1}$, while for VRH, $\ln(\sigma) \alpha T^{-1/4}$. This mechanism is observed in the W/ZnO:B/W device structure, as reported by Fu-Chiu [150]. The *J-E* curve in HRS suggests hopping conduction in the high electric field region (larger than 0.35 MV/cm). Yan *et al.* [143] verified that hopping conduction dominates in the LRS and coexists with Schottky emission in the HRS in TiW/Cu_2O/Cu devices. In the LRS, the $\ln(\sigma) \alpha T^{-1/4}$ plot fits the VRH model, where carriers move by hopping through the filaments which connect the top and bottom electrodes. In the HRS, due to the filament rupturing, a Schottky barrier is formed at the Cu_2O/Cu interface and copper vacancies accumulate at the TiW/Cu_2O interface. Consequently, the carriers move by hopping between the remaining section of the filament and emit at the Cu_2O/Cu interface. Therefore, charge carriers can jump from one site to another and follow the hopping conduction mechanism in the case of a high density of trap sites within the resistive switching matrix.

3.4.2.5 Space – Charge – Limited – Current (SCLC) Conduction

Space-Charge-Limited-Current (SCLC) is a common conduction mechanism that explains charge carrier transport in some semiconductors and insulators. SCLC occurs when electric charge is injected from a metal into an insulating material. The build-up of injected charge creates a region of space charge and an associated electric field that limits further current from passing into the insulator. It is considered a bulk limited process because the injected charge creates a region of space charge in the bulk of the material, in contrast to electrode limited process that occurs at the interface between the metal and insulator.

The charge carriers can be injected in trap sites, e.g. impurities or defects, whilst others participate in current flow across the insulator. The SCLC mechanism can be identified whenever three different regions are observed in a $\log J - \log V$ plot [137,139]. In the low electric field region, the rate of charge carrier injection is low and less than that of thermally activated carriers. The $\log J - \log V$ plot in this region is explained by Ohm's law: the current is linearly proportional to voltage ($I \alpha V$) with a slope equal to 1. This region is defined as the Ohmic region, and the current density in this region is given by Eq. (3.30). Increasing the applied electric field leads to an increase in the rate of injection of charge carriers and, as a result, the concentration of injected charge carriers becomes larger than that of thermally activated carriers. Under these circumstances, the traps start to fill up, and current passing through the insulator is limited by the space charge. The log $J - \log V$ plot of this regime shows a square dependence of current on voltage ($I \alpha V^2$) with a slope equal to 2. This region is known as trap-controlled space charge limited current (TC-SCLC), and the current density relationship in this region is expressed by Eq. (3.31). As the voltage increases further, and specifically once a threshold voltage, known as the trap-filled limit voltage (V_{th}) has been exceeded, the current density resulting from space charge limited current is described by the Mott-Gurney Law and also referred to as trap-filled space charge limited current (TF-SCLC) regime. In this region, all traps are totally filled, and the injected charge carriers are free from trapping. The log $J - \log V$ plot of this regime again shows a square dependence of current on voltage ($I \alpha V^2$), with a slope equal to 2. The current density expression of the trap-filled (TF-SCLC) region is given by Eq. (3.33). A typical log $J - \log V$ plot of SCLC showing these three transition regions is shown in Fig. 3.17.

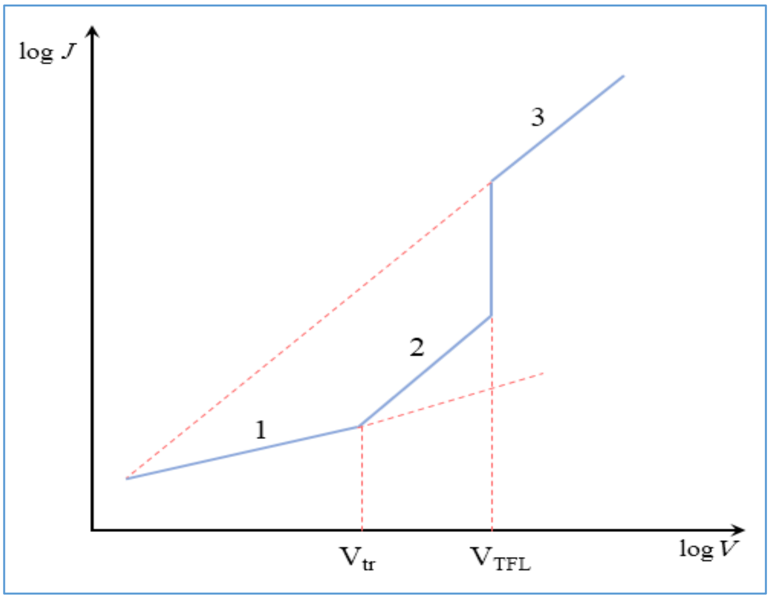

Figure 3.17: Schematic representation the log J - log V plot of SCLC. (1) Ohmic region, (2) TC-SCLC region (partially filled-traps), and (3) Mott-Gurney region (all traps are filled). V$_{tr}$ *is transition voltage, and V*$_{TFL}$ *is trap filled limit voltage.*

Ohmic region:

$$J_{Ohm} = q n_0 \mu \frac{V}{d} \tag{3.30}$$

Trap-controlled space charge limited current (TC-SCLC) region:

$$J = \frac{9}{8} \mu \varepsilon \theta \frac{V^2}{d^3} \tag{3.31}$$

$$\theta = \frac{N_C}{g_n N_t} \exp\left(\frac{E_t - E_c}{kT}\right) \tag{3.32}$$

Mott-Gurney law, trap-filled space charge limited current (TF-SCLC), region:

$$J_{Mott-Gurney} = \frac{9}{8}\mu\varepsilon\frac{V^2}{d^3} \tag{3.33}$$

The separation between regions 2 and 3 in Fig 3.17 represents the transition from the trapped carrier regime to the free carriers regime. The required voltage to set this transition is given by:

$$V_{TFL} = \frac{qN_t d^2}{2\varepsilon} \tag{3.34}$$

In the above, q is the electronic charge, n_0 is the charge carrier density in thermal equilibrium μ is the carrier mobility, V is the applied voltage, d is the thickness of the insulator layer, ε is the dielectric permittivity of the insulator, N_c is the density of states in conduction band, N_t is the concentration of traps, g_n is the degeneracy of the conduction band, E_c is the conduction band edge energy, E_t is the trap energy, k is Boltzmann's constant, T is the absolute temperature, and θ is the ratio of trapped and free charge carriers. θ is equal to 1 in region 3 where all the traps are totally filled.

This conduction mechanism has been reported in several resistive switching devices. Devices with conduction governed by SCLC should show the above mentioned distinct regions when the I-V curve plotted in the log $I - \log V$ scale. As reported by Chen *et al.*[148], SCLC is the responsible conduction mechanism in Al/ZnO/Si devices in the LRS. The I-V characteristics show an Ohmic behaviour (I α V) with a slope equal to 1.05 in the low voltage regime and followed by partly filled traps region and fully filled traps region in the high voltage regime. SCLC observed to be the governing conduction in the HRS in Au/ZnO nanorods/AZO devices fabricated by Sun *et al.* [24]. The log *I* versus log *V* fits well the three portions of SCLC conduction with different slopes. The Ohmic behaviour (I α V) dominates at low applied voltage with a slope equal to 1, followed by the square law ($I \alpha V^2$) regime at high applied voltage with a slope equal to 1.89, then the trap-free square law at very strong injection region. Further, as reported by Kim *et al.* [22], in both HRS and LRS, SCLC is the dominant conduction mechanism in resistive switching device based on TiO_2 thin films sandwiched between Pt top and bottom electrodes. The logarithmic *I-V* plots in HRS and LRS at different temperatures are both in good agreement with the SCLC mechanism in which the three regions are observed. Therefore, observation of three distinct regimes; Ohmic behaviour (I α V), Mott-Gurney square low, and an abrupt increase in current at high voltages in the *I-V* curve plotted on a logarithmic scale indicates SCLC.

3.5 Valence Change Memories (VCM)

The valence change switching mechanism is considered one of the most common mechanisms that has been used to explain the switching process in RRAM devices based on binary metal oxides and perovskites as a switching layer in the MIM structure. Basically, RRAM cell based on VCM consists of switching matrix e.g. binary metal oxide layer sandwiched between two electrodes; anode and cathode. It is well known that the binary metal oxides have defects such as oxygen vacancies which can play a key role in the resistive switching mechanism in this type of memristors.

The resistive switching in VCM is based on generation and migration of oxygen vacancies in transition metal oxides upon the applied electric field. This results in an enhancement or a depletion of oxygen vacancies that changes the valence state of the transition metal cations, resulting in a local change in the electronic structure of the material [32]. Because of the change in valence of the material, this class of resistive switching memory is called valence change memory (VCM). These oxygen vacancies are much more mobile than the transition metal cations. Usually, the pristine RRAM device shows low conductivity and an electroforming process is required to activate the device by the application of high voltage (higher than the set voltage). Once activated, the device can be switched between ON and OFF states by changing the magnitude and/or the polarity of applied voltage. A high local temperature can be formed due to the high current pass through the insulator layer during the electroforming process. This may lead to local structural changes by forming e.g. oxygen vacancies and oxygen anions within an insulator layer [154]. The formation of oxygen vacancies and oxygen anions can be given by:

$$O_o \rightarrow V_o^{2+} + O_i^{2-} \tag{3.35}$$

where O_o,V_o^{2+}, and O_i^{2-} represent the oxygen atoms, the oxygen vacancies and the oxygen anions, respectively.

When a voltage is applied in one direction, the oxygen anions move toward the anode, an oxidation process occurs, leading to the evolution of oxygen bubbles. This reaction process can be expressed by:

$$O_i^{2-} \rightarrow 2e^- + 1/2O_2\uparrow \quad (3.36)$$

Oxygen vacancies, on the other hand, migrate to the cathode and as a result an oxygen-deficient region forms and extends to the anode. At this region, metal cations accumulate and at the same time trap the electrons emitted from the cathode.

This reaction is given by:

$$M^{z+} + ne^- \rightarrow M^{(z-n)+} \quad (3.37)$$

where M^{z+} represents the positive metal cations.

Oxygen vacancies can arrange themselves to form a conductive pathway across the insulator layer and connect the top and bottom electrodes. As a result of the formation of conductive pathway, the resistance of RRAM device switches from the HRS to the LRS (set process). In contrast, by changing the polarity of the applied voltage, oxygen anions move backwards to the cathode. Consequently, the conductive filament may rupture and the reset process of bipolar RRAM device takes place. In a unipolar RRAM device, however, the reset process may be attributed to the dissolution or deformation of a conductive filament caused by Joule heating [154]. The conductive filament rupture in bipolar and unipolar resistive switching occurs due to the recombination of oxygen anions with oxygen vacancies in the CF region, e.g,

$$O_i^{2-} + V_o^{2+} \rightarrow O_o \tag{3.38}$$

A schematic diagram of VCM switching is illustrated in Fig. 3.18. The formation and rupture of a CF (set and reset processes) in VCM RRAM devices has been observed using *in-situ* TEM techniques as reported in [113,155].

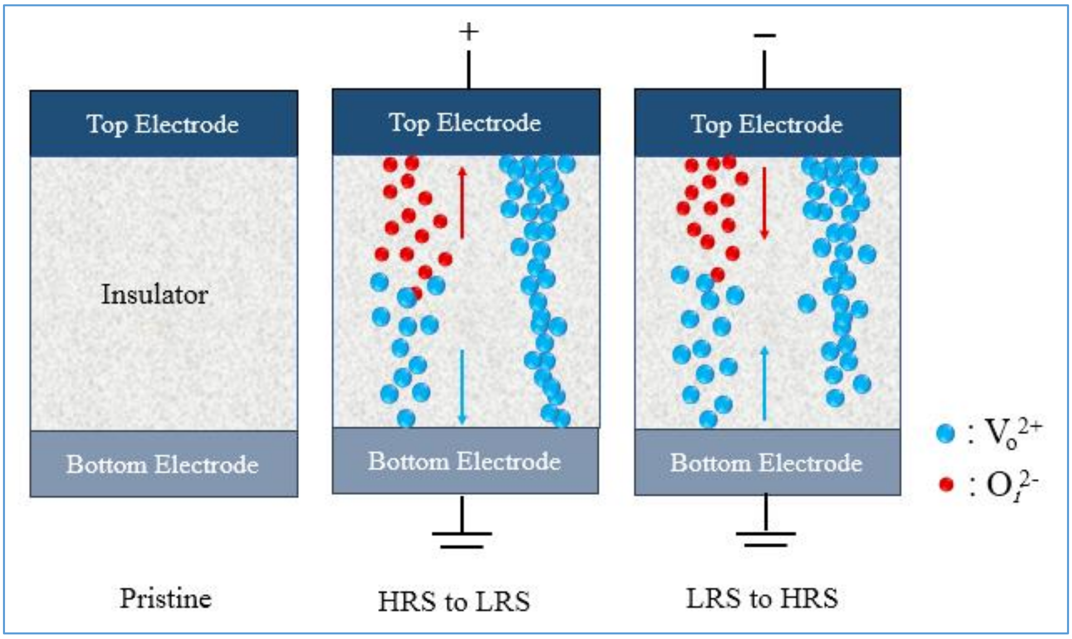

Figure 3.18: Schematic diagram illustrating VCM in an MIM structure.

3.6 Electrochemical Metallization Memory (ECM)

Electrochemical metallization memory (ECM), and also referred to as conductive bridge memory is an increasingly important area in non-volatile RRAM devices applications. ECM is similar to VCM in that the resistive switching mechanism relies on the formation and rupture of CFs, but ECM involves mobile metallic cations rather than oxygen vacancies. Fig. 3.19 illustrates the basic operation of an ECM cell within the MIM structure.

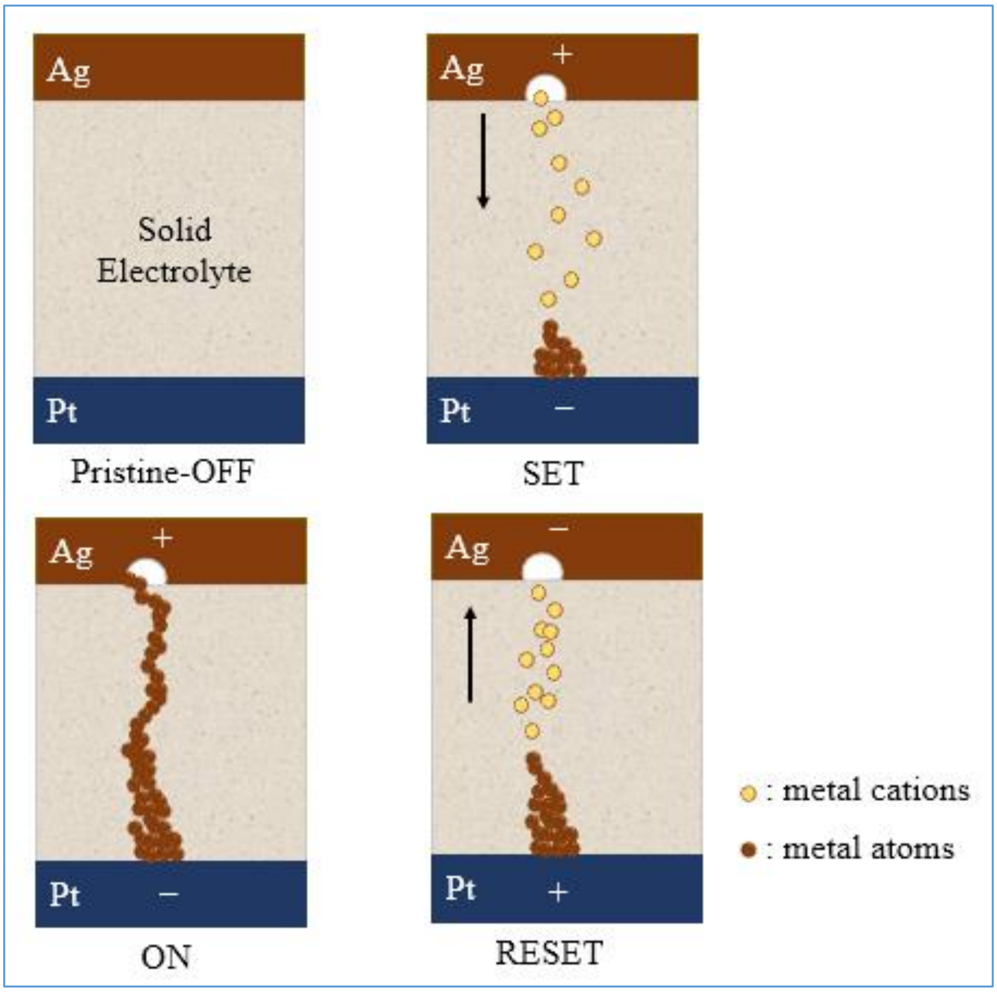

Figure 3.19: Schematic diagram illustrating the basic principle of resistive switching in ECM based RRAM devices using an Ag active electrode and a Pt inert electrode as an example, with a solid electrolyte between them.

The ECM unit cell consists of a solid electrolyte sandwiched between two metal electrodes. A variety of materials can be used as solid electrolytes such as metal oxides, chalcogenides, and organics with thicknesses of a few tens of nanometre. One of the metal electrodes should be chemically inert, such as Au, Pt, and W, while the other should be chemically active, such as Cr, Ag and Ni. This electrode plays an essential role in the switching mechanism by providing the ECM cell with metallic cations. The pristine ECM cell often shows high resistance, and a forming step is needed to activate it [27,32,129]. After the forming step, application of a positive voltage to the chemically active electrode causes dissolution of electrode atoms due to the oxidation reaction at the electrode/solid electrolyte interface. This reaction is given by:

$$M \rightarrow M^{z+} + ze^{-} \qquad (3.39)$$

where M denotes the metal atoms, and M^{z+} donates the metal cations.

As a result of the oxidation reaction, metal cations diffuse into the solid electrolyte film and migrate towards the inert electrode under the effect of the electric field. Once reached, metal atoms are formed through a reduction reaction by electrons emitted from the inert electrode, e.g.

$$M^{z+} + ze^{-} \rightarrow M \qquad (3.40)$$

These metal atoms accumulate on the surface of the electrode, and a growth of a conductive bridge across the solid electrolyte takes place. When the conductive bridge/filament is formed and connected with the opposite active electrode, the device switches to the LRS. It can maintain its resistance state until the opposite voltage polarity is applied. Application of a negative voltage to the active electrode causes a dissolution of the CF. The dissolution process starts from the weakest point in the CF and continues until the rupture of CF, which switches the device again to its initial state (HRS). Joule heating, especially in unipolar resistive switching, is also expected to cause the rupture of CF at the narrowest region due to the large current passing through it [27,32,129]. Unipolar and bipolar ECM devices have been reported in [21,156] respectively.

3.7 Memristor Applications

Besides non-volatile memory applications, memristors can also be used in other fields, such as analogue circuits, digital circuits, sensor networks, neuromorphic computing systems, and chaotic systems. The following is a brief description of memristor applications as non-volatile memory and neuromorphic systems applications.

3.7.1 Non-Volatile Memory

One of the most considerable potential applications of memristors is non-volatile resistive random access memory (NVRRAM). Memristors are two terminal devices that can be fabricated into crossbar structure which provides the potential for high-density data storage cells. Practically, this architecture can be achieved using the simple MIM structure where the insulator matrix is positioned in between the bottom and top electrodes. Crossbar memristors consist of horizontal and vertical lines network, and each crosspoint of a horizontal line (word line) and vertical line (bit line) represents a memristor cell. Other architectures can also be used to synthesise memristors, such as planar structure and vertical structure which is used in this research. The resistance of memristor decreases (ON state) and increases (OFF state) by changing the polarity and magnitude of applied bias. The ON and OFF states of memristors represent the codes 1 and 0 for digital applications. For non-volatile memory applications, memristors offer advantages of a CMOS integrated circuits technology and high scalability down to 5x5 nm cell dimensions size [157] which is considered impossible to achieve by other current technologies. They have been also showed high on/off ratio of more than 10^7, excellent speed switching time with 10 ns, and long endurance of over 10^{12} cycles and data retention time of more than 2.5 x 10^5 s [158,159]. Additionally, low power operation and easy fabrication and inexpensive solution process of organic material, make memristors a promising non-volatile memory technology.

3.7.2 Neuromorphic Systems

Another significant and promising application of memristors is their use in neuromorphic computing applications. Electronic switching in memristors is very similar to that of synapses in biological systems. Therefore memristors can be used to develop computing systems that mimic the learning and information processing capability of biological brains. The development of systems such as this have many advantages for the real-time processing of large amounts of sensory information such as that used for image and voice recognition.

Biological neurons consist of soma, axon, axon terminals, and dendrites as shown in Fig. 3.20. The soma role is to unify all the signals of dendrites and to organise the firing rate of signals *via* the axon. The spikes propagate through the axon and transmit to the next neuron through the synapses. The axon terminals are specialized to release the neurotransmitters of the pre-synaptic neuron [160]. The synapses, which are 20–40 nm wide gaps between the axon end (axon terminal of the pre-synaptic) and the dendrites of the post-synaptic, transmit the signal either chemically by releasing neurotransmitters or electrically depending on the type of the synapse. The synapses contribute to the computation by changing their connection strength as a result of neuronal activity, which is known as synaptic plasticity. Synaptic plasticity is the mechanism that is believed to underlie learning and memory of the biological brain. Memristors have the capability to work as an electronic synapse using the advantages of the nanoscale fabricating cell size and the non-volatile property which are both characteristics required in the implementation of synapse systems.

Nanosize crossbar memristor devices have been demonstrated as synapses in neuromorphic circuits based on co-sputtered Ag/Si layer integrated with CMOS by Sung *et al.*, [161]. A co-sputtering of Ag and Si switching layer with a well designed Ag/Si mixture ratio resulted in a formation of a Ag-rich (low resistivity) region and a Ag-poor (high resistivity) region. Under applied voltage, a uniform conduction front between the Ag-rich and Ag-poor regions can be occurred by movement of Ag nanoparticles that incorporated into the Si medium. The continuous motion of

Ag nanoparticles front and back results in an analogue switching between two resistance states. In crossbar device structure, each crosspoint forms a synapse that consists of a pre-neuron (bottom electrode) and a post-neuron (top electrode) with the active layer in between as shown in Fig. 3.20.

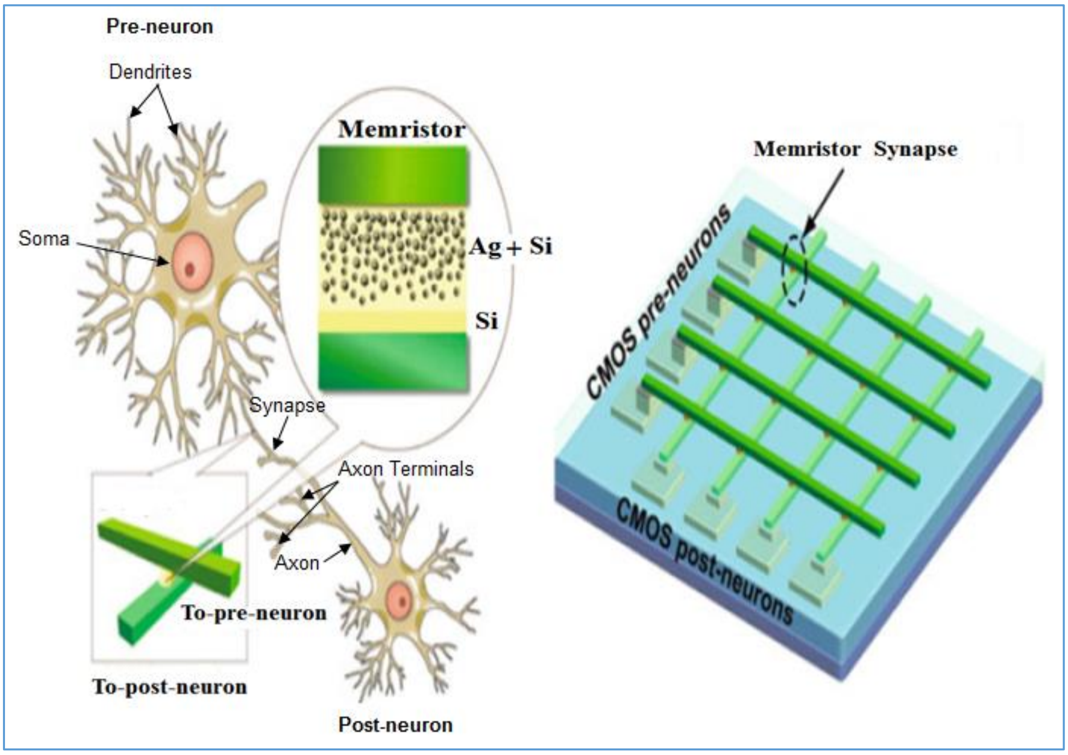

Figure 3.20: Schematic showing the nanoscale crossbar memristor devices and its application in neuromorphic systems as a synapse (right), and pre- and post-synaptic neurons (left) taken from [161].

The resistance state of memristor switches between the HRS and the LRS when an electric field is applied. Electrical signals or ion flows can change the synaptic weight in biological systems. Similarly, the electronic synaptic weight in neuromorphic systems can also be altered by changing the conductance of memristor by applying an electric field between the pre-neuron and the post-neuron. In addition, the increase and decrease in memristor conductance can be utilised in the learning process in neuromorphic computing systems. For example, synaptic plasticity shows a potentiation and depressing response and Spike Timing Dependent Plasticity (STDP) as well as Long-Term Potentiation (LTP) and Long-Term Depression (LTD) behaviours [160]. In the biological neurons, hippocampal neurons, for example, the STDP depends on the relative time arriving of presynaptic and postsynaptic spiking. Repetitive spiking of the presynaptic neuron before the postsynaptic neuron causes a strengthening of synaptic plasticity and that results in a Long-Term Potentiation (LTP). While repetitive spiking of the postsynaptic neuron before the presynaptic neuron causes a weakening of synaptic plasticity and that leads to a Long-Term Depression (LTD) [162]. The STDP of cultured hippocampal neurons is shown in Fig. 3.21.

Memristor can mimic the biological synapse as shown in Fig. 3.22. The figure shows the STDP characteristics of a memristor based on a chalcogenide as a resistive switching material. As shown in the figure, long-term potentiation (LTP) takes place due to the presynaptic spike precedes the postsynaptic spike ($\Delta t > 0$), while long-term depression (LTD) occurs due to the postsynaptic spike precedes the presynaptic spike ($\Delta t < 0$). These memristor behaviours are demonstrated in this research work and will be presented in the result sections of chapter five and six.

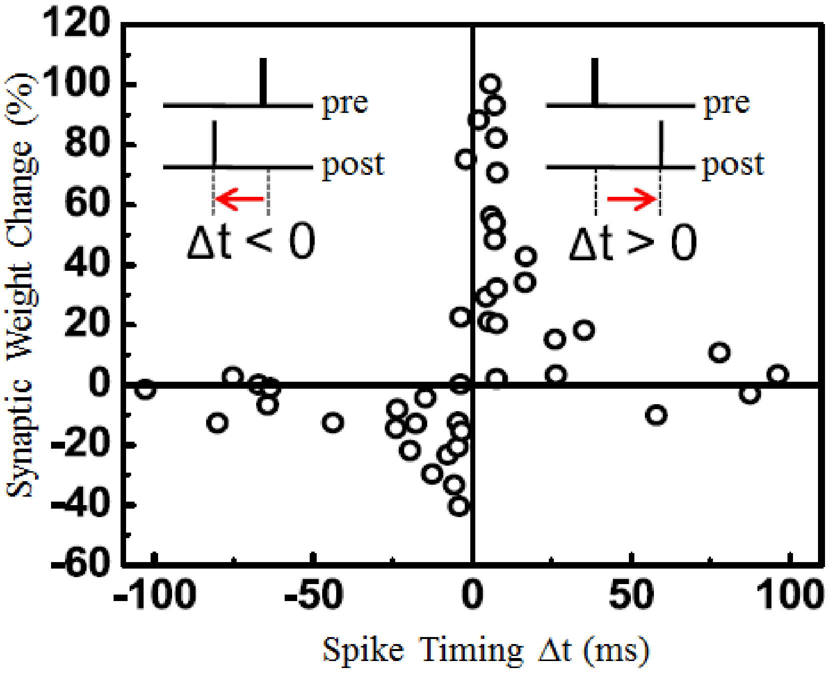

Figure 3.21: STDP characteristics of hippocampal neurons taken from [162].

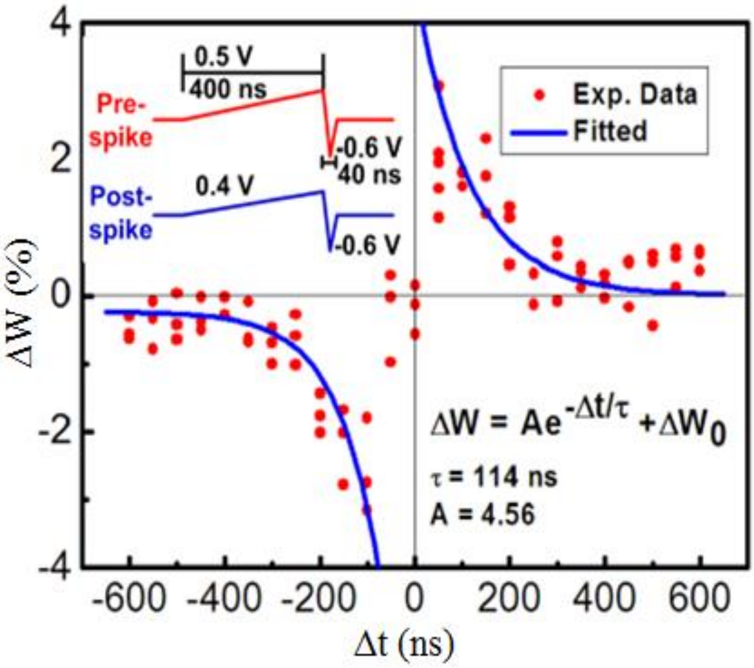

Figure 3.22: the STDP characteristics of synapsis memristor based on $Ge_2Sb_2Te_5$ film sandwiched between two electrodes of TiW taken from [163].

Chapter 4. Experimental Methodology

In this chapter, the materials and processes used to fabricate the optical non-volatile memory devices are presented. The chapter begins with a description of the properties and applications of ZnO semiconductors and poly(disperse red 1 acrylate) polymer materials. The methodology for growth of the vertically aligned ZnO nanorod thin films using a microwave oven approach is then given followed by a description of the techniques used to deposit (*via* spin-coating) a thin polymeric film over the ZnO layer. The chapter also includes details of the preparation of polymer/metal nanoparticle hybrid devices, metal evaporation of the device electrodes and techniques used to characterise the devices including Dektak, SEM, TEM, and electrical and optical measurements.

4.1 Zinc Oxide (ZnO)

Recently, ZnO has received considerable attention due to its various applications in industry and scientific research, such as photodetectors, light-emitting diodes, transparent thin film transistors, solar cells, sensors, transparent conductive electrodes, and optical waveguides. ZnO is an n-type semiconductor with a direct bandgap of 3.37 eV and large exciton binding energy of the order of 60 meV at room temperature [164]. Due to its wide bandgap and transparency, it is considered a good candidate to develop transparent solid-state electronic and optoelectronic devices in wavelengths ranging from blue to UV. The ZnO bandgap can be modified by doping with other materials. For instance, the bandgap of ZnO increases to ~ 4.0 eV or decreases to ~3.0 eV by substituting Mg or Cd, respectively [165].

The most common crystal structure of ZnO is a hexagonal wurtzite with lattice parameters a = 3.2495 °A, and c = 5.2069 °A. In the tetrahedral arrangement, each Zn atom is surrounded by four O atoms and *vice-versa*. The hexagonal wurtzite structure of ZnO is illustrated in Fig 4.1. However, ZnO can be found in different structures, but they are uncommon, such as the zinc blende structure which can be obtained when ZnO is grown on a cubic substrate, and the cubic rock-salt structure by growing ZnO at high pressures [166].

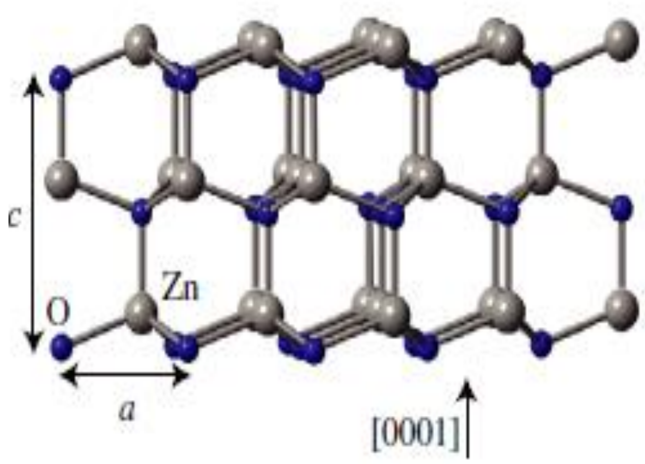

Figure 4.1: A Schematic illustration the hexagonal wurtzite structure of ZnO taken from [164].

ZnO has unintentional point defects that form during the growth processes. These defects include; vacancies (atoms absent from their regular positions in the lattice), interstitials (additional atoms in the lattice), and antisites (an O atom occupying a Zn atom site and *vice-versa*). These defects may affect the optical and electrical properties of ZnO. However, it is still under debate whether the n-type conductivity of ZnO is caused by unintentional point defects [167] or something else like hydrogen, which can be found in most of the growth environments [164].

ZnO can be synthesised in many nanostructures, such as nanowires, nanorods, nanorings, nanobelts, nanotubes, and nanoparticles using different fabrication techniques. Fig. 4.2 shows a collection of ZnO nanostructures prepared from solid powder using thermal evaporation under different conditions [168]. Among these nanostructures, one-dimensional (1D) ZnO nanorods have attracted a lot of interest due to their applications as solar cells [169], LEDs [170], gas sensors [171], and resistive switching memories [24].

Here, optical memristor devices based on vertically aligned ZnO nanorods embedded within an optically active polymer are developed. In particular, vertically aligned ZnO nanorods are grown using a simple and cheap microwave-assisted hydrothermal technique which will be described in section 4.4.

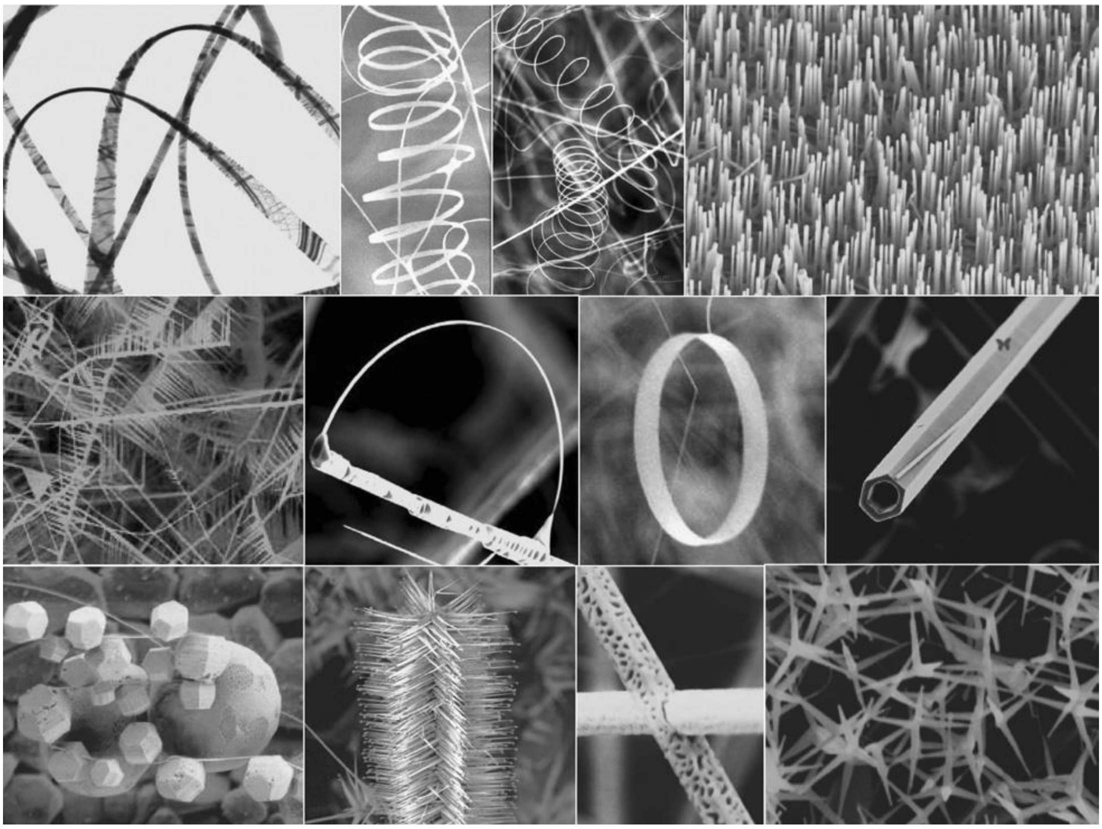

Figure 4.2: A collection SEM images of ZnO nanostructures taken from [168].

4.2 Gold Nanoparticles

For the past few decades, nanostructured materials, such as nanotubes, nanorods, nanobelts, nanoflakes, and nanoparticles have received significant attention due to their unique optical, electronic and chemical properties which differ from that of the bulk materials. Gold nanoparticles, in particular, have been introduced as promising materials for a wide range of useful applications, such as plasmonics, photovoltaic cells, biological sensors, drug delivery, and catalysis [172]. Au NPs have also been used to fabricate hybrid and non-hybrid material devices in the field of nonvolatile resistive switching memory with different cell configurations [173].

Au NPs can be synthesised with sizes ranging from 1 to 100 nm in different shapes by using a top-down approach or a bottom-up approach. In the top-down approach, Au NPs are produced from shattering of gold bulk into nanoscale particles. This approach utilizes several physical techniques, e.g. laser ablation, ion sputtering, and arc discharge for Au NP production. On the other hand, the creation of Au NPs in the case of bottom-up approach is achieved by constructing the material from the atomic scale. Chemical techniques, e.g. chemical reduction from a solution of hydrochloroauric acid ($HAuCl_4$) are common methods used to produce nanoparticles [174]. Au NPs can be functionalised by covering them with capping agents, such as citrate acid, tannic acid, polyvinyl pyrrolidone (PVP), polyethylene glycol (PEG), and bovine serum albumin (BSA) [174]. This process is required to improve the stability of Au NPs and make them suitable for a specific application. The physical and chemical properties of Au NPs are different from those of the gold bulk, and they can be modified by changing the features of Au NPs: size, shape, clustering, and surface ligands. For example, spherical Au NPs with a diameter range of 2-100 nm in aqueous solution show an optical absorption peak from 500-550 nm due to the surface plasmon band which emerges from collective vibrations of the conduction electrons excited by incident photons, whilst this band is missing in the case of bulk material or nanoparticles with diameters less than 2 nm. The performance of devices based on Au NPs is also dependent on these features. From the nonvolatile memory applications point of view, the size of Au NPs affects the performance of resistive switching devices. The ON/OFF ratio, for instance, has been increased by decreasing the size of Au NPs. Smaller Au NPs have a reduced capacity for charge storage. This leads to an increase in the OFF resistance, and as a result, an increase of the ON/OFF ratio [175].

Hybrid organic-inorganic composites are a major area of interest within the field of electronic and optoelectronic devices. Specifically, nanoparticles blended with polymer hosts have emerged as promising candidates for non-volatile memory application owing to their significant characteristics: easy, fast, and low-cost fabrication process using spin-coating techniques at room temperature, operation with low power, high on/off ratios, fast read/write cycles, and fabrication on light and cheap substrates. In general, the wide band gap of polymers results in low conductivity. Their conductivity, however, can be increased by doping with conducting NPs. Devices can be formed in a simple MIM structure in which organics or hybrid organic-inorganic materials are sandwiched between two electrodes. Bipolar and unipolar resistive switching behaviours have been demonstrated in several switching devices based on organics and nanocomposites as active switching materials. The performance and characteristics of these devices, such as ON/OFF ratio, retention, endurance, switching behaviour and switching threshold voltages can be modified by controlling the concentration of nanomaterials, e.g. NPs, in host organic matrices [120]. Several conduction mechanisms have been proposed in these systems. These mechanisms include Space-Charge-Limited-Current (SCLC), Schottky emission, thermionic emission, Ohmic conduction, hopping conduction, and tunnelling current [120], which are explained in chapter 3.

4.3 Azobenzene Polymers

Azobenzene Polymers are a major area of interest in the field of optical switching. Azobenzene polymers are organic molecules that consist of two phenyl rings around the azo (−N=N−) bond. Azobenzenes can be found in two geometric isomers; *trans* (*E*) and *cis* (*Z*), as shown in Fig. 4.3. At room temperature, the *trans* isomer is considered more stable than the *cis* isomer. In addition, the *trans* isomer has almost no dipole moment and tends to be planar with the distance between the two carbon atoms in the 4- and 4'-positions about 9.0 Å, whereas the *cis* isomer has a dipole moment of 3 Debye and tends to be twisted with a 5.5 Å distance between the two carbon atoms in the 4- and 4'-positions [176].

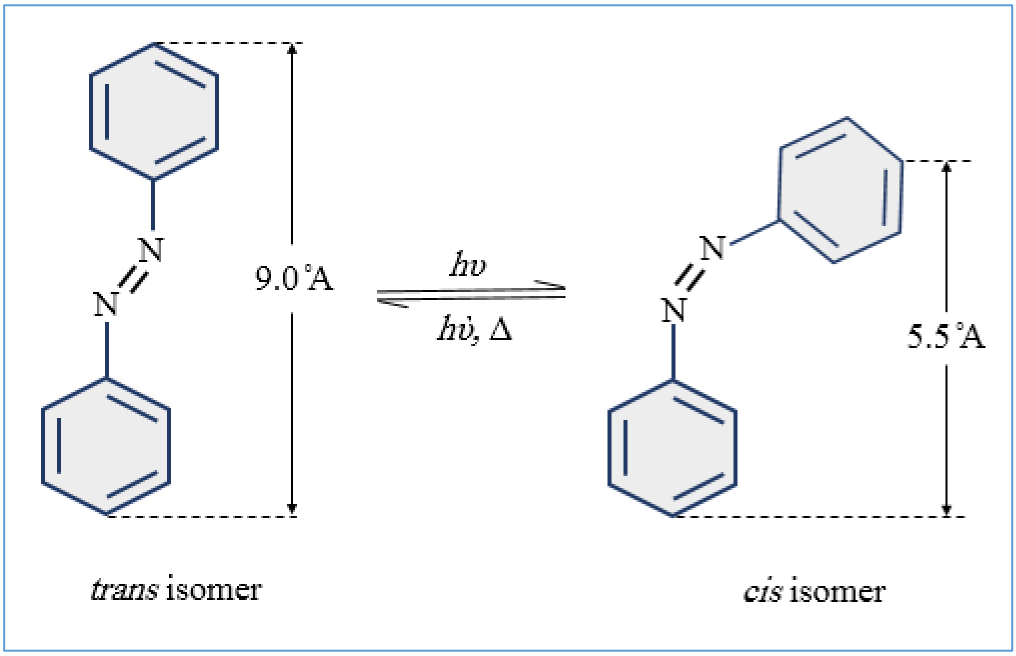

Figure 4.3: Trans and cis isomers of azobenzene, which may be interchanged through photoisomerization process.

Azobenzenes can be divided into three categories: unsubstituted azobenzene type, aminoazobenzene type (4-nitro-4´-hydroxyazobenzene (NHA), that has ortho- or para- substitutes with the $-NH_2$ group, and pseudo-stilbenes type (Disperse Red 1 (DR1), with amino and nitro groups at the 4- and 4ʾ- positions. These three azobenzene molecules types and their absorption spectra are illustrated in Fig. 4.4.

One of the most important properties of azobenzenes is the photoisomerization process that changes the conformation of the molecule. Upon irradiation by light with wavelength in the range of 380-600 nm the azobenzene chromophores undergo to a reversible switch from the *trans* to the *cis* configuration. The *cis* isomers, however, can be switched again to their initial stable state (to the *trans* isomers) *via* thermal relaxation or through irradiation with another wavelength. The time for thermal relaxation can range from milliseconds to days, depending on the substitutes and local ambient of experiment. It is worth mentioning that a single wavelength can cause a continuous cyclical photoisomerization from the *trans* isomer to the *cis* isomer and *vice-versa* in some azobenzene molecule types, e.g. pseudo-stilbenes, due to the overlap of the absorption spectra of the two isomers [177].

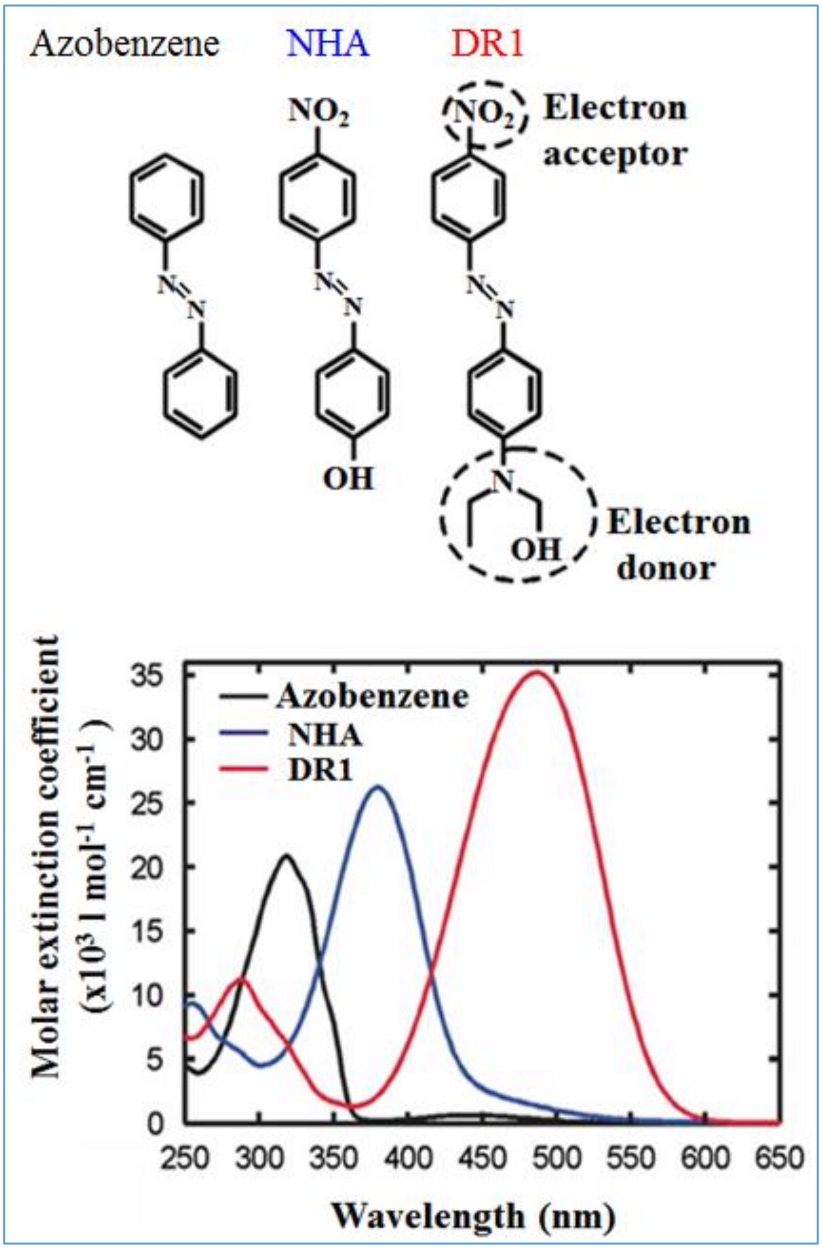

Figure 4.4: Azobenzene molecule types and their absorption spectra. Azobenzene (top left), aminoazobenzene (4-nitro-4´-hydroxyazobenzene (NHA) (top middle), and pseudo-stilbenes (Disperse Red 1 (DR1) (top right) [177].

To produce large macroscopic expansion and contraction effects, the molecules need to be aligned. This can be achieved by irradiation with different light polarisations [178]. Although the photoisomerization mechanism is still unclear and debatable, it can be attributed to one of two mechanisms: rotation or inversion, as shown in Fig. 4.5. Photoisomerization happens through rotation about the −N=N− double bond in the case of rotation mechanism, whereas through the reversal of one of the N−C bonds in the case of inversion mechanism [176,177].

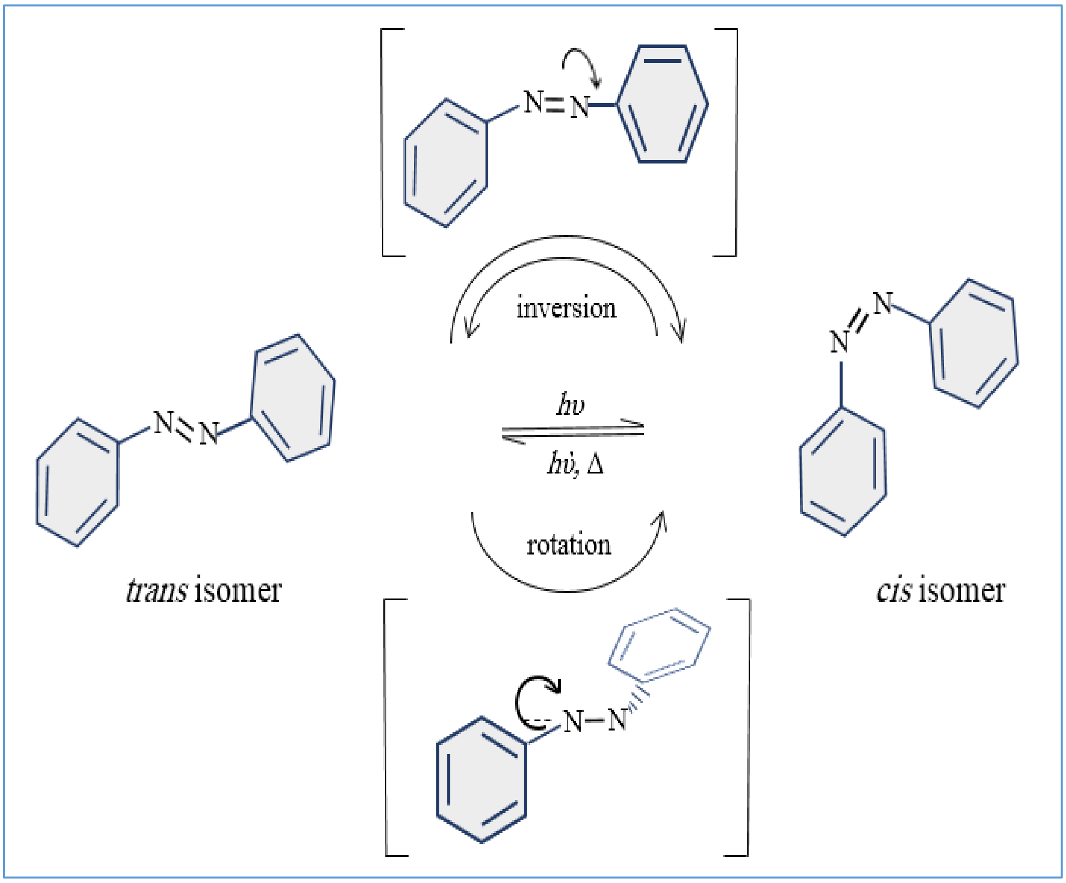

Figure 4.5: A schematic of photoisomerization mechanisms between trans and cis isomers.

Moreover, azobenzene polymers undergo to a photomechanical effect due to the photoisomerization process. The azobenzene polymer thin films can be photo-expanded and photo-contracted with a change in volume of up to 17%. This photomechanical effect does not only depend on the wavelength/polarisation of incident light but also on the temperature, light power and irradiation time [179,180].

Azobenzene Polymers and azobenzene-containing liquid crystal (LC) polymers have been suggested as promising candidates for several applications, such as photo-robotics, photomechanical actuation, gratings, optical polarizers, wavelength filters, and as photonic bandgap materials [177].

4.4 Device Fabrication Procedure

The two main hybrid material device structures investigated in this thesis consist of vertically aligned ZnO nanorods embedded within a PDR1A layer and Au NPs blended within a PDR1A layer. Both optical devices consist of the active layer sandwiched between an electrically conductive and optically transparent indium tin oxide (ITO) bottom electrode and an aluminium (Al) top electrode, giving an overall structure of ITO/ZnO/PDR1A/Al and ITO/Au NPs:PDR1A/Al. The ITO-coated glass substrates with sheet resistance (R_s) of = 80 – 120 Ω and ITO thin film thickness of 120 – 160 nm were purchased from Delta Technologies. The fabrication used to synthesise the ZnO/PDR1A based optical memory devices will be explained in detail in section 4.4.1. The fabrication method of optical memory devices consisting of Au NPs:PDR1A is given in section 4.4.2 and 4.4.3. The instruments used for characterization and measurements of morphology, chemical composition, absorption spectra, film thickness, and electrical measurements combined with optical modulation are described in section 4.5.

4.4.1 Fabrication of ZnO/PDR1A Based Devices

4.4.1.1 Seed Layer

Prior to the growth of ZnO nanorods, a seed layer is required to provide nucleation sites for ZnO nanorods. ITO-coated glass substrates were cleaned with acetone, propan-01-ol, and de-ionized (DI) water for 5 min each using sonication. The substrates were then rinsed with DI water and dried under N_2 flow. A 10 mM seed solution was prepared by dissolving a 0.22 g of zinc acetate dehydrate $Zn(CH_3COO)_2.2H_2O$ (99%, Sigma-Aldrich) in 200 ml of propan-01-ol. This seed solution was spin coated three successive times on cleaned ITO-coated glass substrates at 2000 rpm for 30 s. After each spin coating step, the substrates were annealed at 350°C for 30 min. The annealing process plays an essential role by decomposing the zinc acetate into zinc oxide crystals. In addition, it increases the adhesion of nucleation sites and aligns them vertically which leads to a better adhesion and vertical alignment of ZnO nanorods.

4.4.1.2 ZnO Nanorod Growth

Vertically aligned ZnO nanorods were grown from the ZnO seeds by submerging the substrates in a growth solution and heating using a scientific microwave (CEM, MARS 5). The 25 mM growth solution was prepared from 1.5 g of zinc nitrate hexahydrate, $Zn(NO_3)_2.6H_2O$ (99%, Sigma-Aldrich) and 0.7 g of hexamethylenetetramine (HMTA) (99%, Sigma-Aldrich), both dissolved in 200 ml of DI water. Each substrate was placed upside down in a separate reaction vessel containing 20 ml of the growth solution. Firstly, the solution was heated slowly to 80°C with a ramp time of 15 min. This was done to achieve uniform growth of the bases of the nanorods without the presence of larger crystallites, which can short circuit the devices. Following this initial growth step, the temperature was maintained at 80°C for another 30 mins. This step is used to grow the nanorods to the desired length which is between 200 nm and 250 nm. After 30 min growth time, the substrates were taken out of the microwave, removed from the growth solution and rinsed with DI water and dried under N_2 flow. The ZnO nanorods growth conditions are summarised in Table 4.1. The seed layer and growth procedures are based on [181,182].

Adding the HMTA provides the growth solution with OH^- ions which facilitate the precipitate the Zn^+ ions in a high pH environment. The growth of ZnO nanorods relies on the following reaction process [183]:

Decomposition reaction:

$$(CH_2)_6N_4 + 6H_2O \rightarrow 6HCHO + 4NH_3$$

Hydroxyl supply reaction:

$$4NH_3 + H_2O \rightarrow NH_4^+ + OH^-$$

Supersaturation reaction:

$$2OH^- + Zn^{+2} \rightarrow Zn(OH)_2$$

ZnO nanorods growth reaction:

$$Zn(OH)_2 \rightarrow ZnO + H_2O$$

Table 4.1: Summary of ZnO nanorod growth conditions.

Growth Technique	**Microwave-Assisted Hydrothermal**
Nanostructure Type	**Vertically aligned ZnO Nanorods**
Substrate	**ITO-Coated Glass**
Reactants	**Zinc Nitrate Hexahydrate and Hexamethylenetetramine (HMTA)**
Temperature	**80°C**
Ramp Time	**15 min**
Growth Time	**30 min**
Power	**100 W**

4.4.1.3 Microwave-Assisted Hydrothermal Technique

ZnO nanorods have been synthesised using various fabrication techniques, such as vapour-liquid-solid (VLS), vapour-solid (VS), thermal evaporation, metal-organic chemical vapour deposition (MOCVD), oxide-assisted growth, template-assisted growth, and microwave-assisted hydrothermal synthesis [168]. Among them, the microwave-assisted hydrothermal method has been introduced as a commercial and low-cost route for fabrication ZnO nanorods because it does not need high temperature, catalysts, high vacuum, and limited substrates as other techniques do. Also, microwave-assisted hydrothermal synthesis has the advantage of the capability to form high purity ZnO nanostructures in shorter periods of time than other techniques.

The basic principle of the microwave-assisted hydrothermal method is schematically shown in Fig. 4.6. The microwave oven consists of several vessels; one of them works as a control vessel that equipped with contactless temperature and pressure sensors to control the pressure and temperature during fabrication process, and others are reaction vessels for nanostructures fabrication process. Additionally, the microwave has a magnetic stirrer to disperse the temperature uniformly and to avoid the localised hot spots during the reaction process. Microwave irradiations propagate through the reaction mixture and transfer into heat. The desired ZnO nanorods features, such as length and diameter can be modified by adjusting the power and growth time [184].

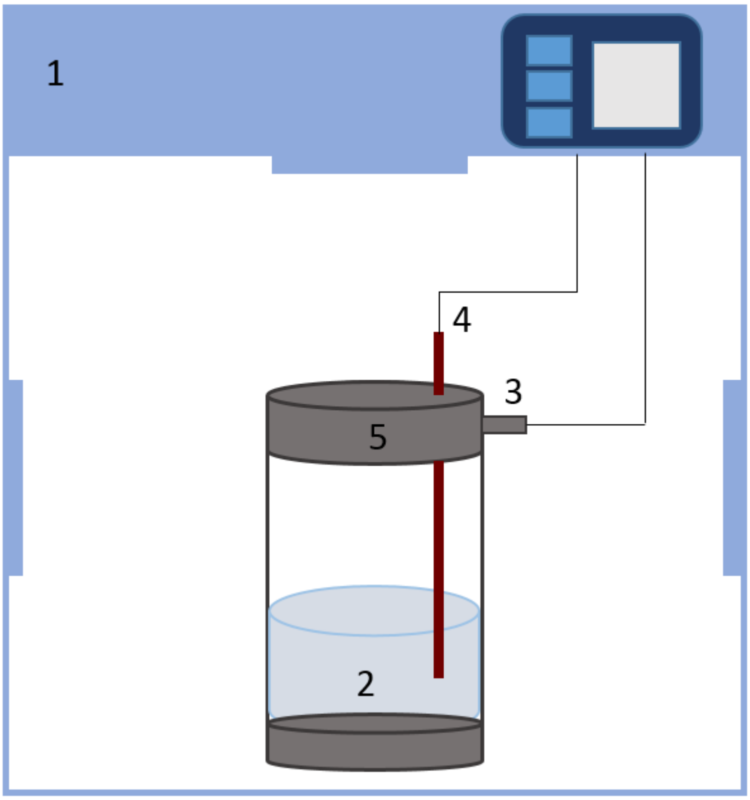

Figure 4.6: Schematic showing the microwave-assisted hydrothermal synthesis method: (1) microwave oven, (2) reaction mixture solution, (3) pressure control, (4) temperature sensor, (5) reaction vessel.

4.4.1.4 PDR1A Deposition

It is well known that ZnO nanorods show resistive switching behaviour when they are sandwiched between two electrodes. Depositing a layer of poly(disperse red 1 acrylate) (PDR1A), which is an optically active material that expands and contracts under optical irradiation, provides an interesting method to modify and study how this affects the resistive switching properties of devices. The PDR1A molecules are shown in Fig. 4.7 and consist of an azobenzene unit in addition to an alkyl chain to improve the stability and mobility of the molecules [185].

To deposit thin films of PDR1A, a 2% (*wt.*) solution was prepared by dissolving PDR1A (Sigma-Aldrich) in tetrahydrofuran (THF). This solution was spin coated onto the ZnO nanorod layer at 1000 rpm for 30 s and then annealed at 90°C for 8 h in vacuum to remove any remaining solvent. Besides these hybrid material devices (ZnO and PDR1A), control devices were fabricated as well. One device consisted of ZnO nanorods sandwiched between ITO and Al, another consisted of a layer of PDR1A sandwiched between ITO and Al.

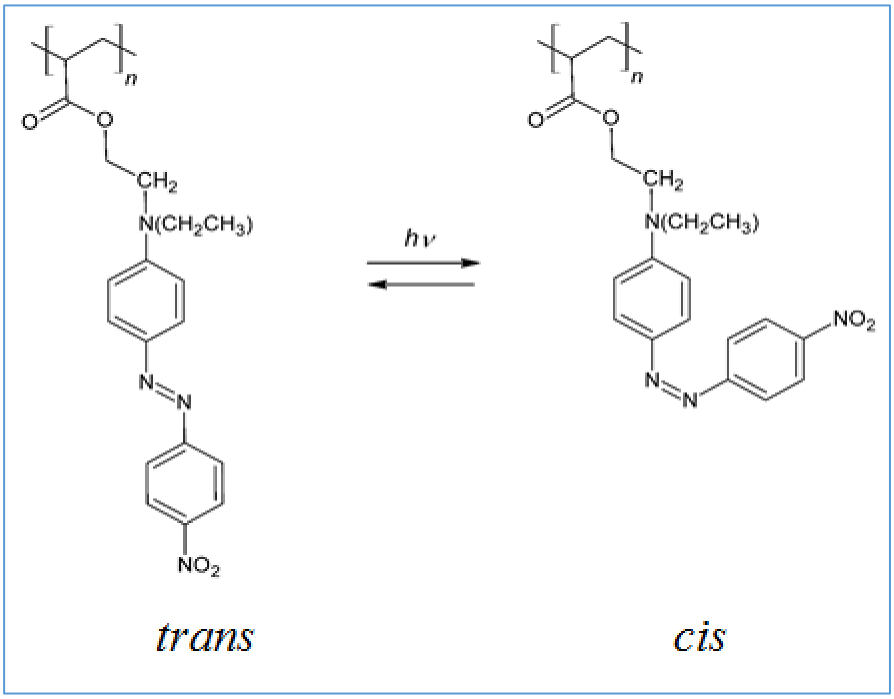

Figure 4.7: The PDR1A molecules in trans and cis forms.

4.4.2 Fabrication of Au NPs:PDR1A-Based Devices

4.4.2.1 Preparation of Au NPs and PDR1A Solutions

In order to fabricate hybrid Au NPs:PDR1A resistive switching devices, two stock solutions were prepared by weight. These solutions include 1% functionalized Au NPs (PlasmaChem) with a diameter of 6-7 nm in toluene and 5% of PDR1A (Sigma Aldrich) in THF.

4.4.2.2 Deposition of Active Switching Thin Films

Prior to the deposition process, the thin film solutions were made by mixing an optically active polymer (PDR1A) solution with an Au NP solution (both solutions were taken from the stock solutions of PDR1A and Au NPs) with mass ratios of (0.001, 0.005, 0.01, 0.05, 0.1, and 0.15) using the formulas (4.1, 4.2, and 4.3) in which the final film will contain the predefined ratios. The active switching thin films of the optical memristors were deposited on the cleaned ITO-coated glass by spin coating at 1000 rpm for 30 s, and then annealed at 90°C for 8 h in vacuum to remove any remaining solvent. In addition, a control device consisting of a thin film of PDR1A without Au NPs was fabricated using the same above-mentioned parameters.

$$M_y = \frac{M_{total}}{1 + R_m \cdot \frac{c_y}{c_x}} \tag{4.1}$$

$$M_x = M_{total} - M_y \tag{4.2}$$

$$R_m = \frac{M_x C_x}{M_y C_y} \tag{4.3}$$

where c_x is the Au NPs concentration (1% in toluene by wt.), c_y is the PDR1A concentration (5% in THF by wt.), M_x is the mass of the Au NP solution, M_y is the mass of PDR1A solution, and R_m is the mass ratio.

The ratio by volume (Rv) and the volume fraction of the Au NPs in PDR1A were calculated using the following equations:

$$Rv = \frac{\rho PDR1A}{\rho AuNPs} Rm \tag{4.4}$$

$$AuVol.Frac. = \frac{1}{1 + \frac{1}{Rv}} \tag{4.5}$$

where ρPDR1A and ρAu NPs are the density of PDR1A, 1.26 g/cm^3, and Au NPs, 19.3 g/cm^3, respectively.

The volume fractions of Au NPs in PDR1A calculated from the above equations are 0.0065 %, 0.0325 %, 0.065 %, 0.325 %, 0.65 %, and 0.96 %.

4.4.2.3 Top Metal Electrodes

The top contacts of aluminium (Al) with a thickness of 200 nm were deposited on the active switching thin films for both kind of devices, (ZnO NRs/PDR1A and Au NPs:PDR1A) by thermal evaporation under vacuum at $2\text{x}10^{-6}$ Torr. A shadow mask containing 400 μm diameter circles was used during the deposition process. A photo of the fabricated optical memristor devices and a schematic of the device showing the ITO/ZnO NRs/PDR1A/Al, and ITO/Au NPs:PDR1A/Al structures are shown in Figs. 4.8 and 4.9, respectively.

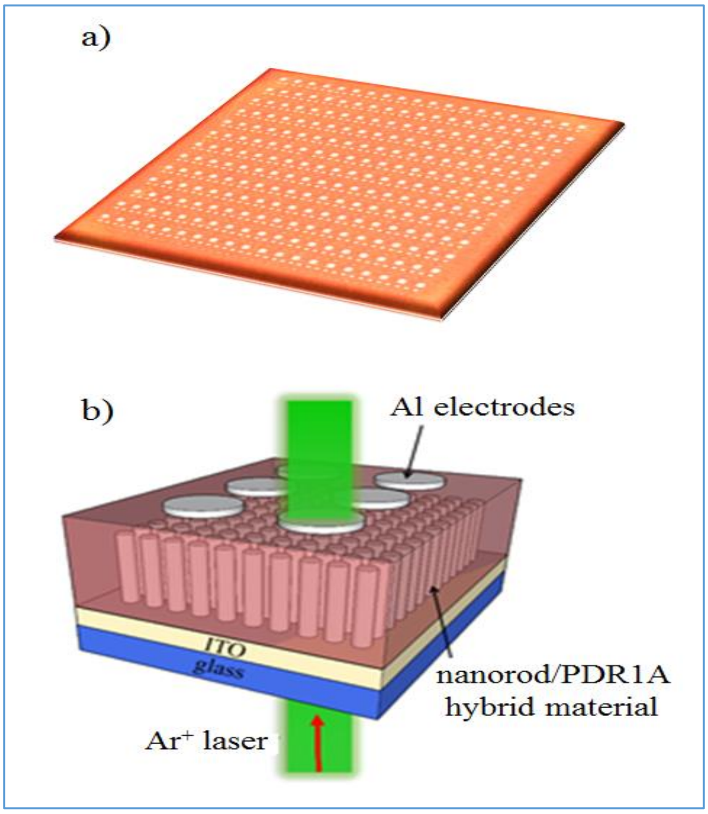

Figure 4.8: (a) Photo of the optical memristor devices after fabrication. (b) Schematic of the optical memristor devices containing ZnO nanorods embedded within PDR1A between ITO and Al contacts.

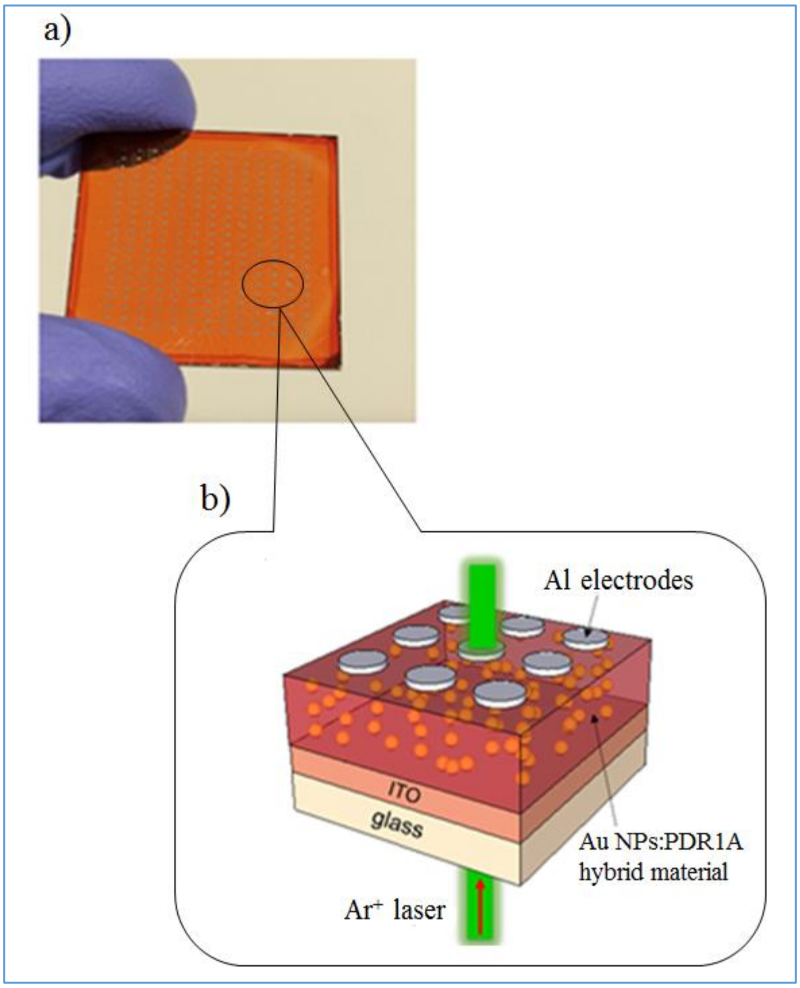

Figure 4.9: (a) Photo of the optical memristor device after fabrication, (b) Schematic of the optical memristor device consisting of Au NPs mixed with PDR1A and deposited between ITO and Al electrodes.

4.4.3 Preparation of TEM Samples

The samples for TEM investigation were prepared by encapsulating the mixed solution of Au NPs and PDR1A in resin. Polished resin blocks were used as substrates. The first step was cleaning the block resin samples with deionized water (DI) for 10 min using ultrasonication, then rinsing with DI water and drying in an N_2 flow. Next, 100 nm of aluminium (Al) was deposited on the resin sample using thermal evaporation under vacuum. Subsequently, a mixed solution of Au NPs and PDR1A with a mass ratio of (R_m= 0.01) was spin coated on the resin sample at 1000 rpm for 30 s and annealed in vacuum at 40°C for 8 h. Afterwards, a second Al thin film with a thickness of 200 nm was deposited using thermal evaporation. Finally, a layer of resin was drop cast on top. The final structure of the sample was resin/Al/Au NPs:PDR1A/Al/resin. For TEM sectioning, the samples were sliced into 90 nm thick lamellae using an ultramicrotome. There are two main advantages of this preparation method. Firstly, the two layers of Al keep the nanocomposite material intact and prevent interaction between the solution and resin. Secondly, encapsulation with two resin layers reduces the structural damage of the nanocomposite layer during sectioning.

4.5 Characterization Techniques

4.5.1 Scanning Electron Microscopy (SEM)

SEM was used to investigate the morphology of ZnO nanorods and ZnO nanorods embedded within the PDR1A polymer. A Cambridge-STEREOSCAN 360 was used in this investigation. SEM is a common technique that has been used in different scientific research fields due to its ability to distinguish nanomaterials and nanostructures at the nanometre scale. In this technique, the nanostructures and nanomaterials can be imaged by focusing an electron beam and scanning over a selected area of the sample. A tungsten filament is usually used as a source of emitted electrons when it is heated to high temperatures by applying a high voltage. These emitted electrons are focused on the surface of the sample by the condenser and objective lenses and accelerated by the anode. Interaction and energy transfer between emitted electrons and a sample take place which generates extra signals (secondary electrons, SE) reflected from the sample. SEMs equipped with detectors to gather the reflected signals and reveal information about the scanned area of the sample. Detected signals are amplified and transferred to the display and recorder units.

4.5.2 Transmission Electron Microscopy (TEM)

Transmission electron microscopy (TEM) is a very useful technique for imaging objects and materials at the nanoscale with near atomic resolution. The TEM technique involves bombarding very thin samples with high energy (200 keV) electrons and measuring the number of electrons that reach the other side. A series of condenser and objective lens above and below the specimen provide focusing of both the primary and transmitted beam. Some electrons are scattered in the process whilst others pass through the specimen and are collected by a detector to reveal the fine structure and morphology of the specimen. The thickness of the sample under study in a TEM is typically less than 100 nm to allow the electrons to be transmitted. The technique is commonly used in physics, chemistry, materials science and biology to characterize a wide range of materials with ultra-high spatial resolution down to the scale of several angstroms. In this thesis work, a TEM was used to investigate the morphology and location of Au NPs embedded within the PDR1A polymer.

4.5.3 Energy Dispersive X-Ray Spectroscopy (EDX)

Energy dispersive x-ray spectroscopy (EDX) is an analytical technique that can be used for elemental analysis and hence can identify the chemical composition of a sample. This technique is usually attached to SEM and TEM instruments. The EDX technique determines the chemical composition of a sample under study depending on the generation of x-rays during the investigation. Incident electrons (emitted from a source of the electron beam in a TEM or SEM) on a sample cause expel electrons from the inner shell (lower energy state) of atoms in the sample into the outer shell (higher energy state). Consequently, holes are generated in the inner shell. However, an x-ray is produced when the excited electrons return from the outer shell into an inner shell. This emitted x-ray then is detected by an energy dispersive spectrometer and can be used to determine the elemental composition of a sample. A JEOL 2010 High-Resolution TEM with EDS capability was used to investigate the morphology and chemical composition of hybrid Au NPs and PDR1A systems.

4.5.4 UV-Visible Spectroscopy

UV-Visible spectroscopy was used to measure the absorbance spectra of ZnO nanorods and PDR1A. A Thermo Scientific, Evolution 220, UV-Visible Spectrophotometer was used. In the UV-visible spectrophotometer, two light sources are used to cover the wavelength range of the UV and visible regions, (200 – 700) nm. Usually, a deuterium lamp is used for the UV range (190-380) nm, and tungsten lamp for the visible range (400 – 700) nm. The beam is separated into different wavelengths by a diffraction grating and only a very narrow range of wavelengths can pass through the slit. The light passes through the sample and a reference simultaneously. The transmitted light from the sample and reference is compared by the spectrophotometer. The light is transferred into the detector to reveal the absorption peak of the sample.

4.5.5 Dektak Profilometry

Characterization of the thickness differences in the PDR1A thin film deposited on glass under optical modulation and thermal relaxation was performed by dektak measurements. A Bruker DektakXT was used in these measurements. Dektak profilometry is a powerful, repeatable, and accurate technique that can be used to measure the thickness, topography and surface roughness of thin films at the nanometre scale. In this technique, a diamond stylus tip is typically used to carry out the measurements through a vertical direction movement to contact the sample surface and a horizontal direction movement across the surface of the specified area of the sample. Analog signal is formed during the vertical movement of the tip and transformed into a digital signal. This digital signal is analysed and sent to the display unit. The stylus tip has a range of radii (50 nm – 25 μm which are selected based on the sample specifications. In addition, scan parameters such as scan speed, scan length, and scan duration are controlled through the software of profilometer.

4.5.6 Electrical Measurements and Optical Modulation

Electrical measurements such as current-voltage characteristics, resistance versus optical cycles, potentiation and depression measurements, STDP measurements, and retention were carried out at room temperature using a probe station equipped with an HP4140B source-meter unit. During these measurements, optical modulation of the memristor devices was also induced using an argon ion laser (Ar^+) tuned to a wavelength of 514 nm. The spot size of the laser beam had a diameter of 3 mm and the average power per unit area of the exposed device was 180 mW/cm^2. Optical modulation of photoexpansion and photocontraction was induced by circularly and linearly polarised Ar^+ laser light, respectively. A schematic diagram of the set up used to achieve these measurements is presented in Fig. 4.10.

An argon ion laser is a gas laser that uses pure argon gas as an active medium. The lasing process occurs through the optical stimulation of ionised argon atoms. It is a continuous and four level laser. The argon ion laser can be tuned to different wavelengths by rotating the prism. These wavelengths include 514 nm (green), 488 nm (blue-green), 457.9 nm (blue), and 351 nm (ultraviolet). The most commonly used is 514 nm, due to its high output power [186]. A typical argon ion laser is constructed from a beryllium oxide tube filled with argon gas. Applying a high voltage between cathode and anode ionizes argon atoms, and generates a high density of argon ions and further excitation of the already excited ions. In order to increase the output power of the Ar^+ beam, a solenoid coil is placed around the beryllium oxide tube to produce a magnetic field which forces the excited ions to be in the centre of the tube instead of the edges [186].

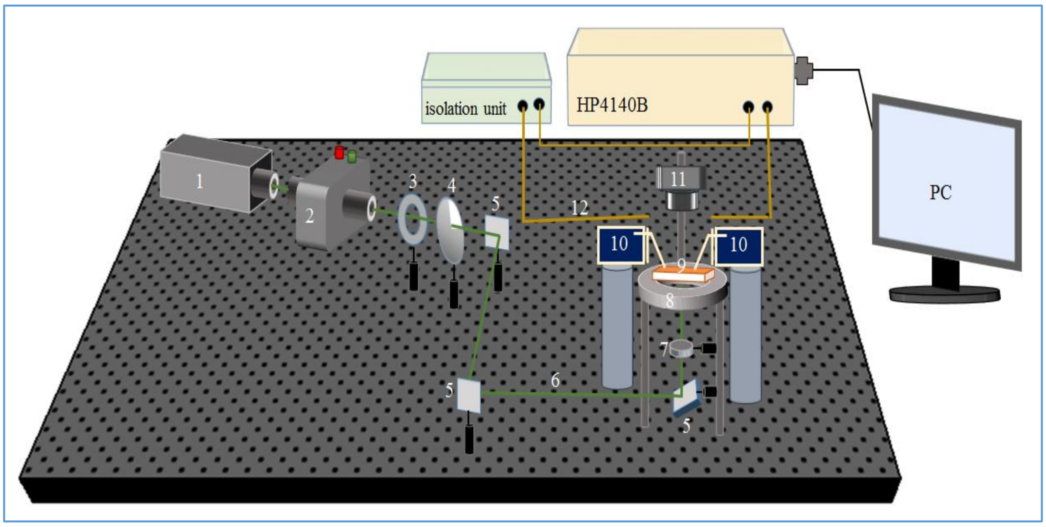

Figure 4.10: A schematic representation the measurements setup. (1) Ar$^+$ laser, (2) shutter, (3) quarter wave plate, (4) neutral density (ND) filter, (5) Mirror, (6) laser beam, (7) lens, (8) stage, (9) sample, (10) probes, (11) camera, (12) connection wires.

To obtain the electrical data of potentiation and depression for ZnO NR and Au NP-based devices, devices were programmed by a series of positive pulses of 2.0 V, 1.0 V, followed by a series of negative pulses of – 2.0 V, – 1.0 V for ZnO NRs, and Au NPs, respectively. For both, a pulse length of 50 ms with a read voltage of 0.15 V for ZnO NRs device and 0.1 V for Au NPs device was used. In the case of optical stimulus, a series of circularly polarised light pulses followed by a series of linearly polarised light pulses with a pulse length of 2 min and a pulse separation of 1 min were used. The current was read continuously using read voltages of 0.15 V for ZnO NRs device and 0.1 V for Au NPs device.

The HP4140B source-measure unit in combination with a Keithley 230 voltage source was used for STDP measurements. To obtain the STDP curves for ZnO NR and Au NP-based devices, the following sequence of pulses were used: (1) an initialization pulse of – 2.0 V for ZnO NRs and – 1.0 V for Au NPs (length 100 ms) was used to reset the device to an initial off state. (2) A read (probe) pulse of 0.15 V (150 ms) was used to determine the conductance state of the device, (3) the synaptic efficacy of the device was modified by applying a single paired spike sequence consisting of two pulses (pre-spike and post-spike) separated by different times ranging from −1.0 to +1.0 s, (4) a final read (probe) pulse of 0.15 V (150 ms) was used to determine the final conductance state of the devices.

Chapter 5. Results: Zinc Oxide Nanorod – PDR1A Hybrid Devices

In this chapter, the results of ZnO NR and PDR1A-based resistive switching memristors are described. In section 5.1, SEM images showing the morphology of ZnO NRs and PDR1A films are reported. Section 5.2 shows the absorption spectra of ZnO NRs and PDR1A films. Section 5.3 reports the results of variation of PDR1A film thickness (expansion and contraction) upon irradiation and thermal relaxation. The electrical and optoelectronic results, as well as the switching mechanism of the ITO/ZnO NRs/PDR1A/Al devices, are presented in section 5.4. In section 5.5, neuromorphic applications of the devices are presented.

5.1 Morphology of ZnO NRs and PDR1A

SEM images of ZnO nanorod arrays grown on an ITO coated glass substrate are shown in Fig. 5.1. The length and diameters of ZnO NRs are 200 nm and 40-60 nm, respectively. Note: the length of ZnO NRs appear in the SEM images to be greater due to the 70º sample tilt. Fig. 5.1 (a) shows the hexagonal structure of ZnO NRs in the top view of the SEM image. Also, it can be seen that the ZnO NRs are very well vertically aligned on the substrate as shown in Fig. 5.1 (b). Fig. 5.1 (c) shows an image of ZnO NRs embedded within a PDR1A thin film.

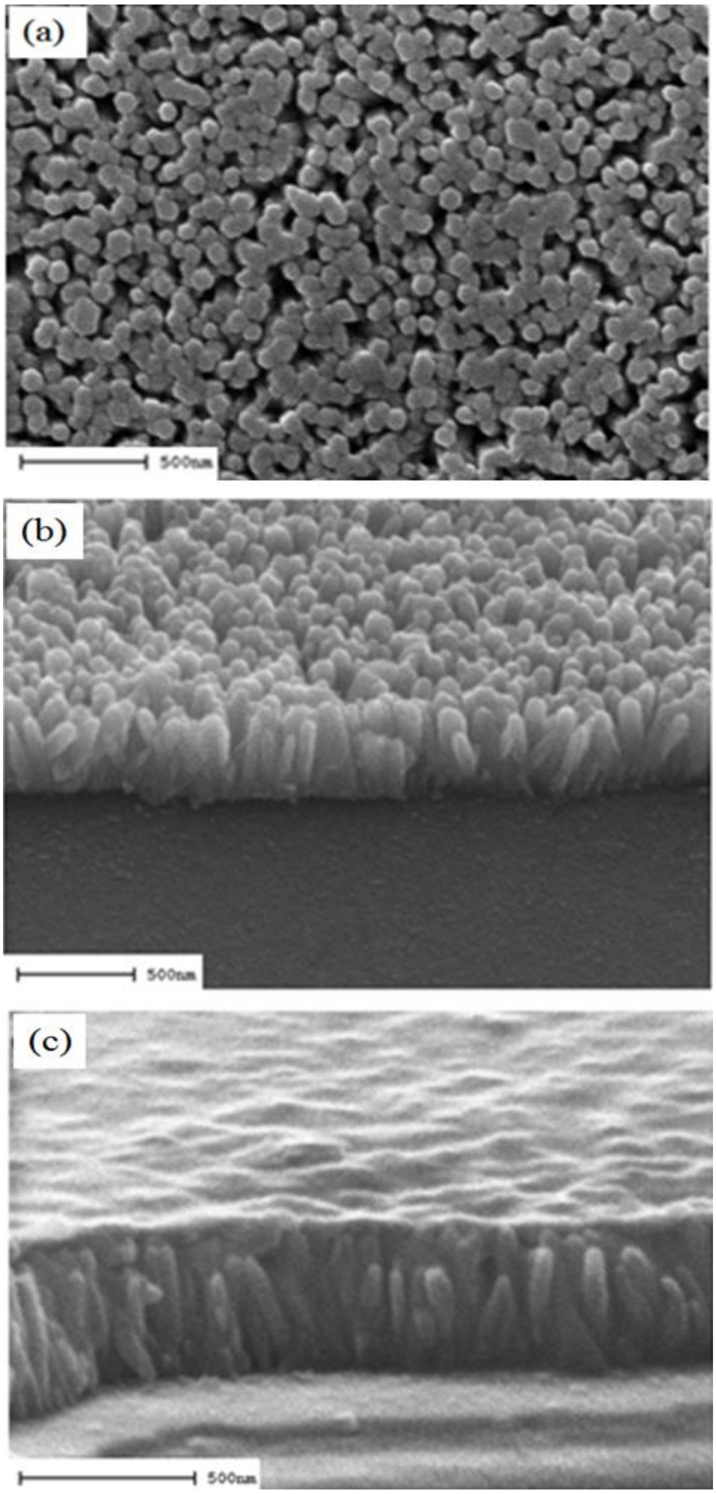

Figure 5.1: SEM images showing ***(a)*** *a top view of vertically aligned ZnO NRs arrays,* ***(b)*** *a vertically aligned ZnO NRs arrays in which the sample was tilted by 70º during imaging, and* ***(c)*** *a thin layer of PDR1A covers and partially diffuses into the ZnO NR voids.*

The thickness of the PDR1A thin film deposited on the glass substrate was 113 nm. In contrast, the SEM image reveals that the thickness of PDR1A film deposited on ZnO NRs film is smaller, which may be attributed to the differences in the wettability and frictional forces between the NR surface and glass. In addition, it can be seen that the PDR1A film covers the ZnO NR tips and permeates into the voids between the nanorods.

5.2 Absorption Spectra of ZnO NRs and PDR1A

The ultraviolet-visible absorption spectrum of the ZnO nanorod arrays is shown in Fig. 5.2. It can be seen that the absorption peak of ZnO nanorod arrays is located at 370 nm due to the large exciton binding energy. This compares well with typical spectra found in the literature [187,188].

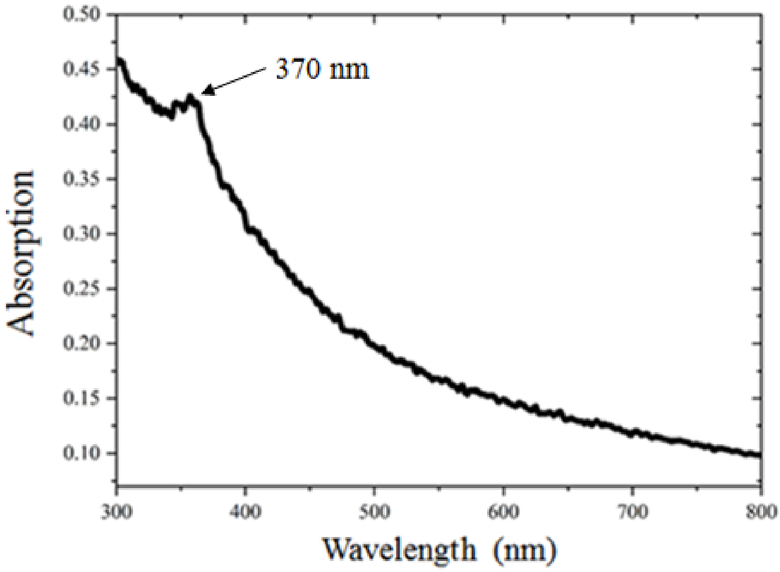

Figure 5.2: UV-Vis absorption spectrum of vertically aligned ZnO nanorod array film prepared at 80°C for 30 min in a microwave oven.

Fig. 5.3 depicts the UV-Vis absorption spectrum of the as-prepared PDR1A film deposited on a glass with a thickness of 113 nm. A broad absorption in the range of 380 – 600 nm can be clearly observed.

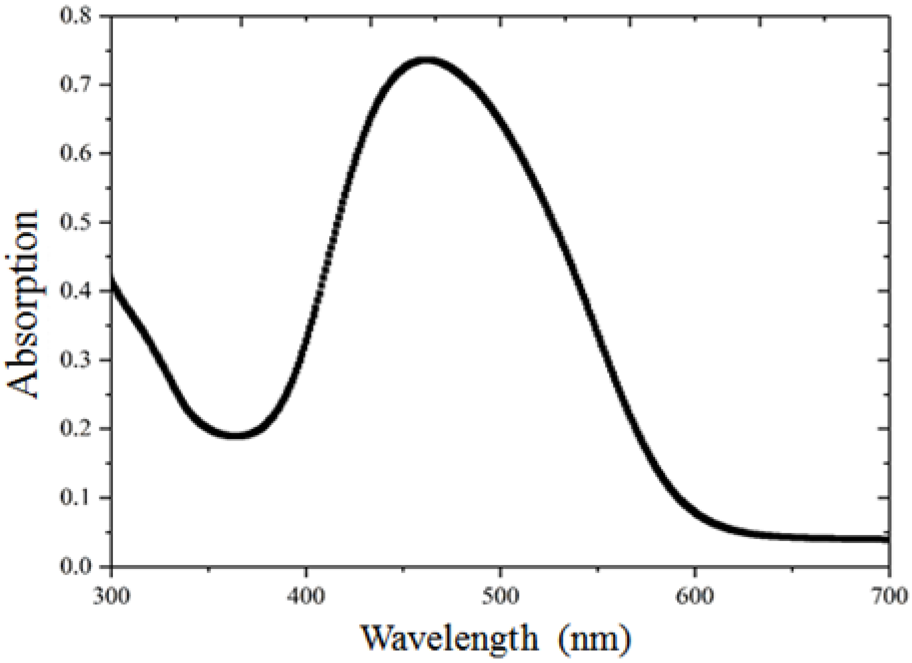

Figure 5.3: UV-Vis absorption spectrum of PDR1A (2% by wt.) film spin-coated on glass at 1000 rpm for 30 s and annealed at 90°C in vacuum for 8h.

5.3 PDR1A Thickness Characterization

The PDR1A thickness versus solution concentration was characterised by Dektak. Different concentrations (1%, 2%, 3% and 5%) of PDR1A dissolved in THF were prepared by weight. These solutions were deposited on glass substrates using spin coating at 1000 rpm for 30 s and then annealed at 90°C for 8 h under vacuum. In this Chapter, 2% of PDR1A in THF was used, with a thickness of about 113 nm.

As illustrated in Fig. 5.4, the film thickness of PDR1A is increased from 80 nm to 200 nm by increasing the solution concentration from 1% to 5%.

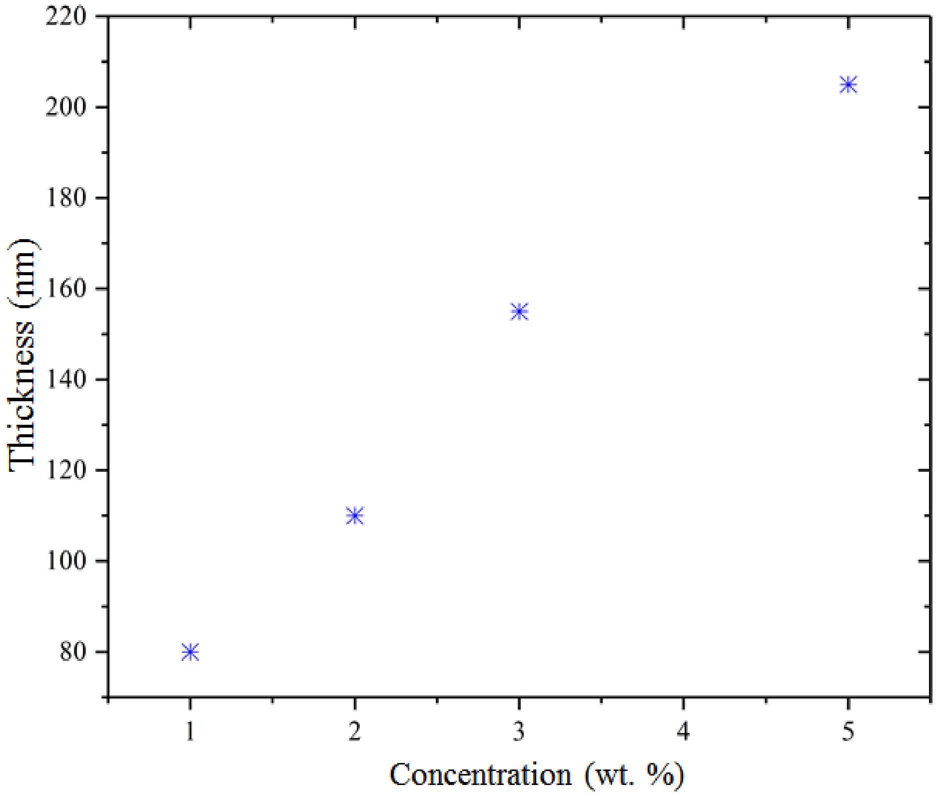

Figure 5.4: PDR1A film thickness vs concentration of PDR1A/THF solution.

Variation of the PDR1A film thickness under optical illumination was measured by Dektak as well. It can be seen from Fig. 5.5 that the thickness of PDR1A increases from 113 nm to 147 nm during the first 20 min of irradiation with circularly polarised light (514 nm) with a power intensity of 180 mW/cm^2. After 20 min irradiation, the PDR1A film thickness is still almost constant. Up to 30% of photoexpansion of film thickness is observed.

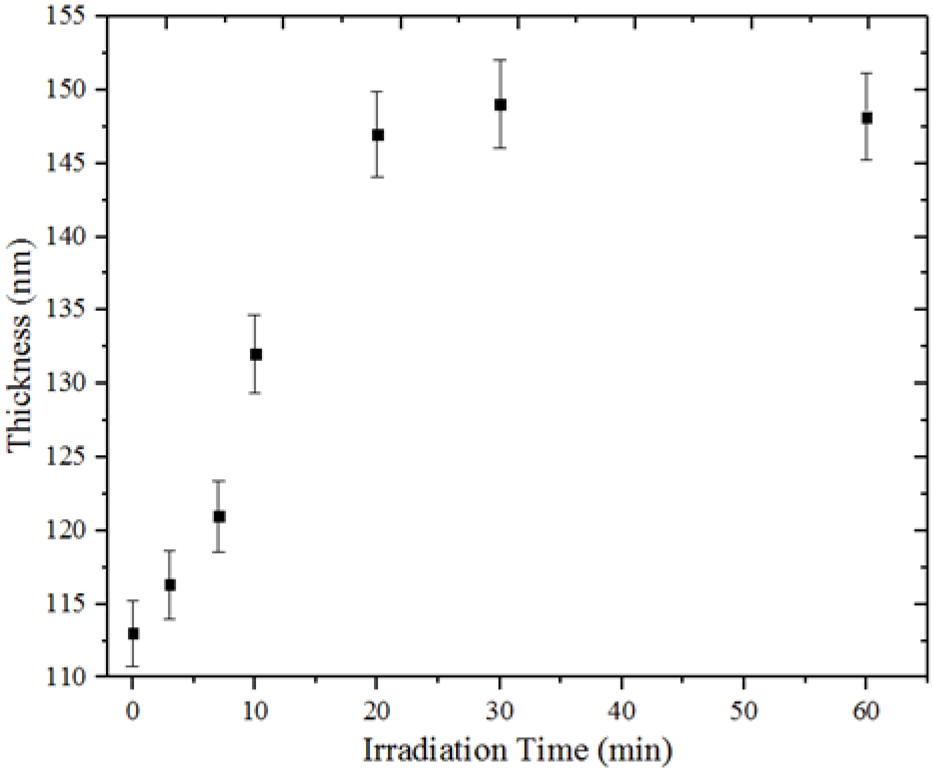

Figure 5.5: PDR1A film thickness vs irradiation time. Circularly polarised light was used to induce the photoexpansion.

The stability of the photoexpanded PDR1A film thickness (pre-irradiated films for 30 min with circularly polarised light) was investigated by monitoring the thickness over a 3 h period after removal of the light source, Fig. 5.6. The graph shows a steady decrease in the thickness of the polymer during the first 120 min but after this period the thickness remains almost the same. Within experimental uncertainty, the thickness of the polymer film after thermal relaxation is the same as the thickness before irradiation, indicating the effect is entirely reversible. PDR1A can also be forced to contract back to its original thickness with a much shorter time constant by irradiation with linearly polarised light. This was achieved by removing the ¼ wave plate and using only the linearly polarised light from the Ar^+ laser. A direct comparison between the forced photo-contraction (red data points) and the thermal relaxation (black data points) is shown in Fig. 5.6 with the inset graph showing the forced relaxation process takes only 15 min, a factor of 8 times faster than the thermal relaxation process.

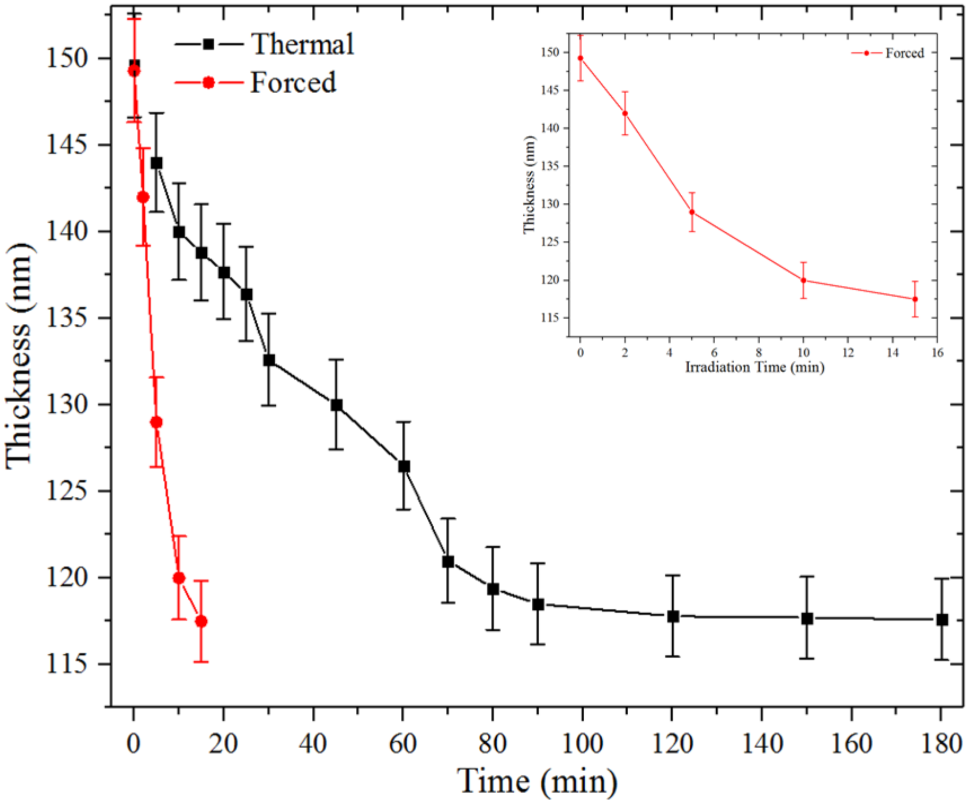

Figure 5.6: Difference of the PDR1A film thickness with time (thermal relaxation) after 30 min irradiation with circularly polarised light (black data) and forced relaxation with continuous linearly polarised light irradiation (red data and inset).

5.4 Electrical Measurements and Optical Modulation

5.4.1 Current – Voltage Characteristics

The optoelectronic properties of the ITO/ZnO/PDR1A/Al memristor devices were studied by doing I-V sweeps before and after laser irradiation. Figs. 5.7 (a) and (b) represent the typical I-V characteristics of optical memristor devices. Voltage was applied to the top Al electrode, and the bottom ITO electrode was grounded. The applied voltage was swept between -2.5 V and +2.5 V (Fig. 5.7 a) and -3 V and 3 V (Fig. 5.7 b) with a current limit of 10 mA. It is worth mentioning that there was no requirement for a electroforming step to activate the device. Bipolar resistive behaviour can be clearly observed. Furthermore, it can be clearly seen that a 20 min laser irradiation by circularly polarised light (red curve) increases both the ON and OFF resistance states (decreased current). The increasing in the resistance is consistent with the increase of PDR1A film thickness. Associated with the change in resistance, a large change in the resistance OFF/ON ratio is observed.

The expansion of the polymer is known to be reversible by thermal relaxation and, in this case, I-V sweeps were taken during the relaxation process (after 60 min, green curve and 120 min, blue curve). After 120 min the polymer has contracted, and the electronic properties of the device have returned back to their original state, as shown in Fig. 5.7 (a).

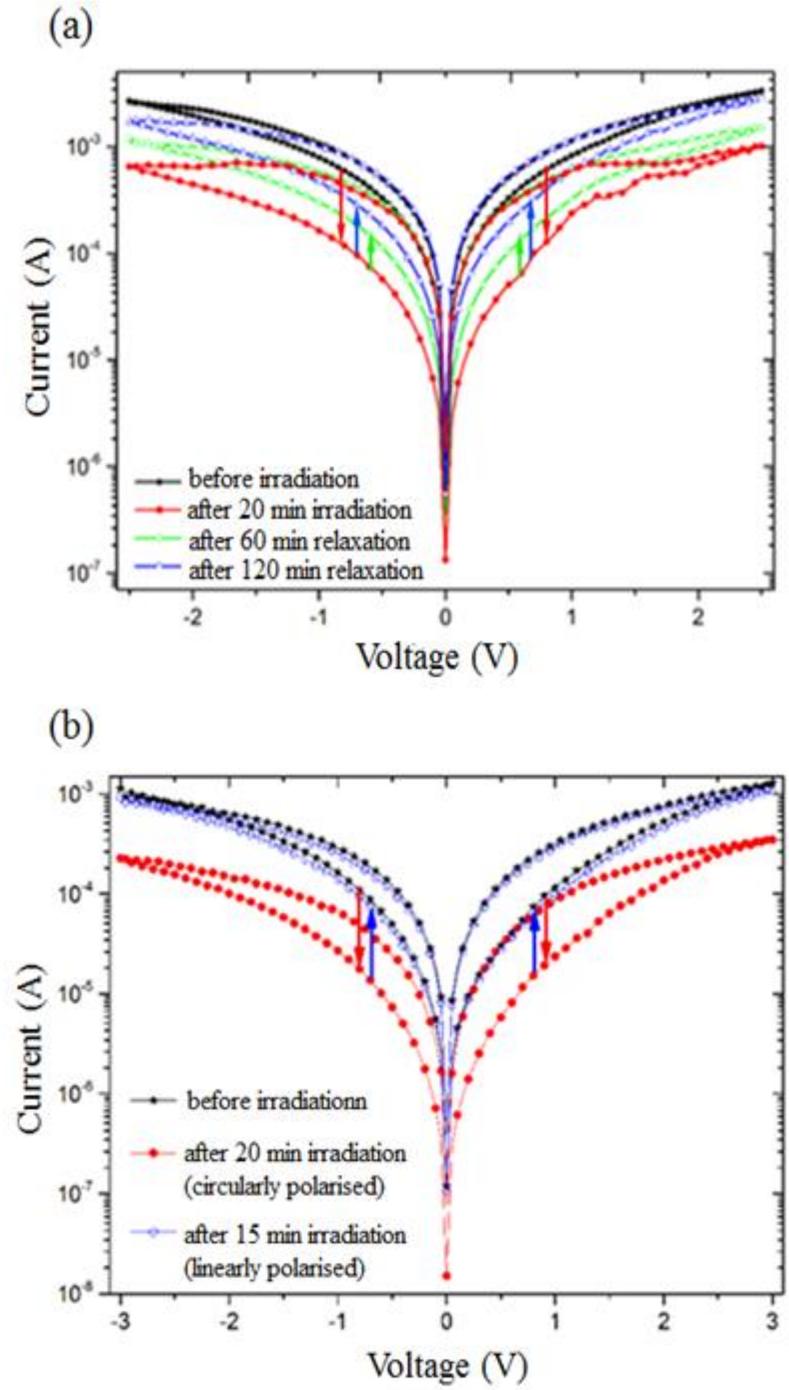

Figure 5.7: Current-voltage sweep of the ZnO/PDR1A memristor devices before irradiation, directly after irradiation for 20 min with circularly polarised 514 nm light (180 mW/cm^2), after 60 min thermal relaxation and 120 min thermal relaxation ***(a)****, and* ***(b)*** *after forced relaxation by irradiation for 15 min with linearly polarized 514 nm light (180 mW/cm^2).*

The forced contraction effect of PDR1A film on memristor devices switching properties was also investigated by irradiation with linearly polarised light. Fig. 5.7 (b) shows the I-V characteristics of a typical memory cell before irradiation (black curve), after 20 min irradiation with circularly polarised light (red curve) and after 15 min irradiation with linearly polarised light (blue). The graph shows that the device resistance in the HRS and LRS states increased upon initial exposure to circularly polarised light and then reverted back to its initial value upon irradiation with linearly polarised light (forced relaxation). Associated with this is also a change in the resistance OFF/ON ratio from approximately 4 to 7, as determined by calculating the inverse gradient at a point close to the origin.

5.4.2 Role of the Insulating PDR1A Film

In order to investigate the effect of a PDR1A film on the resistive switching behaviour, three types of memristor devices were fabricated. The first device contains only a vertically aligned ZnO NRs with an ITO/ZnO NR/Al structure. The second device consists of only a PDR1A film, ITO/PDR1A/Al. The third one is a hybrid material device that consists of vertically aligned ZnO NRs and a film of PDR1A, which has an ITO/ZnO NR/PDR1A/Al sandwich structure. A comparison of the I-V characteristics of the three device types is shown in Fig. 5.8. The ZnO NRs exhibited typical bipolar resistive switching and the highest conductivity. In contrast, the device consisting only of an insulating film of PDR1A showed a negligible resistive switching behaviour and the lowest conductivity, which can be attributed to the low conductivity of insulating materials. However, the addition of

PDR1A to the vertically aligned ZnO NRs enhanced the ON/OFF ratio, and at the same time decreased the current of about one order of magnitude in comparison with the device that based only on the ZnO NRs.

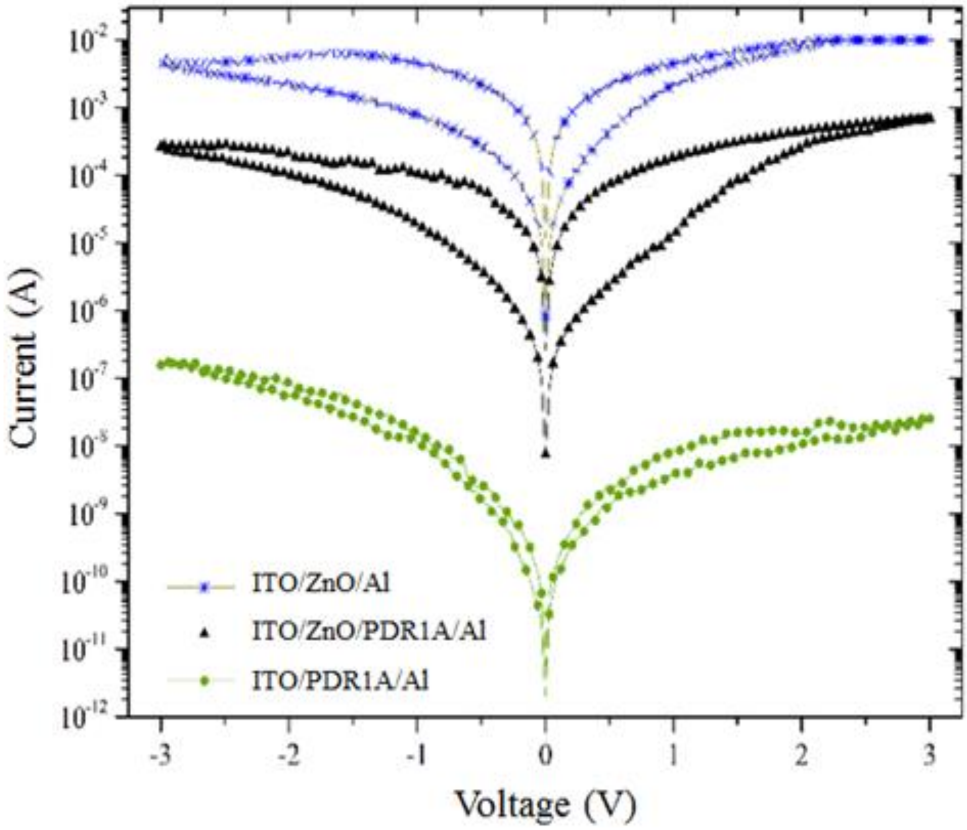

Figure 5.8: The I-V characteristics of resistive switching devices based on an ITO/ZnO NR/Al structure (blue curve), ITO/ZnO NR/PDR1A/Al structure (black curve), and an ITO/PDR1A/Al structure (green curve).

5.4.3 Conduction Mechanisms

Fig. 5.9 (a) shows the typical I-V characteristic of a RRAM device based on hybrid materials of ZnO NRs and PDR1A. Bipolar resistive switching behaviour can be seen, where the device SETs and RESETs in the positive and negative polarities of applied voltage, respectively. The device shows a pinched hysteresis loop, which represents the fingerprint of a memristor. The applied voltage was swept between –3 V and 3 V with a compliance current of 10 mA to protect the device from breakdown during measurements. Initially, the device was in the HRS with the current gradually increasing for the applied voltage range between –3 V and 1.5 V. From 1.5 V to 3 V, the current increased rapidly and the device switched from the HRS to the LRS (SET process). The device remained in the LRS when the applied voltage was reversed. At –2.5 V, however, the current decreased and the device switched back to the HRS (RESET process).

There are several conduction mechanisms can be suggested to interpret current transport in memristor devices based on binary metal oxides and insulators. The conduction of the hybrid organic-inorganic materials, however, is more complicated. Herein, the charge transport mechanisms responsible for the conduction in the ITO/ZnO NR/PDR1A/Al structure were investigated through the log-log plot of the I-V curve as illustrated in Fig. 5.9 (b). Five consecutive regimes of conduction on the log-log I-V curve were observed during the transition from the high resistance state to the low resistance state. This indicates that space charge limited current (SCLC) is the dominant conduction mechanism. This conduction mechanism will be discussed in chapter 7.

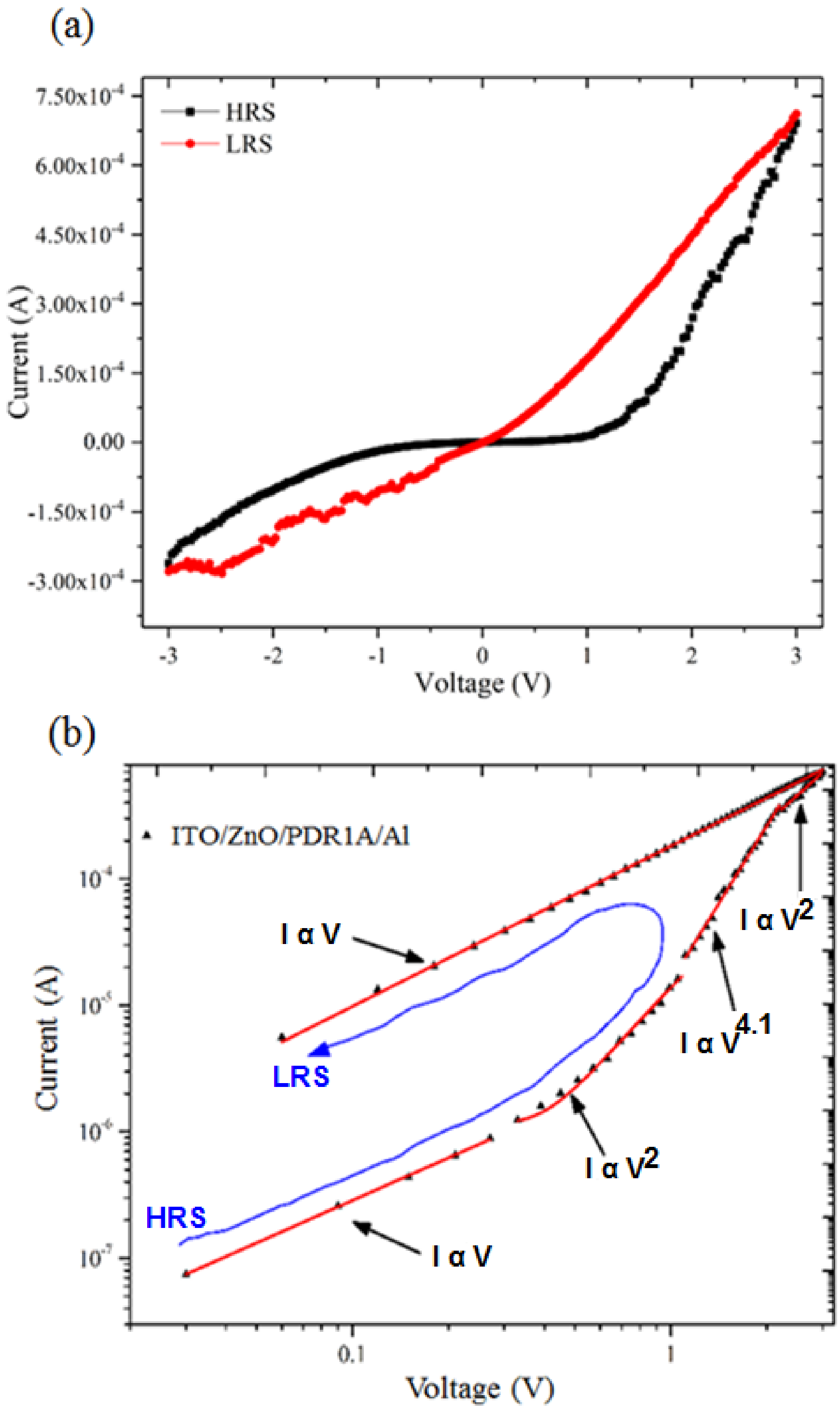

Figure 5.9: ***(a)*** *Plot of a typical I-V curve showing bipolar resistive switching and* ***(b)*** *I-V curve fitting for a device consisting of ITO/ZnO/PDR1A/Al structure. The lines are fits to various transport models that are expected to occur in the transition from the high-resistance state (HRS) to the low-resistance state (LRS).*

5.4.4 Reliability

To examine the reliability of the ZnO NR/PDR1A-based optical memristor device, two scenarios were used. The first was to repeat the I-V sweeps. Fig. 5.10 presents 20 successive I-V sweeps were taken over the range of – 2.5 V to 2.5 V. It is apparent from this graph that the device exhibited good reliability, and no degradation was observed after 20 consecutive I-V sweeps.

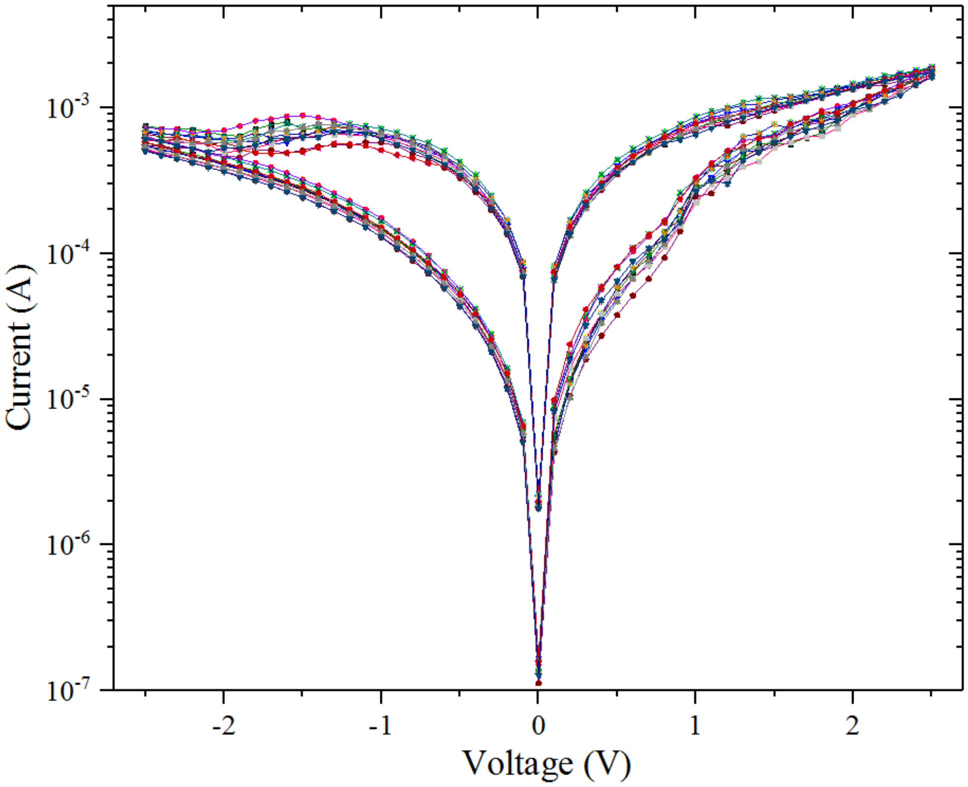

Figure 5.10: 20 successive I-V sweeps of an ITO/ZnO NR/PDR1A/Al device.

The second scenario is based on data retention measurements, as shown in Fig. 5.11. The ON and OFF resistance states were tested under a constant applied voltage of

0.1 V for up to 5 h. The OFF/ON ratio of 3 remained almost the same and no significant degradation was observed during the time period of the test. As shown the device has exhibited a slight increase in the high resistance state after 10^3 s with some fluctuations after 10^4 s which can be attributed to the electrical stress and unstable contact between the probes and electrodes caused by movements and vibrations in the lab. This investigation shows that the ZnO NR/PDR1A-based resistive switching cells have a good data retention and have potential for nonvolatile memory applications.

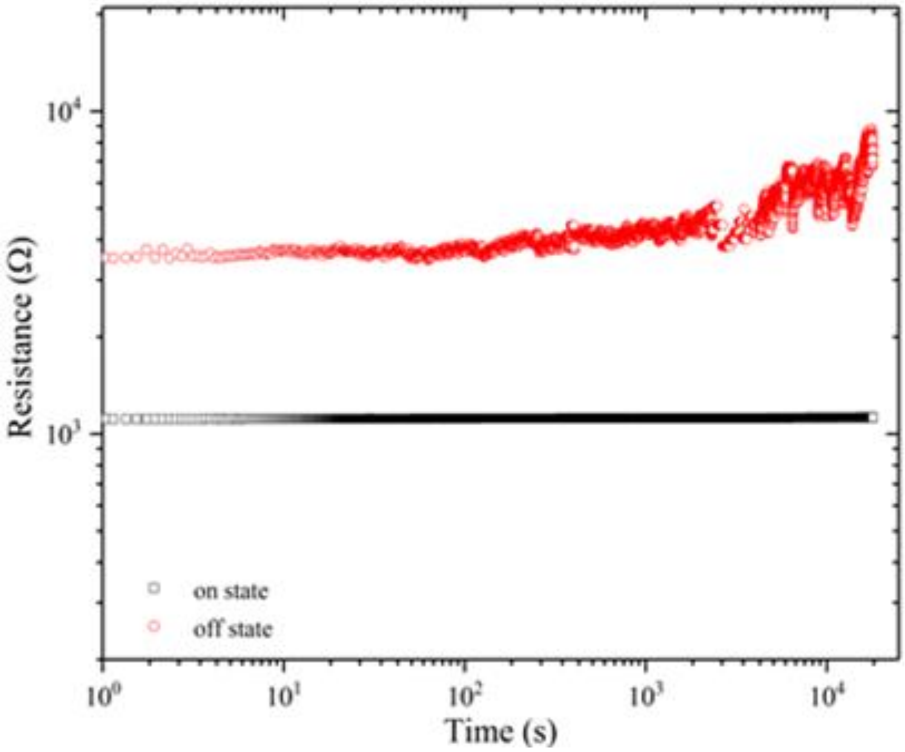

Figure 5.11: Data retention characteristics of ITO/ZnO NRs/PDR1A/Al memristor device measured at 0.1 V.

5.4.5 Reversible Optoelectronic Cycles

Reversible optoelectronic cycling of the ITO/ZnO NR/PDR1A/Al resistive switching memory was investigated. This investigation was achieved by repeated irradiation of the device with 20 min cycles of circularly and linearly polarised light. Fig. 5.12 shows the typical optoelectronic response of the device resistance in the OFF state (black data) and the ON state (red data) as a function of time. The resistance of the LRS switched from approximately $5x10^3$ Ω to $2x10^4$ Ω upon irradiation with circularly polarised light and reverted back into its initial state by irradiation with linearly polarised light. Similarly, the resistance of HRS switched approximately from $3x10^4$ Ω to $1x10^5$ Ω upon irradiation with circularly polarised light and switched back into its initial value by irradiation with linearly polarised light.

5.5 Neuromorphic Computing Applications

Memristors can be used not only as a resistive switching cell for data storage but also in other potential applications like the neuromorphic computing systems. Memristors are two terminal devices that can behave as biological synapses. In biological systems, synapses in the brain “learn and function” by adapting to repeated signalling events and the regulation of the synaptic weight occurs through the ionic flow between each two neighbouring neurones (Hebbian theory) [189]. Similarly, memristors’ conductance or resistance for neuromorphic system applications can be incrementally modified by the charge or flux pass through a memristor device. Synaptic plasticity is a measure of this response over time and involves either a weakening or strengthening of the synaptic connection. In memristors, this is akin to a measurement of the device resistance under an electrical pulses stimuli which lead to increase the device resistance in one direction and decrease it in another direction.

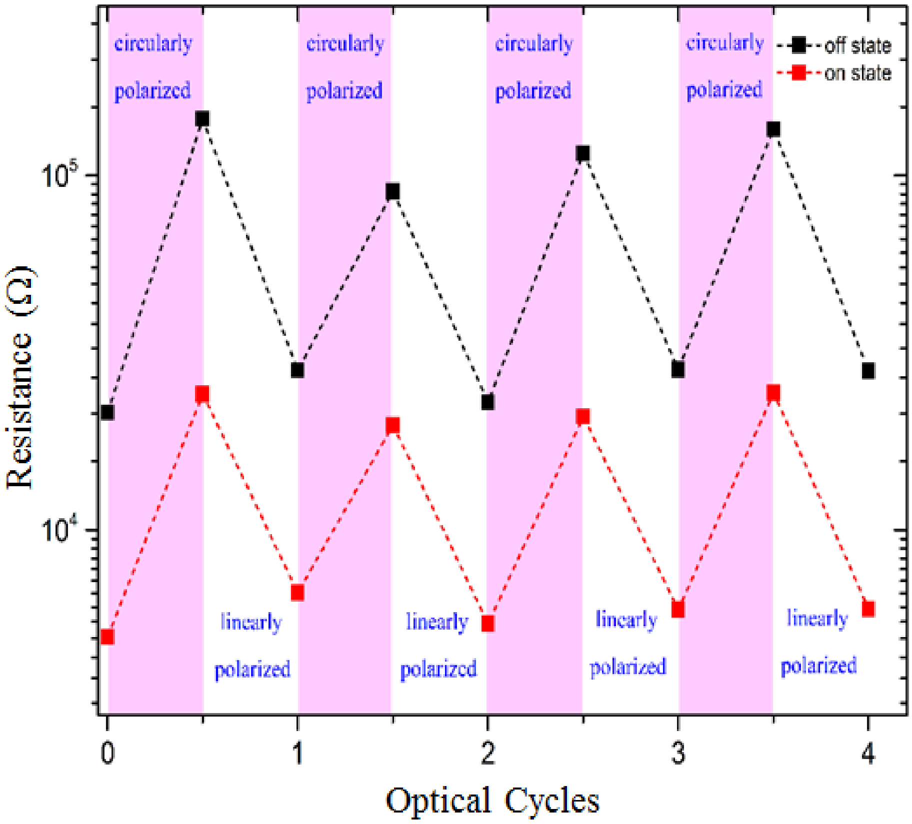

Figure 5.12: Reversible optoelectronic cycles of the memristor resistance of the ON and OFF states during circularly and linearly polarised irradiation (180 mW/cm^2) as a function of time.

Here, besides the electrical stimulus, optical pulses were also utilised to investigate the ability to control the neuromorphic learning properties of ZnO NR/PDR1A-based memristor devices. Fig. 5.13 (a) shows the results of applying a series of electrical pulses on the synaptic strength of the device. Applying electrical pulses of 2 V with 50 ms pulse length incrementally increases the synapse conductance (potentiation), whereas applying electrical pulses of –2 V incrementally decreases the synapse conductance (depression). A similar effect was also achieved by applying a series of optical pulses of circularly and linearly polarised light as shown in Fig. 5.13 (b). The resistance of device was measured at a continued read voltage of 0.15 V with 2 min pulse length and 1 min separation time between pulses (2 min on and 1 min off). Circularly and linearly polarised Ar^+ laser pulses of intensity 180 mW/cm^2 for 20 min each were used to induce the incremental potentiation and depression effect. The figure shows that repeated exposure to pulses of circularly polarised light followed by pulses of linearly polarised light caused firstly depression, as shown by a decrease in the conductance, and then potentiation, as indicated by an increase of conductance. Interestingly, the response of the device for electrical pulses seems to be linear for both the potentiation and depression, whereas, in the case of optical stimulation, depression is more highly non-linear than potentiation. This indicates that the device shows two different dynamical processes upon an external stimuli. The two dynamical processes provide a functionality for potential neuromorphic applications and non-volatile memory applications that need linear behaviour and non-linear behaviour, respectively. These results demonstrate that the synaptic plasticity of the memristor device can be modified by not only the electrical stimulus but also optical stimulus.

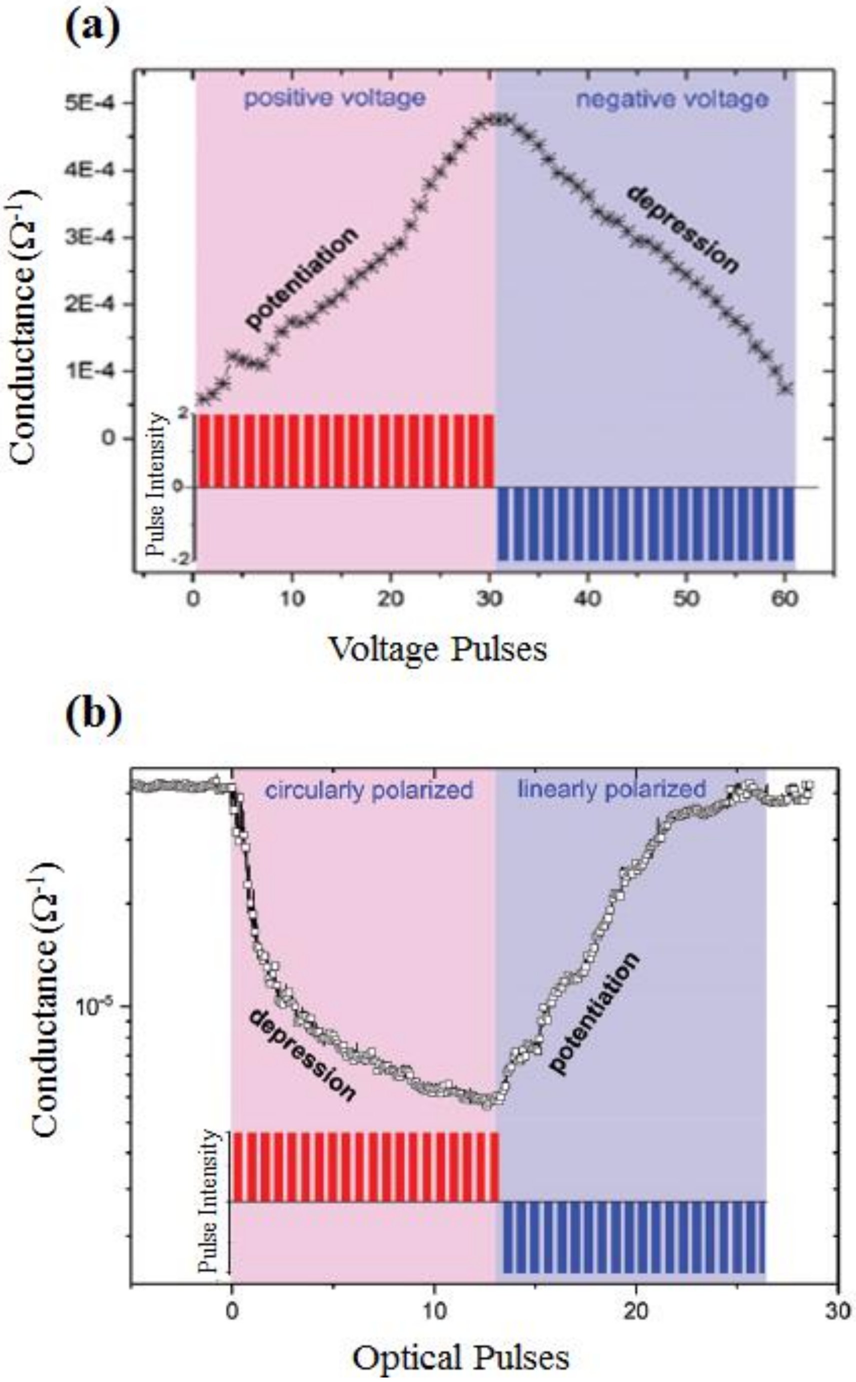

Figure 5.13: Classical habituation phenomenon controlled electrically (a) using voltage pulses of 2 V for potentiation and –2 V for depression with 50 ms pulse length, and optically (b) as demonstrated by the incremental increase (potentiation) and decrease (depression) of the conductance of the LRS state with repeated pulses of circularly polarised light (red) and linearly polarised (blue).

Spike-timing-dependent plasticity (STDP) is also a key tenet of Hebbian learning and has been shown to be linked with sensory perception, spatial reasoning, language and conscious thought in the neocortex. In STDP, learning and information storage is dependent upon the difference in arrival times of action potentials from neighbouring neurons, called pre-synaptic and post-synaptic spikes. The arrival of overlapping pulses can strengthen (potentiation) the synaptic weight if the pre-synaptic pulse arrives before post-synaptic pulse or weakening (depression) the synaptic weight if the post-synaptic pulse arrives before the pre-synaptic pulse. In the case of memristors, the synaptic weight can be quantified by measuring the change in conductivity of the device [190].

Optical modulation of the synaptic weight (ΔG/G) of ITO/ZnO NR/PDR1A/Al resistive switching memory devices was investigated. The STDP of the memristor device before and after 10 and 20 minutes circularly polarised irradiation using an Ar^+ laser (180 mW/cm2) is shown in Fig. 5.14. In this experiment, the STDP results are achieved by measuring the variation in memristor conductance (ΔG/G) with different arrival times (Δt) of pre- and post-synaptic pulses. The parameters used in this experiment are a simple waveform (the shape of the voltage pulse used to simulate the action potentials is shown by the inset in Fig. 5.14), reset voltage of – 2 V, 0.1 s reset pulse length, 3 V for the pre and post voltage pulses, and 0.15 V read voltage. The synaptic efficacy of the memristor is shifted due to the variation of PDR1A film thickness after irradiation. The results of this study provide insights into the possibility to control the properties of the synaptic efficacy *via* optical means.

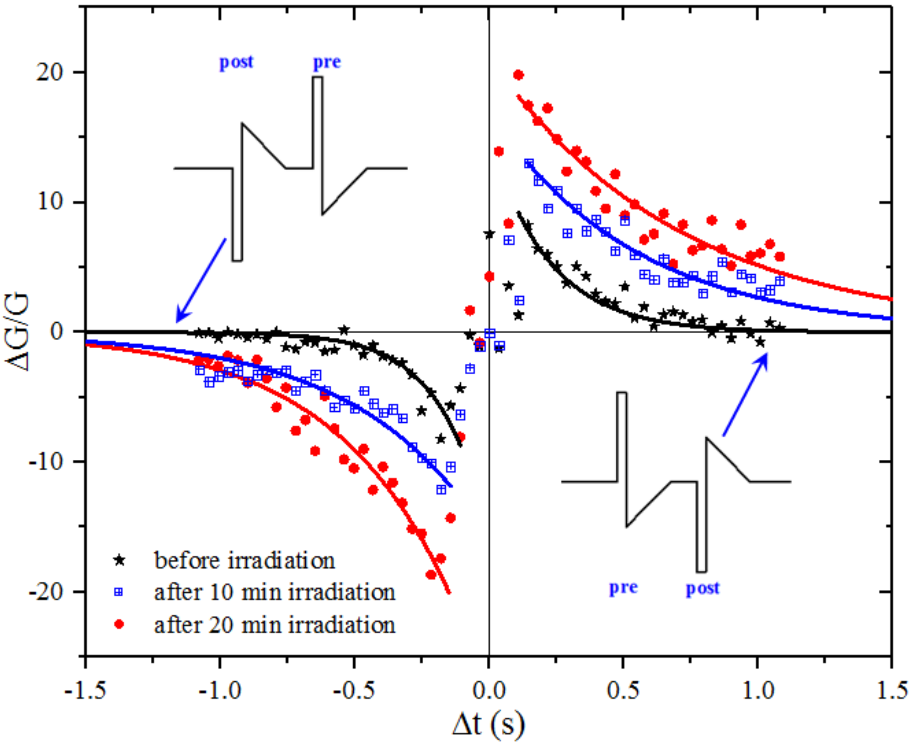

Figure 5.14: Optical modulation of the STDP synaptic weight, before optical irradiation (black data), and after 10 min (blue data) and 20 min (red data) irradiation with circularly polarised light as shown by a shift in curves before and after optical irradiation.

The lines are fits to the asymmetric Hebbian STDP learning rule [162,191]

$$\Delta w = \begin{cases} A_+ e^{-|\Delta t|/\tau_+} & if\ \ \Delta t > 0 \\ A_- e^{-|\Delta t|/\tau_-} & if\ \ \Delta t < 0 \end{cases} \tag{5.1}$$

where Δw is the change in the synaptic weight, Δt is the time difference between the pre and post spikes, and $A_\pm$, $\tau_\pm$ are parameters representing the amplitude of $\Delta G/G$ and time constants, respectively.

Long-term memory (LTM) state and short-term memory (STM) state and the transition from one state to another are essential features in synaptic device applications and can be linked with long-term plasticity (LTP) and short-term plasticity (STP), respectively. Although the LTM exhibits a long data retention time which is important for non-volatile memory applications, the STM (a short retention time of seconds or minutes) is also required to improve the flexibility of data storage and for deleting information that is no longer needed. In the following, we show how the optical memristor device can be used to control the lifetime of memory states, allowing short-term, medium-term and long-term (non-volatile) memory storage. In this experiment, the measurements were performed on the memristor device in the LRS by applying a read voltage pulse of 0.1 V and 1 s pulse width with 30 s separation between pulses. Fig. 5.15 illustrates three different scenarios were used to measure the retention time of the ITO/ZnO NR/PDR1A/Al memristor device. The first scenario represents the long-term memory (non-volatile) state of the memristor in the ON state without any optical irradiation (black data). In this case, there is no change in the resistance over the measured period of time. The second scenario demonstrates the medium-term memory state where the measurements were carried out after photoexpansion of the PDR1A film in the optical memristor by irradiation with a circularly polarised Ar^+ laser for 30 min with 180 mW/cm^2 power. In this case, the LRS resistance decreased with time, over a

45 min time period. That is consistent with the slow thermal relaxation of the PDR1A material back to its original state (blue data).

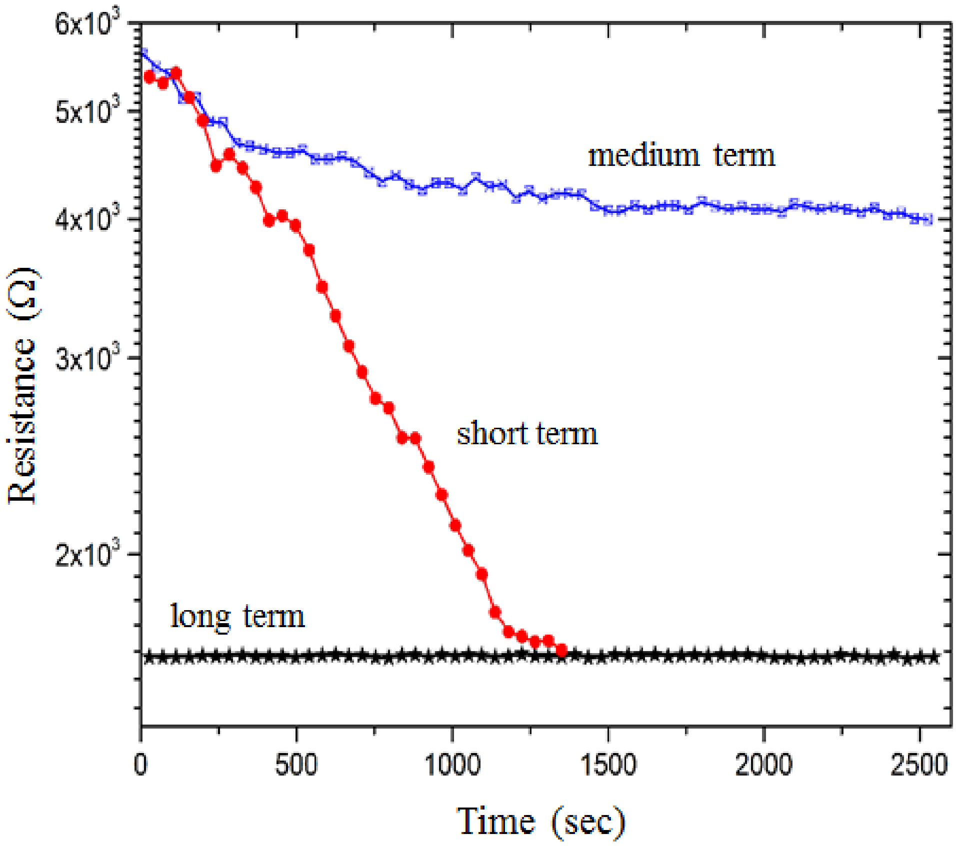

Figure 5.15: Optical modulation of memory retention as shown by the resistance of the LRS state, without irradiation (long-term), after irradiation with circularly polarised light and during thermal relaxation (medium-term) and after irradiation with circularly polarised light but during irradiation with linearly polarised light (short-term).

The third scenario shows the short-term memory state. In this scenario, the same conditions were used to expand the PDR1A material and then the LRS resistance was measured during 20 min irradiation with linearly polarised light in order to make the polymer to contract quicker than the thermal relaxation process (red data). These results confirmed that the memristor retention lifetime can be controlled and switched from LTM to STM by an optical stimulus using a specific wavelength and polarisation light.

Chapter 6. Results: Gold Nanoparticles – PDR1A Hybrid Devices

In this chapter, the results from Au NP:PDR1A-based RRAM devices are reported. The chapter begins with results of a TEM study of the morphology of Au NPs within the PDR1A, as described in section 6.1. In section 6.2, EDX results of Au NPs and PDR1A films are reported. Section 6.3 reports the results of the variation of PDR1A film thickness (expansion and contraction) upon irradiation and thermal relaxation. The electrical and optoelectronic results as well as the conduction mechanism of ITO/Au NP:PDR1A/Al RRAM devices are demonstrated in section 6.4. Section 6.5 shows the applications of the devices in neuromorphic computing applications.

6.1 Transmission Electron Microscopy (TEM)

The morphology of the thin film consisting of Au NPs mixed with PDR1A was investigated by TEM. A cross-sectional TEM image showing the Au NPs: PDR1A composite with a volume fraction of Rv*=~0.065% is shown in Fig. 6.1. The Au NP: PDR1A thin film was sandwiched between the bottom and top Al layers, which had thicknesses of 100 nm and 200 nm, respectively. The figure shows some bumps at the bottom resin/Al interface due to the roughness of the resin sample. Note that the deposition step of the two Al layers is essential to avoid any mixing between hybrid material and resin. Also, the presence of these two Al layers makes the hybrid Au NP: PDR1A thin film more clear. Moreover, in order to protect or to minimize the Au NP: PDR1A thin film from damage which may occur during slicing, the sample was strengthened by encapsulation in resin.

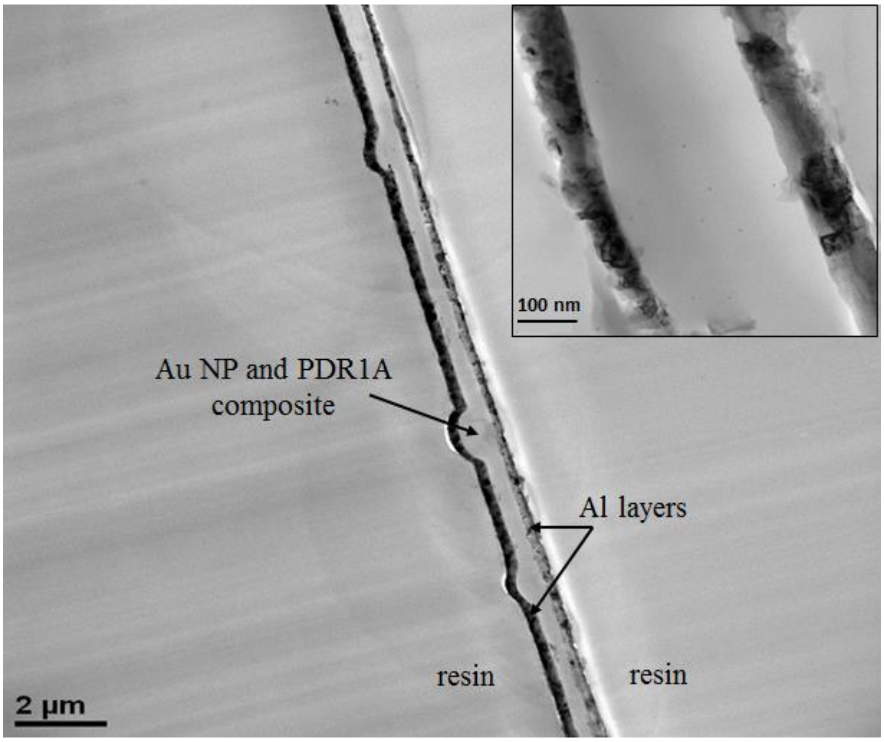

Figure 6.1: Cross-sectional TEM image of the Au NPs embedded within the optically active polymer PDR1A layer with a volume fraction of Rv=~0.065% sandwiched between two layers of Al and encapsulated in resin.*

Fig. 6.2 shows a cross-sectional TEM image of the Au NP: PDR1A thin film deposited on a resin block substrate and sandwiched between Al layers. It can be seen that the nanoparticles do not have a homogeneous distribution in the polymer across the thin film, but instead form small agglomerations that are mostly situated at the top polymer/Al interface. The figure also shows that not all of the nanoparticles have migrated to the top polymer/Al interface during the annealing process and that some remain in the bulk of the PDR1A material.

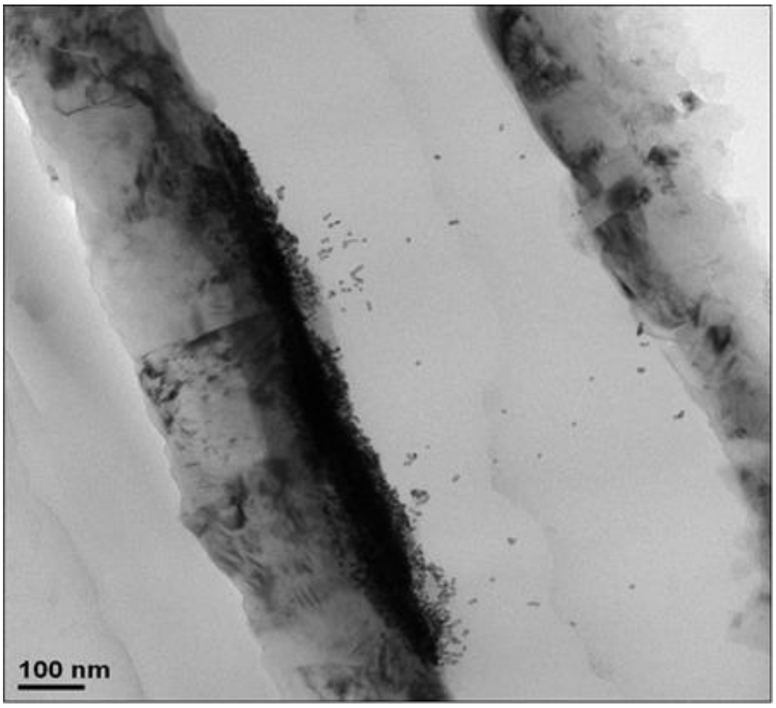

Figure 6.2: Cross-sectional TEM image of the Au NP:PDR1A system prepared at a volume fraction of Rv=~0.065% sandwiched between two layers of Al and encapsulation in resin block. The Au NPs have a poor homogeneous dispersion across the thin film and form predominantly agglomerates situated at the top polymer/Al interface*.

Further TEM investigations on different regions of the device show that in a very few places, the Au NPs form a partially conductive pathway or extended cluster across the thin film that almost connects the two Al layers, as shown in Fig. 6.3. The pathway is expected to be conductive since the nanoparticles are located close enough together to permit inter-particle electron tunnelling and there are sufficient nanoparticles to permit a type of percolative transport from one electrode to another. It is unfeasible to cross-section and image the entire device, but based on the results we speculate that within a single device just a few pathways exist where a complete conductive pathway forms. The optical expansion of the PDR1A material causes these pathways to break which explains the large changes observed in the device resistance during optical irradiation. The observation of quantized conductance values during the expansion and contraction process supports the idea that there are just a few pathways present in the device.

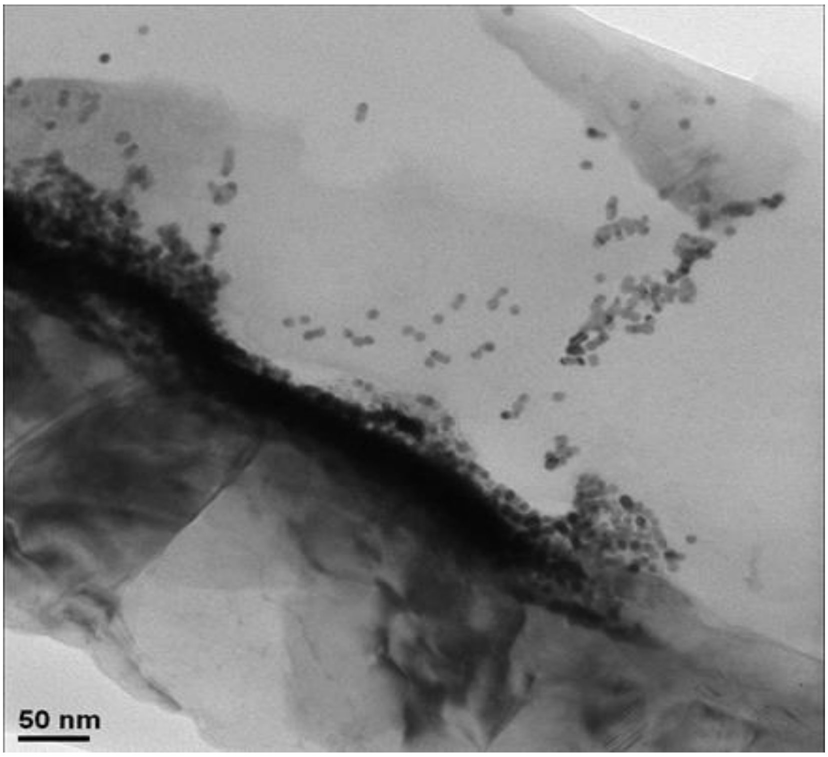

Figure 6.3: Cross-sectional TEM image of the Au NP:PDR1A thin film sandwiched between two layers of Al and encapsulation in resin block. Conductive pathways or extended clusters of Au NPs are formed in some regions of the film.

6.2 Energy Dispersive X-Ray Spectroscopy (EDX)

To investigate the elemental composition of the nanocomposite thin film, energy dispersive x-ray spectroscopy (EDX) in the TEM was used. Fig. 6.4 shows the EDX spectra of the nanocomposite thin film prepared by deposition a mixture solution of Au NPs and PDR1A at a critical volume fraction of Rv*=~0.065%.

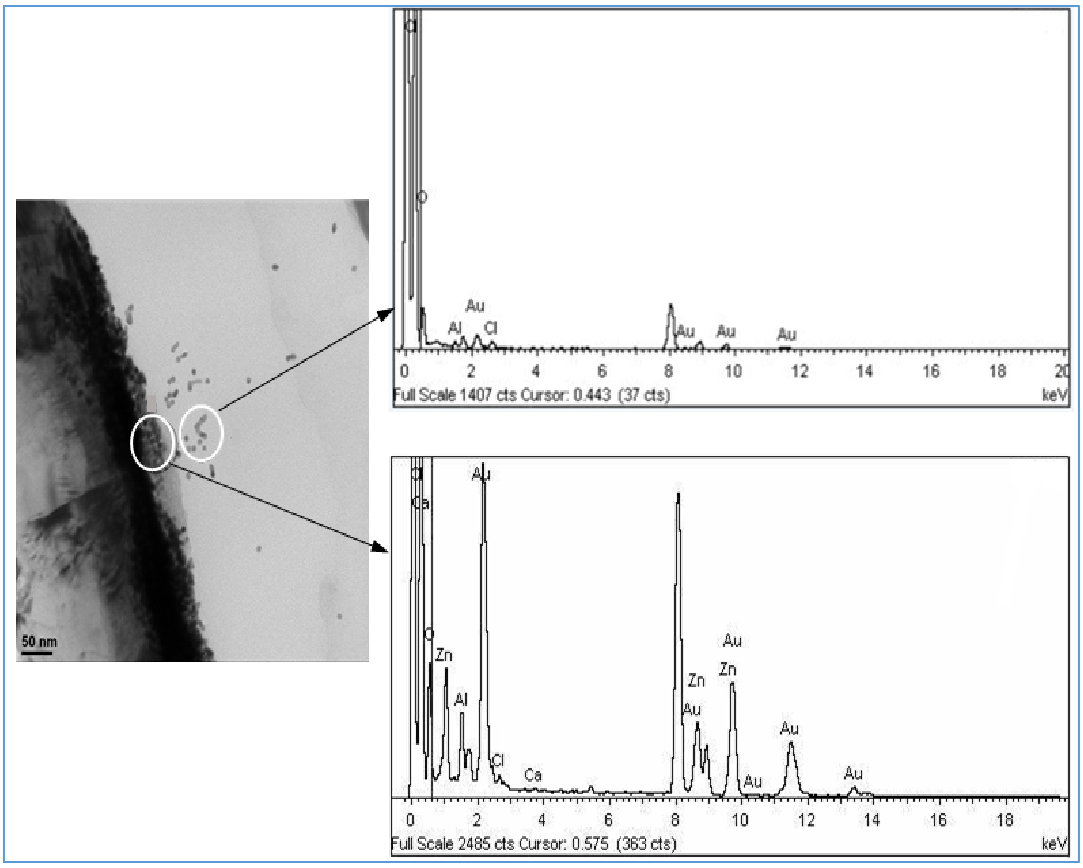

Figure 6.4: EDX spectrum of Au NPs blended with the optically active polymer PDR1A. The TEM image shows the regions used for the EDX investigation.

The prepared thin film was also sandwiched in between two Al layers and encapsulated in resin. The EDX results were taken from two regions; from the hybrid Au NP:PDR1A thin film and at the polymer/Al interface as shown from the TEM image. The results reveal weak EDX signals in the hybrid film region where the Au NPs are dispersed in the polymer whereas strong signals at the interface region which confirm the agglomeration of Au NPs at the polymer/Al interface. The signal for Al originated from the deposited Al layer. The carbon and oxygen signals may come from the organic molecules of PDR1A. In addition, the presence of chlorine, zinc, and calcium signals in the EDX spectra may come from the contaminated diamond and tweezers used in slicing the samples.

6.3 Expansion and Contraction of PDR1A Films

The expansion effect in the PDR1A film thickness under optical irradiation was investigated using Bruker DektakXT profile system. In this experiment, the variations in the film thickness upon optical exposure were measured on a series of PDR1A polymer thin films spin-coated on a glass substrate. Fig. 6.5 illustrates the changes in the PDR1A film thickness as a result of irradiation for 2 h with circularly polarised Ar^+ laser tuned to a wavelength of 514 nm and a power intensity of 180 mW/cm^2. From the graph, we can see that the film thickness of PDR1A polymer increases substantially from 200 nm to 237 nm. The expansion of the PDR1A thin film thickness is ~18% for the first 30 min and then is nearly constant for the remaining irradiation period of time. It is worth mentioning that the thickness of the PDR1A thin film is unchanged after 30 min exposure time while its colour started to change from red to white. This indicates that the long exposure time could cause a saturation or even damage the PDR1A thin film.

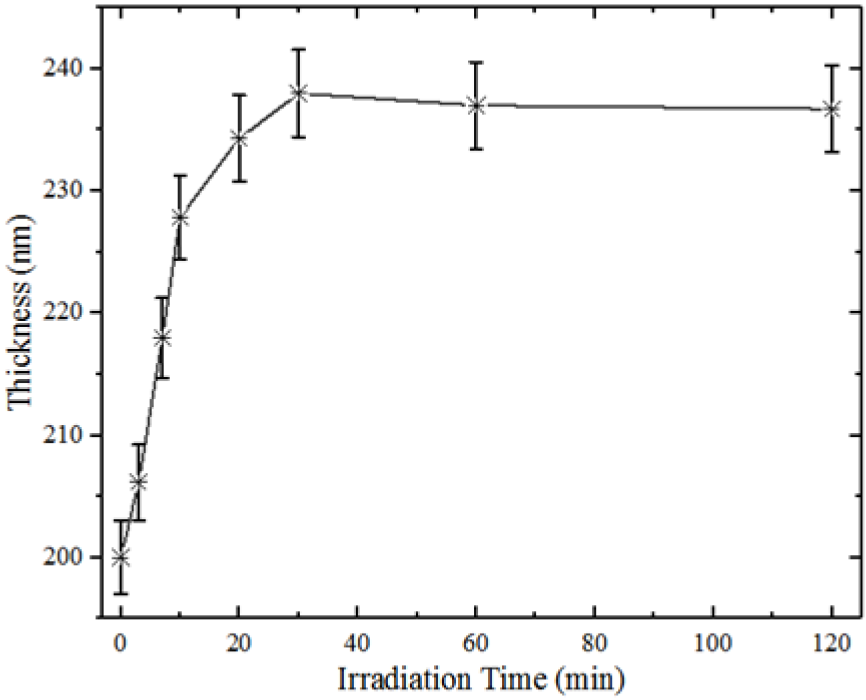

Figure 6.5: The increase of the PDR1A film thickness upon irradiation with a circularly polarised Ar$^+$ laser (514 nm, 180 mW/cm^2).

The contraction effect in the PDR1A film was also studied in two scenarios. This experiment was achieved using an initial expanded PDR1A thin film. The first scenario was based on the thermal relaxation of the PDR1A film at room temperature for 3 h, as shown in Fig. 6.6 (blue curve). The result shows that the film thickness decreases from 237 nm to 207 nm after 120 min and remains almost at this thickness for the remaining relaxation time. The second scenario, however, was carried out by optical means. In this scenario, the PDR1A thin film was returned to its initial thickness by irradiation with linearly polarised light of an Ar^+ laser (514 nm, 180 mW/cm^2) for 20 min, see Fig. 6.6 (red curve). What is interesting about the forced relaxation is the contraction process is a factor of 6 times faster than the thermal relaxation approach.

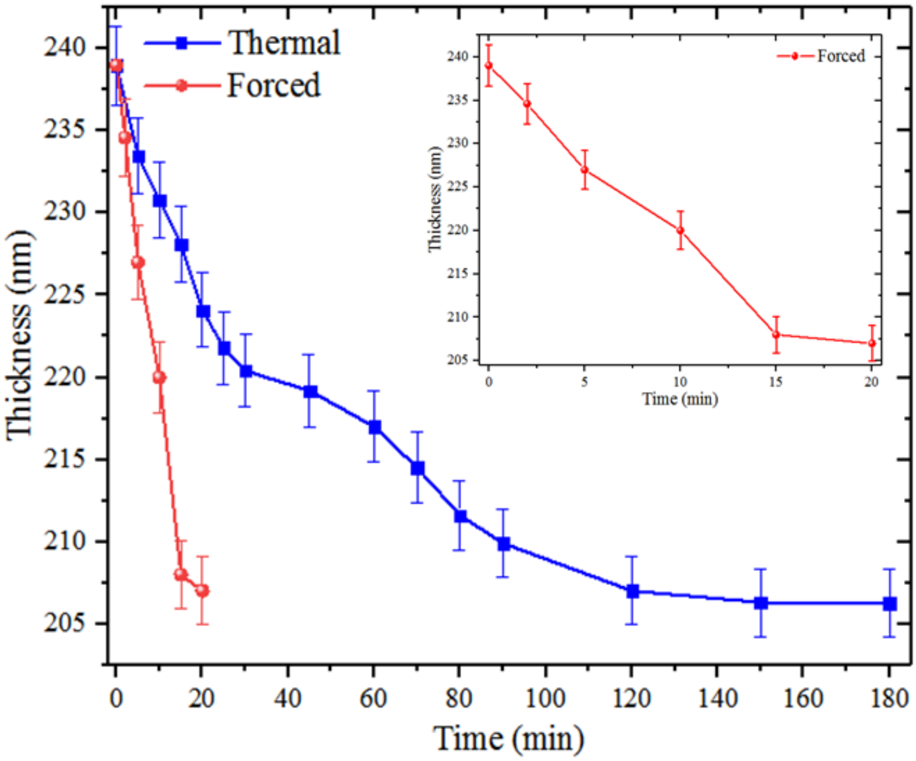

Figure 6.6: The relaxation of the PDR1A film thickness thermally (blue curve) at room temperature, and optically (red curve) upon irradiation with a linearly polarised Ar^+ laser (514 nm, 180 mW/cm^2).

6.4 Electrical Characterization and Optical Modulation

6.4.1 Conductivity Measurements

The electrical conductivity of insulators can be modulated by adding some fillers, e.g. metal nanoparticles to form nanocomposites. In this work, the electrical conductivity of the ITO/Au NP:PDR1A/Al resistive memory as a function of the Au NPs content at room temperature was studied. Fig. 6.7 shows a considerable dependence of electrical conductivity of the Au NPs and PDR1A composite on the Au NP concentration.

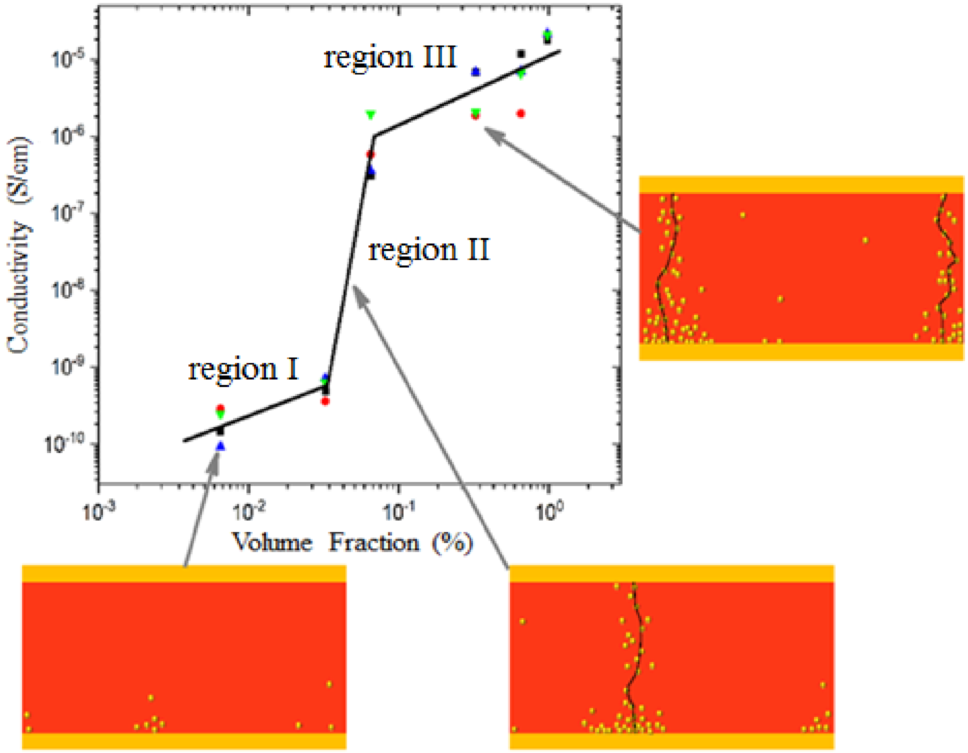

Figure 6.7: Conductivity versus volume function of Au NPs concentration in an optically active PDR1A polymer. A large enhancement in the electrical conductivity of the system takes place at a critical Au NP content (R_v=~0.065%), representing the creation of conductive pathways between the two electrodes.*

The conductivity was measured at 0.3 V. It can be clearly observed that the conductivity is insignificant at low concentration of Au NPs, region I, in which the system behaves as an insulator. On the other hand, a further increase in the Au NPs concentration and especially at the critical volume fraction of Rv*= ~ 0.065% results in a large enhancement of the electrical conductivity of the system of more than 3 orders of magnitude, region II. Note, the device prepared at the critical volume fraction of Rv*= ~ 0.065% will be named as sample A. However, the conductivity of the nanocomposite slowly increases with increasing the concentration of the Au NPs above the critical volume fraction, region III.

The optoelectronic response of the hybrid memristor device (sample A) was also investigated. Fig. 6.8 illustrates the change of the device's conductivity upon optical irradiation using Ar^+ ion laser tuned to 514 nm with a power intensity of 180 mW/cm^2. As shown from the graph, the device's conductivity decreases of about 3 orders of magnitude (red arrow) as a result of 30 min irradiation with circularly polarised light. In contrast, the device can be switched back into its initial conductivity state by irradiation with linearly polarised light for 15 min (blue arrow). The figure also shows a small reversible change in the electrical conductivity of a device that contains no Au NPs (only PDR1A) upon irradiation with circularly and linearly polarised light.

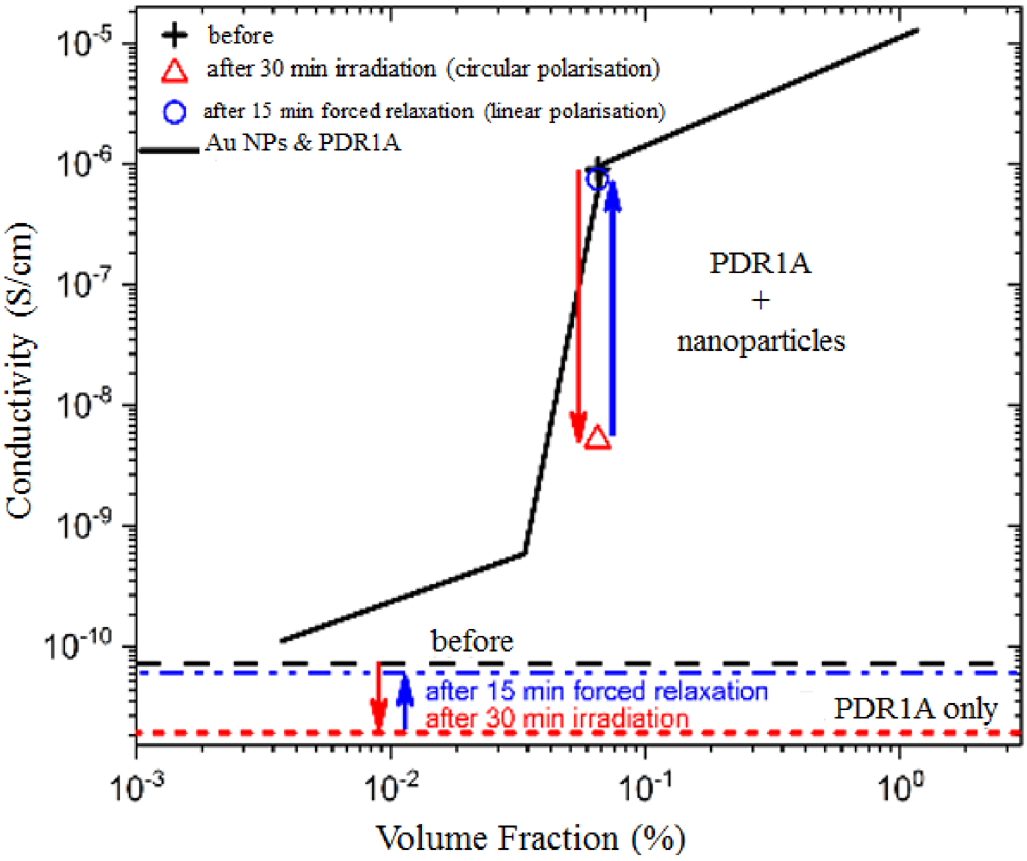

Figure 6.8: Changes in the device conductivity as a result of irradiation with circularly (30 min) and linearly (15 min) polarised Ar$^+$ laser.

The repeatability of the optoelectronic response of the Au NP:PDR1A device (sample A) was examined as well, as shown in Fig. 6.9. The device shows a significant and repeatable decrease and increase in its electrical conductivity upon optical irradiation with circularly and linearly polarised light, respectively. These results suggest that the device conductivity can be cycled several times between the ON and OFF states by changing the PDR1A film thickness upon irradiation that causes a rupture and re-connection of the conductive pathways of Au NP between the two electrodes.

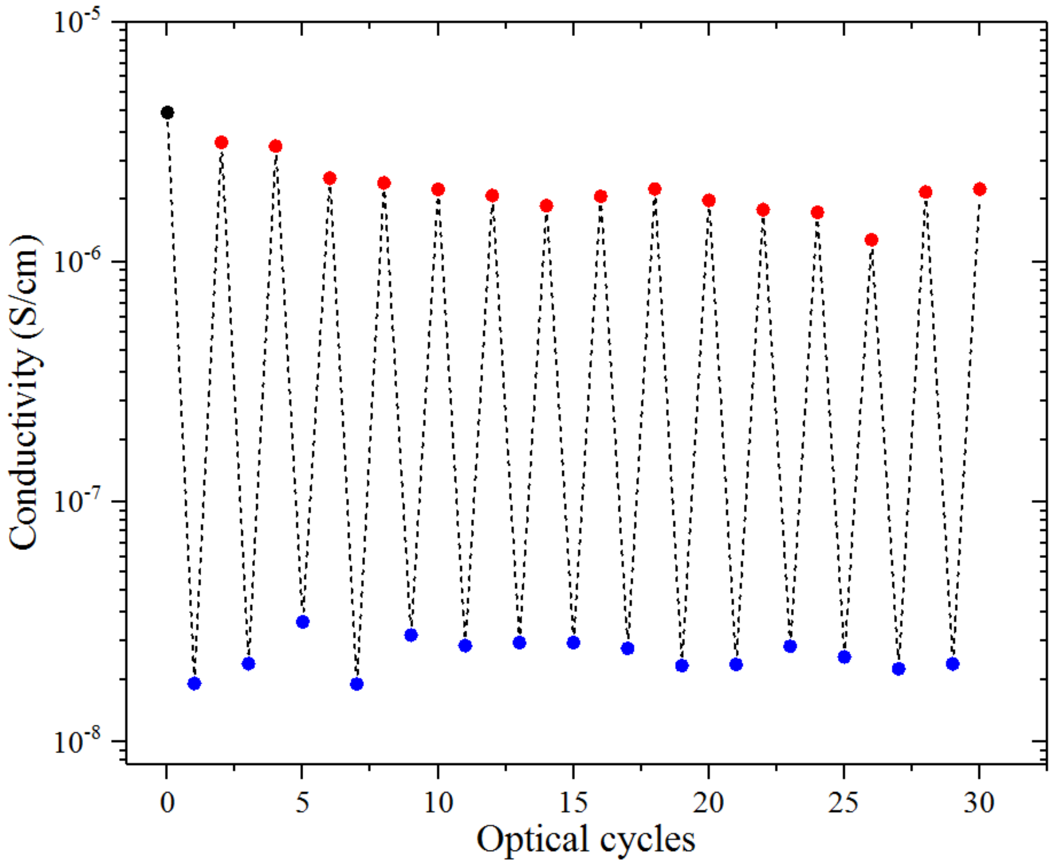

Figure 6.9: Cycled optoelectronic response showing the changing of the device conductivity during irradiation with circularly for 30 min (blue points) and linearly for 15 min (red points) polarised Ar$^+$ laser. The black point shows the initial (fresh) device conductivity state (before irradiation).

To further investigate the expansion/contraction effect of the PDR1A film thickness during optical irradiation on the device conductivity, a transient conductivity measurement at room temperature was performed. Fig. 6.10 presents the transient conductivity results for sample A obtained from successive optical irradiation with circularly and linearly polarised light. The conductivity of the device before and after irradiation is almost constant. Nonetheless, the device conductivity decreases and increases during optical exposure with circularly and linearly polarised light, respectively. Also, a plateau region is apparent, in which the conductivity of the device is still the same for the time period between 1100 s and 2700 s. The results clearly suggest that the expansion and contraction of the PDR1A film thickness upon optical irradiation cause the rupturing and re-connection of the conductive pathways.

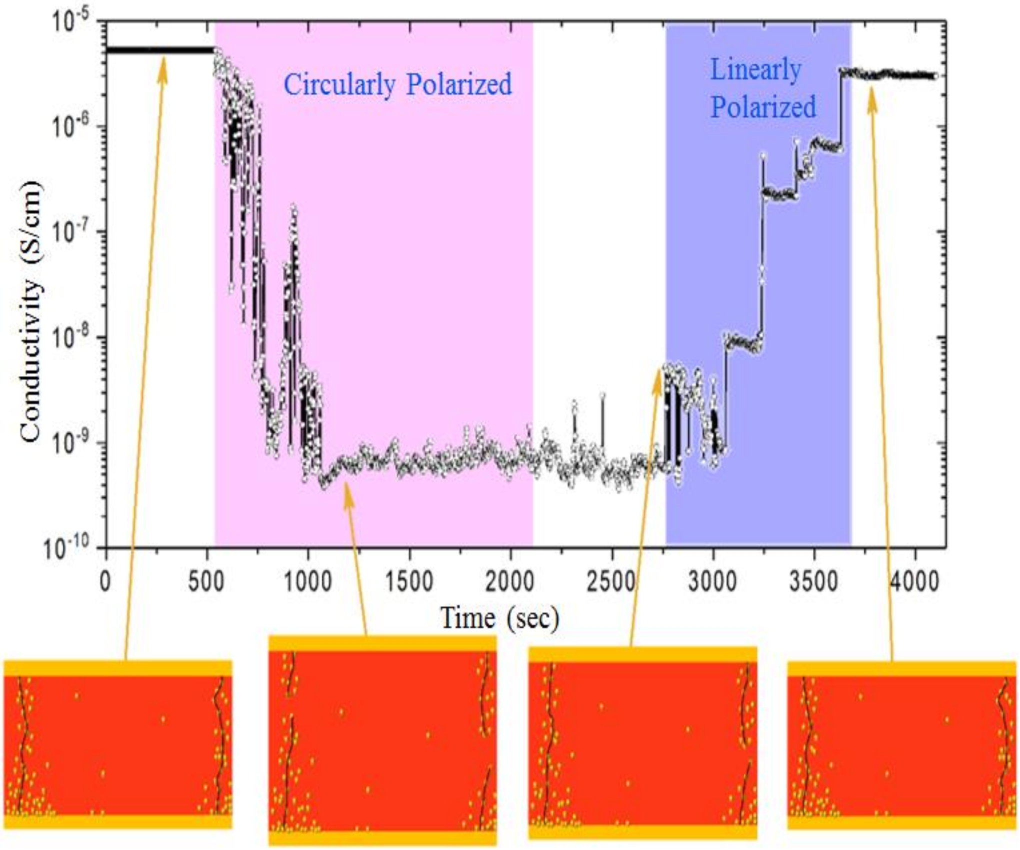

Figure 6.10: Conductivity transient during optical irradiation with circularly polarised light for 30 min and then linearly polarised light for 15 min.

6.4.2 Current – Voltage Characteristics

The electrical characterization of the novel resistive memory devices is presented in the following section. These devices with an ITO/Au NP: PDR1A/Al structure were fabricated by embedding the gold nanoparticles in the optically active PDR1A polymer. It was found that electroforming processes are not needed to activate switching in these devices. Fig. 6.11 shows the I-V curves of several devices prepared with different concentrations of Au NPs. These I-V curves were obtained by sweeping the device between -1V and 1V with a compliance current of

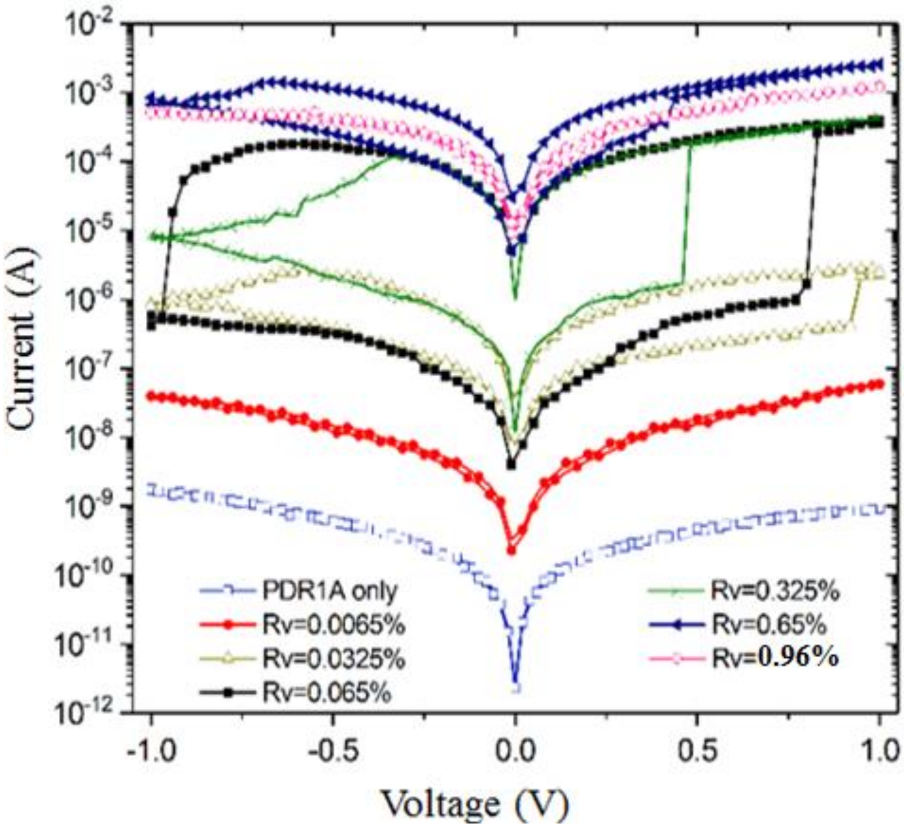

Figure 6.11: Current-Voltage characteristics of the optical memristor devices with an ITO/Au NPs: PDR1A/Al configuration prepared at different Au NPs loading.

10 mA to prevent device breakdown. In this experiment, the voltage was applied to the top electrode of Al whereas the bottom electrode of ITO was grounded. From the graph, the conduction behaviour of these devices shows a strong dependence on the nanoparticle concentration. The graph indicates that resistive switching does not occur at either low or high nanoparticle loading, since in the insulating regime charge injection is limited as there are few nanoparticles for charge storage, whereas in the highly conducting regime, charge cannot be stored since it is easily drained away through the conducting material. Instead, resistive switching occurs between these two extreme values and the resistance OFF/ON maximum ratio coincides with the critical volume fraction, R_V* (sample A). It should be noted that the SET voltage of these devices decreases with increasing the content of Au NPs due to the increase of electrical conductivity of nanocomposite films as shown in Fig. 6.12. The increased electrical conductivity may be induced by increasing the number of conductive filaments within the PDR1A film.

Turning now to investigate the effect of optical irradiation on the resistive switching behaviour of hybrid material RRAM device. In this investigation, sample A was used due to its typical bipolar resistive switching and a significant ON/OFF ratio, as reported in Fig.6.11. Fig. 6.13 illustrates the I-V sweeps of the device which were taken before irradiation (black curve), after 30 min irradiation with circularly polarised light, (red curve), and after forced relaxation using linearly polarised light for 15 min, (blue curve). As a fresh device, the HRS is initially observed when the device is swept from negative to positive applied voltage. The current increases with the applied voltage and then an abrupt switching from the HRS to the LRS was observed at a SET voltage of 0.6 V. The device remains in the LRS state while sweeping the device back from the positive to a negative voltage and then switches back to the HRS state at – 0.6 V, RESET process.

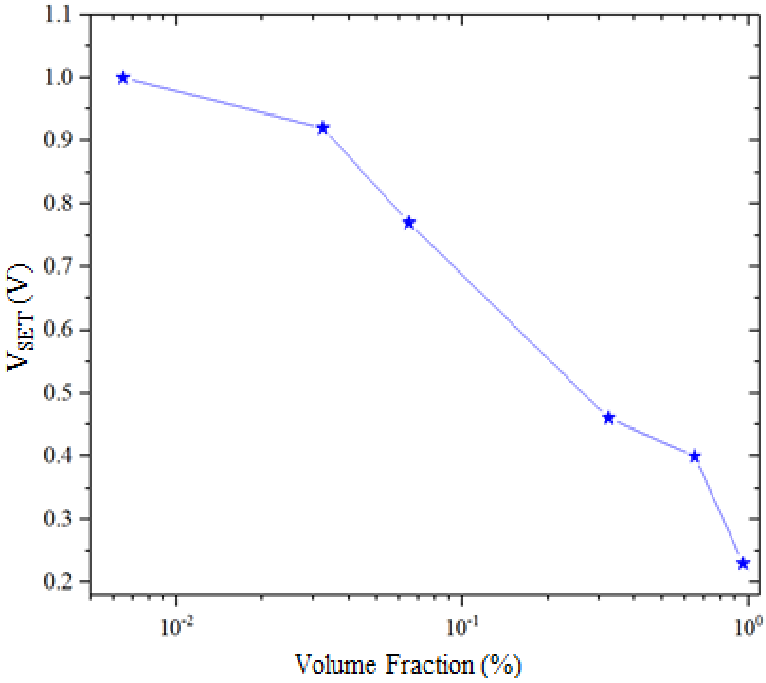

Figure 6.12: V_{SET} versus volume function of Au NPs concentration in an optically active PDR1A polymer.

Interestingly, a 30 min optical exposure of the device to circularly polarised light results in a considerable increase in the resistive switching behaviour. The resistance in the ON state before and after irradiation remains the same in the positive voltage region of the I-V sweep, but increases in the negative region of the I-V sweep. However, the photoexpansion of the PDR1A film thickness causes a large increase in the resistance of the HRS state, increasing the ON/OFF ratio by three orders of magnitude with sudden SET and RESET processes at about 0.7 V and – 0.9 V, respectively.

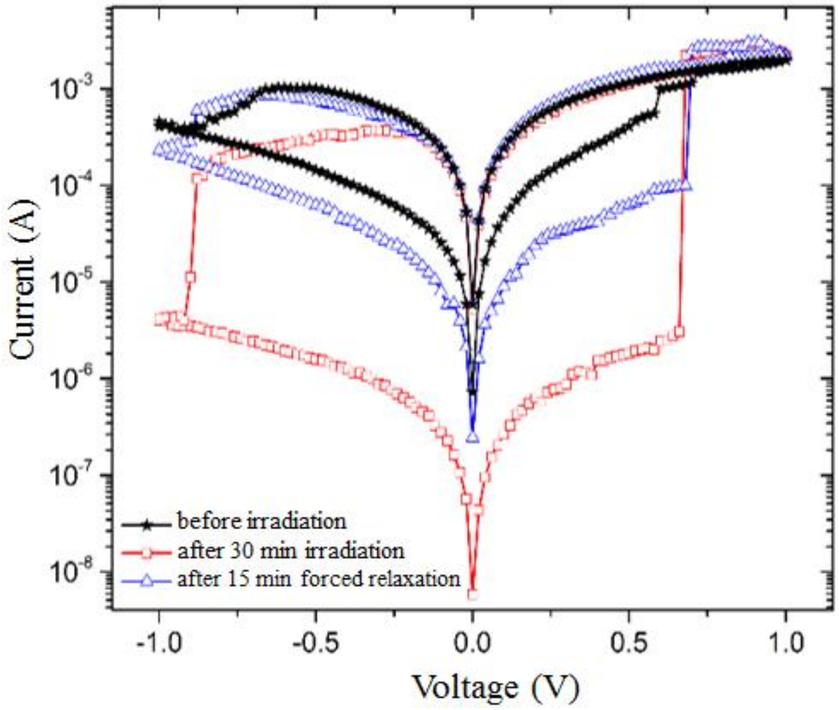

Figure 6.13: The effect of irradiation on the switching behaviour of the Au NP:PDR1A optical memristor device (sample A). Sweeps were taken before irradiation, (black curve), after 30 min irradiation with circularly polarised light, (red curve), after 15 min irradiation with linearly polarised light, (blue curve).

On the other hand, the photocontraction effect in the PDR1A film thickness takes place when the device exposure to the linearly polarised light for 15 min. Consequently, the device shows a full return into its initial ON resistance value but the OFF resistance state remains higher than the initial value.

In order to examine whether the change in device resistance and the increase of the ON/OFF ratio is due to the effect of photoexpansion and photocontraction upon optical irradiation and nothing else, a control device consisting of only a PDR1A layer sandwiched between the ITO bottom electrode and the Al top electrode was tested under the same conditions. Fig. 6.14 shows the effect of optical irradiation on the device conductivity and switching behaviour of a control device (no Au NPs).

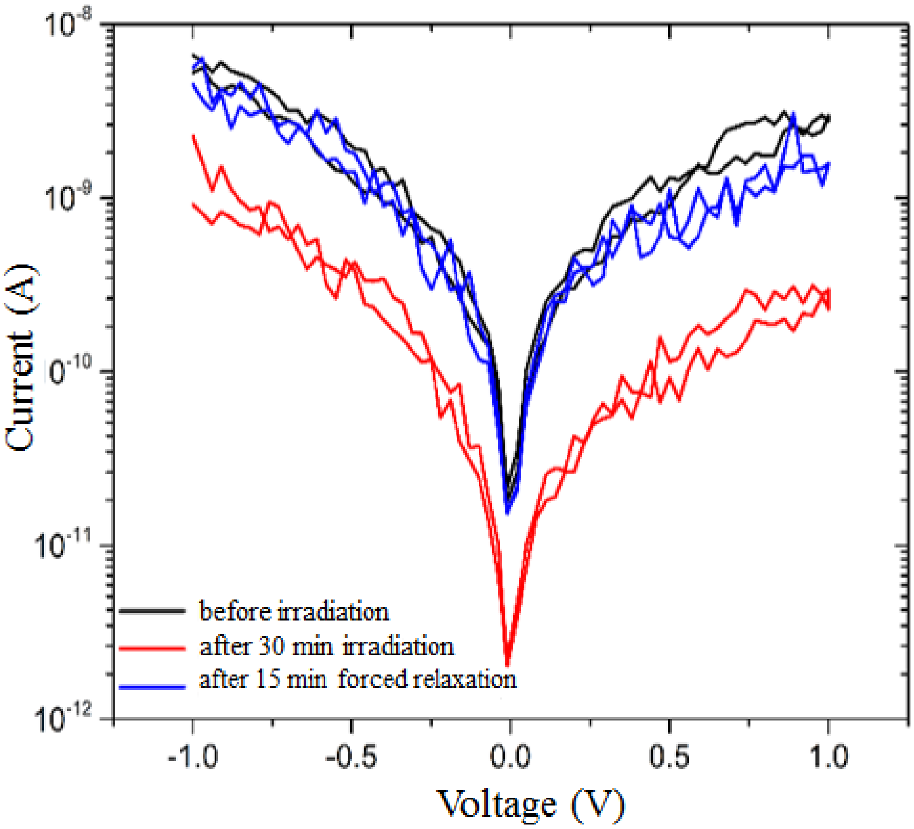

Figure 6.14: I-V characteristics of a control device with an ITO/PDR1A/Al structure presenting the change in the device current as a result of optical irradiation with circularly (red curve) and linearly (blue curve) polarised light.

The figure shows that the device conductivity decreases and then shifts back to its original value as a result of successive irradiation with circularly polarised light for 30 min and linearly polarised light for 15 min, respectively. Nevertheless, there is no change in the switching behaviour before and after irradiation. The results of this figure clearly suggest that the change in the device conductivity is due to the photomechanical effect in the PDR1A which occurs during the optical irradiation.

6.4.3 Conduction Mechanism

In this section, the conduction mechanism of an ITO/Au NP:PDR1A/Al resistive memory device (sample A) is presented. Before explaining the conduction mechanism, it is necessary to elucidate the resistive switching characteristics. The I-V curve of this device, Fig. 6.15 (a), (the same I-V sweep in Fig. 6.11), clearly demonstrates hysteresis loop, a fingerprint of the resistive memory devices. In addition, the device showed a large separation between ON and OFF states of more than two orders of magnitude. Initially, the device was in the OFF state for the applied voltage range between −1 V and 0.7 V. Once the applied voltage reached 0.8 V the current increased suddenly, switching the device from the HRS state to the LRS state, SET process. If the applied voltage is switched off, the device will remain in the LRS state. The device remained in the LRS state until the reversed applied voltage reached to − 0.6 V, the RESET process took place, switching the device back to its initial HRS state.

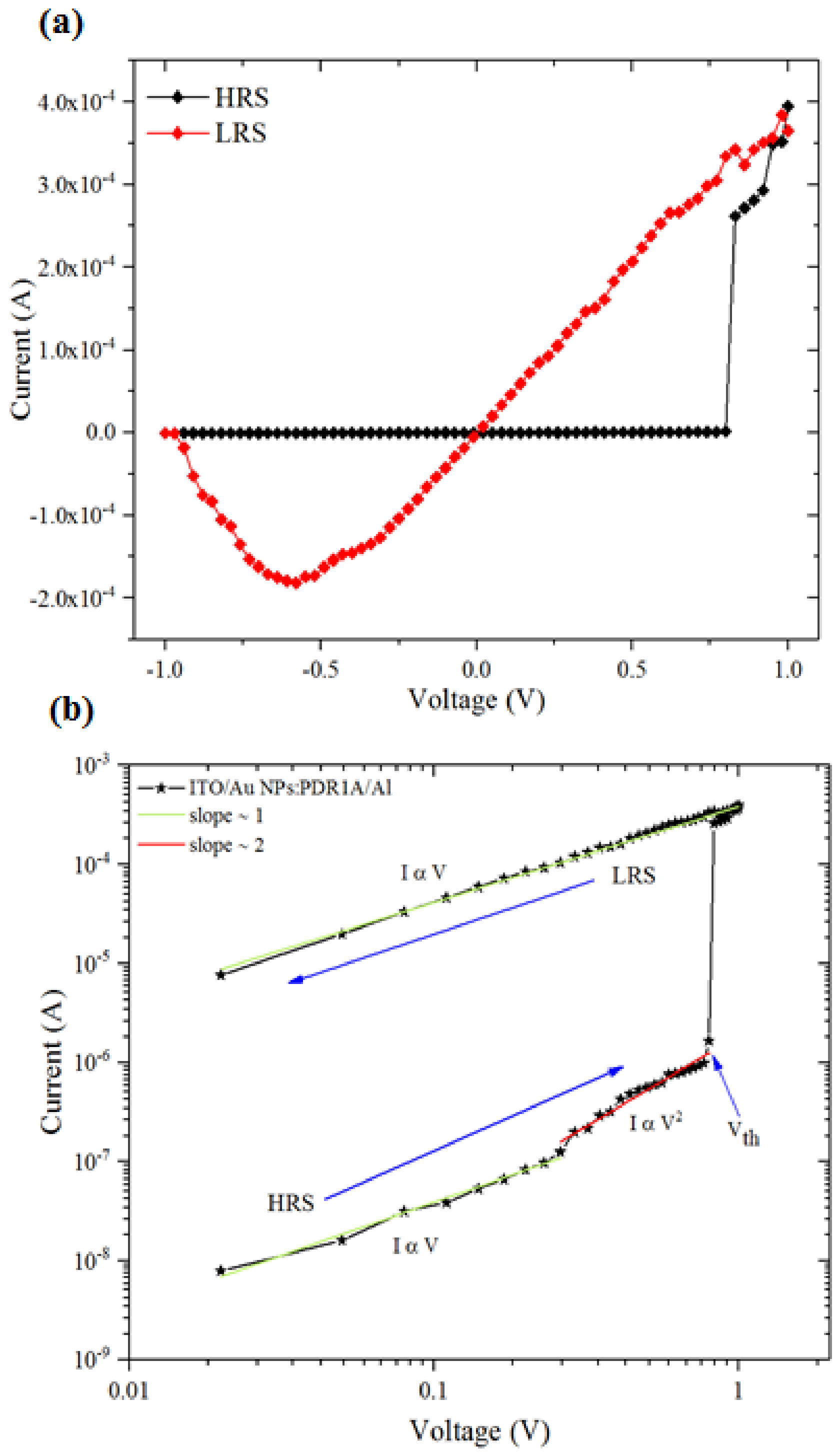

*Figure 6.15: **(a)** A linear plot of the typical I-V curve showing bipolar resistive switching and **(b)** the I-V characteristics plotted in the log-log scale for sample A, with SCLC fits.*

To identify the conduction mechanism of the device the data were fitted by plotting the positive part of the I-V curve on a log-log scale as shown in Fig. 6.15 (b). It seems that the switching mechanism is dominated by the space charge limited current (SCLC) conduction in which three main regions for the fitted I-V curve can be clearly seen.

Previous work has found that Al metal atoms can diffuse into the organic layer during evaporation of the top metal electrodes [9,192–194]. These atoms can act as trapping sites or can form conductive filaments within the organic layer that affect the resistive switching properties. To investigate this possibility in our devices, we investigated devices that contained only the insulating polymer, PDR1A or PMMA. We also investigated whether there were any differences in switching with Au or Al electrodes. We found no resistive switching occurred in devices containing just the polymer, PDR1A or PMMA, which indicates that there is no significant diffusion of atoms from the electrodes into the polymer. In the case of devices with different metal electrodes, Fig. 6.16 shows a comparison between two devices with Al and Au top electrodes. The results show that there is no effect on the resistive switching properties by changing the top electrode. The two curves do show some slightly differences in the set voltages and the shape of the hysteresis loops but this was not systematically observed.

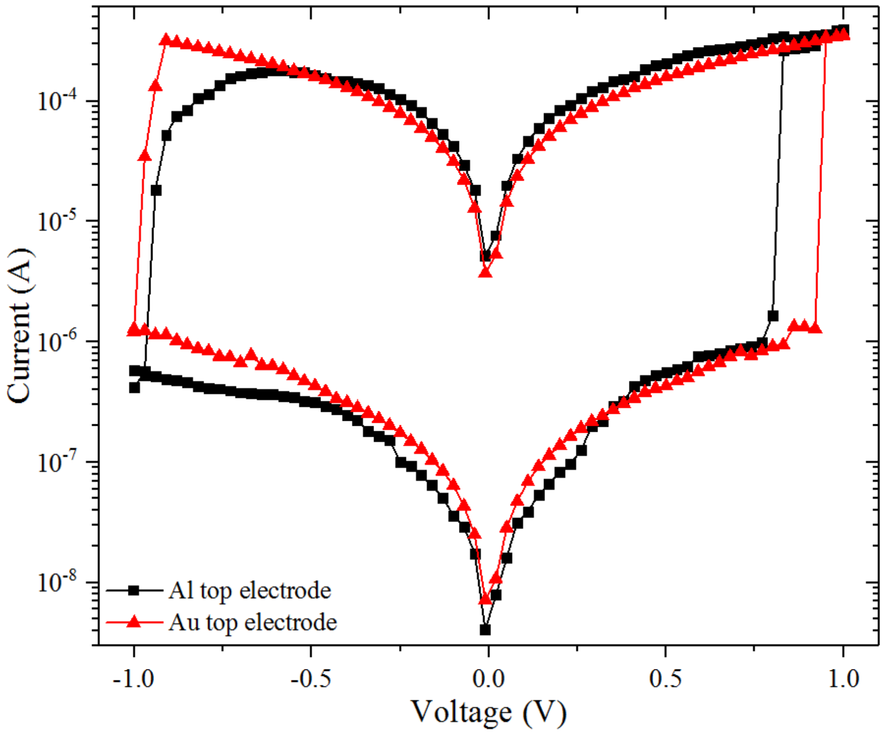

Figure 6.16: I-V characteristics of the optical memristor (sample A), with Al and Au top electrodes for a comparison.

Further, the resistive switching for three device sizes was investigated to identify whether the resistive switching is filamentary dependent or size (interface) dependent. Fig. 6.17 shows the I-V characteristics of the optical resistive switching device (sample A) with three different contact diameters: 100 µm, 200 µm, and 400 µm. The ON current for the 100 µm and 200 µm device sizes is higher than the 400 µm device size, whereas the OFF current for the 200 µm and 400 µm device sizes is lower than the 100 device size. The graph therefore demonstrates no obvious trend in the magnitude of the ON and OFF currents with electrode size, indicating that there is no dependency of the resistive switching on the device size. It is therefore unlikely that the switching in these devices is size dependent because the resistance for both the HRS and LRS states do not decrease with increasing the device size. This suggests that resistive switching in the device is filamentary-based instead of an interface based mechanism. A more complete study down to much smaller electrode areas (1 μm) would be however needed to clarify this result with greater certainty.

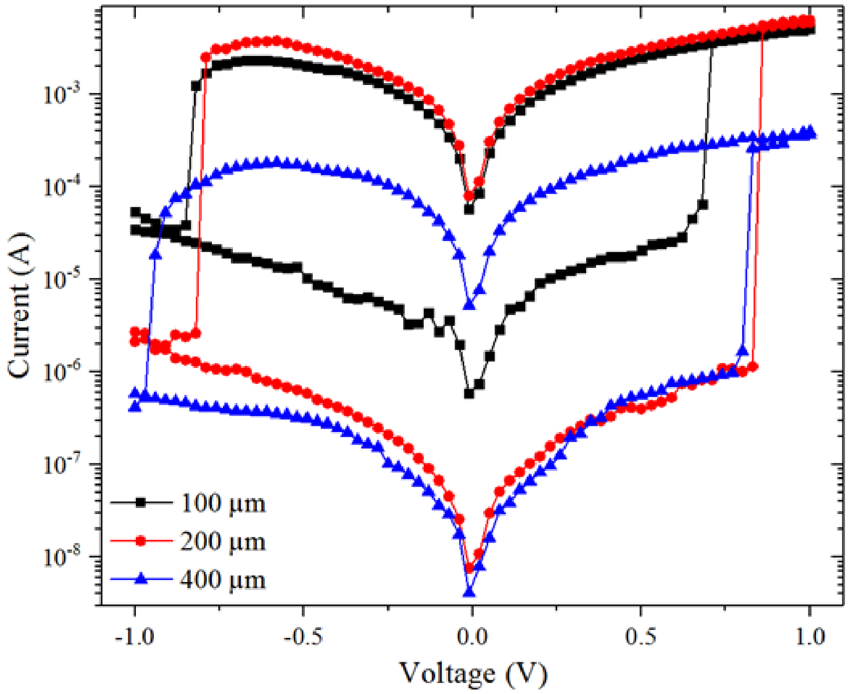

Figure 6.17: I-V characteristics of the optical memristor (sample A), with three different device sizes.

6.4.4 Reversible Optoelectronic Characteristics

The optoelectronic characteristics of an ITO/Au NP: PDR1A/Al resistive memory device (sample A) were carried out to test the reproducibility of the device performance during the repeated optical irradiation cycles. The optoelectronic response represented by the current of the device as a function of time is shown in Fig. 6.18. This investigation was based on successive I-V sweeps (five min between each sweep) during repeated irradiation cycles for 20 min with circularly and linearly polarised light. The device was swept between –1 V and 1 V with a current limit of 10 mA. The current at V = 0.3 V was extracted from these I-V sweeps and plotted to get the points for the LRS (ON state) and the HRS (OFF state) state. No significant change is apparent in the ON state of the device.

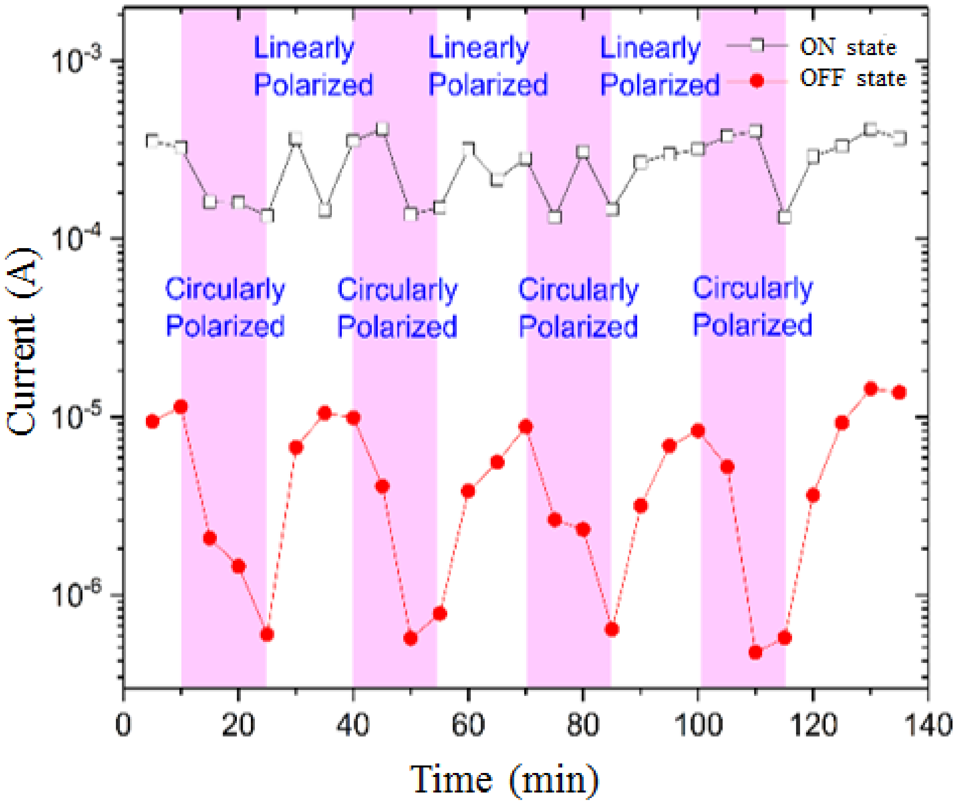

Figure 6.18: Reversible optoelectronic cycles of the memristor device as a function of time, showing the ON and OFF state current during illumination with circularly and linearly polarised light.

However, the OFF state current varies upon optical exposure cycles. The periodicity of the variation matches that of the cycling of the circularly polarised and linearly polarised irradiation. This small change in the ON state can be attributed to the existence of a large number of conductive pathways which drain the charge away. In contrast, the large response of the device in the OFF state may be due to the fact that the number of the conductive pathways is much lower which makes the probability of charge storage by the Au NPs larger. The results clearly show the ability to modulate the electronic properties of the resistive memory device optically with a high degree of reproducibility.

6.5 Neuromorphic Computing Applications

One of the most important potential applications of memristor devices is the simulation of synapses in synaptic networks. Here, the possibility to optically modify the behaviour of a memristor as an artificial synaptic device will be examined. In this study, the memristor device (sample A) with an ITO/Au NP: PDR1A/Al structure was used. Fig.6.19 demonstrates the potentiation and depression induced *via* electrical and optical pulses. Fig. 6.19 (a) shows the incremental increase (potentiation) and decrease (depression) of conductance obtained when the synapse was programmed by a series of voltage pulses of ±1 V with 50 ms pulse width and read voltage of 0.1 V. In Fig. 6.19 (b), the potentiation and depression induced by optical pulses is shown. The data in this figure were obtained by measuring the current continuously at a constant reading voltage of 0.1 V during successive optical pulses. The synapse was programmed by a series of 15

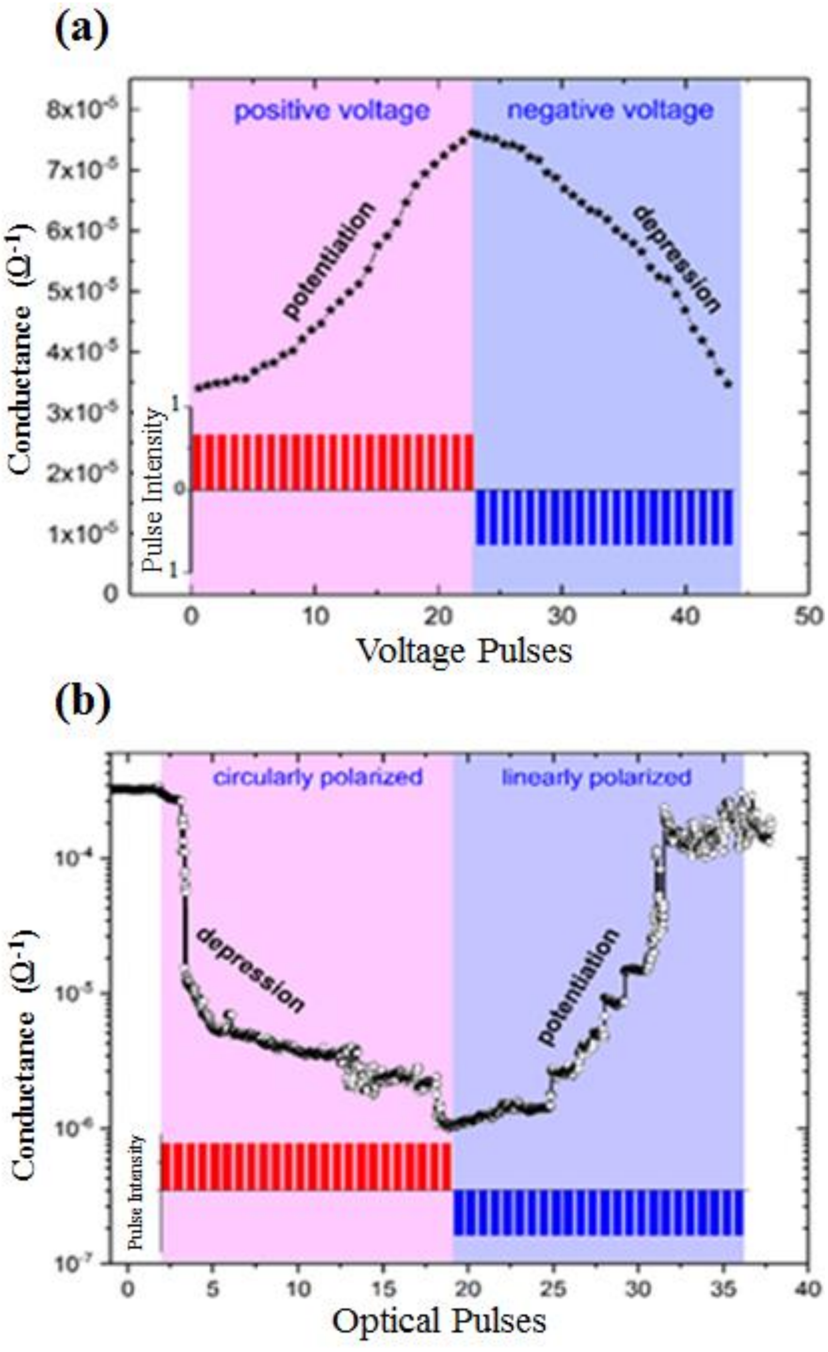

*Figure 6.19: Memristor synapse response to **(a)** electronic pulses of ±1 V with 50 ms pulse width, and **(b)** optical programming pulses with 2 min pulse width, both showing incremental increase (depression) and decrease (potentiation) effects.*

optical pulses (2 min on and 1 min off), (depression), followed by a series of 10 optical pulses (2 min on and 1 min off), (potentiation), using circularly and linearly polarised Ar^{+} laser light, respectively. It is apparent from the graph that the synapse conductance before illumination is almost constant with time. However, the circularly polarised optical pulses cause an expansion of the PDR1A film thickness, as expected from the photoisomerization effect. This effect leads to breakage the conductive pathways and results in a sharp decrease in the device conductance of more than two orders of magnitude. Conversely, the device shows the opposite response when linearly polarised light pulses were applied. It is interesting to note that the device returned back to its original conductance value with some jumps in the conductance during the applied optical pulses. These results suggest a clear correlation between the breaking/re-connection of filamentary pathways and the decrease/increase of device conductance upon irradiation. In addition, these results suggest that the conductance of the memristor synapse can be entirely modulated by the optical stimulus.

Another significant concept of synaptic learning rule is Spike-Timing-Dependent-Plasticity (STDP). STDP relies on the differences in the arrival times of the pre-synaptic and post-synaptic spikes. Potentiation of the synaptic weight occurs when the pre-synaptic spike arrives before the post-synaptic spike. Whilst the depression will take place if the pre-synaptic spike arrives after the post-synaptic spike. The synaptic weight of the memristor″synapsè can be determined by measuring the device conductance change (ΔG/G). Fig.6.20 presents the STDP behaviour of sample A before and after 30 min illumination with circularly polarised light.

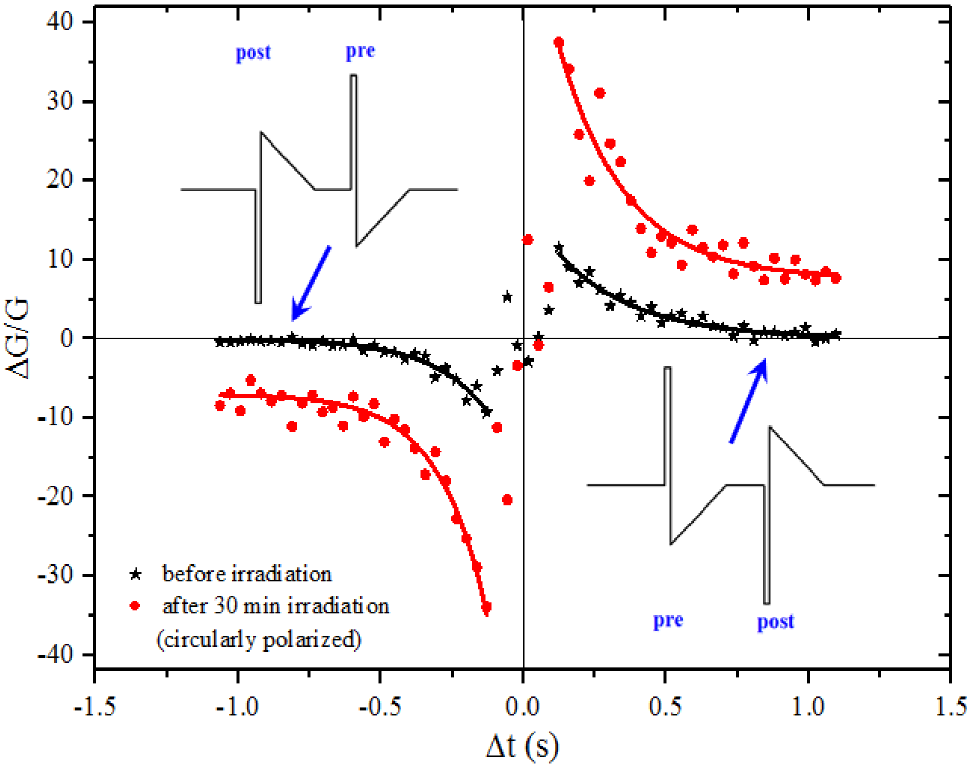

Figure 6.20: Optical modulation of the STDP of the ITO/Au NP:PDR1A/Al memristor synapse, before irradiation, (black curve), and after 30 min irradiation with circularly polarised light, (red curve). The lines are fits to the asymmetric Hebbian STDP learning rule.

The lines are fits to the asymmetric Hebbian STDP learning rule [162,191]

$$\Delta w = \begin{cases} A_+ e^{-|\Delta t|/\tau_+} & if\ \ \Delta t > 0 \\ A_- e^{-|\Delta t|/\tau_-} & if\ \ \Delta t < 0 \end{cases} \tag{6.1}$$

where Δw is the change in the synaptic weight, Δt is the time difference between the pre and post spikes, and $A_{\pm}$, $\tau_{\pm}$ are parameters representing the amplitude of ΔG/G and time constants, respectively.

When the memristor is exposed to the circularly polarised Ar^+ laser for 30 min, a significant change in the synaptic weight (ΔG/G) was observed, as shown by a difference of ~25 between the maximum value of the red and black curves at ΔT = 0.125 s. It is therefore likely that such connection exists between the change in the synaptic weight (ΔG/G) and the variation in the PDR1A film thickness induced by the optical stimulus.

Lastly, the optical control of the retention time of sample A was investigated. Fig. 6.21 shows how optical illumination can be used to control the retention time of the resistive switching memory state, enabling three different types of memory state. A long-term memory (non-volatile) state is shown for the LRS state where the resistance of the device is unchanged over the period of the test. This involves normal operation of the device using electrical means (pulsing) only. The device can be switched between the HRS and LRS state and the operation is non-volatile. A medium-term memory state can made by irradiating the LRS state with circularly polarized light. With this operation, the device is switched to a new resistive state but the storage is not permanent since over time the device resistance reverts back to its original state *via* a thermal relaxation mechanism. A short-term memory state can also be made by first irradiating the LRS state with circularly polarized light, to set the state, followed by irradiation with linearly polarized light. In this case, the initial stored state reverts back to its original state with a much quicker rate (~5 times faster) than *via* the thermal relaxation process. What is interesting from this investigation is the jumps in the resistance of the medium-term and short-term memory which can support the idea of rupture and re-connection of individual conductive pathways as a result of thermal relaxation and forced relaxation of the PDR1A film.

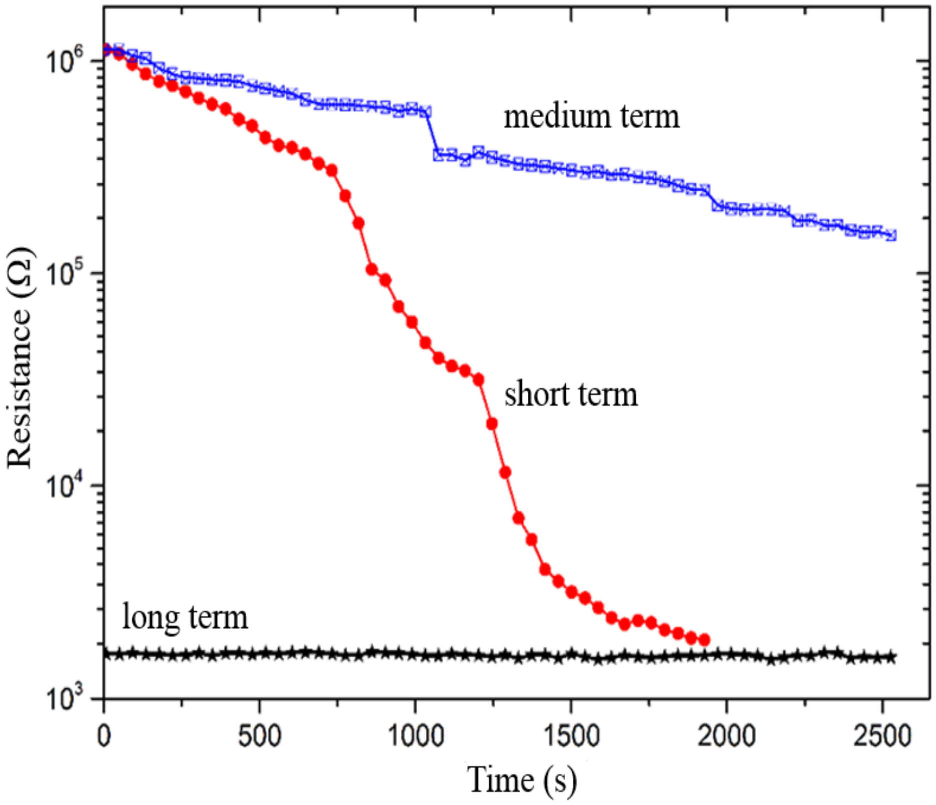

Figure 6.21: Modulation of memory retention time of a resistive memory with an ITO/Au NPs: PDR1A/Al configuration showing the resistance change during optical relaxation (red data), and thermal relaxation (blue data). The device also shows non-volatile behaviour (black data) where the device resistance remains almost constant.

Chapter 7. Discussion

In this chapter, the results reported in the previous two chapters are discussed. The chapter is divided into three main sections. Section 7.1 and 7.2 discuss the results of the ZnO NRs and Au NPs optical memristor devices, respectively. The application of both types of devices in neuromorphic computing systems is discussed in section 7.3.

7.1 ZnO NR Based Devices

7.1.1 Morphology of ZnO NRs and PDR1A

The SEM images, Fig. 5.1, of ZnO NRs which were produced by the microwave-assisted hydrothermal technique, indicate that the structure of ZnO NRs is uniform with a high packing density over all the substrate. The hexagonal structure and vertical alignment of ZnO NRs can be distinguished clearly from the top view and tilted SEM images respectively. In addition, the ZnO NRs possess strong adhesion with the substrate: there is no individual NRs that were separated and grown in different directions on the surface of the substrate. This high quality of ZnO NRs can be attributed to the good quality of the nucleation seed layer. The seed layer and annealing process play an important role in morphology, vertical growth, crystallinity and adhesion of ZnO NRs. It is observed that the seed layer formed by spin coating of the seed solution three successive times with annealing at 350°C after each spin coating produces a high density and vertically aligned ZnO NRs. The effect of no annealing and annealing at different temperatures of the seed layer on the ZnO NRs structure was also investigated (the results are not shown here). The results of this investigation showed that the ZnO NRs grown with no annealing of the seed layer or with annealing at temperatures lower than 150°C produce low packing density and randomly oriented ZnO NRs. These results seem to be consistent with other research, which found that the annealing process at high temperatures (150-350°C) is needed for high-quality structure and alignment of ZnO NRs [181].

Fig. 5.1 (c) indicates that the spin-coating and annealing process used to deposit the PDR1A material on top of the ZnO nanorods causes an infiltration of the polymer material into the gaps between NRs, as shown by the undulation of the PDR1A top surface. Moreover, the PDR1A thin film covers all of the tips of NRs, reducing the possibility of direct-short circuits between the ends of the nanorods and the top metal electrode.

7.1.2 UV-VIS Spectra of ZnO NRs and PDR1A

The optical properties of ZnO NRs and PDR1A films were investigated by UV-Vis spectroscopy, as reported in Figures 5.2 and 5.3. As-prepared ZnO NRs thin films on glass show a wide absorption band covering the visible and ultraviolet regions with an exciton peak centred at 370 nm. The most interesting finding in the UV-Vis spectroscopy investigation was no other peaks are detected in the broad spectrum. This may be explained by the fact that the thin film is ZnO material. This finding is in good agreement with the absorption peak of ZnO NRs which fabricated by other researchers [188,195].

The absorption spectrum of the as-prepared PDR1A thin film deposited on a glass substrate is shown in Fig. 5.3. Azobenzene molecules show a range of electronic absorption spectra from the ultraviolet region to the red visible region. This broad absorption spectrum can be limited to a specific spectrum region by ring substitutions, such as amino and nitro groups [177]. It is worth mentioning that PDR1A is a type of pseudo-stilbene azobenzene molecule which has an electron donor and acceptor substitutions (amino and nitro groups) at the 4 and 4´ positions. The UV-Vis spectroscopy results show that the absorption spectrum of PDR1A thin film has a wide band at 460 nm. The observed absorption peak could be attributed to the amino and nitro substitutions which have a significant influence on the energy of $\pi\rightarrow\pi^*$ and $n\rightarrow\pi^*$ transitions. As reported by others [196,197], introducing electron-donating/electron-withdrawing or push/pull substitutions at the 4 and 4´ positions resulted in long wavelength absorption spectra with overlapping of the $\pi\rightarrow\pi^*$ and $n\rightarrow\pi^*$ transitions. It is found that the two energy transitions occurred in the UV-Vis region, due to the excitation of a delocalized π-electron of the N-N double bond and the excitation of an electron localized on one of the nitrogen atoms, respectively [198]. In the case of unsubstituted azobenzene molecules, the $\pi\rightarrow\pi^*$ transition in the UV region dominates at ambient conditions for the *trans* isomer whereas the $n\rightarrow\pi^*$ transition shows low intensity for the *cis* isomer. However, the absorption spectra can be tuned between UV and visible (green) regions by substituting the azobenzene molecules with electron-donating and/or accepting units. For PDR1A, the push/pull units of pseudo stilbenes allows asymmetric electron distribution, overlapping the two $\pi \rightarrow \pi^*$ and $n \rightarrow \pi^*$ band transitions, and as a result shifts the absorption spectra from the UV region to the long wavelength visible region.

7.1.3 Expansion and Contraction of PDR1A Films

Expansion and contraction of azobenzene polymers upon irradiation with different polarities of incident light and exposure time have been previously reported [179]. For example, the film thickness of PDR1A polymer was observed to increase by 17% with exposure to 488 nm wavelength light [179]. This photoexpansion is attributed to an accumulation of the PDR1A chromophores with an out of plane alignment. Upon irradiation with wavelength and polarization specific light the PDR1A molecules undergo a *trans–cis* photochemical isomerization. However, due to the overlap of the two absorption bands for the *trans–cis* and *cis–trans* transitions, *trans–cis–trans* cycling occurs, which means the molecule switches from one state to another and then back to the original state. This repetitive cycling is expected to play a central role in the process of aligning chromophores. Circularly polarised light prevents the orientation of the chromophores perpendicular to the direction of the beam (since all orientated azobenzene groups are activated) but tends to align the chromophores in the direction of the beam (since they become inert to the light). In the case of linearly polarised light, the chromophores tend to align in the direction perpendicular to the polarization of the beam as only those molecules that have a dipolar component along the laser polarization will be photoisomerized. In the former case, as the laser beam is perpendicular to the thin film, the chromophores tend to become oriented in the out-of-plane direction, causing an expansion of the thin film, whilst in the latter case, the orientation of the chromophores in-plane causes a reduction in film thickness.

In this work, the film thickness of PDR1A was similarly shown to be modifiable by light. In typical experiments, Fig 5.5, it was found the thin-film thickness increases by 30% upon exposure to circularly polarised light. After 30 min irradiation, the PDR1A film thickness remains unchanged, which indicates that the vast majority of the chromophores that are able to rotate have rotated.

PDR1A thin films in their expanded state could also be contracted close to their original state by either turning off the laser light or by exposing the polymer to linearly polarised light, as shown in Fig. 5.6. Interestingly, the forced relaxation is faster than thermal relaxation by a factor of 8. This has important application in artificial neural networks since the effect can be used to provide long-term and short-term memory behaviour. The contraction effect can be explained by the conversion of *cis-rich* isomers into the *trans* isomers, which rearranges the azobenzene chromophores into their original states.

7.1.4 Electrical Measurements and Optical Modulation

7.1.4.1 Current-Voltage Characteristics

In this study, we investigated the effect of the photoisomerization process in PDR1A films on the electronic properties of ITO/ZnO NR/PDR1A/Al memristor devices. This investigation reveals that the electronic properties of memristor devices are variable and tunable by irradiation with a specific wavelength and polarisation. The sections below discuss the electronic properties of memristors and how they can be modified *via* optical irradiation.

To begin with, as reported in Fig. 5.5, the PDR1A thin film exhibits an increase in its thickness upon irradiation with circularly polarised light at $\lambda = 514$ nm. As a result, the resistance of optical memristor device increases, as shown in Fig. 5.7. The resistance in both states (HRS and LRS) increases and the current shifts down from $2x10^{-3}$ A before irradiation to $6.2x10^{-4}$ A after 20 min irradiation Fig. 5.7 (a), and from $1x10^{-3}$ before irradiation to $1.8x10^{-4}$ A after 20 min irradiation, Fig. 5.7 (b). It should also be noted that the R_{OFF}/R_{ON} ratio increases after irradiation from approximately 4 to 7. These results are likely to be related to the additional resistance caused by photoexpansion of PDR1A film. Nevertheless, due to the reversible behaviour of the isomerization process, the PDR1A thin film can revert back into its original thickness either by thermal or forced relaxation under irradiation. Indeed, the results of Fig. 5.7 (a and b) show that the devices switch back to initial resistances when the devices are left to relax thermally for 2 h at room temperature or by forced relaxation under irradiation with linearly polarised light for 15 min. The results indicate the expansion or contraction of the polymer by irradiation with light shifts the entire hysteresis loop to either lower or higher current, respectively, without significant changes in either the shape of the curve or the threshold switching voltage. This suggests that the expansion/contraction process of PDR1A film affects only the conduction between the ZnO nanorods and the top metal electrode, and that the change in path length is the predominant reason why the conductance shifts to higher or lower values.

In order to investigate the effect of optical irradiation on the charge carriers localised in defect states of ZnO NR thin films, the I-V characteristics were measured in dark and during irradiation with circularly polarised light. In this investigation, a control device consisting of the ITO/ZnO NRs/Al structure was used. It was found that a small increase in photocurrent occurs in ZnO upon irradiation because of the photoexcitation of charge carriers localised in defect states [199]. However, the observed photoresponse in our device is small. Further, the current increased upon irradiation whereas it decreased for the devices comprising ZnO NRs and PDR1A. The measured change was less than 5%, in contrast with the change of about 1 order of magnitude current decreasing observed in the devices with a ITO/ZnO NR/PDR1A/Al structure. Therefore, this study indicates that the photoexcitation of trapped charge carriers in ZnO NRs film has no considerable effect in these device measurements.

7.1.4.2 Role of the PDR1A Film in the Electrical Switching Properties

We turn now to the role of the insulating PDR1A film in the resistive switching of the memristor devices. As reported in Fig. 5.8, the device consisting of just the ZnO NR film (i.e. no polymer layer) sandwiched between the ITO and Al electrodes shows bistable switching and high conductivity, which is not desirable for memory applications that operate at low power. Replacement of the ZnO NRs films with just a thin film of PDR1A instead produced very low conductivity and negligible hysteresis between the HRS and LRS. However, the hybrid memristor device containing both the ZnO NR and PDR1A materials shows clear bipolar switching behaviour with relatively small power use. The addition of a PDR1A film deposited between the ZnO NRs and Al increases the resistance of both the ON and OFF states and also increasing the R_{OFF}/R_{ON} ratio. It is difficult to explain this enhancement in the R_{ON}/R_{OFF} ratio, but it might be explained by introducing a large number of charge trapping centres in the PDR1A film which enhance the resistance contrast [45]. The enhancement of resistance contrast could also be attributed to the generation of local internal electric fields in the PDR1A film [41]. Increasing the PDR1A film thickness upon illumination may increase the possibility of capturing the injected carriers by traps in PDR1A film as well as the ZnO film which leads to a high electric field in the PDR1A film. As a result, conductive filaments of fully occupied traps can be formed in the PDR1A, and that could increase the resistance contrast. Additionally, the deposition of PDR1A film can also inhibit the short circuits between the ITO and Al electrodes that can be formed through the penetrating of Al material between the gaps in the ZnO NRs film during the evaporation process of Al top electrodes.

Some studies have shown that interdiffusion of metal atoms into the organic layer either during the deposition of the top metal electrode or upon application of a potential can modulate the switching directly (e.g. filament formation) or affect the resistive switching properties [9,192–194]. They found the interdiffusion of gold atoms to the organic layer generally occurs at low deposition rate of 0.35 Å/min and substrate temperature of 70 °C [200]. Studies of this nature were not conducted in this thesis, but we found no evidence of this in our work since devices with only a PMMA or PDR1A layer exhibited no switching, in contrast to others who observed a diffusion of Al atoms [193] and Ag atoms [201] into the organic layers. They found that the resistive switching properties, e.g. the forming step and the resistivity of HRS are dependent on the presence and nature of these metal atoms. In the case of our devices, we found no difference in switching properties when either Au or Al electrodes were used.

7.1.4.3 Conduction Mechanism

Generally, bipolar resistive switching has been reported in memristor devices based on ZnO thin films and nanowires [19,72]. Resistance switching in these systems is explained by the formation and rupture of conductive filament bridges formed through redox reactions and the movement of oxygen vacancies. Bipolar resistive switching has also been observed in memristor devices consisting of organic-inorganic composites, such as ZnO nanorods embedded within PMMA [55], and ZnO nanoparticles mixed with PMMA [202]. Switching in the ZnO NP:PMMA matrix-based devices has been attributed to a charging effect involving the enhancement/reduction of an internal electrical field. However, the observed resistive switching in the ZnO NR/PMMA based resistive memory devices was explained by the migration of oxygen vacancies and/or zinc interstitials along the surface of the nanorods, since the mobility of defects is generally expected to be much higher at surface and grain boundaries than in the bulk [203]. In the case of ZnO NP:PMMA hybrid devices, an abrupt switching from SET to RESET and *vice versa* with a high ON/OFF ratio was observed. In contrast, a complex transition from HRS to LRS was demonstrated in the case of ZnO NR/PMMA-based hybrid devices. Similarly, our hybrid memristor devices containing ZnO NR/PDR1A also show a complex transition between ON and OFF states and switch at low bias as demonstrated in Fig. 5.9 (a). In addition, no forming step is needed to initiate switching. This could be attributed to the large abundance of pre-existing oxygen vacancies in the ZnO [204].

To identify the conduction mechanisms of the ITO/ZnO NR/PDR1A/Al devices, the I-V curve in Fig. 5.9 (a) was replotted in the log I versus log V scale (Fig. 5.9 (b)). The log-log curve fitting shows five distinct regions, which describe the conduction mechanisms in the HRS and LRS. In the case of the HRS, the charge transport follows Ohmic conduction in the voltage region from 0 to $V \leq 0.3$. This region shows linear behaviour, and a small current passes through the device, with a dependence on V of $I \propto V^{\alpha}$,with $\alpha \approx 1.1$. Conduction in this region is dominated by free charge carriers which are thermally generated. The voltage regions following this, however, exhibit nonlinear conduction at higher voltages. Charge transport in device in the region of $0.3 \leq V \leq 1.0$ can be described by trap-controlled space charge limited conduction (TC-SLCLC) with a gradual increase in current, and this is referred as a Mott-Gurney region, $I \propto V^2$. This is because the increase of applied potential increases the density of free charge carriers injected over the metal/ZnO Schottky barrier. This region can be described by the Mott-Gurney law [139], as given by:

$$J = \frac{9\varepsilon\mu V^2}{8d^3} \tag{7.1}$$

where J is the current density, ε is the dielectric constant, μ is the free carrier mobility, V is the applied voltage, and d is the insulator/metal oxide layer (thin film) thickness.

In the region of $1.0 \leq V \leq 2.0$, trap filling commences and there is a shift to a much steeper rate of current increase having $I \propto V^{\alpha}$, where $\alpha \approx 4.1$. This could represent the filling of trap states with energy below the LUMO level and the transition point at ≈ 2.0 V would indicate that all traps are filled with transport changing to a new regime, having $I \propto V^2$ over the region of $2.0 \leq V \leq 3.0$. Conduction in this region can be ascribed to trap-filled space charge limited conduction (TF-SCLC). However, in the case of the LRS, the conduction mechanism is completely dominated by Ohmic conduction for the return voltage region from 3 V to 0 V. This region shows linear behaviour with $I \propto V^{\alpha}$, $\alpha \approx 1.2$. No change in slope is seen over all the positive voltage regime, which means that the trapped charges have long lifetime and need a high negative voltage to be removed from their trap states. This Ohmic behaviour in the LRS is widely expected to be related to the conductive pathways formed by oxygen vacancies in the ZnO NR film [205]. This complex switch between ON and OFF states has been reported in several resistive switching devices based on hybrid and non-hybrid ZnO materials [51,55,206].

Although the SCLC charge injection/trapping model fits well the I-V curves some questions remain on the validity of this model to describe this system. Firstly, a relatively large barrier is expected for electron injection from the electrodes into the LUMO levels of PDR1A. The energy gap between the HOMO and LUMO levels of PDR1A [207] is expected to be ~3.7eV and in the case of our previous study based on PMMA, ~5.6 eV. However, recently it has been shown [208] that ZnO can act as a buffer layer between an insulator and metal electrode by forming an ohmic contact that permits electron injection into the conduction band of an insulator. In this study, based on a high quality, thermally grown SiO_2 as an insulator, SCLC behaviour was observed when negative voltages were applied to the metal cathode, but for positive voltages, rectification was observed. In contrast, our devices behave symmetrically with application of either positive or negative applied voltages. The difference in the anode materials used in the two studies is unlikely to account for the absence of the rectification, since the ITO work function, ϕ ~ 4.7 eV, is not too different to that of the heavily doped Si substrate, ϕ ~ 5.1 eV, used in the buffer layer study.

A mitigating effect might be the very high electric field across the PMMA layer, which could provide electron transport across PMMA layer. From the SEM image shown in Fig. 5.1 (c) the shortest distance between the Al electrode and the ends of the ZnO nanorods is likely to be only ~20 nm and a 2 V potential difference would equate to an electric field of 10^6 V/cm. In this regime, Fowler-Nordheim tunnelling could play a role [209]. However, at such high electric fields, other effects emerge that can provide charge transport through the dielectric. In particular, contact at the metal-polymer interface induces the formation of oxidized and reduced states that act like localized acceptor and donor states, enabling charge injection and transport *via* resonant tunnelling across the polymer layer in both moderate and high field regimes [210].

Lastly, we note that the presence of water molecules in the hybrid device may also be involved in the electronic conduction and memristor switching. There is an increasing awareness of the role that water plays in the memristor switching properties of metal oxide based devices [211,212], and PDR1A and PMMA are likely to contain significant amounts of water as both are hygroscopic materials due to the presence of polar carboxylic groups. Water also affects the surface states of zinc oxide, which dissociates upon chemisorption and act as electron donors [213]. Furthermore, the high electric fields present in the hybrid device could be sufficient enough to dissociate water, which as shown by Onsager [214] occurs at fields greater than at ~7x10^5 V/cm. Thus a possible switching mechanism could be the migration of OH^- from the ZnO surface into the polymer under the application of an applied field, thereby switching the device from a high resistance to a low resistance state. The high electric field and dissociation of water in the polymer could further contribute to the source of OH^- ions and migration effect. Upon reversal of the field direction, these would be driven in the opposite direction, switching the device back into the high resistance state. Whether this dominates other mechanisms or is sufficiently fast enough remains to be determined.

7.1.4.4 Data Retention

Data retention time is one of the key performance indicators used in memory technology. The term “data retention” is used to refer to the capability of memristor device to maintain its resistance states (ON and OFF states) over a period of time. For nonvolatile storage applications, the target time of data retention should be at least 10 years [215]. The data retention test in our memristor devices, see Fig. 5.11, demonstrates a good stability and the ON/OFF ratio of 3 remains almost constant with little degradation in the HRS over the period of the test (5 h). The results clearly indicate that the device can retain the stored information for a long period of time, even with instability and vibrations in the lab during the experiment. These results confirm the nonvolatile property of our devices, which is in a good agreement with other memristor devices based on ZnO NRs [45,50]. To date, several treatment methods have been used to improve the resistive switching properties, such as data retention time, endurance, and ON/OFF ratio for ZnO based devices. For instance, ZnO films doped with Mn impurities have retention times $>10^7$ s [19], with Ti impurities have retention times $>10^5$ s [216], and using multilayer structure to sandwich the ZnO films, e,g, ITO/ZnO/Ti/ZnO/Al, retention times $>10^6$ s [217]. Although our devices show a good retention time without any treatment, further work is needed to improve and establish the data retention time, for example, investigating the temperature effect on the device performance which may increase during the operation of memory cell.

7.1.4.5 Reversible Optoelectronic Cycles

With respect to repeatable performance, the ITO/ZnO NR/PDR1A/Al resistive switching device exhibits a reversible optoelectronic response for optical irradiation with time. As reported in Fig. 5.12, both the HRS and the LRS show an increasing and decreasing in resistance magnitude during irradiation with repeated cycles of circularly and linearly polarised light, respectively. The single most notable observation to emerge from the results is the repeatable switching forth and back for the two resistance states of memristor device. The observed increasing and decreasing of the device resistances upon irradiation could be attributed to the reversible expansion and contraction effect in the PDR1A film thickness. These kind of measurements are more likely the same of the write (code 1) and erase (code 0) cycles measurements that can be tested for a memristor to evaluate the device performance. The write/erase cycles, in general, can be achieved by applying a sequence of electrical positive and negative pulses with a fast programming speed, e.g. 5 ns [19]. In the same manner, light pulses could be used to stimulate the memristor state between ON and OFF states (write/erase). It is evident from these results that the switching process in the hybrid material of ZnO NR and PDR1A-based devices is repeatable from cycle to cycle. Also, these results suggest a new level of functionality that provides a promising candidate of optical RRAM devices in which their electronic properties can be controlled by optical means. Nevertheless, more work needs to be done to improve the programming speed of our devices from minutes scale to milliseconds or micro/ nanoseconds scale.

7.2 Au NPs Based Devices

7.2.1 Morphology and Chemical Composition of Au NP:PDR1A Nanocomposite

The TEM study, Figs. 6.2 and 6.3, provides two significant findings. The first one is that most of the Au NPs form clusters at the polymer/air interface rather than a uniform dispersion in the polymer in which only a few nanoparticles are dispersed in the polymer matrix, Fig. 6.2. The Au NPs clusters likely to form an intermediate layer between the PDR1A and the top Al layer. It is worth to note that the top aluminium layer was deposited after the annealing process. This finding may be explained by the fact that the clusters were formed by migration of the nanoparticles which are initially suspended in the polymer to the polymer/air interface induced by the thermal annealing process of the composite film at 90°C for 8 h. Migration of the nanoparticles to the polymer/air interface during thermal annealing has been studied intensively in the literature and is due to competitive thermodynamic based entropic processes [218]. Presence of the nanoparticles within the composite system induces the entropic penalty on the PDR1A chains. Since the individual PDR1A chains extend and stretch around the gold nanoparticles to achieve a regular dispersion, an entropic gain arises to expel the nanoparticles to the free surface (polymer/air interface). This process pushes the nanoparticles out of the composite system and results in a forming of clusters at the polymer/air interface even the nanoparticles are initially suspension and soluble in the hybrid system. The second important finding to emerge from the TEM study, Fig. 6.3, is that some of these nanoparticle clusters are extended across the PDR1A matrix to form a partially connected conductive pathways between the top and bottom Al layers. Since the TEM result shows an image of a nanoscale region, some of these pathways could fully connect the top and bottom Al layers within the 400 µm diameter device size. These conductive pathways may play a key role for the charge transport through tunnelling and also the change in the conductivity between the ON and OFF states upon irradiation. The role of these filamentary pathways in the resistive switching will be explained in detail in the electrical discussion section.

As part of the TEM studies, energy dispersive X-ray spectrum (EDX) analysis was used to identify the objects in the TEM images, reported in Fig. 6.4. The EDX results prove the presence of the Au NPs for the selected areas in the TEM image. The appearance of the Au peak at the polymer/aluminium interface region higher than the middle region indicates that a considerable amount of Au NPs is clustered at the polymer/air interface. The presence of Al peaks in both regions came from the evaporation process of the top and bottom Al layers. However, the Al signal from the middle region is lower than the interface region, and that can be attributed to the fact that some of Al atoms are diffused into the PDR1A film during thermal evaporation process or moved from the Al layers during slicing the TEM samples. The EDX also showed signals of Cl, Zn, and Ca which are more likely came from a contaminated diamond knife used for slicing the samples.

7.2.2 Electrical Characterization and Optical Modulation

Generally, the properties of insulating materials, for example, the electrical conductivity can be tuned by embedding metallic nanoparticles in a matrix host. These properties are extremely dependent on the size, shape, distribution, and loading content of embedded nanoparticles. Here, the created system shows not only a resistive switching behaviour but also offers a new generation of switching memory devices that their electronic properties can be controlled by optical stimuli. The most important finding to emerge from the analysis is that the electrical properties of the created nanocomposite system exhibited a strong dependence on the connection and rupture of filamentary paths of the Au NPs in the PDR1A polymer, and that resulted in a sharp transition in the material conductivity. Breaking and re-connection of the conducting paths occur when the PDR1A film expands and contracts upon illumination with circularly and linearly polarised light, respectively.

7.2.2.1 Conductivity Measurements

The electrical conductivity of the hybrid system as a function of gold volume fraction (%) is reported in Fig. 6.7. The devices fabricated at low concentration of Au NPs showed a gradual increase in the conductivity with increasing the Au NPs loading, but it is still low value (region I in Fig. 6.7). The observed low conductivity of this region is likely related to the large separation between the individual Au NPs within the polymer matrix which makes the charge carrier relatively immobile. The probability of these NPs to form an inter-connected conductive pathways is very low because of the effective obstacle of the surrounding insulating nature of PDR1A polymer. According to this, the conduction mechanism is dominated by thermally activated charge carriers in these devices [219]. Increasing the Au NPs concentration and specifically at the R_v*, the conductivity increases rapidly with more than three orders of magnitude as shown by region II in Fig. 6.7. This large increase in the conductivity can be attributed to the extended clusters and/or creation of metallic bridges between the two metal electrodes as observed by the TEM images. In this case, the electrical conduction mechanism could be dominated by metallic or tunnelling conduction or both depending on whether the formed conductive bridges are fully or partially interconnected. Further increase in the Au NPs concentration increases the conductivity but with a small gradient as shown in Fig. 6.7, region III. This means that the number of extended clusters or conductive bridges is increased within the polymer matrix. In this case, continuous conductive bridges form, and accordingly the metallic conduction transport dominates instead of tunnelling. These results confirm that there is an intrinsic correlation between the morphology of the film and electrical conductivity.

Modulating the conductivity of sample A by optical means is demonstrated in Figs. 6.8-6.10. The device with only few filamentary pathways within the polymer matrix makes it very sensitive to any slight disruption. Indeed, we see that the device switched from its high conductivity state (~10^{-6} S/cm) to low conductivity state (~10^{-9} S/cm) with a change of three orders of magnitude after 30 min irradiation with circularly polarised light. This is because the photoexpansion of the PDR1A film, which causes a breakage of the conductive paths and switches the device to the HRS state. On the other hand, due to the photocontraction of PDR1A film induced by 15 min irradiation with linearly polarised light, the device switched back to its original conductivity state. It seems possible that the reversible switch in the device conductivity is due to the re-connection of the conductive pathways upon illumination. Interestingly, the device showed a repeatable switching response between the low and high conductivity states as shown in Fig. 6.9. It should be important to note that the device with no Au NPs does not show this significant change (only a factor of ~4) between the two conductivity states upon irradiation with the same above irradiation conditions. This effect is also confirmed by the conductivity transient measurements which demonstrated in Fig. 6.10, where the conductivity switched to the OFF/ON state with a change of four orders of magnitude during the optical illumination with circularly/linearly polarised light. It is notable that rapid jumps in the conductivity values occurred which is in a good agreement with the idea of the re-connection and rupture of individual conductive pathways.

Optically SET/RESET with electronically read is similar to the write/erase cycles that use positive and negative electrical pulses to switch the device between two resistance states. Despite these promising results, as mentioned before, further work is needed to improve the speed switching due to the low SET/RESET speeds in these devices that take 15/30 min, in contrast to the previous electrically fast switching speeds reported in [19] with a nanosecond time scale (5 ns) SET/RESET processes in ZnO films based-devices.

7.2.2.2 Current-Voltage Characteristics

The loading content of nanoparticles and morphology play a vital role in the resistive switching properties of resistive memory devices [119,220]. Additionally, it is found that embedding a sufficient content of NPs can not only modify the electrical properties of the insulating material but also improve the charge storage/memory effect of the hybrid systems [116,221], in which the embedded NPs can act as trapping centres for charge carriers within the forbidden band gap of an insulator. Our experimental results indicate that the electrical switching behaviour of PDR1A devices with Au NPs is strongly dependent on the concentration of the Au NPs within the PDR1A film. The obtained results reveal that there is no resistive switching for the devices fabricated neither at low nor high concentration of Au NPs, as depicted previously in Fig. 6.11. The lack of switching and high resistivity in the case of low concentration Au nanoparticle devices are more likely related to the low content of Au NPs which are insufficient to support the charge storage and transport as well as the insulating nature of PDR1A polymer. In the case of high concentration, the high conductivity could be attributed to the increasing number of the conductive paths which resulted in easily drain the charges away from the bulk hybrid system to the metal electrodes. As a result, this reduces the lifetime of stored charges and the ON/OFF ratio. However, the devices fabricated at concentrations in between these two extreme values exhibit a good ON/OFF ratio, and in particular the sample A. The SET voltages of these devices decreases with increasing the concentration, and that might be also related to the increasing number of the conductive paths within the hybrid system.

We move on now to determine the effect of optical illumination on the resistive switching properties. The typical bipolar switching (sample A) was demonstrated formerly in Fig. 6.13. A 30 min illumination expands the PDR1A film and modifies the ON/OFF ratio from less than 1 order of magnitude before irradiation to 3 orders of magnitude after irradiation by increasing the resistance of the HRS state. The enhancement of ON/OFF ratio can be attributed to the rupture of conductive pathways and increase the separation between Au NPs upon irradiation, which increase the HRS state and the possibility of trapping for long lifetime instead of easily dissipated the charge carrier away to the electrodes *via* conducting pathways. Due to the 15 min forced relaxation of PDR1A film, the device reverted back to its initial ON and OFF states. The device does not show a full contraction in which the

ON/OFF ratio after forced relaxation is larger than before irradiation. This could be related to the residual of free volume in the PDR1A film that can occur during the repeated *trans-cis-trans* isomerization cycles [222,223]. The LRS, however, whether before or after irradiation does not show a significant change upon irradiation. This is also observed when the device exposed to the successive circularly/linearly polarised light cycles as shown in Fig. 6.18. Although the response of the device in the LRS state is not as good as in the HRS state, the device, therefore, shows a repeatable response with optical illumination cycles.

7.2.2.3 Conduction Mechanism

The current conduction mechanism corresponding to the electrical bistability in our system (sample A) is attributed to the SCLC. The log I-log V curve fitting (Fig. 6.15 (b)) shows three distinct regions, which explain the conduction mechanism in the HRS and the LRS. In the case of the HRS, the charge transport follows Ohmic conduction in the applied voltage region from 0 to $V \leq 0.5$. This region exhibits linear behaviour, and a small current passes through the device, with a dependence on V of $I \propto V$ with a slope of ~1. This indicates that the Ohmic behaviour is dominated and the charge transport results from the thermally generated carriers. Charge transport in device in the applied voltage region of $0.5 \leq V \leq 0.7$ can be described by the trap-controlled space charge limited current (TC-SCLC), and this is called as a Mott-Gurney law. In this region, the device remains in the high resistance state but the current exhibits the voltage square dependence, $I \propto V^2$, with a slope of ~2. This region can be described by the Mott-Gurney law [139], as given by:

$$J = \frac{9\varepsilon\mu V^2}{8d^3} \tag{7.1}$$

where J is the current density, ε is the dielectric constant, μ is the free carrier mobility, V is the applied voltage, and d is the insulator/metal oxide layer (thin film) thickness.

Once the applied voltage reached the threshold voltage of 0.8 V, all traps are filled and an abrupt transition in the current takes place, switching the device to the LRS (ON) state. Conduction in this region can be ascribed to trap-filled space charge limited conduction (TF-SCLC). In the case of the LRS, the conduction mechanism is completely dominated by Ohmic conduction for the return voltage region from 1 V to 0 V. This region shows linear dependence of current with the applied voltage, $I \propto V$, with a slope of ~1. There is substantial evidence to support the mechanism also occurs in nanoparticle-based systems [224–227].

In terms of the Simmons model [64], the switching in our devices is consistent with N-shaped or voltage controlled negative differential resistance [228], since the I-V curves, shown in Fig. 6.15 (a), exhibit the typical non-linear differential resistance effect. When the device is in the low resistance state, and the voltage is ramped from zero to a more negative potential, a local maximum of the current is observed at V_{Max}, followed by a region of negative differential resistance and transition to a high resistance state as electrons are injected into traps. If the voltage is removed, the device remains in the off state. In the alternate scenario, when the device is in the high resistance state, and the voltage is ramped from zero to a more positive voltage, the device exhibits a transition at a threshold voltage, V_{th}, to a low resistance state due to removal of the stored charge. Interestingly, the devices in their pristine state always start in the high resistance state, and the first sweep results in switching to a low resistance state, irrespective of the direction of the first sweep. Since the reverse scenario is generally expected in such a model, it could indicate that the nanoparticles are already partially charged or the first sweep initiates a forming-like step in the system.

There is also an ongoing debate as to whether there is filament formation from the dissolution of the electrodes or electrochemically active materials within the device structure [32]. In the latter case, we find no evidence of this since we do not observe resistive switching in devices without gold nanoparticles and the applied voltages use (sweeping between ±1 V) for switching in nanoparticle containing devices are much lower than that used elsewhere, e.g. up to 8 V [229], which may preclude dissolution of the electrode material. We have also used aluminium as well as gold as the top electrodes in our systems which are generally less mobile than the more favoured silver electrode material used in many of these systems [32,230].

7.3 Neuromorphic Computing Applications

In this section, the potential of the optical memristor devices in neuromorphic applications is discussed. It has been demonstrated that memristors simulate the learning properties of biological synapses [231]. In the human brain, there are about 10^{11} neurons and about 10^{15} synapses which connect each neuron with others [232]. Synapses transfer the spikes or signals generated by neurons from one neuron to the adjacent neuron, known as a pre-synaptic neuron and a post-synaptic neuron, respectively. The connection strength of synapses depends on the synaptic weight. In biological synapses, the connection strength between two neurons is modified by the ionic flow through the synaptic gap, and it is widely believed that the adaption of synaptic weight enables biological systems to learn [232]. Correspondingly, memristors emulate the biological synapse configuration and function in which each cross-point between the top electrode (pre-synaptic neuron) and bottom electrode (post-synaptic neuron) represent a synapse for neuromorphic computing applications. Furthermore, the synaptic weight in a memristor is determined by measuring the conductance of memristor. This conductance relies on the total charge passing through a memristor, and it can be altered by voltage pulses.

In order to be used in neuromorphic applications, memristors need to show incrementally increase (potentiation) and decrease (depression) in the conductance upon an external stimuli [161,233,234]. We see that the synaptic weight in our ZnO NR-based devices and Au NP-based devices showed potentiation and depression upon electrical and optical pulses as previously demonstrated in Figs. 5.13 (a and

b) and 6.19 (a and b), respectively. A series of positive/negative electrical pulses incrementally increased/decreased the conductance of both types of devices. Similarly, a series of linearly/circularly optical light pulses incrementally increased/decreased the conductance of both types of devices. Interestingly, the devices show incrementally linear potentiation and depression in the case of electrical pulses, whereas, more highly non-linear incremental depression than potentiation in the case of optical pulses. In the former case, the linearity of incremental increase and decrease in the synaptic weight most likely indicates that the operation of the device was at potentials in the linear regime of the current-voltage curve. Longer or larger magnitude pulses would have most likely given non-linear effects as predicted by the shape of the I-V hysteresis curves of memristors. In the latter case, the non-linearity of conductance change is more related to the optical expansion and contraction properties of the PDR1A material, which as shown by the graph in Figs. 5.5 and 6.5 saturates after a period of time.

Spike-timing-dependent plasticity (STDP) is also a key tenet of Hebbian learning and has been shown to be linked with sensory perception, spatial reasoning, language and conscious thought in the neocortex [235]. In STDP, learning and information storage are dependent on the difference in arrival times of action potentials from neighboring neurons, called pre-synaptic and post-synaptic spikes. As reported in Figs. 5.14 and 6.20, the memristor synaptic weight ($\Delta G/G$) was modulated by light by measuring the synaptic efficacy before and after irradiation with circularly polarised light. The STDP characteristics shifts after illumination with circularly polarised light, as expected from the variation of the PDR1A film thickness. The effect is reversible *via* irradiation with linearly polarised light and can be modulated by varying the irradiation time or laser intensity. The obtianed STDP data are in a good agreement with the biological STDP data measured in hippocampal synapses by Bi and Poo [162], and also consistent with electronic synapses based on memristors [161,163,236].

Practically, this could be carried out by optically addressing single memristors in circuits, or in more complex artificial brain-like systems, *via* stimulating regions containing many memristors. The latter effect is certainly significant in biological brains since it is well known that learning is not necessarily associated with changes in individual synapses but the collective change of many synapses in a specific region. In this work we have focused on the control of a single memristor device. The development of a system fully capable of emulating the brain's complex functions would require the orchestration of a complex network of billions of memristors divided into regions each having different functionality and learning characteristics. The dual control of a memristor both optically and electronically would support this ability to develop greater complexity. For example, light can provide hierarchical control, facilitating such processes as memory consolidation, synaptic pruning and conversion of short-term to long-term memory.

Light could be used as a means to refresh synaptic circuits that are no longer required, such as old memories. Instead of discarding the memristor synapses, their synaptic weight could be modified, so they are instead free to learn new information. In this context, the ability to control the speed of forgetting is also important and in Figs. 5.15, and 6.21 we show how the optical memristors can be used to control the retention time of memory states, allowing short-term memory and medium-term memory. The devices also exhibit long-term (non-volatile) memory. This involves operation of the memristor device by purely electrical signals (i.e. without any optical stimulus). The short-term and medium-term memory processes are similar to short-term plasticity (STP) and long-term plasticity (LTP) processes in biological systems, which involve enhancement of the connection strength between two neurons but with different decay rates back towards their initial states. However, since we have defined the synaptic efficacy in terms of resistance (conductance could instead be used), a more precise definition, in our case would be that the devices exhibit short-term depression (STD) and long-term depression (LTD) since the optical irradiation by circularly polarised light diminishes the conductivity (increases the resistivity) of the device. In the case of the medium-term memory effect observed in this work, the switch back of memory to its initial state is a spontaneous event and is therefore consistent with LTD, but in the case of the short-term memory effect, the process is a little different as it is an activity dependent process involving optical stimulation.

The ability to dynamically switch between these types *via* optical means could has important applications in adaptive electronics and reconfigurable circuits as a means to modify functionality or stored information. Optically controllable short-term and long-term memory and dynamic modification of the retention time of stored information could also have application in freeing up information that is stored for different purposes. For example, the medium term memory approach would enable data to be stored for a reasonable amount of time before being automatically forgotten. This would save the system energy and time in having to perform a specific erase process. In an artificial intelligent system an application of this could include memory needed for episodic memory or used to give spatial awareness. In the short memory scenario, optical irradiation could be used to erase data that is not needed for a long period of time, applications could include memory used in numerical calculations, logic operations or cache memory. In the latter case, improved switching times are likely needed, but perhaps not significantly so, since short-term memory in biological systems is approximately only 10–20 seconds and signalling processes themselves are typically only of the order of millisecond.

Chapter 8. Conclusions and Future Work

This chapter summarises the main conclusions of this thesis and provides some suggestions for future research in the optical memristors field.

8.1 Conclusions

In this thesis, novel optical resistive switching devices exhibiting an optical SET and RESET functionality are demonstrated for the first time. The devices exhibit all of the nonvolatile electronic resistive switching properties of normal memristor devices but can also be switched ON and OFF by purely optical means. Illumination by light can also be used to modulate or fine-tune the electronic switching properties of the device; for example, the resistance OFF/ON ratio can be modified. The work has important applications in reconfigurable and adaptive electronics, photonic memories and, as demonstrated in the thesis, can also be used to control the learning properties of memristor devices through spike-timing-dependent-plasticity (STDP), which is important in neuromorphic computing applications.

The main thesis work centres around composite materials consisting of zinc oxide nanorods or gold nanoparticles embedded in an optically active polymer. The polymer, poly(disperse red 1 acrylate) (or PDR1A) expands or contracts upon illumination with wavelength- and polarisation-specific light, which modifies the electronic transport and switching properties of the device. In the case of the metal nanoparticle system, the devices exhibit clear switching between the ON and OFF states by purely optical means. The resistance OFF/ON ratio is large, and this has been optimized by creating filamentary-like conduction pathways of gold nanoparticles within the device, that break or re-connect under optical irradiation.

In the case of ZnO NR-based optical devices, the fabrication methods used were successful in producing reliable and high performance devices. A microwave-assisted hydrothermal technique was used to fabricate a thin-film “forest” of vertically aligned ZnO NRs. The SEM results show the thin-film to be of high quality, having high density nanorod growth with good vertical alignment and uniform coverage across the surface. The method also has the advantages of low cost, low temperature (ambient) growth and a simple means of fabrication using solution processing techniques. This contrasts with other techniques that often require high temperatures and pressures. The deposition of the PDR1A polymer material is also *via* solution processing. The spin-coating technique is simple, fast and low-cost. The PDR1A polymer is deposited on top of the ZnO NR surface and serves as a barrier layer between the ZnO NRs and the Al top contact, preventing short-circuiting of the top electrode with the ZnO nanorods, and improving the switching performance of the devices. It also lowers the operating current of the device, which has the advantage of decreasing the power consumption. The PDR1A film thickness characterization reveals that the maximum expansion of PDR1A after 30 min irradiation by circularly polarised light is ~18% and 30%, depending on the initial film thickness.

The I-V characteristics of ITO/ZnO NR/PDR1A/Al optical memristors show a pinched hysteresis loop with bipolar resistive switching properties. The devices exhibit a complex transition between the HRS and LRS states and a relatively small (~10) resistance OFF/ON ratio. The fitted I-V curve demonstrates that the conduction mechanism is dominated by space-charge-limited-current (SCLC). It is observed that the optoelectronic properties of devices can be optically modified *via* expansion and contraction of PDR1A film. Indeed, irradiation with circularly polarised light for 30 min increases the ON and OFF resistance states and improves the OFF/ON ratio by a factor of 4. Irradiation with linearly polarised light for 15 min or thermal relaxation for 120 min contracts the PDR1A film, and that causes the ON and OFF resistance states to revert back to their initial states. It is also found that optical irradiation can be used to switch the retention time of ZnO NR-based devices between short-term, medium term and long-term (non-volatile) behaviour.

Au NP:PDR1A optical memristors were also produced using a solution processing technique that is fast, simple and low-cost. The electrical conductivity of this hybrid system was found to be strongly dependent on the nanoparticle concentration. It was found the conductivity of the devices increased with nanoparticle concentration and in particular, a critical volume fraction, $Rv^* = \sim 0.065\%$, was found that had a conductivity that was more than three orders of magnitude greater than devices without nanoparticles. Examination of these devices by TEM , demonstrated that the critical volume fraction was due to the formation of conductive nanoparticle pathways (filaments) that bridge (or partially bridge) between the top and bottom electrodes. The most obvious finding to emerge from these filaments/bridges is they are very sensitive to contraction and expansion of the PDR1A material, which can be controlled by wavelength and polarisation-specific light. The expansion and contraction of PDR1A polymer upon illumination with circularly and linearly polarised light cause rupture and re-connection of the pathways, respectively, that causes the optical RESET and SET processes, respectively. The TEM results, further, identify that the Au NPs are not homogenously distributed within the PDR1A film, but occur in clusters at the interface of the PDR1A and Al electrode.

The Au NP:PDR1A optical memristors exhibit bipolar switching properties with a sharp transition between the ON and OFF states. SCLC appears to play a role in the conduction mechanism as shown by I-V curve fits. Moreover, a negative differential resistance (NDR) is observed at negative potentials, which is a signature of a charge trapping mechanism first proposed by Simmons. From the optoelectronic studies, the devices exhibited large optical switching effects with high reproducibility. However, it was noticed that the HRS state is affected more by the optical expansion/contraction process than the LRS state. This could be due to better charge storage properties of the expanded polymer state, since the conduction pathways are broken more than in the normal (contracted) polymer state. Optical illumination of the Au nanoparticle/PDR1A devices was also found to modify the I-V characteristics, the ON and OFF resistance states, the resistance OFF/ON ratio, and the data retention times, as was similarly observed in the ZnO nanorod/PDR1A devices. The devices also showed potentiation and depression of the memristor states by optical means and optically tunable STDP learning.

A significant achievement of this work is the development of a new type of device that exhibits both electronic and optical switching. This has application in a number of areas. In optoelectronics, the devices could be used as optical switches in integrated photonic circuits and optical computing systems, as well as systems that need to be adaptive and reconfigurable (by light). In neuromorphic computing applications, the dynamic and spatial patterning of memristor arrays by light opens the route to dynamically tunable and reprogrammable synaptic circuits as well as the ability to impart hierarchical control in artificial intelligent systems. Although there are many potential applications, the main limitation of the devices are the slow optical switching speeds of the devices, typical 30 mins for an optical SET and 15 mins for an optical RESET. This is much too slow for practical purposes and would need to be greatly improved, especially for applications in photonic circuits. However, although the speed of the devices is slow, ultra high-speed switching (i.e. nanosecond, femtosecond) is not a necessity for all applications. We envisage that switching speeds of the order of 20 ms would be sufficient in neuromorphic computing systems, since this is the typical switching speeds of synapses in most biological systems, including that present in human brains.

8.2 Future Work

This section proposes some ideas for future development of the optical memristor devices as well as some potential areas of their application:

1. Development of devices with much faster optical switching times is necessary to take this technology forward for commercial applications. Switching speeds of the order of milliseconds are useful for neuromorphic applications since these are the typical switching speeds found in biological brains. In the area of photonic devices, fast switching speeds of the order of microseconds or nanoseconds would be needed.

2. Fabricating optical memristors with crossbar architecture with ITO top and bottom electrodes for high-density memory applications.

3. Planar optical memristor devices (horizontal) could be investigated as these may be simpler to integrate into neural networks.

4. Development of optical memristor cellular neural network cameras for ultra-fast processing of video information. Systems of this nature can be used to alleviate bottlenecks associated with the large transfer of information across bus lines to the CPU. Reduced information is sent to the CPU since some of the pre-processing of the images (e.g. filtering, edge detection) is done at the level of the optics.

References

[1] Jeong DS, Thomas R, Katiyar RS, Scott JF, Kohlstedt H, Petraru a, et al. Emerging memories: resistive switching mechanisms and current status. Reports Prog Phys 2012;75:76502. doi:10.1088/0034-4885/75/7/076502.

[2] Åkerman J. Toward a Universal Memory. Science (80-) 2005;308:508–10. doi:10.1126/science.1110549.

[3] Xie Y. Emerging Memory Technologies Design, Architecture, and Applications. 2014. doi:10.1007/978- 14419- 9551- 3.

[4] Li H, Chen Y. Nonvolatile Memory Design: Magnetic, Resistive, and Phase Change. CRC Press (Taylor and Francis Group), 2011, ISBN: 13: 978-1-4398-0746-0.

[5] Ando K, Watanabe S, Mooser S, Saitoh E, Sirringhaus H. Solution-processed organic spin-charge converter. Nat Mater 2013;12:622–7. doi:10.1038/nmat3634.

[6] Goswami S, Matula AJ, Rath SP, Hedström S, Saha S, Annamalai M, et al. Robust resistive memory devices using solution-processable metal-coordinated azo aromatics. Nat Mater 2017;16:1216–24. doi:10.1038/nmat5009.

[7] Maiti DK, Debnath S, Nawaz SM, Dey B, Dinda E, Roy D, et al. Composition-dependent nanoelectronics of amido-phenazines: non-volatile RRAM and WORM memory devices. Sci Rep 2017;7:1–10. doi:10.1038/s41598-017-13754-w.

[8] Ouyang J, Chu C-W, Szmanda CR, Ma L, Yang Y. Programmable polymer thin film and non-volatile memory device. Nat Mater 2004;3:918–22. doi:10.1038/nmat1269.

[9] Tondelier D, Lmimouni K, Vuillaume D, Fery C, Haas G. Metal/organic/metal bistable memory devices. Appl Phys Lett 2004;85:5763–5. doi:10.1063/1.1829166.

[10] Tseng RJ, Huang J, Ouyang J, Kaner RB, Yang Y. Polyaniline

nanofiber/gold nanoparticle nonvolatile memory. Nano Lett 2005;5:1077–80. doi:10.1021/nl050587l.

[11] Son D, Park D, Kim J. Bistable organic memory device with gold nanoparticles embedded in a conducting poly (N-vinylcarbazole) colloids hybrid. J Phys Chem C 2010;115:2341–8.

[12] Maier P, Hartmann F, Rebello Sousa Dias M, Emmerling M, Schneider C, Castelano LK, et al. Light sensitive memristor with bi-directional and wavelength-dependent conductance control. Appl Phys Lett 2016;109. doi:10.1063/1.4955464.

[13] Chua LO. Memristor—The Missing Circuit Element. IEEE Trans Circuit Theory 1971;18:507–19. doi:10.1109/TCT.1971.1083337.

[14] Andrew Adamatzky and Leon Chua. Memristor Networks. Springer; 2014. doi:10.1007/978-3-319-02630-5.

[15] Strukov DB, Snider GS, Stewart DR, Williams RS. The missing memristor found. Nature 2008;453:80–3. doi:10.1038/nature08166.

[16] Chua L. If it’s pinched it’s a memristor. Semicond Sci Technol 2014;29:104001. doi:10.1088/0268-1242/29/10/104001.

[17] Kvatinsky S, Friedman EG, Kolodny A, Weiser UC. The desired memristor for circuit designers. IEEE Circuits Syst Mag 2013;13:17–22. doi:10.1109/MCAS.2013.2256257.

[18] Vourkas I, Sirakoulis GC. Memristor-Based Nanoelectronic Computing Circuits and Architectures. 2015. doi:10.1007/978-3-319-22647-7.

[19] Yang YC, Pan F, Liu Q, Liu M, Zeng F. Fully Room-Temperature-Fabricated Nonvolatile Resistive Memory for Ultrafast and High-Density Memory Application. Nano Lett 2009;9:1636–43.

[20] Avila-Niño JA, Sustaita AO, Reyes-Reyes M, López-Sandoval R. Effect of the thickness of insulator polymeric films on the memory behavior: The case of the polymethylmethacrylate and the polystyrene. J Nanotechnol 2011;2011:1–9. doi:10.1155/2011/702464.

[21] Tsunoda K, Fukuzumi Y, Jameson JR, Wang Z, Griffin PB, Nishi Y. Bipolar resistive switching in polycrystalline TiO2 films. Appl Phys Lett

2007;90:10–3. doi:10.1063/1.2712777.

[22] Kim KM, Choi BJ, Lee MH, Kim GH, Song SJ, Seok JY, et al. A detailed understanding of the electronic bipolar resistance switching behavior in Pt/TiO $_2$ /Pt structure. Nanotechnology 2011;22:254010. doi:10.1088/0957-4484/22/25/254010.

[23] Seo S, Lee MJ, Seo DH, Jeoung EJ, Suh D, Joung YS, et al. Reproducible resistance switching in polycrystalline NiO films Reproducible resistance switching in polycrystalline NiO films 2014;5655:1–4. doi:10.1063/1.1831560.

[24] Sun Y, Yan X, Zheng X, Liu Y, Zhao Y, Shen Y, et al. High on-off ratio improvement of ZnO-based forming-free memristor by surface hydrogen annealing. ACS Appl Mater Interfaces 2015;7:7382–8. doi:10.1021/acsami.5b01080.

[25] Beck A, Bednorz JG, Gerber C, Rossel C, Widmer D, Beck A, et al. Reproducible switching effect in thin oxide films for memory applications 2011;139:1–4. doi:10.1063/1.126902.

[26] Verrelli E, Gray RJ, O'Neill M, Kelly SM, Kemp NT. Microwave oven fabricated hybrid memristor devices for non-volatile memory storage. Mater Res Express 2014;1:46305. doi:10.1088/2053-1591/1/4/046305.

[27] Ouyang J. Emerging Resistive Switching Memories. Springer; 2016. doi:10.1007/978-3-319-31572-0.

[28] Chua LO, Kang SM. Memristive Devices and Systems. Proc IEEE 1976;64:209–23. doi:10.1109/PROC.1976.10092.

[29] Kawahara T, Ito K, Takemura R, Ohno H. Spin-transfer torque RAM technology: Review and prospect. Microelectron Reliab 2012;52:613–27. doi:10.1016/j.microrel.2011.09.028.

[30] Garcia V, Fusil S, Bouzehouane K, Enouz-Vedrenne S, Mathur ND, Barthélémy A, et al. Giant tunnel electroresistance for non-destructive readout of ferroelectric states. Nature 2009;460:81–4. doi:10.1038/nature08128.

[31] Bedeschi F, Fackenthal R, Resta C, Donzè EM, Jagasivamani M, Buda EC,

et al. A Bipolar-Selected Phase Change Memory Featuring Multi-Level Cell Storage. Solid -State Circuits 2009;44:217–27.

[32] Waser R, Dittmann R, Staikov C, Szot K. Redox-based resistive switching memories nanoionic mechanisms, prospects, and challenges. Adv Mater 2009;21:2632–63. doi:10.1002/adma.200900375.

[33] Zhu XJ, Shang J, Li RW. Resistive switching effects in oxide sandwiched structures. Front Mater Sci 2012;6:183–206. doi:10.1007/s11706-012-0170-8.

[34] Peng C-N, Wang C-W, Chan T-C, Chang W-Y, Wang Y-C, Tsai H-W, et al. Resistive switching of Au/ZnO/Au resistive memory: an in situ observation of conductive bridge formation. Nanoscale Res Lett 2012;7:559. doi:10.1186/1556-276X-7-559.

[35] Long BD, Li YB, Jha R. Switching Characteristics of Ru/HfO2/TiO2-x/Ru RRAM Devices for Digital and Analog Nonvolatile Memory Applications. IEEE Electron Device Lett 2012;33:706–8. doi:Doi 10.1109/Led.2012.2188775.

[36] Szot K, Speier W, Bihlmayer G, Waser R. Switching the electrical resistance of individual dislocations in single-crystalline SrTiO3. Nat Mater 2006;5:312–20. doi:10.1038/nmat1614.

[37] Liu CY, Wu PH, Wang A, Jang WY, Young JC, Chiu KY, et al. Bistable resistive switching of a sputter-deposited Cr-doped SrZrO3 memory film. IEEE Electron Device Lett 2005;26:351–3. doi:10.1109/LED.2005.848073.

[38] Mutiso RM, Kikkawa JM, Winey KI. Resistive switching in silver/polystyrene/silver nano-gap devices. Appl Phys Lett 2013;103. doi:10.1063/1.4831876.

[39] Vasu KS, Sampath S, Sood AK. Nonvolatile unipolar resistive switching in ultrathin films of graphene and carbon nanotubes. Solid State Commun 2011;151:1084–7. doi:10.1016/j.ssc.2011.05.018.

[40] Ouyang J, Yang Y. Polymer:metal nanoparticle devices with electrode-sensitive bipolar resistive switchings and their application as nonvolatile memory devices. Appl Phys Lett 2010;96. doi:10.1063/1.3324696.

[41] Son DI, Kim TW, Shim JH, Jung JH, Lee DU, Lee JM, et al. Flexible organic bistable devices based on graphene embedded in an insulating poly(methyl methacrylate) polymer layer. Nano Lett 2010;10:2441–7. doi:10.1021/nl1006036.

[42] Son D, Park D, Choi WK, Cho S, Kim W, Kim TW. Carrier transport in flexible organic bistable devices of ZnO nanoparticles embedded in an insulating poly (methyl methacrylate) polymer layer. Nanotechnology 2009;20:195203–9. doi:10.1088/0957-4484/20/19/195203.

[43] Oh K, Jeon W, Lee SS. One-dimensional TiO2@Ag nanoarchitectures with interface-mediated implementation of resistance-switching behavior in polymer nanocomposites. ACS Appl Mater Interfaces 2012;4:5727–31. doi:10.1021/am301362f.

[44] White SI, Vora PM, Kikkawa JM, Fischer JE, Winey KI. Temperature-dependent resistive switching in bulk silver nanowire-polystyrene composites. J Phys Chem C 2010;114:22106–12. doi:10.1021/jp108191q.

[45] Valanarasu S, Kathalingam A, Rhee J-K, Chandramohan R, Vijayan TA, Karunakaran M. Improved Memory Effect of ZnO Nanorods Embedded in an Insulating Polymethylmethacrylate Layer. J Nanosci Nanotechnol 2015;15:1416–20. doi:10.1166/jnn.2015.9034.

[46] Gul F, Efeoglu H. Bipolar resistive switching and conduction mechanism of an Al/ZnO/Al-based memristor. Superlattices Microstruct 2016;101:172–9. doi:10.1016/j.spmi.2016.11.043.

[47] Peng S., Zhuge F, Li R-WL, Fu B, Zhang H, Li J, et al. Mechanism for resistive switching in chalcogenide-based electrochemical metallization memory. Appl Phys Lett 2012;100. doi:10.1063/1.4921089.

[48] Lee S, Kim H, Yun D-J, Rhee S-W, Yong K. Resistive switching characteristics of ZnO thin film grown on stainless steel for flexible nonvolatile memory devices. Appl Phys Lett 2009;95:1–3. doi:10.1063/1.3280864.

[49] Qiu J, Shih A, Zhou W, Mi Z, Shih I. Effects of metal contacts and dopants on the performance of ZnO-based memristive devices. J Appl Phys

2011;110. doi:10.1063/1.3599952.

[50] Lai Y, Qiu W, Zeng Z, Cheng S, Yu J, Zheng Q. Resistive Switching of Plasma–Treated Zinc Oxide Nanowires for Resistive Random Access Memory. Nanomaterials 2016;6:9. doi:10.3390/nano6010016.

[51] Younis A, Chu D, Lin X, Yi J, Dang F, Li S. High-performance nanocomposite based memristor with controlled quantum dots as charge traps. ACS Appl Mater Interfaces 2013;5:2249–54. doi:10.1021/am400168m.

[52] Wang J, Sun B, Gao F, Greenham NC. Memristive devices based on solution-processed ZnO nanocrystals. Phys Status Solidi Appl Mater Sci 2010;207:484–7. doi:10.1002/pssa.200925467.

[53] Qi J, Olmedo M, Ren J, Zhan N, Zhao J, Zheng JG, et al. Resistive switching in single epitaxial ZnO nanoislands. ACS Nano 2012;6:1051–8. doi:10.1021/nn204809a.

[54] Qi J, Olmedo M, Zheng J-G, Liu J. Multimode Resistive Switching in Single ZnO Nanoisland System. Sci Rep 2013;3:1–6. doi:10.1038/srep02405.

[55] Tseng ZL, Kao PC, Shih MF, Huang HH, Wang JY, Chu SY. Electrical bistability in hybrid ZnO nanorod/polymethylmethacrylate heterostructures. Appl Phys Lett 2010;97:95–8. doi:10.1063/1.3511756.

[56] Cheng B, Zhao J, Xiao L, Cai Q, Guo R, Xiao Y, et al. PMMA interlayer-modulated memory effects by space charge polarization in resistive switching based on CuSCN-nanopyramids/ZnO-nanorods p-n heterojunction. Sci Rep 2015;5:1–9. doi:10.1038/srep17859.

[57] Anoop G, Panwar V, Kim TY, Jo JY. Resistive Switching in ZnO Nanorods/Graphene Oxide Hybrid Multilayer Structures. Adv Electron Mater 2017;3:1–9. doi:10.1002/aelm.201600418.

[58] Verbakel F, Meskers SCJ, Janssen RAJ. Electronic memory effects in diodes from a zinc oxide nanoparticle- polystyrene hybrid material. Appl Phys Lett 2006;89:1–4. doi:10.1063/1.2345612.

[59] Yun DY, Kwak JK, Jung JH, Kim TW, Son DI. Electrical bistabilities and carrier transport mechanisms of write-once-read-many-times memory

devices fabricated utilizing ZnO nanoparticles embedded in a polystyrene layer. Appl Phys Lett 2009;95:1–4. doi:10.1063/1.3243463.

[60] Son DI, You CH, Jung JH, Kim TW. Carrier transport mechanisms of organic bistable devices fabricated utilizing colloidal ZnO quantum dot-polymethylmethacrylate polymer nanocomposites. Appl Phys Lett 2010;97:1–4. doi:10.1063/1.3454774.

[61] Thanh Dao T, Viet Tran T, Higashimine K, Okada H, Mott D, Maenosono S, et al. High-performance nonvolatile write-once-read-many-times memory devices with ZnO nanoparticles embedded in polymethylmethacrylate. Appl Phys Lett 2011;99:2009–12. doi:10.1063/1.3665937.

[62] Park KH, Jung JH, Li F, Son DI, Kim TW. Carrier transport mechanisms of nonvolatile memory devices based on nanocomposites consisting of ZnO nanoparticles with polymethylmethacrylate nanocomposites sandwiched between two C60 layers. Appl Phys Lett 2008;93:1–3. doi:10.1063/1.2992203.

[63] Li F, Kim TW, Dong W, Kim YH. Formation and electrical bistability properties of ZnO nanoparticles embedded in polyimide nanocomposites sandwiched between two C60 layers. Appl Phys Lett 2008;92:1–3. doi:10.1063/1.2830617.

[64] Simmons JG, Verderber RR. New Conduction and Reversible Memory Phenomena in Thin Insulating Films. Proc R Soc A Math Phys Eng Sci 1967;301:77–102. doi:10.1098/rspa.1967.0191.

[65] Jin Z, Liu G, Wang J. Organic nonvolatile resistive memory devices based on thermally deposited Au nanoparticle Advertisement : Organic nonvolatile resistive memory devices based on thermally deposited Au nanoparticle. AIP Adv 2013;3:1–7. doi:10.1063/1.4804948.

[66] Ouyang J, Chu CW, Sieves D, Yang Y. Electric-field-induced charge transfer between gold nanoparticle and capping 2-naphthalenethiol and organic memory cells. Appl Phys Lett 2005;86:1–3. doi:10.1063/1.1887819.

[67] Bozano LD, Kean BW, Beinhoff M, Carter KR, Rice PM, Scott JC. Organic

Materials and Thin-Film Structures for Cross-Point Memory Cells Based on Trapping in Metallic Nanoparticles. Adv Funct Mater 2005;15:1933–9. doi:10.1002/adfm.200500130.

[68] Simon DT, Griffo MS, DiPietro RA, Swanson SA, Carter SA. Admittance spectroscopy of polymer-nanoparticle nonvolatile memory devices. Appl Phys Lett 2006;89:1–3. doi:10.1063/1.2357560.

[69] Khurana G, Misra P, Kumar N, Kooriyattil S, Scott JF, Katiyar RS. Enhanced resistive switching in forming-free graphene oxide films embedded with gold nanoparticles deposited by electrophoresis. Nanotechnology 2016;27:1–7. doi:10.1088/0957-4484/27/1/015702.

[70] Tseng RJ, Huang J, Ouyang J, Kaner RB. Polyaniline Nanofiber / Gold Nanoparticle Nonvolatile Memory. Nano 2005;5:1–4. doi:10.1021/nl050587l.

[71] Son D, Park D, Choi WK, Cho S, Kim W, Kim TW. Carrier transport in flexible organic bistable devices of ZnO nanoparticles embedded in an insulating poly (methyl methacrylate) polymer layer. Nanotechnology 2009;20:195203–9. doi:10.1088/0957-4484/20/19/195203.

[72] Yang Y, Zhang X, Gao M, Zeng F, Zhou W, Xie S, et al. Nonvolatile resistive switching in single crystalline ZnO nanowires. Nanoscale 2011;3:1917–21. doi:10.1039/c1nr10096c.

[73] Ouyang J. Materials effects on the electrode-sensitive bipolar resistive switches of polymer:gold nanoparticle memory devices. Org Electron Physics, Mater Appl 2013;14:1458–66. doi:10.1016/j.orgel.2013.03.026.

[74] Ungureanu M, Zazpe R, Golmar F, Stoliar P, Llopis R, Casanova F, et al. A light-controlled resistive switching memory. Adv Mater 2012;24:2496–500. doi:10.1002/adma.201200382.

[75] Park J, Lee S, Yong K. Photo-stimulated resistive switching of ZnO nanorods. Nanotechnology 2012;23:1–6. doi:10.1088/0957-4484/23/38/385707.

[76] Emboras A, Goykhman I, Desiatov B, Mazurski N, Stern L, Shappir J, et al. Nanoscale plasmonic memristor with optical readout functionality. Nano

Lett 2013;13:6151–5. doi:10.1021/nl403486x.

[77] Hoessbacher C, Fedoryshyn Y, Emboras A, Melikyan A, Kohl M, Hillerkuss D, et al. The plasmonic memristor: a latching optical switch. Optica 2014;1:198–202. doi:10.1364/OPTICA.1.000198.

[78] Huebner CF, Tsyalkovsky V, Bandera Y, Burdette MK, Shetzline JA, Tonkin C, et al. Nonvolatile optically-erased colloidal memristors. Nanoscale 2015;7:1270–9. doi:10.1039/c4nr05167j.

[79] Bogle K, Narwade R, Phatangare A, Dahiwale S, Mahabole M, Khairnar R. Optically modulated resistive switching in BiFeO3 thin film. Phys Status Solidi 2016;213:2183–8. doi:10.1002/pssa.201533035.

[80] Mosciatti T, Bonacchi S, Gobbi M, Ferlauto L, Liscio F, Giorgini L, et al. Optical Input/Electrical Output Memory Elements based on a Liquid Crystalline Azobenzene Polymer. ACS Appl Mater Interfaces 2016;8:6563–9. doi:10.1021/acsami.5b12430.

[81] Attianese D, Petrosino M, Vacca P, Concilio S, Iannelli P, Rubino A, et al. Switching device based on a thin film of an Azo-containing polymer for application in memory cells. IEEE Electron Device Lett 2008;29:44–6. doi:10.1109/LED.2007.910792.

[82] Lim SL, Li NJ, Lu JM, Ling QD, Zhu CX, Kang ET, et al. Conductivity switching and electronic memory effect in polymers with pendant azobenzene chromophores. ACS Appl Mater Interfaces 2009;1:60–71. doi:10.1021/am800001e.

[83] Min M, Seo S, Lee SM, Lee H. Voltage-controlled nonvolatile molecular memory of an azobenzene monolayer through solution-processed reduced graphene oxide contacts. Adv Mater 2013;25:7045–50. doi:10.1002/adma.201303335.

[84] Sun G. Exploring Memory Hierarchy Design with Emerging Memory Technologies. Volume 267. Springer; 2014. doi:10.1007/978-3-319-00681-9.

[85] Kinney WI, Shepherd W, Miller W, Evans J, Womack R. A non-volatile memory cell based on ferroelectric storage capacitors. 1987 Int Electron

Devices Meet 1987:850–1. doi:10.1109/IEDM.1987.191567.

[86] Manglani V, Agnihotri A. Remanent Polarized Ferroelectric Non-Volatile Random Access Memory 2012;I.

[87] Search H, Journals C, Contact A, Iopscience M, Address IP. Ferroelectric Nonvolatile Memory Technology and Its Applications n.d.;1516.

[88] Liu X, Liu Y, Chen W, Li J, Liao L. Ferroelectric memory based on nanostructures. Nanoscale Res Lett 2012;7:285. doi:10.1186/1556-276X-7-285.

[89] Bottger U, Summerfelt SR. Ferroelectric Random Access Memories. Nanoelectron Inf Technol 2003;12:565–90. doi:10.1166/jnn.2012.6651.

[90] Amanuma K, Hase T, Miyasaka Y. Preparation and ferroelectric properties of SrBi2Ta2O9 thin films. Appl Phys Lett 1995;66:221. doi:10.1063/1.113140.

[91] B-E Park, K Takahashi and HI. Fabrication and Electrical Properties of Pt/(Bi,La)4 TiO12/HfO2/Si structures. J Korean Phys Soc 2005;46:346–9. doi:10.1149/1.2755636.

[92] Chen KH, Cheng CC, Chen YC, Chang TC. Reliability of Ba(Zr<sub>0.1</sub>Ti<sub>0.9</sub>)O<sub >3</sub> Ferroelectric Thin Films under Various Frequencies for Nonvolatile Memory Application. Key Eng Mater 2007;336–338:73–5. doi:10.4028/www.scientific.net/KEM.336-338.73.

[93] Liu W, Ren X. Large piezoelectric effect in Pb-free ceramics. Phys Rev Lett 2009;103. doi:10.1103/PhysRevLett.103.257602.

[94] Auciello O, Scott JF, Ramesh R. The Physics of Ferroelectric Memories. Phys Today 1998;51:22. doi:10.1063/1.882324.

[95] Scott JF, de Araujo CAP. Ferroelectric Memories. Science (80-) 1989;246:4936. doi:10.1126/science.246.4936.1400.

[96] Meena J, Sze S, Chand U, Tseng T-Y. Overview of emerging nonvolatile memory technologies. Nanoscale Res Lett 2014;9:526. doi:10.1186/1556-276X-9-526.

[97] Sheikholeslami A, Gulak PG. A survey of circuit innovations in

Ferroelectric random-access memories. Proc IEEE 2000;88:667–89. doi:10.1109/5.849164.

[98] Gaidis MC. Magnetoresistive Random Access Memory. Nanotechnology 2010:685–97. doi:10.1002/9783527628155.nanotech033.

[99] Grynkewich G, Åkerman J, Brown P, Butcher B, Dave RW, DeHerrera M, et al. Nonvolatile Magnetoresistive Random-Access Memory Based on Magnetic Tunnel Junctions. MRS Bull 2004;29:818–21. doi:10.1557/mrs2004.234.

[100] Ikeda S, Hayakawa J, Lee YM, Matsukura F, Ohno Y, Hanyu T, et al. Magnetic tunnel junctions for spintronic memories and beyond. IEEE Trans Electron Devices 2007;54:991–1002. doi:10.1109/TED.2007.894617.

[101] Tehrani S, Slaughter JM, Deherrera M, Engel BN, Rizzo ND, Salter J, et al. Magnetoresistive random access memory using magnetic tunnel junctions. Proc IEEE 2003;91:703–14. doi:10.1109/JPROC.2003.811804.

[102] Slaughter JM. Materials for Magnetoresistive Random Access Memory. Annu Rev Mater Res 2009;39:277–96. doi:10.1146/annurev-matsci-082908-145355.

[103] Prince B. Emerging memories: technologies and trends. 2002.

[104] Wang L, Yang CH, Wen J. Physical principles and current status of emerging non-volatile solid state memories. Electron Mater Lett 2015;11:505–43. doi:10.1007/s13391-015-4431-4.

[105] Ovshinsky SR. Reversible electrical switching phenomena in disordered structures. Phys Rev Lett 1968;21:1450–3. doi:10.1103/PhysRevLett.21.1450.

[106] Karpov I V., Mitra M, Kau D, Spadini G, Kryukov YA, Karpov VG. Fundamental drift of parameters in chalcogenide phase change memory. J Appl Phys 2007;102. doi:10.1063/1.2825650.

[107] Burr GW. Phase change memory technology. J Vac Sci 2010;2004:903. doi:10.1116/1.3301579.

[108] Wong H-SP, Raoux S, Kim S, Liang J, Reifenberg JP, Rajendran B, et al. Phase Change Memory. Proc IEEE 2010;98:2201–27.

doi:10.1109/JPROC.2010.2070050.

[109] Zhou P, Zhao B, Yang J, Zhang Y. A Durable and Energy Efficient Main Memory Using Phase Change Memory Technology. Isca ’09 2009;37:14–23. doi:10.1145/1555815.1555759.

[110] Lai S, Lowrey T. OUM - A 180 nm nonvolatile memory cell element technology for stand alone and embedded applications. Int Electron Devices Meet Tech Dig (Cat No01CH37224) 2001:36.5.1-36.5.4. doi:10.1109/IEDM.2001.979636.

[111] Raoux S, Rettner CT, Jordan-Sweet JL, Kellock AJ, Topuria T, Rice PM, et al. Direct observation of amorphous to crystalline phase transitions in nanoparticle arrays of phase change materials. J Appl Phys 2007;102. doi:10.1063/1.2801000.

[112] Pirovano A, Redaelli A, Pellizzer F, Ottogalli F, Tosi M, Ielmini D, et al. Reliability study of phase-change nonvolatile memories. IEEE Trans Device Mater Reliab 2004;4:422–6. doi:10.1109/TDMR.2004.836724.

[113] Kwon D-H, Kim KM, Jang JH, Jeon JM, Lee MH, Kim GH, et al. Atomic structure of conducting nanofilaments in TiO2 resistive switching memory. Nat Nanotechnol 2010;5:148–53. doi:10.1038/nnano.2009.456.

[114] Yu S, Guan X, Wong HSP. Conduction mechanism of TiNHfO xPt resistive switching memory: A trap-assisted-tunneling model. Appl Phys Lett 2011;99. doi:10.1063/1.3624472.

[115] Son JY, Shin YH. Direct observation of conducting filaments on resistive switching of NiO thin films. Appl Phys Lett 2008;92. doi:10.1063/1.2931087.

[116] Lin HT, Pei Z, Chen JR, Hwang GW, Fan JF, Chan YJ. A new nonvolatile bistable polymer-nanoparticle memory device. IEEE Electron Device Lett 2007;28:951–3. doi:10.1109/LED.2007.903944.

[117] Tang A, Qu S, Hou Y, Teng F, Tan H, Liu J, et al. Electrical bistability and negative differential resistance in diodes based on silver nanoparticle-poly(N-vinylcarbazole) composites. J Appl Phys 2010;108. doi:10.1063/1.3506708.

[118] Tseng RJ, Ouyang J, Chu C-W, Huang J, Yang Y. Nanoparticle-induced negative differential resistance and memory effect in polymer bistable light-emitting device. Appl Phys Lett 2006;88:123506. doi:10.1063/1.2187407.

[119] Yang Y, Ouyang J, Ma L, Tseng RJH, Chu CW. Electrical switching and bistability in organic/polymeric thin films and memory devices. Adv Funct Mater 2006;16:1001–14. doi:10.1002/adfm.200500429.

[120] Cho B, Song S, Ji Y, Kim TW, Lee T. Organic resistive memory devices: Performance enhancement, integration, and advanced architectures. Adv Funct Mater 2011;21:2806–29. doi:10.1002/adfm.201100686.

[121] Tu CH, Lai YS, Kwong DL. Memory effect in the current - Voltage characteristic of 8-hydroquinoline aluminum salt films. IEEE Electron Device Lett 2006;27:354–6. doi:10.1109/LED.2006.872915.

[122] Terai M, Fujita K, Tsutsui T. Electrical bistability of organic thin-film device using Ag electrode. Japanese J Appl Physics, Part 1 Regul Pap Short Notes Rev Pap 2006;45:3754–7. doi:10.1143/JJAP.45.3754.

[123] Wolf C, Nau S, Sax S, Busby Y, Pireaux JJ, List-Kratochvil EJW. Resistive switching based on filaments in metal/PMMA/metal thin film devices. Jpn J Appl Phys 2015;54. doi:10.7567/JJAP.54.120301.

[124] Lai YS, Tu CH, Kwong DL, Chen JS. Bistable resistance switching of poly(N-vinylcarbazole) films for nonvolatile memory applications. Appl Phys Lett 2005;87:1–3. doi:10.1063/1.2051801.

[125] Chu CW, Ouyang J, Tseng JH, Yang Y. Organic donor-acceptor system exhibiting electrical bistability for use in memory devices. Adv Mater 2005;17:1440–3. doi:10.1002/adma.200500225.

[126] Liu G, Ling Q, Yeow E, Teo H, Zhu C, Chan DS, et al. Electrical Conductance Tuning and Bistable Switching in Poly(N- vinylcarbazole)-Carbon Nanotube Composite Films. ACS Nano 2009;3:1929–37.

[127] Son DI, Park DH, Kim J Bin, Choi JW, Kim TW, Angadi B, et al. Bistable organic memory device with gold nanoparticles embedded in a conducting poly(N -vinylcarbazole) colloids hybrid. J Phys Chem C 2011;115:2341–8. doi:10.1021/jp110030x.

[128] Kim D-IS and J-HK and D-HP and WKC and FL and JHH and TW. Nonvolatile flexible organic bistable devices fabricated utilizing CdSe/ZnS nanoparticles embedded in a conducting poly N-vinylcarbazole polymer layer. Nanotechnology 2008;19:55204. doi:10.1088/0957-4484/19/5/055204.

[129] Tetzla R. Memristors and memristive systems(2).pdf.pdf. Springer; 2014. doi:10.1007/978-1-4614-9068-5.

[130] Sawa A. Resistive switching in transition metal oxides. Mater Today 2008;11:28–36. doi:10.1016/S1369-7021(08)70119-6.

[131] Wong HSP, Lee HY, Yu S, Chen YS, Wu Y, Chen PS, et al. Metal-oxide RRAM. Proc IEEE 2012;100:1951–70. doi:10.1109/JPROC.2012.2190369.

[132] Hong S, Auciello O, Wouters D. Emerging Non-Volatile Memories. 2008.

[133] Chang W-Y, Lai YC, Wu TB, Wang SF, Chen F, Tsai MJ. Unipolar resistive switching characteristics of ZnO thin films for nonvolatile memory applications. Appl Phys Lett 2008;92:022110 (1-3). doi:10.1063/1.2834852.

[134] Xu N, Liu LF, Sun X, Chen C, Wang Y, Han DD, et al. Bipolar switching behavior in TiN/ZnO/Pt resistive nonvolatile memory with fast switching and long retention. Semicond Sci Technol 2008;23:1–4. doi:10.1088/0268-1242/23/7/075019.

[135] Zidan MA, Fahmy HAH, Hussain MM, Salama KN. Memristor-based memory: The sneak paths problem and solutions. Microelectronics J 2013;44:176–83. doi:10.1016/j.mejo.2012.10.001.

[136] Kügeler C, Meier M, Rosezin R, Gilles S, Waser R. High density 3D memory architecture based on the resistive switching effect. Solid State Electron 2009;53:1287–92. doi:10.1016/j.sse.2009.09.034.

[137] Lim EW, Ismail R. Conduction Mechanism of Valence Change Resistive Switching Memory: A Survey. Electronics 2015;4:586–613. doi:10.3390/electronics4030586.

[138] Murphy EL, Good RH. Thermionic Emission, Field Emission, and the Transition Region. Phys Rev 1956;102:1464–73. doi:10.1103/PhysRev.102.1464.

[139] Chiu F. A Review on Conduction Mechanisms in Dielectric Films. Adv Mater Sci Eng 2014;ID 578168:18. doi:10.1155/2014/578168.

[140] R. Kassing, P. Petkov, W. Kulisch and CP. Functional Properties of Nanostructured Materials 2005:529.

[141] Wu S, Ren L, Qing J, Yu F, Yang K, Yang M, et al. Bipolar Resistance Switching in Transparent ITO / LaAlO 3 / SrTiO 3 Memristors. ACS Appl Mater Interfaces 2014;6:8575–9.

[142] Wang W, Panin GN, Fu X, Zhang L, Ilanchezhiyan P, Pelenovich VO, et al. MoS2 memristor with photoresistive switching. Sci Rep 2016;6:31224. doi:10.1038/srep31224.

[143] Yan P, Li Y, Hui YJ, Zhong SJ, Zhou YX, Xu L, et al. Conducting mechanisms of forming-free TiW/Cu<inf>2</inf>O/Cu memristive devices. Appl Phys Lett 2015;107. doi:10.1063/1.4928979.

[144] Entner R. Modeling and Simulation of Negative Bias Temperature Instability 2007:137.

[145] He G. and SZ. High-k Gate Dielectrics for CMOS Technology. Singapore: WILEY-VCH; 2012.

[146] Lau WS. An Extended Unified Schottky-Poole-Frenkel Theory to Explain the Current-Voltage Characteristics of Thin Film Metal-Insulator-Metal Capacitors with Examples for Various High-k Dielectric Materials. ECS J Solid State Sci Technol 2012;1:N139–48. doi:10.1149/2.006301jss.

[147] Nagashima K, Yanagida T, Oka K, Kawai T. Unipolar resistive switching characteristics of room temperature grown SnO2 thin films. Appl Phys Lett 2009;94:2–4. doi:10.1063/1.3156863.

[148] Chen C, Pan F, Wang ZS, Yang J, Zeng F. Bipolar resistive switching with self-rectifying effects in Al/ZnO/Si structure. J Appl Phys 2012;111:1–7. doi:10.1063/1.3672811.

[149] Chiu F-C, Li P-W, Chang W-Y. Reliability characteristics and conduction mechanisms in resistive switching memory devices using ZnO thin films. Nanoscale Res Lett 2012;7:178. doi:10.1186/1556-276X-7-178.

[150] Chiu F-C. Conduction Mechanisms in Resistance Switching Memory

Devices Using Transparent Boron Doped Zinc Oxide Films. Materials (Basel) 2014;7:7339–48. doi:10.3390/ma7117339.

[151] Y. Sharma, P. Misra, S. P. Pavunny and r. SK. Unipolar resistive switching behavior of high-k ternary rare-earth oxide LaHoO3 thin films for non-volatile memory applications. MRS Symp Proc 2015;1729. doi:10.1557/opl.2015.92.

[152] Hummel RE. Electronic Properties of Materials. Springer; 2005.

[153] Awais MN, Muhammad NM, Navaneethan D, Kim HC, Jo J, Choi KH. Fabrication of ZrO2 layer through electrohydrodynamic atomization for the printed resistive switch (memristor). Microelectron Eng 2013;103:167–72. doi:10.1016/j.mee.2012.09.005.

[154] Hu SG, Wu SY, Jia WW, Yu Q, Deng LJ, Fu YQ, et al. Review of Nanostructured Resistive Switching Memristor and Its Applications 2014;6:729–57. doi:10.1166/nnl.2014.1888.

[155] Chen JY, Hsin CL, Huang CW, Chiu CH, Huang YT, Lin SJ, et al. Dynamic evolution of conducting nanofilament in resistive switching memories. Nano Lett 2013;13:3671–7. doi:10.1021/nl4015638.

[156] Ahn Y, Choi YJ, Park JW, Lee JH, Kim GH, Kim YS, et al. Electrode engineering for improving resistance switching of Sb 2O5 films. Appl Phys Express 2013;6:1–4. doi:10.7567/APEX.6.091102.

[157] Prodromakis T, Toumazou C. A review on memristive devices and applications. 2010 IEEE Int Conf Electron Circuits, Syst ICECS 2010 - Proc 2010:934–7. doi:10.1109/ICECS.2010.5724666.

[158] Lee M-J, Lee CB, Lee D, Lee SR, Chang M, Hur JH, et al. A fast, high-endurance and scalable non-volatile memory device made from asymmetric Ta2O5−x/TaO2−x bilayer structures. Nat Mater 2011;10:625–30. doi:10.1038/nmat3070.

[159] Kuang Y, Huang R, Tang Y, Ding W, Zhang L, Wang Y. Flexible single-component-polymer resistive memory for ultrafast and highly compatible nonvolatile memory applications. IEEE Electron Device Lett 2010;31:758–60. doi:10.1109/LED.2010.2048297.

[160] Robert Kozma REPGEP. Advances in Neuromorphic Memristor Science and Applications. Springer; 2012. doi:10.1007/978-94-007-4491-2.

[161] Jo SH, Chang T, Ebong I, Bhadviya BB, Mazumder P, Lu W. Nanoscale memristor device as synapse in neuromorphic systems. Nano Lett 2010;10:1297–301. doi:10.1021/nl904092h.

[162] Bi GQ, Poo MM. Synaptic modifications in cultured hippocampal neurons: dependence on spike timing, synaptic strength, and postsynaptic cell type. J Neurosci 1998;18:10464–72. doi:10.1038/25665.

[163] Li Y, Zhong Y, Xu L, Zhang J, Xu X, Sun H, et al. Ultrafast Synaptic Events in a Chalcogenide Memristor. Sci Rep 2013;3:1619. doi:10.1038/srep01619.

[164] Janotti A, Van de Walle CG. Fundamentals of zinc oxide as a semiconductor. Reports Prog Phys 2009;72:1–29. doi:10.1088/0034-4885/72/12/126501.

[165] C. Jagadish and SP. Zinc Oxide Bulk, Thin Films and Nanostructures. Elsevier Ltd; 2006.

[166] Hadis Morkoç ÜÖ. Zinc Oxide: Fundamentals, Materials and Device Technology - Morkoç - Wiley Online Library. WILEY-VCH; 2009.

[167] Liu L, Mei Z, Tang A, Azarov A, Kuznetsov A, Xue QK, et al. Oxygen vacancies: The origin of n-type conductivity in ZnO. Phys Rev B - Condens Matter Mater Phys 2016;93:1–6. doi:10.1103/PhysRevB.93.235305.

[168] Yi G-C, Wang C, Park W Il. ZnO nanorods: synthesis, characterization and applications. Semicond Sci Technol 2005;20:S22–34. doi:10.1088/0268-1242/20/4/003.

[169] Law M, Greene LE, Johnson JC, Saykally R, Yang P. Nanowire dye-sensitized solar cells. Nat Mater 2005;4:455–9. doi:10.1038/nmat1387.

[170] Sun XW, Huang JZ, Wang JX, Xu Z. LETTERS A ZnO Nanorod Inorganic / Organic Heterostructure Light-Emitting Diode Emitting at 342 nm. Nano Lett 2008;8:1219–23. doi:10.1021/nl080340z.

[171] Wan Q, Li QH, Chen YJ, Wang TH, He XL, Li JP, et al. Fabrication and ethanol sensing characteristics of ZnO nanowire gas sensors. Appl Phys Lett 2004;84:3654–6. doi:10.1063/1.1738932.

[172] Alex S, Tiwari A. Functionalized Gold Nanoparticles: Synthesis, Properties

and Applications—A Review. J Nanosci Nanotechnol 2015;15:1869–94. doi:10.1166/jnn.2015.9718.

[173] Lee J-S. Recent progress in gold nanoparticle-based non-volatile memory devices. Gold Bull 2010;43:189–99. doi:10.1007/BF03214986.

[174] Sharma N, Bhatt G, Kothiyal P. Gold Nanoparticles synthesis, properties, and forthcoming applications – A review. Indian JPharmBiolRes 2015;3:13–27.

[175] Baker CO, Shedd B, Tseng RJ, Martinez-morales AA, Ozkan CS. Size Control of Gold Nanoparticles Grown on Polyaniline Nano fi bers for Bistable Memory Devices. ACS Nano 2011;5:3469–74.

[176] Merino E, Ribagorda M. Control over molecular motion using the cis-trans photoisomerization of the azo group. Beilstein J Org Chem 2012;8:1071–90. doi:10.3762/bjoc.8.119.

[177] Mahimwalla Z, Yager KG, Mamiya JI, Shishido A, Priimagi A, Barrett CJ. Azobenzene photomechanics: Prospects and potential applications. vol. 69. Springer; 2012. doi:10.1007/s00289-012-0792-0.

[178] Natansohn, A, Rochon P., Gosselin J. XS. Azo Polymers for Reversible Optical Storage. 1. Poly[4’- [[2- (acr yloyloxy)ethyll ethylaminol-4-ni troazo benzene]. Macromolecules 1992;25:2268–73. doi:10.1021/ma00034a031.

[179] Yager KG, Tanchak OM, Godbout C, Fritzsche H, Barrett CJ. Photomechanical effects in azo-polymers studied by neutron reflectometry. Macromolecules 2006;39:9311–9. doi:10.1021/ma0617320.

[180] Barrett CJ, Mamiya J, Yager KG, Ikeda T. Photo-mechanical effects in azobenzene-containing soft materials. Soft Matter 2007;3:1249. doi:10.1039/b705619b.

[181] Greene LE, Law M, Tan DH, Montano M, Goldberger J, Somorjai G, et al. General route to vertical ZnO nanowire arrays using textured ZnO seeds. Nano Lett 2005;5:1231–6. doi:10.1021/nl050788p.

[182] Unalan HE, Hiralal P, Rupesinghe N, Dalal S, Milne WI, Amaratunga GAJ. Rapid synthesis of aligned zinc oxide nanowires. Nanotechnology

2008;19:255608. doi:10.1088/0957-4484/19/25/255608.

[183] Ladanov M, Ram MK, Matthews G, Kumar A. Structure and Opto-electrochemical Properties of ZnO Nanowires Grown on n -Si Substrate. Langmuir 2011;27:9012–7.

[184] Schmidt R, Prado-gonjal J, Morán E. Microwaves : Microwave-Assisted Hydrothermal Synthesis of Nanoparticles 2016;12:561–72.

[185] Menzel H, Weichart B, Hallensleben ML. Langmuir-Blodgett-films of photochromic polyglutamates II Synthesis and spreading behaviour of photochromic polyglutamates with alkylspacers and -tails of different length. Polym Bull 1992;27:637–44. doi:10.1007/BF00310794.

[186] S. S, Zeng H., Guo C. CW. Nanomaterials Processing and Characterization with Lasers. Weinheim, Germany: WILEY-VCH Verlag GmbH & Co. KGaA; 2012.

[187] Chen J-Y, Hsu F-C, Sung Y-M, Chen Y-F. Enhanced charge transport in hybrid polymer/ZnO-nanorod solar cells assisted by conductive small molecules. J Mater Chem 2012;22:15726. doi:10.1039/c2jm31605f.

[188] Hou X, Wang L. Controllable fabrication and photocatalysis of ZnO/Au nanohybrids via regenerative ion exchange and reduction cycles. RSC Adv 2014;4:56945–51. doi:10.1039/C4RA10785C.

[189] Hebb DO. The Organization of Behavior. Wiley, 1949:335.

[190] Serrano-Gotarredona T, Masquelier T, Prodromakis T, Indiveri G, Linares-Barranco B. STDP and sTDP variations with memristors for spiking neuromorphic learning systems. Front Neurosci 2013;7:1–15. doi:10.3389/fnins.2013.00002.

[191] Li Y, Zhong Y, Zhang J, Xu L, Wang Q, Sun H, et al. Activity-dependent synaptic plasticity of a chalcogenide electronic synapse for neuromorphic systems. Sci Rep 2014;4:1–7. doi:10.1038/srep04906.

[192] Bozano LD, Kean BW, Beinhoff M, Carter KR, Rice PM, Scott JC. Organic materials and thin-film structures for cross-point memory cells based on trapping in metallic nanoparticles. Adv Funct Mater 2005;15:1933–9. doi:10.1002/adfm.200500130.

[193] Tang W, Shi HZ, Xu G, Ong BS, Popovic ZD, Deng JC, et al. Memory Effect and Negative Differential Resistance by Electrode- Induced Two-Dimensional Single- Electron Tunneling in Molecular and Organic Electronic Devices. Adv Mater 2005;17:2307–11. doi:10.1002/adma.200500232.

[194] You YT, Zeng Q, Yao Y, Wang ML, Wu B, He Y, et al. Field-induced evolution of metallic nano-tips in indium tin oxide-tris-(8-hydroxyquinoline) aluminum-aluminum device. Appl Phys Lett 2012;100. doi:10.1063/1.3697829.

[195] Mostafaei A, Zolriasatein A. Synthesis and characterization of conducting polyaniline nanocomposites containing ZnO nanorods. Prog Nat Sci Mater Int 2012;22:273–80. doi:10.1016/j.pnsc.2012.07.002.

[196] Samanta S, Beharry AA, Sadovski O, McCormick TM, Babalhavaeji A, Tropepe V, et al. Photoswitching Azo compounds in vivo with red light. J Am Chem Soc 2013;135:9777–84. doi:10.1021/ja402220t.

[197] Dong M, Babalhavaeji A, Samanta S, Beharry AA, Woolley GA. Red-Shifting Azobenzene Photoswitches for in Vivo Use. Acc Chem Res 2015;48:2662–70. doi:10.1021/acs.accounts.5b00270.

[198] Yager KG, Barrett CJ. Novel photo-switching using azobenzene functional materials. J Photochem Photobiol A Chem 2006;182:250–61. doi:10.1016/j.jphotochem.2006.04.021.

[199] Liu P, She G, Liao Z, Wang Y, Wang Z, Shi W, et al. Observation of persistent photoconductance in single ZnO nanotube. Appl Phys Lett 2009;94:1–4. doi:10.1063/1.3082173.

[200] Dürr AC, Schreiber F, Kelsch M, Carstanjen HD, Dosch H, Seeck OH. Morphology and interdiffusion behavior of evaporated metal films on crystalline diindenoperylene thin films. J Appl Phys 2003;93:5201–9. doi:10.1063/1.1556180.

[201] Busby Y, Nau S, Sax S, List-Kratochvil EJW, Novak J, Banerjee R, et al. Direct observation of conductive filament formation in Alq3 based organic resistive memories. J Appl Phys 2015;118:1–6. doi:10.1063/1.4928622.

[202] Ramana CV V, Moodely MK, Kannan V, Maity A, Jayaramudu J, Clarke W. Fabrication of stable low voltage organic bistable memory device. Sensors Actuators, B Chem 2012;161:684–8. doi:10.1016/j.snb.2011.11.012.

[203] Lanza M, Bersuker G, Porti M, Miranda E, Nafría M, Aymerich X. Resistive switching in hafnium dioxide layers: Local phenomenon at grain boundaries. Appl Phys Lett 2012;101:1–5. doi:10.1063/1.4765342.

[204] Heluani SP, Braunstein G, Villafuerte M, Simonelli G, Duhalde S. Electrical conductivity mechanisms in zinc oxide thin films deposited by pulsed laser deposition using different growth environments. Thin Solid Films 2006;515:2379–86. doi:10.1016/j.tsf.2006.04.038.

[205] Zheng K, Zhao JL, Leck KS, Teo KL, Yeo EG, Sun XW. A ZnTaOx Based Resistive Switching Random Access Memory. ECS Solid State Lett 2014;3:Q36–9. doi:10.1149/2.0101407ssl.

[206] Huang CH, Huang JS, Lai CC, Huang HW, Lin SJ, Chueh YL. Manipulated transformation of filamentary and homogeneous resistive switching on ZnO thin film memristor with controllable multistate. ACS Appl Mater Interfaces 2013;5:6017–23. doi:10.1021/am4007287.

[207] Poprawa-Smoluch M, Baggerman J, Zhang H, Maas HPA, De Cola L, Brouwer AM. Photoisomerization of disperse red 1 studied with transient absorption spectroscopy and quantum chemical calculations. J Phys Chem A 2006;110:11926–37. doi:10.1021/jp054982b.

[208] Lee E, Lee J, Kim J-H, Lim K-H, Seok Byun J, Ko J, et al. Direct electron injection into an oxide insulator using a cathode buffer layer. Nat Commun 2015;6:6785. doi:10.1038/ncomms7785.

[209] Hümmelgen IA, Roman LS, Nart FC, Péres LO, De Sá EL. Polymer and polymer/metal interface characterization via Fowler-Nordheim tunneling measurements. Appl Phys Lett 1996;68:3194–6. doi:10.1063/1.116056.

[210] Lewis TJ. Charge transport, charge injection and breakdown in polymeric insulators. J Phys D Appl Phys 1990;23:1469–78. doi:10.1088/0022-3727/23/12/001.

[211] Valov I, Linn E, Tappertzhofen S, Schmelzer S, Van Den Hurk J, Lentz F, et al. Nanobatteries in redox-based resistive switches require extension of memristor theory. Nat Commun 2013;4:1771–9. doi:10.1038/ncomms2784.

[212] Tsuruoka T, Terabe K, Hasegawa T, Valov I, Waser R, Aono M. Effects of moisture on the switching characteristics of oxide-based, gapless-type atomic switches. Adv Funct Mater 2012;22:70–7. doi:10.1002/adfm.201101846.

[213] Nakagawa M. and Mitsudo H. Anomalous Temperature Dependence of the Electrical Conductivity of Zinc Oxide thin Films. Surf Sci 1986;175:157–76.

[214] Onsager L. Deviations from Ohm's law in weak electrolytes. J Chem Phys 1934;2:599–615. doi:10.1063/1.1749541.

[215] Yingtao L, Shibing L, Qi L, Hangbing L, Su L, Ming L. An overview of resistive random access memory devices. Optoelectronics 2011;56:3072–8. doi:10.1007/.

[216] Li H, Chen Q, Chen X, Mao Q, Xi J, Ji Z. Improvement of resistive switching in ZnO film by Ti doping. Thin Solid Films 2013;537:279–84. doi:10.1016/j.tsf.2013.04.028.

[217] Qin SC, Dong RX, Yan XL. Memristive behavior of ZnO film with embedded Ti nano-layers. Appl Phys A Mater Sci Process 2014;116:1–7. doi:10.1007/s00339-014-8450-z.

[218] Gupta S, Zhang Q, Emrick T, Balazs AC, Russell TP. Entropy-driven segregation of nanoparticles to cracks in multilayered composite polymer structures. Nat Mater 2006;5:229–33. doi:10.1038/nmat1582.

[219] Wei H, Eilers H. Electrical conductivity of thin-film composites containing silver nanoparticles embedded in a dielectric fluoropolymer matrix. Thin Solid Films 2008;517:575–81. doi:10.1016/j.tsf.2008.06.093.

[220] Scott BJC, Bozano LD. Nonvolatile Memory Elements Based on Organic Materials. Adv Mater 2007;19:1452–63. doi:10.1002/adma.200602564.

[221] Mukherjee B, Mukherjee M. Nonvolatile memory device based on Ag nanoparticle: Characteristics improvement. Appl Phys Lett 2009;94.

doi:10.1063/1.3127233.

[222] Algers J, Sperr P, Egger W, Liszkay L, Kögel G, De Baerdemaeker J, et al. Free volume determination of azobenzene-PMMA copolymer by a pulsed low-energy positron lifetime beam with in-situ UV illumination. Macromolecules 2004;37:8035–42. doi:10.1021/ma0486086.

[223] El Halabieh RH, Mermut O, Barrett CJ. Using light to control physical properties of polymers and surfaces with azobenzene chromophores. Pure Appl Chem 2004;76:1445–65. doi:10.1351/pac200476071445.

[224] Prime D, Paul S, Josephs-Franks PW. Gold nanoparticle charge trapping and relation to organic polymer memory devices. Philos Trans R Soc A Math Phys Eng Sci 2009;367:4215–25. doi:10.1098/rsta.2009.0141.

[225] Jin Z, Liu G, Wang J. Organic nonvolatile resistive memory devices based on thermally deposited Au nanoparticle. AIP Adv 2013;3. doi:10.1063/1.4804948.

[226] Lin HT, Pei Z, Chan YJ. Carrier transport mechanism in a nanoparticle-incorporated organic bistable memory device. IEEE Electron Device Lett 2007;28:569–71. doi:10.1109/LED.2007.899668.

[227] Zhong S, Duan S, Cui Y. Electrode dependence of resistive switching in Au/Ni–Au nanoparticle devices. RSC Adv 2014;4:40924–9. doi:10.1039/C4RA05662K.

[228] Pagnia H, Sotnik N. Bistable switching in electroformed metal–insulator–metal devices. Phys Status Solidi 1988;108:11–65. doi:10.1002/pssa.2211080102.

[229] Nau S, Sax S, List-Kratochvil EJW. Unravelling the nature of unipolar resistance switching in organic devices by utilizing the photovoltaic effect. Adv Mater 2014;26:2508–13. doi:10.1002/adma.201305369.

[230] Cho B, Yun JM, Song S, Ji Y, Kim DY, Lee T. Direct observation of Ag filamentary paths in organic resistive memory devices. Adv Funct Mater 2011;21:3976–81. doi:10.1002/adfm.201101210.

[231] Chua L. Memristor, Hodgkin-Huxley, and edge of chaos. Nanotechnology 2013;24:1–14. doi:10.1088/0957-4484/24/38/383001.

[232] Kuzum D, Yu S, Philip Wong H-S. Synaptic electronics: materials, devices and applications. Nanotechnology 2013;24:1–22. doi:10.1088/0957-4484/24/38/382001.

[233] Snider GS. Self-organized computation with unreliable, memristive nanodevices. Nanotechnology 2007;18. doi:10.1088/0957-4484/18/36/365202.

[234] Prezioso M, Merrikh-Bayat F, Hoskins BD, Adam GC, Likharev KK, Strukov DB. Training and operation of an integrated neuromorphic network based on metal-oxide memristors. Nature 2015;521:61–4. doi:10.1038/nature14441.

[235] Markram H, Lubke J, Frotscher M, Sakmann B. Regulation of {S}ynaptic {E}fficacy by Coindence of Postsynaptic APs and EPSPs. Science (80-) 1997;275:213–5.

[236] Wang Z, Yin M, Zhang T, Cai Y, Wang Y, Yang Y, et al. Engineering incremental resistive switching in TaO: Xbased memristors for brain-inspired computing. Nanoscale 2016;8:14015–22. doi:10.1039/c6nr00476h.